Modeling and simulations of marine sectors of the Antarctic ice sheet across various spatial scales: the subglacial environment and its impact on instabilities

Thesis submitted by Thomas Gregov
in partial fulfillment of the requirements for the degree of Doctor of Philosophy (PhD) in Engineering Science (ULiège) and in Sciences (ULB)
February 2025

Supervisors: Professor Maarten Arnst (Université de Liège)
Aerospace and Mechanical Engineering
Computational and Stochastic Modeling
and Professor Frank Pattyn (Université libre de Bruxelles)
Geosciences, Environment and Society
Laboratoire de Glaciologie

Thesis jury :
Maarten Arnst (Université de Liège)
Benjamin Dewals (Université de Liège)
Elisa Mantelli (Ludwig-Maximilians-Universität München)
Frank Pattyn (Université libre de Bruxelles)
Mauro Perego (Sandia National Laboratories)
Laurence Rongy (Université libre de Bruxelles)

FREEDOM TO RESEARCH

First printing, February 2025

Thesis jury:

The present dissertation has been evaluated by the members of the Jury (sorted by alphabetical order):

Maarten Arnst	(Supervisor)	Université de Liège;
Benjamin Dewals	(Chair)	Université de Liège;
Elisa Mantelli		Ludwig-Maximilians-Universität München;
Frank Pattyn	(Co-supervisor)	Université libre de Bruxelles;
Mauro Perego		Sandia National Laboratories;
Laurence Rongy		Université libre de Bruxelles.

Funding:

This research was financially supported by the Fonds de la Recherche Scientifique de Belgique (F.R.S.-FNRS) through a Research Fellowship, by the Fonds David et Alice Van Buuren and the Fondation Jaumotte-Demoulin, and by the School of Engineering of the Université de Liège.

A scientific stay at Sandia National Laboratories was supported by the F.R.S.-FNRS through a mobility grant and by Wallonie-Bruxelles International (WBI) though an excellence fellowship (WBI.World).

Computational resources have been provided by the Consortium des Équipements de Calcul Intensif (CÉCI), funded by the F.R.S.-FNRS under Grant No. 2.5020.11 and by the Walloon Region.

Modeling and simulations of marine sectors of the Antarctic ice sheet across various spatial scales: the subglacial environment and its impact on instabilities

Thomas Gregov

Abstract

The Antarctic ice sheet is a major potential contributor to future sea-level rise, and its marine regions, containing both grounded and floating sections, represent non-linear physical systems potentially subject to tipping points. The subglacial environment of these marine sectors plays a crucial role in marine ice-sheet dynamics, yet it remains challenging to model due to the many unknowns surrounding it. This thesis aims to understand how subglacial conditions impact instabilities in marine ice sheets based on three original contributions that rely on analytical and numerical approaches across various spatial scales.

The first contribution examines grounding-line flux conditions which are semi-analytical expressions used to determine ice flux at the grounding line. These flux conditions depend on the friction law that is used to model the interactions between the ice and the bed on the grounded area of marine ice sheets. We generalize the flux conditions, historically derived for Weertman and Coulomb friction laws, to accommodate more complex laws like the Budd friction law, which includes the effective pressure applied by the ice on the bed, and hybrid laws combining viscous and plastic behavior. Using asymptotic developments, we demonstrate the existence and uniqueness of solutions to this boundary-layer problem and propose explicit flux expressions that remain valid in cases of steep slopes and low friction coefficients.

The second contribution presents a fast and simplified subglacial hydrological model for the Antarctic ice sheet, incorporating efficient and inefficient drainage systems and accounting for both hard and soft bed types. Applied to Thwaites Glacier, this model shows that subglacial hydrology accelerates grounding-line retreat, with the retreat rates being a function of the efficiency of the drainage system and of the type of bed. We also highlight that the retreat dynamics near the grounding line are primarily driven by steep effective pressure gradients, rather than by the absolute value of effective pressure itself.

The third contribution of this thesis investigates the effect of pinning points –locations where the ice temporarily grounds on bedrock peaks, adding stability to the ice sheet– on ice-sheet dynamics, particularly on the grounding line, the boundary between grounded and floating ice. We show that a singular behavior can arise at these points, where the linearized problem associated with the mass and momentum-balance equations becomes ill-defined, with infinite gradients in the momentum-balance equation. This singularity raises important questions about current models and how grounding lines are treated in numerical simulations, indicating the need for alternative formulations to improve modeling accuracy.

Overall, this thesis demonstrates the significance of subglacial conditions on Antarctic marine ice-sheet dynamics and proposes advancements to improve their modeling. These findings suggest that refining predictions in response to a changing climate will require model developments that better represent local ice-bedrock interactions and the spatial-temporal evolution of subglacial hydrology.

Key-words: marine ice sheets, numerical simulations, boundary layers, basal friction, subglacial hydrology.

Modélisation et simulations de secteurs marins de la calotte antarctique sur plusieurs échelles spatiales : l'environnement sous-glaciaire et son impact sur les instabilités

Thomas Gregov

Résumé

La calotte glaciaire de l'Antarctique est un contributeur potentiel majeur à la future hausse du niveau global des mers, et ses régions marines, composées à la fois de sections ancrées dans la roche et de régions flottant sur l'océan, représentent des systèmes physiques non linéaires susceptibles de former des points de basculement. Le milieu sous-glaciaire de ces secteurs marins joue un rôle crucial dans la dynamique des calottes glaciaires marines, mais reste difficile à modéliser en raison des nombreuses inconnues le caractérisant. Cette thèse vise à comprendre comment les conditions sous-glaciaires influencent les instabilités des calottes marines, grâce à trois contributions originales s'appuyant sur des approches analytiques et numériques à différentes échelles spatiales.

La première contribution de cette thèse se concentre sur les conditions de flux qui sont des expressions semi-analytiques permettant de déterminer le flux de glace à la ligne d'ancrage. Ces conditions de flux dépendent de la loi de friction utilisée pour modéliser les interactions entre la glace et la roche dans la zone ancrée des calottes glaciaires marines. Nous généralisons les conditions de flux, historiquement dérivées pour les lois de Weertman et de Coulomb, afin de les adapter à des lois plus complexes comme la loi de Budd, qui inclut la pression effective que la glace exerce sur le substrat rocheux, ainsi qu'à des lois hybrides combinant un comportement visqueux et plastique. En utilisant des développements asymptotiques, nous montrons l'existence et l'unicité des solutions de ce problème de couche limite et proposons des expressions explicites du flux adaptées aux situations de pentes importantes et de faibles coefficients de friction.

La deuxième contribution propose un modèle hydrologique sous-glaciaire simplifié et rapide pour la calotte antarctique, intégrant à la fois des systèmes de drainage efficaces et inefficaces, et prenant en compte différents types de lits rocheux (déformable et rigide). Appliqué au glacier Thwaites, ce modèle montre que l'hydrologie sous-glaciaire accélère le retrait de la ligne d'ancrage, les taux de retrait étant fonction de l'efficacité du système de drainage et du type de lit rocheux. Nous soulignons également que la dynamique de retrait près de la ligne d'ancrage est principalement influencée par les forts gradients de pression effective, plutôt que par la valeur absolue de la pression effective elle-même.

La troisième contribution étudie l'effet des points de contact –les zones où la glace s'ancre temporairement sur des pics du substrat rocheux, stabilisant ainsi la calotte glaciaire– sur la dynamique de ces calottes, en particulier sur la ligne d'ancrage, limite entre la glace ancrée et la glace flottante. Nous montrons qu'un comportement singulier peut apparaître à ces points, où le problème linéarisé associé aux équations de conservation de masse et de quantité de mouvement devient mal défini, avec des gradients infinis dans l'équation de la quantité de mouvement. Cette singularité soulève des questions importantes concernant les modèles actuels et la manière dont les lignes d'ancrage sont traitées dans les simulations numériques, suggérant le besoin de formulations alternatives pour améliorer la précision des modèles.

En conclusion, cette thèse démontre l'importance des conditions sous-glaciaires dans la dynamique des parties marines de la calotte antarctique et propose des avancées pour améliorer leur modélisation. Ces travaux suggèrent que, pour affiner les prédictions dans un contexte de changement climatique, il est nécessaire de développer des modèles capables de mieux représenter les interactions locales entre la glace et le substrat rocheux, ainsi que l'évolution spatio-temporelle de l'hydrologie sous-glaciaire.

Mots-clés: calottes glaciaires marines, simulations numériques, couches limites, friction basale, hydrologie sous-glaciaire.

Acknowledgments

Bien que la défense d'une thèse représente l'accomplissement d'un travail de recherche personnel, il n'en reste pas moins qu'une thèse est également le fruit de questionnements, échanges, collaborations, discussions avec de nombreuses personnes. Je tiens ici à les remercier.

Tout d'abord, je tiens à remercier mes promoteurs, Maarten Arnst et Frank Pattyn. Merci à Maarten de m'avoir proposé ce sujet de recherche, et de m'avoir supervisé pendant ces plus de quatre années. Merci également pour tes nombreux retours sur mes travaux, tant sur ce manuscrit que sur les articles scientifiques que nous avons co-écrits. Merci à Frank de m'avoir accueilli aussi chaleureusement au sein du Laboratoire de Glaciologie alors que tu ne me connaissais que très peu. Merci pour ton optimisme et ton enthousiasme.

I wish to thank Benjamin Dewals, Elisa Mantelli, Mauro Perego, and Laurence Rongy for accepting to be a part of my thesis jury. I also want to thank you for taking the time to read my thesis, for your suggestions for improvement, and for the scientific discussions.

Je voudrais également remercier l'ensemble des membres de mon comité d'accompagnement, Jean-Marie Beckers, Benjamin Dewals, François Fripiat et Christophe Geuzaine pour avoir suivi l'avancement de ma thèse tout au long de ces années. Merci pour votre temps et vos retours toujours positifs.

During my thesis, I had the opportunity to go abroad thanks to a scientific stay. I wish to thank Kim Liégeois and Mauro Perego for making this trip possible and for making it a memorable experience. I really enjoyed my stay and it is in great part thanks to you.

J'aimerais également remercier mes collègues de l'Université de Liège. Au sein du laboratoire de Computational & Stochastic Modeling, merci à Arnaud B., Arnaud R., Joffrey, Martin et Romin pour avoir été d'excellents collègues de groupe et de bureau. Merci aux membres du prestigieux groupe 'manger midi' avec qui il est toujours possible d'échanger sur nos recherches respectives, mais surtout d'entrer dans des discussions particulièrement sensées (aucune ironie ici bien sûr). Une mention particulière à Adrien, Amaury, Arnaud, Nayan et Nicolas pour les sorties en conférence, les quelques repas et bières partagés, et les discussions autour de nos (més)aventures pendant la thèse. J'espère que vous savez maintenant ce que sont la shallow-shelf approximation (à dire très vite) et les ice (high) sheets.

À l'Université libre de Bruxelles, j'aimerais remercier l'ensemble des membres du Laboratoire de Glaciologie pour avoir été des super collègues. Merci pour les repas de midi et les sorties Pickwick. J'aimerais remercier plus particulièrement Elise, Sarah et Vio. Merci à Elise pour ta bonne humeur et pour m'avoir épaulé dans la deuxième partie de ma thèse. Il est fréquent d'entendre que le parcours d'un thésard prend la forme d'une première partie un peu laborieuse qui commence à s'éclairer à partir d'un moment clé. Je ne déroge pas à la règle; dans mon cas, ce 'tipping point' fut clairement la conception de notre papier commun. Merci également pour les relectures attentives, en particulier sur ce qui concerne l'hydrologie. Merci à Sarah pour le soutien et les discussions que nous qualifierons de schtroumpferies. Merci à Vio pour les discussions, conseils et suggestions toujours pertinents.

Je voudrais de plus remercier l'ensemble des personnes que j'ai pu rencontrer le long de cette thèse, que ce soit lors de conférences, de séjours de recherche ou d'écoles d'été.

Enfin, je voudrais remercier ma famille et mes amis pour leur soutien continu.

Contents

1 Introduction **3**
1.1 Context . . . 3
1.1.1 The climate system of the 21st century . . . 3
1.1.2 The cryosphere . . . 4
1.1.3 Marine sectors of the Antarctic ice sheet . . . 6
1.2 Motivation . . . 9
1.3 Overview of the manuscript . . . 11

I Modeling marine ice sheets: an overview **13**

2 Mechanics of marine ice sheets **15**
2.1 Introduction . . . 15
2.2 Continuum mechanics . . . 15
2.2.1 Kinematics . . . 15
2.2.2 Dynamics . . . 18
2.3 Ice flow . . . 19
2.3.1 Rheology . . . 19
2.3.2 Thermal properties . . . 23
2.3.3 Balance equations . . . 23
2.3.4 Initial and boundary conditions . . . 24
2.4 Summary of the governing equations . . . 29
2.4.1 Equations for ice flow . . . 29
2.4.2 Challenges . . . 30
2.4.3 Limitations . . . 31
2.5 Interactions with other components of the Earth System . . . 32
2.5.1 Ice-atmosphere interactions . . . 32
2.5.2 Ice-ocean interactions . . . 33
2.5.3 Ice-bedrock interactions . . . 33

3 Stress approximations for ice flow **35**
3.1 Motivation . . . 35
3.2 Principal approximations . . . 36
3.2.1 Blatter–Pattyn model . . . 36
3.2.2 Shallow-shelf approximation . . . 38
3.2.3 Shallow-ice approximation . . . 39
3.2.4 Summary . . . 41
3.3 Approximations to higher-order models . . . 41
3.3.1 Hybrid models . . . 41
3.3.2 Depth-integrated models . . . 42
3.3.3 Multilayer models . . . 42

3.4 Practical aspects . . . 42
3.4.1 Validity of the approximations . . . 42
3.4.2 Implementations . . . 43

4 The subglacial environment **45**
4.1 Introduction . . . 45
4.2 Basal friction . . . 45
4.2.1 Hard beds . . . 46
4.2.2 Soft beds . . . 52
4.2.3 Towards a unified friction law . . . 55
4.3 Subglacial hydrology . . . 56
4.3.1 Effective pressure and hydraulic potentials . . . 56
4.3.2 Hard beds . . . 57
4.3.3 Soft beds . . . 62
4.3.4 Multi-drainage models . . . 70

List of symbols **75**

II Original contributions 83

5 Extension of grounding-line flux conditions **85**
5.1 Introduction . . . 85
5.2 Problem formulation . . . 86
5.2.1 Governing equations . . . 87
5.2.2 Friction laws . . . 89
5.2.3 Dimensionless formulation . . . 91
5.2.4 Flux conditions . . . 91
5.3 Generalization to the Budd friction law . . . 92
5.3.1 Derivation of the flux condition . . . 93
5.3.2 Analysis of the leading-order dynamical system . . . 95
5.3.3 Existence of a boundary layer . . . 98
5.4 Generalization to hybrid friction laws . . . 100
5.5 Effect of α, β, and γ . . . 102
5.5.1 Non-vanishing friction law with $\gamma \sim 1$: negligible membrane-stress divergence . . . 104
5.5.2 Vanishing friction law: non-negligible membrane-stress divergence . . . 106
5.5.3 Non-vanishing friction law with $\gamma \ll 1$ . . . 107
5.6 Verification with numerical experiments . . . 108
5.6.1 Set-up . . . 108
5.6.2 Flux conditions for the Budd and hybrid friction laws . . . 109
5.6.3 Effect of α, β, and γ . . . 111
5.7 Discussion . . . 113
5.7.1 Specifications of the obtained flux conditions . . . 113
5.7.2 Limitations . . . 114
5.8 Conclusion . . . 115
5.9 Appendix A: Analysis of the leading-order dynamical system: vanishing friction at the grounding line . . . 117
5.9.1 Problem formulation . . . 117
5.9.2 Principle of the analysis . . . 117
5.9.3 Derivation of the intermediary properties . . . 118
5.10 Appendix B: Numerical solving strategy for finding $\tilde{Q}_{\mathrm{gl}}$ . . . 119

6 A fast and simplified subglacial hydrological model **121**
6.1 Introduction . . . 121
6.2 Model description . . . 123
6.2.1 Ice-flow model . . . 123
6.2.2 Hydrological model . . . 123
6.3 Idealized experiments . . . 131
6.3.1 Experimental setup . . . 131
6.3.2 Results: the efficient to inefficient switch . . . 132
6.3.3 Results: perturbation experiment . . . 134
6.4 Application to Thwaites Glacier . . . 134
6.4.1 Experimental setup . . . 134
6.4.2 Results: subglacial hydrology on homogeneous beds . . . 135
6.4.3 Results: subglacial hydrology on heterogeneous beds . . . 137
6.5 Discussion . . . 137
6.5.1 Influence of subglacial conditions . . . 139
6.5.2 Hydrological feedback . . . 140
6.5.3 Model limitations . . . 141
6.6 Conclusions . . . 141
6.7 Appendix A: List of symbols . . . 143
6.8 Appendix B: The effective pressure near the grounding line: a boundary-layer analysis . . . 144
6.8.1 Problem statement . . . 144
6.8.2 Dimensionless equations . . . 144
6.8.3 Outer solution . . . 145
6.8.4 Inner solution . . . 145
6.8.5 Composite solution . . . 146
6.9 Appendix C: Effect of the coupling frequency between the hydrological and ice-sheet models . . . 146
6.9.1 MISMIP . . . 147
6.9.2 Thwaites . . . 147
6.10 Appendix D: Influence of the unconstrained parameters of the hydrological model . . . 147

7 Singularity at pinning points **149**
7.1 Introduction . . . 149
7.2 Model . . . 151
7.2.1 Notations . . . 151
7.2.2 Strong formulation . . . 151
7.2.3 Weak formulation . . . 155
7.3 Grounding-line motion and singularity . . . 155
7.3.1 The linearized problem . . . 155
7.3.2 Singularity . . . 157
7.3.3 A regularized approach . . . 157
7.4 Numerical experiments . . . 159
7.4.1 Set-up . . . 160
7.4.2 Stress distribution . . . 161
7.4.3 Steady states . . . 161
7.4.4 Transient states . . . 166
7.5 Discussion . . . 167
7.5.1 Impact of pinning points . . . 167
7.5.2 Origin of the singularity . . . 170
7.5.3 Perspectives . . . 171
7.6 Conclusion . . . 172
7.7 Appendix A: Analytical expressions of the terms appearing in the linearized problem . . . 173

7.7.1 Residuals . . . 173
7.7.2 Gâteaux differentials . . . 173
7.8 Appendix B: Proofs of the propositions . . . 174
7.9 Appendix C: Continuation methods . . . 175
7.9.1 Pseudo-arclength continuation . . . 176
7.9.2 Objective-based continuation . . . 176

III Conclusions and directions for future work 179

8 Conclusions and perspectives 181
8.1 Summary and conclusions . . . 181
8.2 Suggestions and perspectives for future work . . . 182
8.2.1 Perspectives related to the original contributions . . . 182
8.2.2 Other perspectives . . . 185

Bibliography 187

1

Introduction

1.1 Context

1.1.1 The climate system of the 21st century

The climate has been of particular interest for several decades. Numerous observations have highlighted rapid changes in key indicators of the climate [Fig. 1.1; IPCC, 2021]. These changes are taking place in all components of the climate system: the atmosphere, cryosphere, biosphere and oceans, and are thus the result of a structural and global modification of the climate. It is now undeniable that these changes are the result of human activity, in particular due the increase in greenhouse gas emissions since the industrial era [Huber and Knutti, 2011; Gillett et al., 2021].

In this context, scientists are attempting to predict how the climate system will evolve over the coming decades and centuries. The aim of such predictions is twofold: first, to quantify the impacts of current anthropogenic activities to inform strategies for mitigating the adverse effects of climate change; second, to identify regions at risk from climate change, thereby facilitating the implementation of effective adaptation measures [Morecroft et al., 2019].

However, there are several major difficulties associated with the study of climate and its evolution. The first is conceptual and may seem obvious: conducting experiments on climate is not feasible. Scientists typically study physical systems through reproducible experiments, allowing them to assess how these systems react to various external stimuli and deduce their underlying dynamics. In the case of climate, this approach is not possible. Thus, scientists rely on modeling to investigate these systems. This involves developing a mathematical model that accurately represents the physical system –in this case, the climate or one of its components– based on established physical principles. The system is then analyzed mathematically, but more importantly, it is explored numerically. The advantage of numerical simulations lies in their ability to modify system parameters and external forcings. Conceptually, this approach functions as a numerical laboratory, similar to experiments conducted in a traditional laboratory. The model can then be modified and recalibrated according to current climate observations [Eyring et al., 2016].

Another difficulty associated with the study of climate concerns its nature. Climate is a physical system that is non-linear and stochastic [Dijkstra, 2013]. As a result, the climate's response to external modifications (e.g., an increase in temperature) is not proportional to changes in the latter. This non-linearity has several consequences. From a theoretical point of view, it greatly complicates the study of such a system, since many complex behaviors can appear in its evolution. In particular, the system will not only depend on its current state but also on its past states; physically, we speak of irreversibility. From a practical point of view, the non-linear nature of the climate system is worrying, as it means that

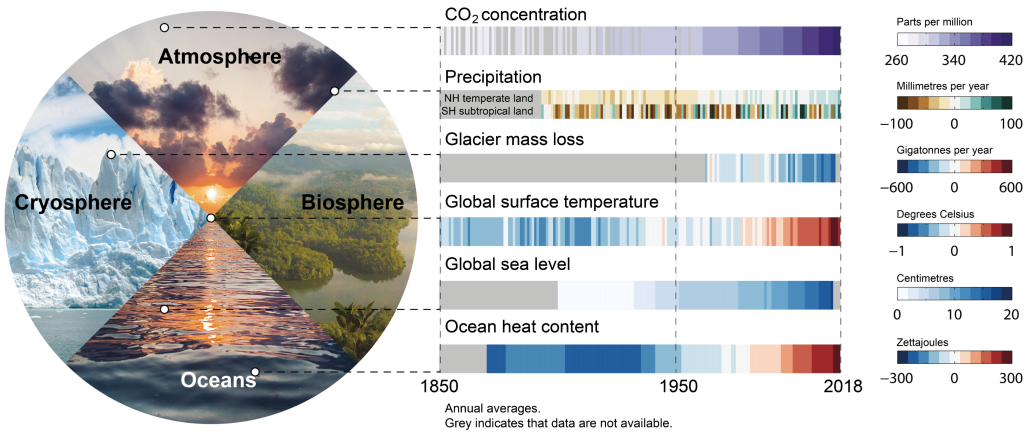

Figure 1.1: Changes in the main components of the climate system (atmosphere, cryosphere, biosphere, and oceans) based on the evolution of six key indicators from 1850 to 2018. Rapid changes in the indicators can be observed, especially in the last 50 years [Credit: Sixth Assessment Report of the IPCC; IPCC, 2021].

climatic changes can occur relatively abruptly, with large and rapid modifications (similar to what is currently being observed, as mentioned above).

These potential abrupt changes to the climate system are of particular interest to scientists and are therefore under close observation [Rosier et al., 2021; Dakos et al., 2024]. This has led them to identify so-called tipping points, which are such that any small subsequent change in the system –whether triggered by external disturbances or fluctuations in internal parameters– will induce qualitative changes in its response. Qualitative change here means that the system's behavior itself is altered; for example, the system may be brought to a new equilibrium state. Such a qualitative change is necessarily associated with significant quantitative changes in the system. A tipping point can be formalized as follows [Lenton, 2011]. Consider a physical system characterized by a feature F. The system depends on a parameter ρ. A tipping point then corresponds to the critical value $\rho = \rho_c$ at which a modification $\delta\rho$ leads to a qualitative change in the system, measured by a threshold value $\hat{F}$, after an observation time T:

$$|\Delta F| := |F(\rho \geq \rho_c + \delta\rho|T) - F(\rho_c|T)| \geq \hat{F} > 0. \tag{1.1}$$

As an illustration, F may represent mean sea level, while ρ corresponds to the global surface temperature. An illustration of tipping points according to the definition (1.1) is shown in figure 1.2. The main tipping points in the climate system are shown in figure 1.3. Note that the polar ice sheets have several tipping points that are likely to occur at relatively low global warming, below 2 °C [Garbe et al., 2020; Winkelmann et al., 2023; Klose et al., 2024]. These regions are therefore of particular interest, and are now described.

1.1.2 The cryosphere

The cryosphere comprises all the frozen parts of the climate system. This includes in particular glaciers, polar ice sheets (Greenland and Antarctica), and frozen ground ice. The focus here is on glaciers and polar ice sheets, for reasons that will become clear later on.

Glaciers and polar ice sheets are vast regions of ice that flow under their own weight. Formally, ice behaves like a shallow, shear-thinning fluid on geophysical time scales (say, of the order of several years): its behavior can be modeled as that of generalized Newtonian fluid with an effective viscosity that is a

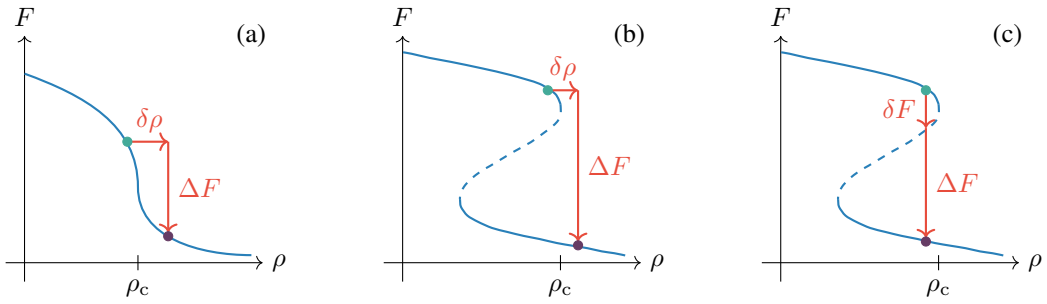

Figure 1.2: Illustration of the concept of tipping point [adapted from Lenton, 2011, 2013]. A tipping point is defined by the position $\rho = \rho_c$ (green point) from which a small perturbation leads to qualitative changes in the system (magenta point). This perturbation can take the form of an external perturbation $\delta\rho$, or of an internal variation δF. Quantitatively, the changes in the system are characterized by a switch ΔF in a feature F of the system. In the plots, the continuous lines correspond to stable equilibrium positions while the dashed ones correspond to unstable equilibrium positions. **(a)** Monostable system, in which the tipping behavior is associated with highly non-linear changes. **(b)** Bistable system, in which the tipping behavior is associated with the crossing of a saddle-node bifurcation. **(c)** Bistable system, in which the tipping behavior is associated with a noise-induced transition.

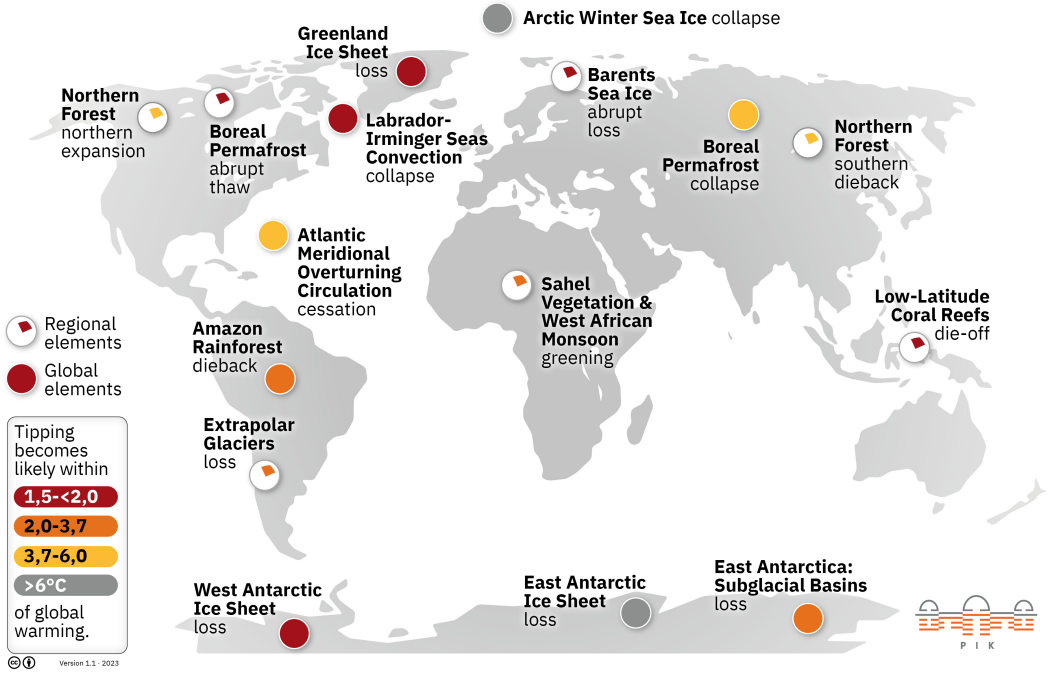

Figure 1.3: Main tipping points in the climate system with associated likelihood in the context of global warming [Credit: Potsdam Institute for Climate Impact Research (PIK)].

decreasing function of the strain rate [Glen, 1955; Schoof and Hewitt, 2013]. In high-altitude regions, ice accumulates thanks to precipitations. It is then carried by the ice flow to lower-altitude regions. In the case of outlet glaciers and marine ice sheets, ice is essentially lost by being discharged in the water through iceberg calving and by melting at the base of floating parts of ice sheets that are in contact with the ocean. This is the case of Antarctica, for example, which is in contact with the Southern Ocean. For land-terminated glaciers, on the other hand, ice is removed at lower altitude through sublimation and melt.

Overall, there is a dynamic balance between the amount of ice mass gained by glaciers and ice sheets and the amount lost. If mass gain exceeds mass loss, these glaciers and ice sheets will grow. On the other hand, if the gain is less than the loss, they will decrease in size. In the latter case, the ice that is lost does not vanish; in fact, it may be released back into the ocean directly (e.g., through discharges in oceans) or indirectly (e.g., through sublimation and then precipitation), ultimately leading to a rise in sea level. All in all, it follows that the evolution of the cryosphere is directly linked to the evolution of sea level. The reason why this rise needs to be monitored is that it has tangible effects on the habitability of various coastal areas, which could be flooded if sea levels were to rise significantly [Nicholls and Cazenave, 2010; Nicholls et al., 2021]. Furthermore, the release of freshwater into the ocean could modify the climate system itself, by altering ocean circulation [Bronselaer et al., 2018; Purich and England, 2023].

To quantify sea-level rise, the global mean-sea level (GMSL), which is defined as a spatially-averaged sea-level rise relative to a reference at a given time, is generally used. Over the period 1993–2018, the GMSL has risen by around 81.2 mm, with an average rate of increase of about 3.25 mm per year. This rise is attributed to several factors: thermal expansion at 45.9% (water takes up more space at higher temperatures), glaciers at 19.4%, the Greenland ice sheet at 15.2%, the Antarctic ice sheet at 8.6%, and the evolution of land-water storage at 10.9% [IPCC, 2021]. Thus, the current rise in GMSL is about half a consequence of thermal expansion, with cryosphere-related components responsible for only a few tens of percent. These data can be misleading as to the future evolution of the GMSL. It does not take into account the total potential effect of cryospheric components, should they melt completely and contribute to the sea-level rise. These potential contributions are given for glaciers: 0.32 ± 0.08 m; for the Greenland ice sheet: 7.42 ± 0.05 m; for the Antarctice ice sheet: 57.90 ± 0.90 m [Morlighem et al., 2017, 2019; Farinotti et al., 2019]. Although its current contribution to sea-level rise is relatively limited, the Antarctic ice sheet therefore has considerable potential for future sea-level rise. This potential is explained by Antarctica's continental dimensions (Fig. 1.4). This is also a first reason why this thesis focuses on sectors of the Antarctic ice sheet, rather than on other components of the cryosphere or of the climate system.

1.1.3 Marine sectors of the Antarctic ice sheet

The marine regions of the Antarctic ice sheet are those in contact with the ocean (Fig. 1.5). They take the form of ice masses that have both a grounded part, resting on bedrock, and a floating part, resting on the ocean. These two regions are separated by what is known as the grounding line. It is therefore important to study the evolution of the grounding line over time, whether through satellite observations or numerical modeling, as it is a proxy for the overall evolution of an ice sheet. In general, a retreating grounding line is associated with a reduction in ice-sheet size, and a positive contribution to sea-level rise.

Marine sectors of the Antarctic ice sheet are subject to a series of complex physical processes taking place on different spatial and temporal scales. These processes are such that the grounding line can evolve on relatively short timescales, depending on external disturbances associated with changes in atmospheric or oceanic conditions [Robel et al., 2018]. This vision of an Antarctic ice sheet that is not simply a passive component of the climate system, with a slow, uncertain and diffusive response, has only recently come into evidence. This has led to a paradigm shift, where marine areas need to be studied in detail, in view of the various mechanical, hydrological, and thermal processes taking place at these locations. Given that these processes are relatively unconstrained, they lead to greater uncertainty in

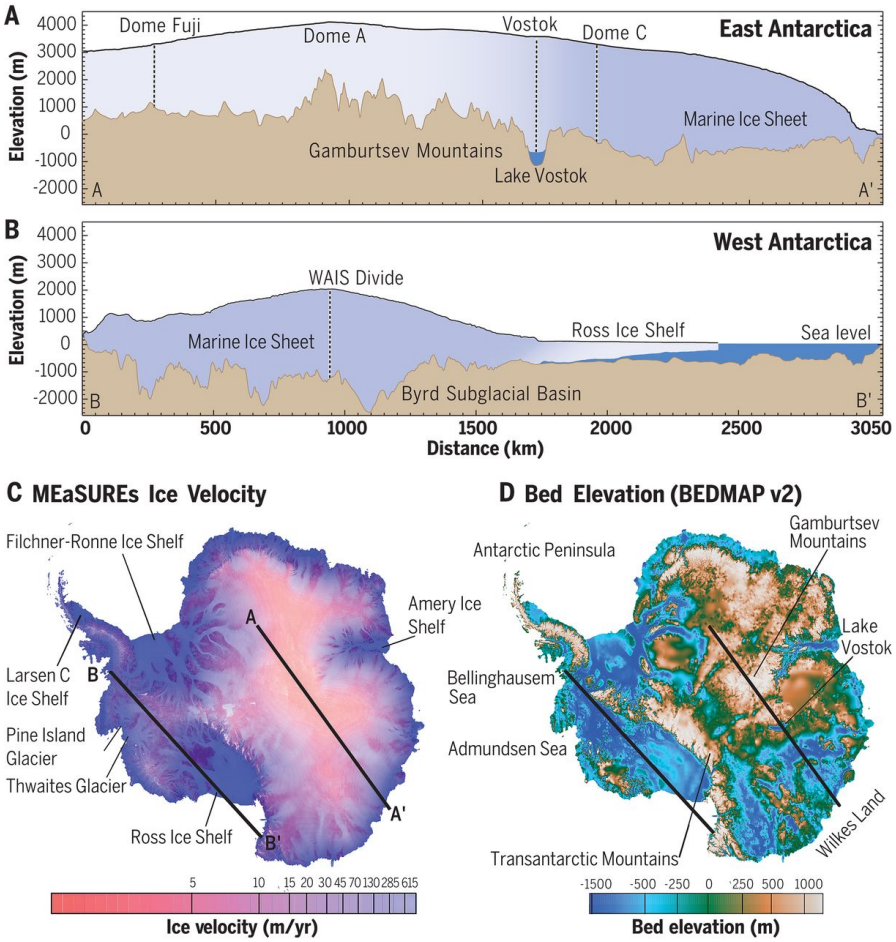

Figure 1.4: Maps of the Antarctic ice sheet [Credit: Bell and Seroussi, 2020].

(a) Photo of ice being discharged in the ocean in a Glacier near the Antarctic Peninsula [Credit: Dr. Alba Martin-Español].

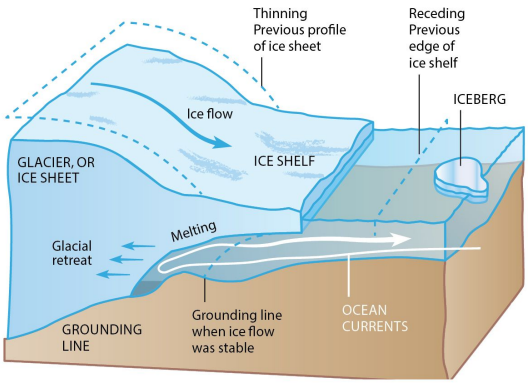

(b) Schematic of the main physical processes [Credit: National Snow and Ice Data Center].

Figure 1.5: Representations of marine ice sheets.

the ice-sheet response to a modification of the climate [Pattyn, 2018; Bulthuis et al., 2019; Pattyn and Morlighem, 2020]. This is a second reason for studying Antarctic marine sectors: they appear to be non-linear systems whose responses are complex. They can also lead to potential tipping points through various instability mechanisms.

The sensitivity of marine regions to external perturbations has been motivated by various instability mechanisms that can destabilize the grounding line, leading to large variations in their positions. A first instability is called 'marine ice-sheet instability' (MISI). Initiated by Weertman [1974], this mechanism suggests that marine ice sheets with a grounding line located on an up-sloping bed are unstable. This is because the ice flux at the grounding line is an increasing function of the ice thickness at that position, so that any initial retreat of the grounding line will be amplified in such areas, since there is then an increase in the outflow of ice. From a mathematical point of view, there is a difficulty in studying marine ice sheets in that the balance of forces is not the same on the grounded and floating parts, since the former is subject to basal friction but not the latter. Despite this, Schoof [2007b,c, 2012] succeeded in formalizing this instability in their seminal papers, thanks to a boundary-layer analysis of a one-dimensional marine ice sheet. In it, they proved that the grounding-line ice flux is indeed an increasing function of the grounding-line thickness, thereby providing a theoretical basis for MISI.

Several studies have attempted to improve our undestanding of MISI. They have highlighted the limitations in Schoof's initial model [2007c], which considered a one-dimensional ice sheet, and have subsequently extended the theory of marine ice sheets [Schoof et al., 2017; Pegler, 2018a,b; Book et al., 2022; Sergienko and Wingham, 2022; Sergienko, 2022a]. One of the factors that can attenuate or even remove MISI concerns the lateral stresses that can be applied to an ice sheet. This forms what is known as 'buttressing', which stabilizes the grounding lines by providing additional resistance to ice motion. In this way, grounding lines on up-sloping beds can remain stable if they are sufficiently laterally-confined. Despite these criticisms, it seems that MISI is a mechanism worthy of attention, as it helps to explain rapid and irreversible grounding-line retreat in regions with up-sloping beds that are not very confined. This is the case of large sectors in West Antarctica (see Fig. 1.4), and this mechanism could trigger a tipping point for this region: if the grounding line retreats too far, it could end up in areas with increasingly deep bedrock, leading to positive feedback and rapid and total collapse of West Antarctica [Favier et al., 2014; Joughin et al., 2014; Ritz et al., 2015; Garbe et al., 2020; Hill et al., 2023; Reese et al., 2023].

Another more fundamental criticism of the MISI concerns the fact that initial studies by Weertman [1974] and Schoof [2007c] considered stationary ice sheets, or ice sheets evolving on relatively large time scales that effectively allowed for a grounding-line motion that is slow. In reality, atmospheric and oceanic forcing can vary in an apparent random fashion on relatively small time scales, which has led some to question the validity of the MISI [Sergienko and Wingham, 2024]. According to them, a retreat of the grounding line over an area with an up-sloping bed would therefore not necessarily be associated with a MISI, but rather with rapid variability in the external conditions that apply to marine ice sheets. However, a bias in this analysis is that it only considers a single trajectory in the forcing. Indeed, the rigorous way to study a system subjected to stochastic forcing is to perform a probabilistic analysis on its response by studying the distribution of responses. By carrying out such an analysis, it can be shown that MISI does indeed appear as a mechanism that increases the probability of grounding-line retreat by skewing the probability distribution of grounding-line retreat so that the latter is more important [Robel et al., 2018, 2019; Mulder et al., 2018; Christian et al., 2020, 2022].

There are other potential instability mechanisms for marine ice sheets. The 'marine ice-cliff instability' (MICI) suggests a positive feedback between calving rate and ice thickness at the caving front, which may lead to an accelerated retreat of the grounding line if this instability is initiated. However, this instability is the source of much research within the scientific community, as it has not yet been observed and there is no consensus on it yet [Edwards et al., 2019; Bassis et al., 2021, 2024; Morlighem et al., 2024]. Finally, it has recently been suggested that the coupling between marine ice sheets and subglacial

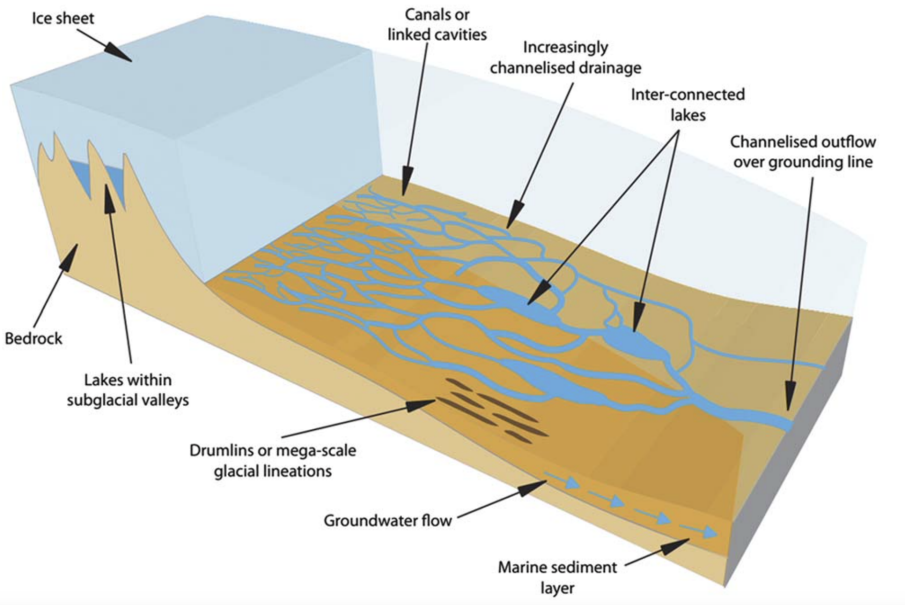

Figure 1.6: Schematic representation of several features of a subglacial hydrology system [Credit: Ashmore and Bingham, 2014].

hydrology could create an additional destabilization mechanism [Lu and Kingslake, 2024; Bradley and Hewitt, 2024].

The evolution of grounding lines depends on several physical processes. Among these, basal conditions play a major role [Brondex et al., 2017, 2019; Bulthuis et al., 2019; Kazmierczak et al., 2022]. At the base of the ice sheets, perturbations in the bedrock elevation slow down the ice flow by providing a form of resistance. Furthermore, the subglacial environment is also made up of a hydrological system that flows, like the ice, from the interior zones to the edges of the ice caps (Fig. 1.6). This hydrological system can lubricate the bed, thereby reducing its resistance. Since the subglacial environment is difficult to access, being located under one or more kilometers of ice, little is currently known about the processes that take place there. This leads to a number of models, both for basal friction and subglacial hydrology [e.g., Weertman, 1957; Schoof, 2005; Werder et al., 2013; Bueler and van Pelt, 2015; Sommers et al., 2018; Gilbert et al., 2022]. The fact that there are several models, and that they are not well constrained by observations, leads to uncertainty in the results of numerical simulations. The study of this subglacial environment therefore appears to be an important research program to improve our understanding of the dynamics of marine ice sheets, as well as the predictions of their evolution.

1.2 Motivation

The motivation for this thesis is based on the following three observations, which were described in the previous section:

i. The Antarctic ice sheet is a major potential contributor to future sea-level rise.

ii. Marine regions of Antarctica, which are marine ice sheets, are non-linear physical systems that could be subject to tipping points.

iii. The subglacial environment of marine ice sheets is an important control on marine ice-sheet dynamics, but there are still many unknowns about its modeling.

Combining these three points, we find that subglacial conditions are one of the major sources of uncertainty on the dynamics of Antarctica and therefore on its contribution to future sea-level rise. The aim of this thesis is to reduce this uncertainty by essentially answering the following overarching question:

How do subglacial conditions impact the dynamics of marine ice sheets?

To do this, we intend to apply a combination of analytical and numerical methods, and build on recent studies of the subglacial environment (bedrock topography, basal friction, and subglacial hydrology). Firstly, Robel et al. [2022a] have recently shown that marine ice sheets possess ambiguous behavior when their grounding lines lie on bed peaks, in that these grounding lines can either persist or retreat from these peaks. This suggests that the bedrock profile beneath the ice plays an important role in the dynamics of marine ice sheets; this had already been highlighted by the MISI. A question remains in that it is not clear whether this ambiguous behavior stems from the locally sharp character of the bed peaks, or whether this ambiguity is associated with the flow of marine ice sheets itself. There have been several numerical studies on bed peaks and in particular on pinning points, which are areas of ice shelves that are in contact with local bed peaks [Favier et al., 2012; Favier and Pattyn, 2015; De Rydt and Gudmundsson, 2016]. However, a theoretical understanding of the effects of (possibly smooth) bed peaks remains unexplored.

In terms of basal friction, the friction law that was most widely used in the glaciological community is the Weertman friction law, which relates basal velocity to basal friction through a power law [Weertman, 1957; Pattyn et al., 2012]. In particular, analytical studies of marine ice sheets, such as that proposed by Schoof [2007b,c] to explain MISI, are usually based on such a law. Such a law represents a viscous behavior for basal friction. However, numerous studies have recently suggested that friction laws should also contain a plastic component, associated with ice sliding on water-filled cavities or on deformable soft beds [Schoof, 2005, 2010a; Gagliardini et al., 2007; Tsai et al., 2015; Zoet and Iverson, 2015, 2020; Joughin et al., 2019; Minchew and Joughin, 2020; Helanow et al., 2021]. This raises the question of the effect of such plastic or visco-plastic laws on the behavior of marine ice sheets, and in particular on the MISI model proposed by Schoof.

Recent studies have also shown that subglacial hydrology has a major impact on the dynamics of the Antarctic ice sheet [e.g., Kazmierczak et al., 2022]. In addition, recent models have shown that subglacial hydrology is not a homogeneous system, but rather takes on a different form depending on the magnitude of the water flow that is transported [Schoof, 2010b; Werder et al., 2013]. The hydrological system can then switch from a distributed, inefficient system to a localized, efficient system. Subglacial hydrology models typically consider flow over a hard bed [Werder et al., 2013; Bueler and van Pelt, 2015; Hoffman et al., 2018; Sommers et al., 2018], despite studies that have shown subglacial hydrology takes a different form over soft beds [Walder and Fowler, 1994; Ng, 2000]. In addition, West Antarctica has been shown to contain both hard and soft beds [Joughin et al., 2009; Schroeder et al., 2014; Muto et al., 2019]. Thus, there is a need to build a model capable of simulating the flow of subglacial water over both hard and soft beds. Finally, the study of the coupling between subglacial hydrology and marine ice sheets is still in its infancy, with studies typically considering a coupling in idealized domains [e.g., Hoffman and Price, 2014; Gagliardini and Werder, 2018; Lu and Kingslake, 2024], or a subglacial hydrology system that does not evolve over time, in particular for studies that are performed over Antarctica [e.g., McArthur et al., 2023; Pelle et al., 2023]. Thus, the study of coupling between ice-sheet dynamics and subglacial hydrology over large-scale areas of interest (typically, West Antarctica) remains to be carried out.

Overall, these considerations lead us to formulate the following research sub-questions, which we will attempt to answer in this thesis:

Q1. How do bed peaks affect grounding-line motion?

Q2. How does the modeling of basal friction impact ice-sheet dynamics, in particular with respect to marine ice-sheet instability and Schoof's model?

Q3. How does an active coupling between marine ice sheets and subglacial hydrology modifies large-scale ice-sheet dynamics?

Q4. How does variability in the efficiency of a subglacial drainage system and in the bed type affects ice-sheet dynamics?

1.3 Overview of the manuscript

The manuscript is structured in three parts (see Tab. 1.1). The first part presents a general overview of the modeling of marine ice sheets. The aim of this part is to present the basics of ice-sheet mechanics, in particular how the equations of classical mechanics apply to the case of ice-sheet flow. As such, this section may be omitted by the reader who is already familiar with the models governing marine ice sheets. This first part is structured as follows. Starting with the equations of continuous mechanics, we first show how these are rewritten in view of the characteristics of ice sheets (Chapter 2). Next, we present the classical approximations used to simplify the stress state in the equations of ice flow (Chapter 3). Finally, an overview is given of the various research studies associated with the subglacial environment (Chapter 4). Particular attention is paid to recent developments in the modeling of basal friction and subglacial hydrology. To simplify the reading of this part, a list of symbols has been included at the end.

Chapter	Name	Type
	I. Modeling marine ice sheets: an overview	
2	Mechanics of marine ice sheets	Review
3	Stress approximations for ice flow	
4	The subglacial environment	
∗	List of symbols	
	II. Original contributions	
5	Extension of grounding-line flux conditions (Contribution 1)	Original
6	A fast and simplified subglacial hydrology model (Contribution 2)	
7	Singularity at pinning points (Contribution 3)	
	III. Conclusions and directions for future work	
8	Conclusions and perspectives	Review/Original

Table 1.1: Structure of the manuscript.

The second part is dedicated to the original contributions of this thesis. It consists of three distinct works that attempt to answer the research questions posed above. The first and second contributions are articles that have already been published in peer-reviewed scientific journals. They are copied in this thesis in the same way as they were published, apart from some minor modifications to the form of equations and figures to make them more easily readable in a thesis manuscript. The third contribution is a report that we aim to transform into a research paper and submit to a scientific journal in the near future. The contributions rely on different methods and address different issues (see Tab. 1.2); hence, they can be read independently from one another.

In the first contribution (Chapter 5), we focus on the effect that friction laws have on the dynamics of marine ice sheets; this addresses Q2. Specifically, we revisit the analytical developments made by Schoof [2007b,c] and Tsai et al. [2015]. Based on an asymptotic analysis near the grounding line, they obtained expressions for the flux at the grounding line as a function of the ice thickness at this location. In the glaciology literature, such expressions are known as 'grounding-line flux conditions'. These authors obtained flux conditions for the Weertman and Coulomb friction laws. We show that their results can be

extended to more general laws such as the Budd friction law. In doing so, we also build a bridge between the results previously obtained by Schoof [2007b,c] and Tsai et al. [2015]. Our results highlight the importance of the behavior of the friction law near the grounding line, and in particular whether this law is such that basal friction vanishes or not at that location. In particular, vanishing friction leads to a complex mechanical equilibrium where viscous, gravitational and frictional stresses are balanced in a boundary layer close to the grounding line.

In the second contribution (Chapter 6), we develop a simplified model of subglacial hydrology capable of handling both efficient and inefficient drainage systems, on both hard and soft beds. Our model is developed to be computationally fast, allowing coupling with an ice-sheet model. Thus, this contribution addresses both Q3 and Q4. We first present the assumptions of the model and how it is implemented. We test it on the idealized case of a one-dimensional marine ice sheet, and then apply it to Thwaites Glacier (West Antarctica). Our results suggest that the inclusion of a hydrological model that evolves as a function of the changes in ice-sheet geometry is essential, as it increases the sensitivity of ice sheets to external perturbations. Moreover, both the efficiency of the drainage system and the type of bed are key parameters determining this increased sensitivity.

In the third contribution (Chapter 7), we focus on the study of pinning points and their effects on the dynamics of marine ice sheets; this addresses Q1. We show that they can generate singularities in the coupling between the equations governing its motion, mass and momentum-balance equations. Importantly, we show that these singularities occur over smooth bedrock profiles. Indeed, the singularities are associated with a difference between the mechanical equilibrium that takes place on the grounded and floating parts of marine ice sheets. Essentially, these arise from the discrete nature of the grounding line, which is such that the grounded/floating transition occurs abruptly. The presence of singularities thus questions question the relevance of a mathematical model based on a grounding line, and suggests that a diffuse grounding-zone model might be more appropriate.

Chapter	Contribution	Methods	Main application
6	#1	perturbation methods / dynamical systems	basal friction
7	#2	hydrology modeling / numerical simulations	subglacial hydrology
5	#3	differential calculus / numerical continuation	pinning points

Table 1.2: Methods and applications of the original contributions of this thesis.

Finally, the third part (Chapter 8) presents the general conclusions of this thesis and suggests various perspectives for extending the research that has been initiated.

Part I

Modeling marine ice sheets: an overview

2

Mechanics of marine ice sheets

2.1 Introduction

In this section we describe the mechanics of marine ice sheets. Since ice sheets have macroscopic dimensions, an ideal framework for studying them is continuum mechanics, which we introduce in section 2.2. Then, in section 2.3, the equations of motion are specialized to the case of ice; ice takes the form of a shear-thinning fluid that flows under its own weight (Fig. 2.1). The resulting system of equations is summarized in section 2.4. Finally, we briefly discuss the ice-atmosphere, ice-ocean, and ice-bedrock interactions in section 2.5.

(a) Elephant Foot Glacier, Greenland [Credit: Dr. Ole Zeising].

(b) Penny Ice Cap, Canada [Credit: NASA].

Figure 2.1: Pictures that show the viscous behavior of ice sheets: on geophysical time scales, ice sheets behave as shear-thinning fluids that flow under their own weight.

This chapter is based on the reference book [Greve and Blatter, 2009] and the lecture notes from the Karthaus summer school [Fowler and Ng, 2021]. References on the subject also include the review article [Schoof and Hewitt, 2013], the glaciology-oriented reference book [Cuffey and Paterson, 2010], and the mathematically-oriented book [Fowler, 2011].

2.2 Continuum mechanics

2.2.1 Kinematics

Let us consider a body whose initial configuration is represented by the set $\Omega_0 \subset \mathbb{R}^3$ (Fig. 2.2). A point in Ω_0 is denoted by $\boldsymbol{X}$ and is referred to as a material point. Over time, this body may move and deform,

and we characterize this motion by the following map:

$$\boldsymbol{\varphi}: \quad \Omega_0 \times]0,T[\to \Omega_t: \quad (\boldsymbol{X},t) \mapsto \boldsymbol{x} = \boldsymbol{\varphi}(\boldsymbol{X},t). \tag{2.1}$$

Here, $]0,T[$ is the interval of time which is of interest for the study of the motion and Ω_t is the position of the body at time t, i.e., $\Omega_t := \boldsymbol{\varphi}(\Omega_0, t)$. It is referred to as the current configuration, and a point in Ω_t is denoted by $\boldsymbol{x}$ and referred to as a spatial point.

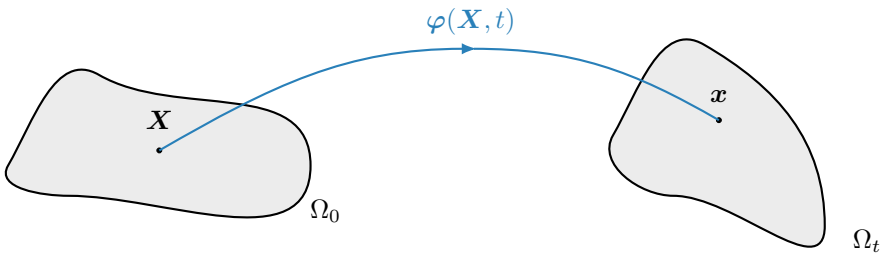

Figure 2.2: Schematic of the motion of a body. Each material point $\boldsymbol{X}$ of the reference configuration Ω_0 is mapped to a spatial point $\boldsymbol{x}$ of the current configuration Ω_t according to $\boldsymbol{x} = \boldsymbol{\varphi}(\boldsymbol{X},t)$.

The mapping $\boldsymbol{\varphi}$ is assumed to be a regular one: it is generally assumed that it is at least continuously differentiable and that it admits, at each time t, an inverse map $\boldsymbol{\varphi}_t^{-1}: \Omega_t \to \Omega_0$ such that

$$\boldsymbol{\varphi}_t^{-1}(\boldsymbol{\varphi}(\boldsymbol{X},t)) = \boldsymbol{X}, \quad \forall\, \boldsymbol{X} \in \Omega_0, \tag{2.2a}$$
$$\boldsymbol{\varphi}(\boldsymbol{\varphi}_t^{-1}(\boldsymbol{x}),t) = \boldsymbol{x}, \quad \forall\, \boldsymbol{x} \in \Omega_t. \tag{2.2b}$$

This construction is particularly convenient because it allows to switch between the reference and current configurations easily. Hence, it makes it possible to describe the motion of the body in terms of both the reference configuration and the current configuration, leaving the physicist to choose the most appropriate configuration for the situation under study. The first approach, in which the motion is described in terms of the material points $\boldsymbol{X} \in \Omega_0$, is known as a Lagrangian approach. The second approach, which considers the spatial points $\boldsymbol{x} \in \Omega_t$, is known as an Eulerian approach.

The material velocity and acceleration $\boldsymbol{V}, \boldsymbol{A}: \Omega_0 \times]0,T[\to \mathbb{R}^3$ are respectively defined as the first and second time derivatives of the mapping $\boldsymbol{\varphi}$: $\boldsymbol{V} := \partial_t \boldsymbol{\varphi}$ and $\boldsymbol{A} := \partial_t^2 \boldsymbol{\varphi}$. In particular, we have the following identity:

$$\boldsymbol{A}(\boldsymbol{X},t) = \frac{\partial \boldsymbol{V}}{\partial t}(\boldsymbol{X},t), \quad \forall\, (\boldsymbol{X},t) \in \Omega_0 \times]0,T[. \tag{2.3}$$

To compute the spatial velocity and acceleration $\boldsymbol{v}, \boldsymbol{a}: \Omega_t \times]0,T[\to \mathbb{R}^3$, we simply express the previous quantities in the reference configuration, thanks to the inverse mapping $\boldsymbol{\varphi}_t^{-1}$:

$$\boldsymbol{v}(\boldsymbol{x},t) := \boldsymbol{V}(\boldsymbol{\varphi}_t^{-1}(\boldsymbol{x}),t), \tag{2.4a}$$
$$\boldsymbol{a}(\boldsymbol{x},t) := \boldsymbol{A}(\boldsymbol{\varphi}_t^{-1}(\boldsymbol{x}),t). \tag{2.4b}$$

It then follows from (2.2) that the material and spatial velocity and acceleration are also related according to the following relations:

$$\boldsymbol{V}(\boldsymbol{X},t) = \boldsymbol{v}(\boldsymbol{\varphi}(\boldsymbol{X},t),t), \quad \forall\, (\boldsymbol{X},t) \in \Omega_0 \times]0,T[, \tag{2.5a}$$
$$\boldsymbol{A}(\boldsymbol{X},t) = \boldsymbol{a}(\boldsymbol{\varphi}(\boldsymbol{X},t),t), \quad \forall\, (\boldsymbol{X},t) \in \Omega_0 \times]0,T[. \tag{2.5b}$$

Based on these relations, the relation between the spatial velocity and the spatial acceleration can be obtained. Indeed, from (2.3) and (2.5) we have

$$\boldsymbol{a}(\boldsymbol{x},t) = \left[\frac{\partial}{\partial t} + \boldsymbol{v}(\boldsymbol{x},t)\cdot\boldsymbol{\nabla}_{\boldsymbol{x}}\right]\boldsymbol{v}(\boldsymbol{x},t). \tag{2.6}$$

Hence, in contrast to the material velocity and acceleration that are simply related to each other by a partial time derivative (see equation (2.3)), the relation between the spatial velocity and acceleration takes the form of a more complex non-linear relationship that involves the spatial velocity itself. There are two components in the right-hand side of (2.6): the first one, the partial time derivative, is due to the change over time of the velocity at a fixed position. The second one is known as the advective or convective part, and is due to the fact that the particle moves, so that it might go into regions that have a different velocity, thereby affecting its acceleration. More generally, consider the time derivative of an Eulerian quantity $f = f(\boldsymbol{x},t)$ which characterizes a material property of the particles of the body. Then, the rate of change of f, when following a particle, is known as the material or total derivative, and is given by the following formula:

Material derivative of an Eulerian quantity

$$\frac{\mathrm{d}f}{\mathrm{d}t} = \frac{\partial f}{\partial t} + \boldsymbol{v}\cdot\nabla_{\boldsymbol{x}} f. \tag{2.7}$$

Just as we can consider the temporal variation of the mapping $\boldsymbol{\varphi}$, we can also consider its spatial variation. To do so, we introduce the deformation gradient $\boldsymbol{F} = \boldsymbol{F}(\boldsymbol{X},t)$ as $\boldsymbol{F} := \boldsymbol{\nabla}_{\boldsymbol{X}}\boldsymbol{\varphi}$, which takes the form of a two-point tensor field. It is such that an infinitesimal vector $\mathrm{d}\boldsymbol{X}$ in the reference configuration is mapped to an infinitesimal vector $\mathrm{d}\boldsymbol{x}$ in the reference configuration:

$$\mathrm{d}\boldsymbol{x} = \boldsymbol{F}\cdot\mathrm{d}\boldsymbol{X}. \tag{2.8}$$

It can also be interesting to look at how the velocity varies spatially. We therefore define the velocity gradient $\boldsymbol{L} = \boldsymbol{L}(\boldsymbol{x},t)$ as $\boldsymbol{L} := \boldsymbol{\nabla}_{\boldsymbol{x}}\boldsymbol{v}$. Because the velocity is associated with the time derivative of $\boldsymbol{\varphi}$, one might expect a relation between the velocity gradient and the time derivative of the deformation gradient. In fact, it can easily be shown that

$$\boldsymbol{L} = (\partial_t \boldsymbol{F})\,\boldsymbol{F}^{-1}. \tag{2.9}$$

Finally, the velocity gradient can be decomposed to characterize the type of motion of a body. Specifically, one can split this tensor into its symmetric and anti-symmetric components, which are respectively denoted by $\boldsymbol{D}$ and $\boldsymbol{W}$:

$$\boldsymbol{L} = \boldsymbol{D} + \boldsymbol{W}, \quad \boldsymbol{D} = \boldsymbol{D}^{\mathrm{T}}, \quad \boldsymbol{W} = -\boldsymbol{W}^{\mathrm{T}}. \tag{2.10}$$

The tensor $\boldsymbol{D}$ is associated to the elongation of the body and is known as the strain-rate tensor. By contrast, the tensor $\boldsymbol{W}$ is associated with the solid-body rotation of the body and is known as the spin-rate tensor. This distinction can be made a bit more explicit thanks to the study of the evolution over time of an infinitesimal vector $\mathrm{d}\boldsymbol{x}$. Thanks to (2.8) and (2.9), we have

$$\frac{\mathrm{d}}{\mathrm{d}t}\mathrm{d}\boldsymbol{x} = \boldsymbol{L}\cdot\mathrm{d}\boldsymbol{x}. \tag{2.11}$$

Because $\boldsymbol{W}$ is anti-symmetric, there exists a unique vector $\boldsymbol{w}$ such that $\boldsymbol{W}\cdot\mathrm{d}\boldsymbol{x} = \boldsymbol{w}\times\mathrm{d}\boldsymbol{x}$. In fact, this vector is nothing else than half the rotational of the velocity field (i.e., half the vorticity field): $\boldsymbol{w} = \boldsymbol{\omega}/2$, in which $\boldsymbol{\omega} := \boldsymbol{\nabla}_{\boldsymbol{x}}\times\boldsymbol{v}$. It follows that we have

$$\frac{\mathrm{d}}{\mathrm{d}t}\mathrm{d}\boldsymbol{x} = \boldsymbol{D}\cdot\mathrm{d}\boldsymbol{x} + \frac{1}{2}\boldsymbol{\omega}\times\mathrm{d}\boldsymbol{x}, \tag{2.12}$$

in which the first component is associated with the elongation of $\mathrm{d}\boldsymbol{x}$, while the second component is associated with its rotation.

In the following sections, we simplify the notations by assuming that all the spatial differential operators are expressed with respect to the current configuration, so we write, e.g., ∇f instead of $\nabla_{\boldsymbol{x}} f$.

2.2.2 Dynamics

Before considering the equations governing the dynamics of continuous materials, it is useful to introduce Reynolds' theorem that allows the rate of change of a quantity f integrated over the material volume Ω_t to be computed:

Reynolds' theorem

$$\frac{\mathrm{d}}{\mathrm{d}t}\int_{\Omega_t} f\,\mathrm{d}\Omega = \int_{\Omega_t}\left[\frac{\partial f}{\partial t} + \operatorname{div}(\boldsymbol{v}f)\right]\mathrm{d}\Omega \tag{2.13a}$$

$$= \int_{\Omega_t}\frac{\partial f}{\partial t}\,\mathrm{d}\Omega + \int_{\partial\Omega_t}(\boldsymbol{v}f)\cdot\boldsymbol{n}\,\mathrm{d}\Gamma. \tag{2.13b}$$

Here, $\partial\Omega_t$ denotes the boundary of the volume Ω_t, and $\boldsymbol{n}$ its outward-facing normal. Hence, the rate of change of an integrated quantity f over the material volume has two contributions: one that is associated with the local change of the quantity f within the domain Ω_t, and one that is associated with the outflow and inflow of f across the boundary $\partial\Omega_t$ of this domain.

Next, we present the fundamental balance principles in their global formulation. To do so, we further consider that the material under study is characterized by a mass density $\rho = \rho(\boldsymbol{x}, t)$ and an internal energy density or specific internal energy $e = e(\boldsymbol{x}, t)$. Mass conservation then takes the following form:

$$\frac{\mathrm{d}}{\mathrm{d}t}\int_{\Omega_t}\rho\,\mathrm{d}\Omega = 0. \tag{2.14}$$

Linear momentum balance, also simply called momentum balance, is given by

$$\frac{\mathrm{d}}{\mathrm{d}t}\int_{\Omega_t}\rho\boldsymbol{v}\,\mathrm{d}\Omega = \int_{\Omega_t}\rho\boldsymbol{f}\,\mathrm{d}\Omega + \int_{\partial\Omega_t}\boldsymbol{t}\,\mathrm{d}\Gamma, \tag{2.15}$$

in which $\rho\boldsymbol{v}$ denotes the linear momentum, $\boldsymbol{f}$ the applied volumetric forces and $\boldsymbol{t}$ the applied surfaces forces. Its angular counterpart is given by

$$\frac{\mathrm{d}}{\mathrm{d}t}\int_{\Omega_t}(\boldsymbol{x}-\boldsymbol{x}_0)\times\rho\boldsymbol{v}\,\mathrm{d}\Omega = \int_{\Omega_t}(\boldsymbol{x}-\boldsymbol{x}_0)\times(\rho\boldsymbol{f})\,\mathrm{d}\Omega + \int_{\partial\Omega_t}(\boldsymbol{x}-\boldsymbol{x}_0)\times\boldsymbol{t}\,\mathrm{d}\Gamma, \tag{2.16}$$

for any arbitrary point $\boldsymbol{x}_0 \in \mathbb{R}^3$. Finally, energy balance takes the form

$$\frac{\mathrm{d}}{\mathrm{d}t}\int_{\Omega_t}\rho\left(e + \frac{1}{2}\|\boldsymbol{v}\|^2\right)\mathrm{d}\Omega = \int_{\Omega_t}\rho\boldsymbol{f}\cdot\boldsymbol{v}\,\mathrm{d}\Omega + \int_{\partial\Omega_t}\boldsymbol{t}\cdot\boldsymbol{v}\,\mathrm{d}\Gamma + \int_{\Omega_t}\rho r\,\mathrm{d}\Omega - \int_{\partial\Omega_t}\boldsymbol{q}\cdot\boldsymbol{n}\,\mathrm{d}\Gamma. \tag{2.17}$$

This last equation corresponds to the first principle of thermodynamics. The left-hand side contains the total energy of the system, made of the internal and kinetic energy. The right-hand side contains four parts: the mechanical power due to volume forces, the mechanical power due to surface forces, the heat production due to a heat source r, and the heat exchange due to the heat flux $\boldsymbol{q}$.

An important quantity that needs to be introduced is the Cauchy stress tensor $\boldsymbol{\sigma} = \boldsymbol{\sigma}(\boldsymbol{x}, t)$, which is the linear map between normal vectors $\boldsymbol{n}$ to a surface and the surface forces $\boldsymbol{t}$ that are applied on it:

$$\boldsymbol{t} = \boldsymbol{\sigma} \cdot \boldsymbol{n}. \tag{2.18}$$

The existence of such a tensor follows from Cauchy's theorem, which is itself a consequence of the momentum balance (2.15). Applying Reynolds' theorem (2.13) together with the definition of Cauchy stress tensor (2.18) and a localization principle allows the global balance principles (2.14)–(2.17) to be converted to their local forms:

Local formulation of balance principles

$$\partial_t \rho + \operatorname{div}(\rho \boldsymbol{v}) = 0, \tag{2.19a}$$

$$\rho \left(\partial_t + \boldsymbol{v} \cdot \boldsymbol{\nabla}\right) \boldsymbol{v} = \rho \boldsymbol{f} + \mathbf{div}\, \boldsymbol{\sigma}, \tag{2.19b}$$

$$\boldsymbol{\sigma} = \boldsymbol{\sigma}^{\mathrm{T}}, \tag{2.19c}$$

$$\rho(\partial_t + \boldsymbol{v} \cdot \nabla) e = \boldsymbol{\sigma} : \boldsymbol{D} - \operatorname{div} \boldsymbol{q} + \rho\, r. \tag{2.19d}$$

This set of coupled partial differential equations is the system of equations that needs to be solved to determine the motion of a body. However, there are several equations lacking to close the system of equations: the constitutive equations and the initial and boundary conditions. Constitutive equations characterize the medium and are therefore material-dependent. Similarly, the initial and boundary conditions that must be enforced depend on the specific situation that is studied.

Conditions at interfaces sometimes take the form of jump conditions, associated with the change in kinematic and dynamical quantities across the interface between two subdomains, e.g., two regions made of different materials. Formally, these jump conditions are obtained by applying the global balance equations (2.14)–(2.17) in a volume that encloses the interface, and making the measure of this volume tend towards zero. Let Γ be the interface separating two media Ω_+ and Ω_-. The jump operator $[\![\cdot]\!]$ is then defined, for a spatial quantity $f = f(\boldsymbol{x})$, as

$$[\![f(\boldsymbol{x})]\!] := \lim_{\substack{\boldsymbol{y} \to \boldsymbol{x} \\ \boldsymbol{y} \in \partial\Omega_+}} f(\boldsymbol{y}) - \lim_{\substack{\boldsymbol{y} \to \boldsymbol{x} \\ \boldsymbol{y} \in \partial\Omega_-}} f(\boldsymbol{y}), \quad \forall\, \boldsymbol{x} \in \Gamma. \tag{2.20}$$

The jump conditions associated with mass balance, momentum balance (both linear and angular), and energy balance are then given by

$$[\![\rho(\boldsymbol{v} - \boldsymbol{v}_{\mathrm{i}}) \cdot \boldsymbol{n}]\!] = 0, \tag{2.21a}$$

$$[\![\boldsymbol{\sigma} \cdot \boldsymbol{n}]\!] - [\![\rho \boldsymbol{v} (\boldsymbol{v} - \boldsymbol{v}_{\mathrm{i}}) \cdot \boldsymbol{n}]\!] = \boldsymbol{0}, \tag{2.21b}$$

$$[\![\boldsymbol{q} \cdot \boldsymbol{n}]\!] - [\![\boldsymbol{v} \cdot \boldsymbol{\sigma} \cdot \boldsymbol{n}]\!] + \left[\!\!\left[\rho \left(e + \tfrac{1}{2}\|\boldsymbol{v}\|^2\right) (\boldsymbol{v} - \boldsymbol{v}_{\mathrm{i}}) \cdot \boldsymbol{n}\right]\!\!\right] = 0. \tag{2.21c}$$

Here, $\boldsymbol{v}_{\mathrm{i}}$ denotes the velocity of the interface, which might be different from the velocity $\boldsymbol{v}$ of the material at that interface.

2.3 Ice flow

2.3.1 Rheology

Physically, ice has a polycrystalline structure. Specifically, ice is made of arrays of hexagonal structures in which the vertices are the oxygen atoms (Fig. 2.3). When an external stress is applied, the structure

is deformed, preferentially along the directions that are such that the hexagonal planes glide along each other. On top of this mechanism, defects (or dislocations) in the lattice facilitate ice deformation through their motion. Considering a lattice as shown in figure 2.3, there are specific directions along which the material can be more easily deformed, and these are typically characterized by the orientation of the unit vector $\boldsymbol{c}$ normal to hexagonal planes. However, in practice, ice is made of a collection of aggregates that are oriented along various directions. If there is no preferred orientation among these aggregates, i.e., if these orientations are uniformly distributed, then ice possesses an isotropic behavior and behaves similarly irrespective of the orientation of the material with respect to that of the applied stress.

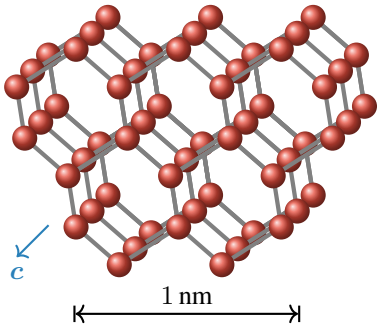

Figure 2.3: Crystal structure of the ice I_h. It takes the form of a wurtzite structure, with stacks of hexagonal rings whose vertices are oxygen atoms (red) and whose edges are hydrogen bonds (gray). The atoms that make up a hexagon are not on the same plane, but on two planes that are slightly shifted so that each atom's neighbours are on the other plane. The vector $\boldsymbol{c}$ is perpendicular to the hexagonal structures.

In a continuum-mechanics approach, we are not interested in the details of the physical structure of materials, but, rather, in the relation between macroscopic measures of applied stress and deformation. This relation will then be the macroscopic image of the modifications in both the stress distribution and the crystal structure of the ice. Figure 2.4 schematically shows such a relation for ice. Here, a lump of ice is submitted to a shear stress τ, leading to a deformation angle γ that increases over time because of ice creep. There are several parts to this mechanical response. First, there is an instantaneous response $\gamma = \gamma_0$ that is associated with an elastic behavior. If the stress continues to be applied, creep is initiated. During an initial phase, known as primary creep, the deformation angle increases but with a shear rate $\dot{\gamma}$ that gets smaller over time. Eventually, a plateau is reached, known as secondary creep, in which the shear rate is constant. Then, tertiary creep begins, in which the shear rate increases again to stabilize towards an ultimate value.

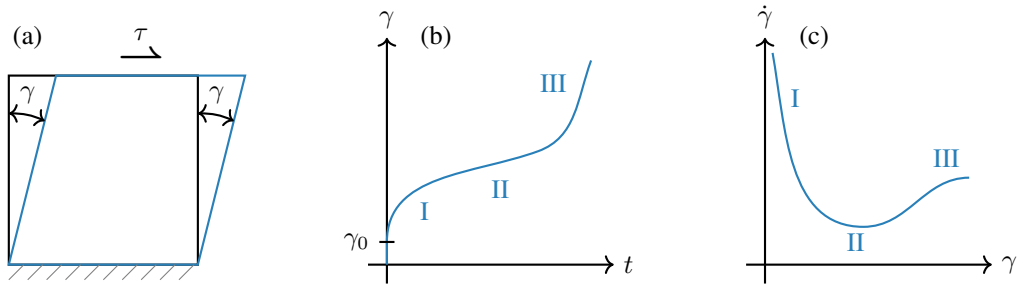

Figure 2.4: Illustration of the creep of ice when submitted to a stress. **(a)** Schematic of a test in which ice is submitted to shear. **(b)** Over time, the deformation angle γ increases according to three regimes: primary creep (I), secondary creep (II), and tertiary creep (III). **(c)** Corresponding shear rate $\dot{\gamma}$.

For geophysical time scales, ice is modeled as an incompressible power-law fluid, with

$$\dot{\gamma} = 2\,A\,\tau^n, \tag{2.22}$$

in which A is a viscosity coefficient and n a viscosity parameter. Fundamentally, this relation is associated with the second regime of ice creep, for which $\dot{\gamma}$ becomes minimal. Hence, some complexity of the ice rheology is dismissed but, as will be seen later, it is found that this simple relation is generally a good model for ice flow. Note that more sophisticated models exist, in which the other creep regimes are also included [Goldsby and Kohlstedt, 2001]. The relation (2.22) can be written in the form a generalized Newtonian constitutive equation in which the effective viscosity η depends on the strain rate:

$$\tau = \eta(\dot{\gamma})\,\dot{\gamma}, \quad \eta(\dot{\gamma}) := \frac{1}{2}A^{-\frac{1}{n}}\left(\frac{\dot{\gamma}}{2}\right)^{\frac{1-n}{n}}. \tag{2.23}$$

Because $n \geq 1$, ice is a shear-thinning fluid: its effective viscosity decreases when the strain rate increases. Given the pioneering research conducted by Glen [1955] and Nye [1953, 1957], such a law is known in the glaciology community as the Glen or Glen–Nye flow law. In the complex-fluids community, it also referred to as the Ostwald–de Waele law [Saramito, 2016]. The viscosity coefficient A depends on temperature; this is not unexpected as creep is associated with the motion of dislocations, which is a temperature-dependent process. The usual model is an Arrhenius-like equation:

$$A(\theta') := A_0 \exp(-Q/R\theta'), \quad \theta' := \theta - c_{\mathrm{t}}p, \tag{2.24}$$

in which A_0 is a prefactor, Q is an activation energy for creep, R is the universal gas constant, θ' is a pressure-corrected temperature, $c_{\mathrm{t}} > 0$ is the Clapeyron slope, and p is the pressure. The relation (2.22), or its equivalent (2.23), together with the temperature dependence (2.24) have been validated in both laboratory and in-situ measurements [e.g., Glen, 1955; Weertman, 1983; Jezek et al., 1985; Budd and Jacka, 1989]. In particular, Glen [1955] has obtained the first striking evidence of a power-law relation (Fig. 2.5). Their measurements suggest that $n \approx 3$ in the power-law relation. We note that recent observations suggest a slightly larger value $n \approx 4$ [Millstein et al., 2022].

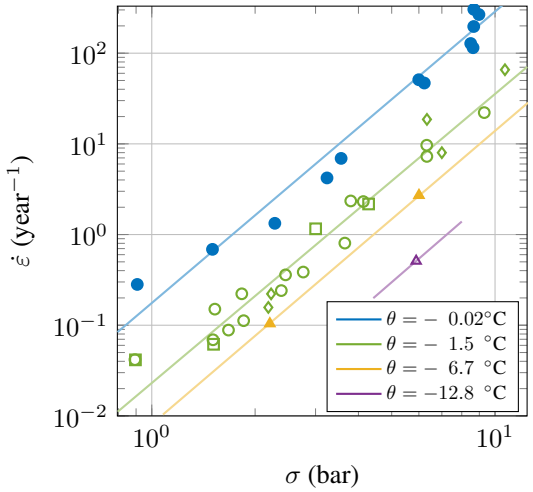

Figure 2.5: Minimum creep rate $\dot{\varepsilon}$ observed as a function of the applied stress σ [adapted from Glen, 1955]. The green symbols correspond to different stress states at $\theta = -1.5$°C: initial values (circles), values after increasing the stress (diamonds), and values after decreasing the stress (squares). The lines are best-fit regressions lines of the form $\dot{\varepsilon} \propto \sigma^n$, with $n = 3.17$.

The rheology equation (2.22) corresponds to a simple shear-test configuration. It therefore remains to generalize it so that it can be used for general three-dimensional cases. A natural method to do so

consists in replacing the shear rate $\dot{\gamma}$ by its three-dimensional equivalent, the strain-rate tensor $\boldsymbol{D}$. In terms of the the Cauchy stress tensor $\boldsymbol{\sigma}$, the constitutive equation of a generalized Newtonian fluid is

$$\boldsymbol{\sigma} = -p\boldsymbol{I} + 2\eta\boldsymbol{D}, \tag{2.25}$$

where $\boldsymbol{I}$ is the identity tensor. The effective viscosity η should furthermore be a function of $\boldsymbol{D}$ instead of $\dot{\gamma}$. To guarantee that this function is independent of the coordinate system, we further require it to be a function of $\boldsymbol{D}$ only through its principal invariants which, by definition, satisfy this constraint:

$$\eta = \eta(\mathrm{I}_{\boldsymbol{D}}, \mathrm{II}_{\boldsymbol{D}}, \mathrm{III}_{\boldsymbol{D}}), \tag{2.26}$$

where

$$\mathrm{I}_{\boldsymbol{D}} := \operatorname{tr} \boldsymbol{D}, \quad \mathrm{II}_{\boldsymbol{D}} := \frac{1}{2}\left[(\operatorname{tr} \boldsymbol{D}^2) - (\operatorname{tr} \boldsymbol{D})^2\right], \quad \mathrm{III}_{\boldsymbol{D}} := \det \boldsymbol{D}. \tag{2.27}$$

Given that ice is modeled as an incompressible fluid, the first invariant $\mathrm{I}_{\boldsymbol{D}}$ vanishes. Furthermore, for a simple-shear test, the third invariant is zero. This suggests to use the second invariant as a generalization of the shear rate $\dot{\gamma}$. In a simple shear test,

$$\frac{\dot{\gamma}}{2} = \sqrt{\mathrm{II}_{\boldsymbol{D}}}, \tag{2.28}$$

so that we write, for consistency,

$$\eta(\boldsymbol{D}) := \frac{1}{2} A^{-\frac{1}{n}} \left(\sqrt{\mathrm{II}_{\boldsymbol{D}}}\right)^{\frac{1-n}{n}}. \tag{2.29}$$

It is convenient to rewrite the square root of the second invariant as a norm on the space of traceless matrices; introducing

$$\|\boldsymbol{D}\|_* := \sqrt{\frac{1}{2}\left[(\operatorname{tr} \boldsymbol{D}^2) - (\operatorname{tr} \boldsymbol{D})^2\right]}, \tag{2.30}$$

the equation for the effective viscosity becomes

$$\eta(\boldsymbol{D}) := \frac{1}{2} A^{-\frac{1}{n}} \|\boldsymbol{D}\|_*^{\frac{1-n}{n}}. \tag{2.31}$$

Overall, the following constitutive equation is obtained for ice flow:

Ice rheology

$$\boldsymbol{\sigma} = -p\boldsymbol{I} + 2\eta(\boldsymbol{D}, \theta')\,\boldsymbol{D}, \quad \eta(\boldsymbol{D}, \theta') := \frac{1}{2}[A(\theta')]^{-\frac{1}{n}} \|\boldsymbol{D}\|_*^{\frac{1-n}{n}}. \tag{2.32}$$

This constitutive equation is obviously a simplification of reality. In particular, several modifications have been introduced in the glaciology literature in order to make it more accurate. We mention these here, as these improvements are important for certain cases, and have been the subject of important research in recent years. A first extension of (2.32) concerns the isotropy assumption. To take into account the effect of the orientation of the crystals, anisotropic models of various complexities have been proposed [e.g., Gillet-Chaulet et al., 2005, 2006]. A practical approach consists in multiplying the ice rheology factor A in equation (2.32) with an enhancement factor E which can be optimized so that the computed velocity surface values match observed ones [Ma et al., 2010]. A second extension is related to the analysis of ice sheets on short time scales, e.g., of the order of days. In that case, the elastic component in the ice response cannot be neglected, and ice is typically modeled as a viscoelastic material. This is particularly important for the modeling of the flexure of ice shelves in response to tides [e.g., Vaughan, 1995]. Finally, a third extension of the viscous rheology (2.32) concerns the addition

of a damage or failure component [e.g., Mobasher et al., 2016; Sun et al., 2017]. This is an area of research that glaciologists have been focusing on in recent years; indeed, although there are widespread observations of damage areas in the shear margins of ice shelves [Lhermitte et al., 2020], these processes are not yet fully understood. Furthermore, this is a problem that is complex due to its multiphysics nature: the intrusion of surface or sea water into ice-shelf faults can lead to damage and, eventually, to rupture [Lai et al., 2020; Hageman et al., 2024].

2.3.2 Thermal properties

Ice is characterized by a heat capacity $c = c(\theta)$ and a heat conductivity $k = k(\theta)$. The internal energy density and heat flux are then given, respectively, by

$$e = \int_{\theta_0}^{\theta} c(\Theta)\,\mathrm{d}\Theta, \tag{2.33a}$$

$$\boldsymbol{q} = -k(\theta)\,\nabla\theta, \tag{2.33b}$$

in which θ_0 is a reference temperature. Given that there is no heat source in ice shets, we set $r = 0$ in the energy-balance equation (2.19d).

An additional assumption on the thermal state of the ice is also made to simplify this overview. It is assumed that, over the whole interior of the ice sheet, ice is in its solid form, so that the temperature is below its pressure melting point. We also assume that at the base of the ice sheet (at the ice-bedrock interface), ice is temperate, i.e., at the pressure melting point.

2.3.3 Balance equations

Given the incompressible nature of ice, its rheology, and its thermal properties, the balance equations (2.19) become

$$\operatorname{div}\boldsymbol{v} = 0, \tag{2.34a}$$

$$\rho(\partial_t + \boldsymbol{v}\cdot\boldsymbol{\nabla})\boldsymbol{v} = -\nabla p + \mathbf{div}(2\eta\boldsymbol{D}) + \rho\boldsymbol{f}, \tag{2.34b}$$

$$\rho c(\partial_t + \boldsymbol{v}\cdot\nabla)\theta = 4\,\eta\,\|\boldsymbol{D}\|_*^2 + \operatorname{div}(k\nabla\theta). \tag{2.34c}$$

Note that the angular momentum balance equation, which requires the Cauchy stress tensor to be symmetric, is automatically satisfied given that ice behaves as a generalized Newtonian fluid.

These equations can still be further particularized to the context of ice flow. Consider the momentum balance equation (2.34b). The only external force that is applied to the ice is gravity. However, a complication here is that this equation only holds for inertial reference frames, while the description of ice is done in a reference frame that is attached to the Earth, which is rotating. As a consequence, one has to consider additional fictitious forces that are associated with this motion: the centrifugal and Coriolis forces. The applied forces are therefore given by

$$\rho\boldsymbol{f} = \rho\boldsymbol{g} - 2\rho\,\boldsymbol{\Omega}\times\boldsymbol{v}, \tag{2.35}$$

where $\boldsymbol{g} = \boldsymbol{\gamma} - \boldsymbol{\Omega}\times(\boldsymbol{\Omega}\times\boldsymbol{x})$ is the effective gravity with $\boldsymbol{\gamma}$ the true gravity, and $\boldsymbol{\Omega}$ is the Earth's Poisson vector. The resulting momentum-balance equation becomes

$$\rho(\partial_t + \boldsymbol{v}\cdot\boldsymbol{\nabla})\boldsymbol{v} = -\nabla p + \mathbf{div}(2\eta\boldsymbol{D}) + \rho\boldsymbol{g} - 2\rho\,\boldsymbol{\Omega}\times\boldsymbol{v}. \tag{2.36}$$

While we expect the pressure, viscous, and gravity terms to be important for the study of ice flows, this might not be the case for the other terms. We therefore assess their importance by comparing the characteristic value of each term with respect to the characteristic value of the pressure gradient. The

scales that are chosen are typical of ice sheets and described in table 2.1. Using these scales yields the following estimation for the relative importance of the horizontal inertial term, the vertical inertial term, and the Coriolis term:

$$\frac{\rho[u]/[t]}{[p]/[x]} \sim 10^{-9}, \quad \frac{\rho[w]/[t]}{[p]/[h]} \sim 10^{-15}, \quad \frac{\rho\|\boldsymbol{\Omega}\|[u]}{[p]/[x]} \sim 10^{-8}. \tag{2.37}$$

Accordingly, we drop these terms from the momentum-balance equation, which becomes

$$-\nabla p + \mathbf{div}(2\eta \boldsymbol{D}) + \rho \boldsymbol{g} = \mathbf{0}. \tag{2.38}$$

Importantly, because the inertial terms are neglected, there is no explicit time dependency in this equation. That does not mean that the ice flow is stationary; by contrast, this means that the ice flow follows the changes in ice geometry and in the boundary conditions by reaching the associated equilibrium. In particular, the ice flow is in quasi-static equilibrium with respect to the ice-sheet geometry.

Name	Symbol	Value	Units
Ice density	ρ	910	$\mathrm{kg\,m^{-3}}$
Gravity acceleration	$\|\boldsymbol{g}\|$	9.81	$\mathrm{m\,s^{-2}}$
Poisson vector magnitude	$\|\boldsymbol{\Omega}\|$	7.29×10^{-5}	$\mathrm{s^{-1}}$
Horizontal extent scale	$[x]$	10^3	km
Thickness scale	$[h]$	1	km
Horizontal velocity scale	$[u]$	10^2	$\mathrm{m\,year^{-1}}$
Vertical velocity scale	$[w]$	10^{-1}	$\mathrm{m\,year^{-1}}$
Pressure scale	$[p]$	10	MPa
Time scale	$[t]$	10^4	year

Table 2.1: Physical parameters and characteristic scales associated with ice flow in ice sheets in order to assess the importance of the various terms in the momentum-balance equation [adapted from Greve and Blatter, 2009]. The scales have been chosen by first setting $[x]$, $[h]$, and $[u]$ according to observed values. Then, the pressure scale was set to $[p] \sim \rho g[h]$ and the time scale to $[t] \sim [x]/[u]$. Finally, the vertical velocity scale was set based on the continuity equation (2.34a), so that $[u]/[x] \sim [w]/[h]$.

2.3.4 Initial and boundary conditions

The system of equations formed by the balance equations presented in the previous subsection requires initial and boundary conditions. We describe these conditions by first introducing the different boundaries of the domains. Then, the conditions associated with each of these boundaries are briefly described. Finally, we comment on the initial conditions.

A schematic of a marine ice sheet is shown in figure 2.6, together with the notations used to define its boundaries. The boundary of the ice-sheet domain Ω_t is partitioned into the following non-overlapping sets:

- Γ_s: upper surface;
- Γ_g: grounded lower surface, where ice is in contact with the bed;
- Γ_f: floating lower surface, where ice is in contact with the ocean;
- Γ_cf: calving front, where ice detaches from the shelf which leads to a discharge of icebergs in the ocean.

All these sets potentially depend on time, as the ice-sheet geometry is expected to evolve as a function of time. In addition to these boundaries, an additional fictitious boundary, the ice divide Γ_d, is often added in numerical simulations with synthetic configurations. It serves as a symmetry plane, so that symmetry conditions are associated to this boundary. The upper and lower surfaces are parametrized by their elevation $z = z_\mathrm{s}$ and $z = z_\mathrm{l}$. The distinction between the grounded and floating regions is made by considering whether the elevation z is greater than or equal to the bedrock elevation z_b:

$$\Gamma_\mathrm{s} = \{\boldsymbol{x} \in \mathrm{cl}(\Omega_t) : z = z_\mathrm{s}\}, \tag{2.39a}$$
$$\Gamma_\mathrm{g} = \{\boldsymbol{x} \in \mathrm{cl}(\Omega_t) : z = z_\mathrm{l},\ z_\mathrm{l} = z_\mathrm{b}\}, \tag{2.39b}$$
$$\Gamma_\mathrm{f} = \{\boldsymbol{x} \in \mathrm{cl}(\Omega_t) : z = z_\mathrm{l},\ z_\mathrm{l} > z_\mathrm{b}\}, \tag{2.39c}$$

where $\mathrm{cl}(\Omega_t)$ denotes the closure of the set Ω_t. Alternatively, these boundaries can be defined using $\bar{\Omega}_t$, which is the projection of $\mathrm{cl}(\Omega_t)$ onto a plane perpendicular to the vertical axis (Fig. 2.6b). In other words, $\bar{\Omega}_t$ is the smallest closed subset of $\mathbb{R}^2$ that contains the (x, y) coordinates of all the points in Ω_t. It can therefore be used to parametrize the boundaries through the elevation functions z_s and z_l:

$$\Gamma_\mathrm{s} = \{(x, y, z_\mathrm{s}(x, y, t)) \mid (x, y) \in \bar{\Omega}_t\}, \tag{2.40a}$$
$$\Gamma_\mathrm{g} = \{(x, y, z_\mathrm{l}(x, y, t)) \mid (x, y) \in \bar{\Omega}_t : z_\mathrm{l} = z_\mathrm{b}\}, \tag{2.40b}$$
$$\Gamma_\mathrm{f} = \{(x, y, z_\mathrm{l}(x, y, t)) \mid (x, y) \in \bar{\Omega}_t : z_\mathrm{l} > z_\mathrm{b}\}. \tag{2.40c}$$

The following geometric constraint is further added to guarantee meaningful boundaries:

$$z_\mathrm{s} \geq z_\mathrm{l} \geq z_\mathrm{b}. \tag{2.41}$$

Finally, we also introduce the grounding line Γ_gl as the transition between the grounded and floating boundaries:

$$\Gamma_\mathrm{gl} := \mathrm{cl}(\Gamma_\mathrm{g}) \cap \mathrm{cl}(\Gamma_\mathrm{f}). \tag{2.42}$$

Physically, the grounding line corresponds to the position where the ice switches from a grounded to a floating configuration (or the opposite). It is an important quantity for the study of the dynamics of ice sheets which will be referred to numerous times in the original contributions of this thesis (Part II of the manuscript).

We now proceed to the description of the boundary conditions. On each boundary, we specify three types of boundary conditions: one associated with its kinematics (the evolution of the boundary), one that is associated with the dynamics (condition on the velocity or stress), and one that is associated with the thermal state (condition on the temperature or heat flux). These conditions are schematized in figure 2.7.

Boundary conditions at the upper surface Γ_s (Fig. 2.7a)

The upper-surface boundary is such that $z = z_\mathrm{s}$. Hence, the following constraint must be satisfied:

$$f_\mathrm{s}(\boldsymbol{x}, t) := z - z_\mathrm{s}(x, y, t) = 0. \tag{2.43}$$

A particle that is located on this boundary and moves with its velocity will by construction stay on this boundary. It follows that the total derivative of (2.43), when taking as velocity the velocity of the boundary, must vanish. This yields the following kinematic equation:

$$\partial_t z_\mathrm{s} + \boldsymbol{u} \cdot \bar{\nabla} z_\mathrm{s} - w = a_\mathrm{s}, \tag{2.44}$$

in which $\boldsymbol{u} = (u, v)$ is the horizontal component of the velocity field, w is the vertical component of the velocity field, and a_s is the surface accumulation rate. The latter is typically associated with input of snow (it is positive if the ice-sheet gains mass due to accumulation). The operator $\bar{\nabla}$ denotes the

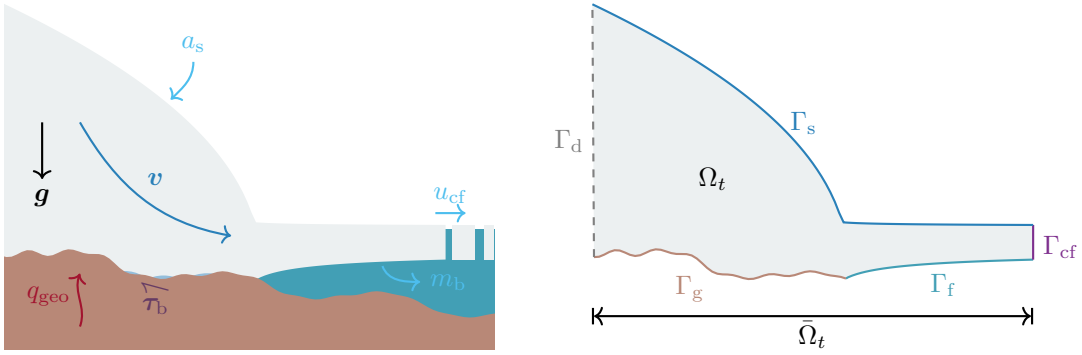

(a) Illustration of physical phenomena.

(b) Notations for the definition of the boundaries.

Figure 2.6: Schematic representation of a marine ice sheet and its boundaries (not at scale). **(a)** Marine ice sheets are subjected to various phenomena. They flow under gravity, which is represented by $\boldsymbol{g}$. They gain mass thanks to snow accumulation, which is modeled through a surface accumulation rate a_s, and loose mass due to melt, mainly below the ice shelf, and to calving at the calving front. **(b)** Boundaries of a marine ice sheet domain Ω_t: upper surface Γ_s, grounded lower surface Γ_g, floating lower surface Γ_f, and calving front Γ_{cf}. The left boundary Γ_d is a fictitious boundary known as an ice divide which serves as a symmetry plane. The set $\bar{\Omega}_t \subset \mathbb{R}^2$ is the projection of the closure of the domain Ω_t onto a plane perpendicular to the vertical axis.

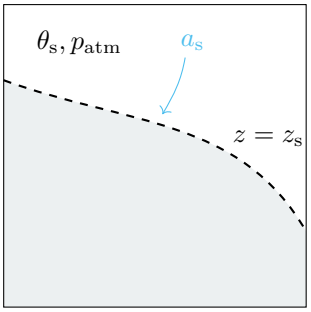

(a) Upper surface Γ_s.

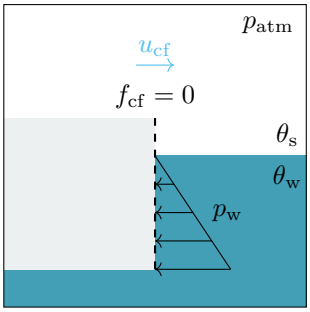

(b) Calving front Γ_{cf}.

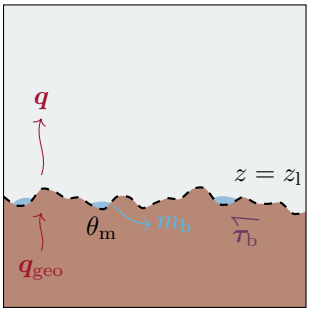

(c) Grounded lower surface Γ_g.

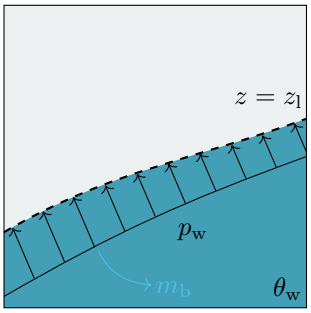

(d) Floating lower surface Γ_f.

Figure 2.7: Schematic of the boundary conditions applied on the boundaries of the ice-sheet domain.

horizontal spatial gradient operator.

For the dynamical condition, we rely on the jump condition (2.21b). Given the small surface velocities, this condition becomes

$$[\![\boldsymbol{\sigma} \cdot \boldsymbol{n}]\!] = \mathbf{0}, \tag{2.45}$$

that is,

$$\boldsymbol{\sigma} \cdot \boldsymbol{n} = -p_{\mathrm{atm}}\, \boldsymbol{n}, \tag{2.46}$$

in which $\boldsymbol{n}$ is the outward-facing normal to the boundary and p_{atm} is the atmospheric pressure. The value of p_{atm} is typically quite small compared to the stresses experienced in ice sheets; hence, it is neglected. This yields the following stress-free condition:

$$\boldsymbol{\sigma} \cdot \boldsymbol{n} = \mathbf{0}. \tag{2.47}$$

For the thermal state at the boundary, we assume that the surface temperature θ_{s} is known, which leads to a Dirichlet condition in terms of the temperature:

$$\theta = \theta_{\mathrm{s}}. \tag{2.48}$$

Boundary conditions at the grounded lower surface Γ_{g} (Fig. 2.7c)

Similarly to the case of the upper surface, a kinematic equation can be obtained. As the lower-surface boundary is such that $z = z_{\mathrm{l}}$, this equation is here given by

$$\partial_t z_{\mathrm{l}} + \boldsymbol{u} \cdot \bar{\nabla} z_{\mathrm{l}} - w = m_{\mathrm{b}}, \tag{2.49}$$

in which m_{b} is the basal melt rate. It corresponds to the rate of ice loss due to melt at the base and is counted positively in case of melt.

In terms of the dynamical condition, a distinction must be made between the normal and tangential conditions. On the one hand, we enforce a no-penetration condition of the ice into the bedrock:

$$\boldsymbol{v} \cdot \boldsymbol{n} \leq 0, \tag{2.50}$$

with $\boldsymbol{n}$ the outward normal to the boundary. Here, the case $\boldsymbol{v} \cdot \boldsymbol{n} < 0$ corresponds to the case where the grounded lower region is moving upward, i.e., where it switches to a the floating configuration. In that case, the normal stress $\sigma_{nn} := (\boldsymbol{\sigma} \cdot \boldsymbol{n}) \cdot \boldsymbol{n}$ in the ice must correspond to the subglacial water pressure p_{w}, i.e.,

$$\sigma_{nn} = -p_{\mathrm{w}}. \tag{2.51}$$

The subglacial water is associated with subglacial conduits in which liquid water flows below the ice sheet. Here, we assume that the pressure p_{w} is known. However, in principle, it is also an unknown of the problem, and a subglacial hydrological model must be considered; this topic is explored in details in section 4.3. If the grounded lower surface is such that $\boldsymbol{v} \cdot \boldsymbol{n} = 0$, then $\sigma_{nn} \leq -p_{\mathrm{w}}$: the ice normal stress must be sufficiently negative (i.e., sufficiently in compression) so that it 'pushes' on the bedrock, preventing a local uplift by the subglacial water. Together, these conditions lead to contact conditions:

$$\boldsymbol{v} \cdot \boldsymbol{n} \leq 0, \tag{2.52a}$$

$$(\sigma_{nn} + p_{\mathrm{w}}) \leq 0, \tag{2.52b}$$

$$(\boldsymbol{v} \cdot \boldsymbol{n})(\sigma_{nn} + p_{\mathrm{w}}) = 0. \tag{2.52c}$$

On the other hand, we fix the tangential component of the traction force to the surface. This tangential component can be written as $\boldsymbol{T}(\boldsymbol{\sigma} \cdot \boldsymbol{n})$, in which $\boldsymbol{T} := (\boldsymbol{I} - \boldsymbol{n} \otimes \boldsymbol{n})$ is the tangential projection operator, with $\boldsymbol{n}$ the outward facing normal:

$$\boldsymbol{T}(\boldsymbol{\sigma} \cdot \boldsymbol{n}) = \boldsymbol{\sigma} \cdot \boldsymbol{n} - \sigma_{nn} \boldsymbol{n}. \tag{2.53}$$

This tangential component is set to a prescribed value $\boldsymbol{\tau}_\mathrm{b}$ that represents the friction at a sub-scale level, e.g. due to roughness in the bedrock:

$$\boldsymbol{T}(\boldsymbol{\sigma}\cdot\boldsymbol{n}) = \boldsymbol{\tau}_\mathrm{b}. \tag{2.54}$$

In general, it depends on many quantities such as the ice-sheet basal velocity as well as the subglacial water pressure; this topic is discussed in section 4.2.

Finally, because we assume that ice is temperate at the base, its value is simply set to the pressure melting point θ_m:

$$\theta = \theta_\mathrm{m}. \tag{2.55}$$

Nonetheless, the particular thermal state at this interface can be further exploited. At the pressure melting point, any surplus in heat leads to additional ice melt, so we expect a balance between latent heat and thermal heat fluxes. Actually, applying the jump condition (2.19d) to the present situation, we obtain

$$m_\mathrm{b} = \frac{q_\mathrm{t} + q_\mathrm{geo} + q_\mathrm{b}}{\rho L}, \tag{2.56}$$

which allows to compute the basal melt which is necessary for the computation of the evolution of the free surface, i.e., equation (2.49). Here, q_t is the conductive heat flux in the ice (caused by thermal gradients), q_geo is the geothermal heat flux that comes from the Earth's core, q_b is the heat dissipation associated with basal processes and L is the latent heat of fusion of ice. The heat flux q_b is typically associated with the energy dissipated by the motion of ice and of subglacial water:

$$q_\mathrm{b} = |\boldsymbol{\tau}_\mathrm{b}\cdot\boldsymbol{u}_\mathrm{b}| + |\boldsymbol{q}_\mathrm{w}\cdot\bar{\nabla}\phi|, \tag{2.57}$$

with $\boldsymbol{u}_\mathrm{b}$ is the basal velocity, $\boldsymbol{q}_\mathrm{w}$ is the subglacial water flux, and ϕ is the hydraulic potential. As previously mentioned, these subglacial quantities are explored in sections 4.2 and 4.3.

Boundary conditions at the floating lower surface Γ_f (Fig. 2.7d)

At the floating lower surface, the kinetic equation obtained for the grounded lower surface, equation (2.49), still holds:

$$\partial_t z_\mathrm{l} + \boldsymbol{u}\cdot\bar{\nabla} z_\mathrm{l} - w = m_\mathrm{b}. \tag{2.58}$$

The only distinction is that the basal melt rate is now associated with sub-shelf melt. It is typically a parametrization of ice-ocean interactions; in contrast to equation (2.56) that only depends on quantities that can be obtained in an ice-sheet model, the sub-shelf melt rate must be computed based on ocean properties obtained thanks to observational data or another model.

The dynamical and thermal boundary conditions take the form of a continuity of the surface traction and of the basal temperature:

$$\boldsymbol{\sigma}\cdot\boldsymbol{n} = -p_\mathrm{w}\boldsymbol{n}, \tag{2.59a}$$

$$\theta = \theta_\mathrm{w}, \tag{2.59b}$$

in which p_w and θ_w are the ocean water pressure and temperature, respectively. Assuming a hydrostatic distribution, the former is given by $p_\mathrm{w} = \rho_\mathrm{w} g(z_\mathrm{sl} - z)$ with ρ_w the water density and z_sl the sea-level elevation.

Boundary conditions at the calving front Γ_cf (Fig. 2.7b)

The calving-front position is characterized by an implicit equation of the form $f_\mathrm{cf}(x, y, t) = 0$, in which f_cf is the function associated with the calving front. If one considers that a particle at the ice-front with the velocity of the calving front stays on it, one gets that the total derivative of f_cf with that velocity must vanish. This yields the kinematic condition

$$\partial_t f_\mathrm{cf} + \boldsymbol{u}\cdot\bar{\nabla} f_\mathrm{cf} = u_\mathrm{cf}, \tag{2.60}$$

in which u_{cf} is the calving-front velocity.

The dynamical and thermal boundary conditions again correspond to a continuity of the surface traction and of the basal temperature:

$$\boldsymbol{\sigma} \cdot \boldsymbol{n} = -p_{\mathrm{cf}} \boldsymbol{n}, \tag{2.61a}$$

$$\theta = \theta_{\mathrm{cf}}. \tag{2.61b}$$

Here, $(p_{\mathrm{cf}}, \theta_{\mathrm{cf}})$ are defined as the pressure and temperature of the atmosphere, $(p_{\mathrm{atm}}, \theta_{\mathrm{s}})$, above sea-level (for $z \geq z_{\mathrm{sl}}$), and as the pressure and temperature of the ocean water, $(p_{\mathrm{w}}, \theta_{\mathrm{w}})$, below sea-level (for $z < z_{\mathrm{sl}}$).

Initial conditions

Finally, initial conditions have to be prescribed. Here, we fix the initial value for the temperature field and for the fields describing the geometry, z_{s}, z_{l}, and f_{cf}:

$$(\theta, z_{\mathrm{s}}, z_{\mathrm{l}}, f_{\mathrm{cf}}) = (\theta^0, z_{\mathrm{s}}^0, z_{\mathrm{l}}^0, f_{\mathrm{cf}}^0), \tag{2.62}$$

in which the zero superscript indicates prescribed values. Note that there is no need to prescribe the initial velocity field, as the the momentum-balance equation does not contain any time derivative, the advective term being neglected due to the geophysical scales.

2.4 Summary of the governing equations

2.4.1 Equations for ice flow

The equations governing ice flow are summarized below. These equations involve three fields, $\boldsymbol{v}$, p, and θ, defined over the domain $\Omega_t \times]0, T[$, that need to be determined.

Summary of equations for ice flow

Balance equations

$$\operatorname{div} \boldsymbol{v} = 0, \quad \text{in } \Omega_t \times]0, T[, \tag{2.63a}$$

$$-\nabla p + \mathbf{div}(2\eta \boldsymbol{D}) + \rho \boldsymbol{g} = 0, \quad \text{in } \Omega_t \times]0, T[, \tag{2.63b}$$

$$\rho c(\partial_t + \boldsymbol{v} \cdot \nabla)\theta = 4\,\eta\, \|\boldsymbol{D}\|_*^2 + \operatorname{div}(k \nabla \theta), \quad \text{in } \Omega_t \times]0, T[, \tag{2.63c}$$

Kinematics

$$\partial_t z_{\mathrm{s}} + \boldsymbol{u} \cdot \bar{\nabla} z_{\mathrm{s}} - w = a_{\mathrm{s}}, \quad \text{on } \bar{\Omega}_t \times]0, T[, \tag{2.64a}$$

$$\partial_t z_{\mathrm{l}} + \boldsymbol{u} \cdot \bar{\nabla} z_{\mathrm{l}} - w = m_{\mathrm{b}}, \quad \text{on } \bar{\Omega}_t \times]0, T[, \tag{2.64b}$$

$$\partial_t f_{\mathrm{cf}} + \boldsymbol{u} \cdot \bar{\nabla} f_{\mathrm{cf}} = u_{\mathrm{cf}}, \quad \text{on } \bar{\Omega}_t \times]0, T[, \tag{2.64c}$$

$$z_{\mathrm{s}} \geq z_{\mathrm{l}} \geq z_{\mathrm{b}}, \quad \text{on } \bar{\Omega}_t \times]0, T[, \tag{2.64d}$$

Boundary conditions at the top surface

$$\boldsymbol{\sigma} \cdot \boldsymbol{n} = \mathbf{0}, \quad \text{on } \Gamma_\mathrm{s} \times]0, T[, \tag{2.65a}$$
$$\theta = \theta_\mathrm{s}, \quad \text{on } \Gamma_\mathrm{s} \times]0, T[, \tag{2.65b}$$

Boundary conditions at the bottom surface

$$\boldsymbol{v} \cdot \boldsymbol{n} \leq 0, \quad \text{on } \Gamma_\mathrm{g} \times]0, T[, \tag{2.66a}$$
$$(\sigma_{nn} + p_\mathrm{w}) \leq 0, \quad \text{on } \Gamma_\mathrm{g} \times]0, T[, \tag{2.66b}$$
$$(\boldsymbol{v} \cdot \boldsymbol{n})(\sigma_{nn} + p_\mathrm{w}) = 0, \quad \text{on } \Gamma_\mathrm{g} \times]0, T[, \tag{2.66c}$$
$$\boldsymbol{T}(\boldsymbol{\sigma} \cdot \boldsymbol{n}) = \boldsymbol{\tau}_\mathrm{b}, \quad \text{on } \Gamma_\mathrm{g} \times]0, T[, \tag{2.66d}$$
$$\theta = \theta_\mathrm{m}, \quad \text{on } \Gamma_\mathrm{g} \times]0, T[, \tag{2.66e}$$
$$\boldsymbol{\sigma} \cdot \boldsymbol{n} = -p_\mathrm{w} \boldsymbol{n}, \quad \text{on } \Gamma_\mathrm{f} \times]0, T[, \tag{2.66f}$$
$$\theta = \theta_\mathrm{w}, \quad \text{on } \Gamma_\mathrm{f} \times]0, T[, \tag{2.66g}$$

Boundary conditions at the calving front

$$\boldsymbol{\sigma} \cdot \boldsymbol{n} = -p_\mathrm{cf}\, \boldsymbol{n}, \quad \text{on } \Gamma_\mathrm{cf} \times]0, T[, \tag{2.67a}$$
$$\theta = \theta_\mathrm{cf}, \quad \text{on } \Gamma_\mathrm{cf} \times]0, T[, \tag{2.67b}$$

Initial conditions

$$(\theta, z_\mathrm{s}, z_\mathrm{l}, f_\mathrm{cf}) = (\theta^0, z_\mathrm{s}^0, z_\mathrm{l}^0, f_\mathrm{cf}^0), \quad \text{at } \Omega_t \times \{t = 0\}. \tag{2.68}$$

2.4.2 Challenges

The system of equations (2.63)–(2.68) presents several difficulties that makes it particularly hard to solve. These difficulties have led researchers to develop new solver strategies to overcome them:

- Large-scale problem: the domain Ω_t on which the equations must be solved is typically of very large scale, with horizontal scales that are of the order of hundreds or thousands of kilometers for ice sheets. Yet, several processes must be solved at a sub-kilometer scale, e.g., grounding-line migration [Durand et al., 2009; Pattyn et al., 2012]. To limit the computational cost due to the scales involved, adaptive-mesh refinement techniques have been implemented in large-scale ice sheet codes [Cornford et al., 2013; Jouvet and Gräser, 2013; Isaac et al., 2015b]. Those techniques allow to refine the computational mesh only in the necessary regions, typically close to the grounding line in which large gradients of the unknown fields are present. Furthermore, codes have been designed so that they can be run on massively parallel architectures, exploiting the structure of both CPUs and GPUs [Watkins et al., 2023].

- Non-linearities: the fact that ice sheets have a viscosity that depends on the strain-rate tensor makes the equations non-linear. Specifically, the effective viscosity is inversely proportional to the magnitude of the strain-rate tensor (equation (2.32)). As a result, the problem is often quite ill-conditioned, and solution methods may fail to converge or converge slowly. Several strategies have been proposed to resolve this difficulty; for example, the use of homotopy confinuation in the Newton solver [Tezaur et al., 2015] or preconditioners that exploit the shallow geometry of ice sheets [Tuminaro et al., 2016; Heinlein et al., 2022].

- In addition, machine-learning techniques are employed to solve the momentum-balance equations rapidly thanks to a previously trained neural network [Jouvet et al., 2021; Jouvet and Cordonnier, 2023; He et al., 2023]. This provides a possible for solution to accelerate ice-sheet simulations which can be slow because of the two previous difficulties.
- Free-surface problem: for each time step, the upper and lower surface as well as the calving front-position must be updated. As there is a coupling between these positions and the velocity field in the ice sheet, this leads to restrictions on the allowable time steps [Bueler, 2022]. Specific time-integration methods can help reduce this effect [Löfgren et al., 2022].
- Evolving grounding line: the positions of the grounded and floating regions are unknowns of the problem that must be determined for each time step, as those typically evolve over time. As a consequence, different boundary conditions at the lower ice-sheet surface may be applied at each time step. Formally, the mechanical problem can be formulated as an obstacle problem, similar to contact problems that can be found in computational mechanics. There are several ways to formalize this problem [e.g., Gagliardini et al., 2007; Schoof, 2011; Stubblefield et al., 2021; de Diego et al., 2022, 2023]; for example, this structure can be identified in the contact conditions identified over the grounded region Γ_{g}, namely equations (2.66a)–(2.66c):

$$\boldsymbol{v} \cdot \boldsymbol{n} \leq 0, \tag{2.69a}$$
$$(\sigma_{nn} + p_{\mathrm{w}}) \leq 0, \tag{2.69b}$$
$$(\boldsymbol{v} \cdot \boldsymbol{n})(\sigma_{nn} + p_{\mathrm{w}}) = 0. \tag{2.69c}$$

  These are illustrated in figure 2.8. This structure was discussed and exploited in Stubblefield et al. [2021] and in de Diego et al. [2022, 2023].
- Initial conditions: the geometry and thermal state at the initial configuration must be determined, on top of material properties (e.g., the enhancement factor of friction coefficients). This yields an inverse problem, in which these fields must be such that the system of equations (2.63) yields quantities that match observations (e.g., surface velocities) [Perego et al., 2014]. A difficulty here is that both there are uncertainties in both the observations and the model, so a proper probabilistic framework is required [Petra et al., 2014; Isaac et al., 2015a].

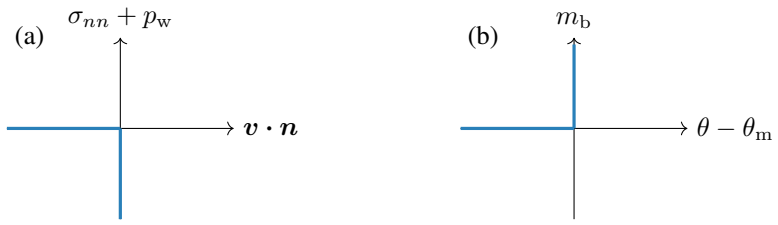

Figure 2.8: Representation of complementarity conditions in the boundary conditions of the thermo-mechanical ice-flow problem. These lead to the formulation of the problem as an obstacle problem. The blue region corresponds to the admissible values of the variables. **(a)** Conditions associated with the contact between the ice and the bedrock in terms of velocity and stress (2.69). **(b)** Conditions associated with the thermal basal conditions (2.70).

2.4.3 Limitations

There are several limitations to the ice-flow model presented here. The two major ones are the absence of damage mechanics and the assumed temperate basal thermal state. We justify these simplifications by the fact that a further discussion of the physics of these mechanisms is not needed for our applications

(Part II). Nonetheless, for the sake of completeness, we briefly discuss these here, with a focus on their implications in terms of model complexity.

Firstly, as mentioned in the rheology discussion (subsection 2.3.1), the new-generation of ice-sheet models includes damage mechanics in their formulation, and we have not described their physics in detail here. A difficulty with the inclusion of damage mechanics in ice-sheet models is that (i) ice can be damaged locally and (ii) this damage is fundamentally a Lagrangian quantity, as it is associated with the ice material itself. This leads to challenges in terms of implementation, as ice-sheet codes are typically large-scale codes that are based on an Eulerian formalism [Duddu and Waisman, 2012; Jiménez et al., 2017].

A second aspect is the thermal state. We have assumed that all the basal ice was temperate, i.e., at the pressure melting point. That is not the case in reality; for example, there are regions in Antarctica where the ground is completely frozen. The distinction between frozen and temperate states yields yet another obstacle problem, with constraints of the form

$$(\theta - \theta_{\mathrm{m}}) \leq 0, \tag{2.70a}$$
$$m_{\mathrm{b}} \geq 0, \tag{2.70b}$$
$$m_{\mathrm{b}}(\theta - \theta_{\mathrm{m}}) = 0, \tag{2.70c}$$

on the grounded lower boundary Γ_{g} (Fig. 2.8). In particular, this means that the inclusion of such a thermal model is not simple. At the same time, the thermal state of ice sheets is thought to be a key factor in their sensitivity to increasing temperatures [Dawson et al., 2022]. An additional difficulty may arise from the presence of sub-temperate sliding zones that are below the pressure melting point but where sliding is permitted [Shreve, 1984; Fowler, 1986b]. These regions have strong implications for ice streams [Mantelli et al., 2019; Mantelli and Schoof, 2019]. Finally, ice above the base can be in a temperate state; the ice sheet is then said to be polythermal. This leads to a region in which ice melts, leading to a mixture of ice and water. To take this phenomenon into account, the energy-balance equation (2.34c) must be modified, and an equation for the moisture evolution must be added [Hutter, 1982; Baral et al., 2001; Schoof and Hewitt, 2016; Hewitt and Schoof, 2017].

2.5 Interactions with other components of the Earth System

2.5.1 Ice-atmosphere interactions

Formally, the effect of the interactions between the atmosphere and the ice is modeled using the net accumulation rate a_{s}. This is the result of a number of phenomena: accumulation by snowfall, ablation by surface erosion, sublimation and meltwater run-off. In a glaciological context, this is often referred to as 'surface mass balance' (SMB). This accumulation term is important in the evolution of ice sheets as it is one of the main controls on their evolution, directly modifying their geometry. Moreover, its evolution is challenging in the context of a warming climate. Indeed, it appears that both precipitation and melt runoff will increase in future climate scenarios, with contrasting tendencies between ice shelves (increase of SMB) and grounded parts (decrease of SMB) [Kittel et al., 2021]. Furthermore, ice-atmosphere interactions are also known to be non-linear phenomena, with processes such as the melt-elevation feedback that is associated with the positive feedback between a shrinking ice sheet and inceased melt at lower elevations [Oerlemans, 1981; Edwards et al., 2014; Levermann and Winkelmann, 2016]. Finally, recent studies have shown that SMB has significant local spatial and temporal variability [Wauthy et al., 2024].

Ideally, the SMB should be calculated based on a regional climate model applied to the ice sheet under study, for example using the `MAR` model [Agosta et al., 2019] or the `RACMO` model [van Wessem et al., 2018]. Given the existing feedbacks between ice-sheet geometry and SMB, this must be done in conjunction with an ice-sheet model. However, this is computationally expensive. Instead, one alternative

is to use a parametrization of the SMB as a function of a reduced number of parameters. A popular parametrization is the 'positive-degree-day' scheme (PDD), which calculates the SMB as a function of the time during which near-surface temperature exceeds freezing [Huybrechts and de Wolde, 1999]. PDD models are computationally cheap and can include the melt-elevation feedback; as such, they have been used in large-scale ice-sheet models [e.g., Garbe et al., 2020; DeConto et al., 2021; Coulon et al., 2024b].

2.5.2 Ice-ocean interactions

The oceans interact with the ice sheets through the sub-shelf melt rate m_b. There are similarities and differences with ice-atmosphere interactions. On the one hand, as with ice-atmosphere interactions, coupling ice-sheet models to oceanographic models is challenging, so a number of simplified models and parametrizations have been developed. Physically, there is a zone called the subglacial plume, where oceanic water interacts with the freshwater that is delivered from the subglacial hydrology at the grounding line and meltwater from the melting of the submerged part of the ice shelves [Hewitt, 2020]. The dynamics of plumes depends on ocean temperatures, ocean stratification and the geometry of the sub-shelf cavities. Several models for sub-shelf melt have been proposed, including the `PICO` model [Reese et al., 2018a] and the plume model [Lazeroms et al., 2019], which are regularly used in large-scale ice-sheet models, as well as simpler algebraic parametrizations relating sub-shelf melt to ocean temperatures far from the ice-ocean interaction zone [Favier et al., 2019; Jourdain et al., 2020; Burgard et al., 2022]. Finally, new models based on neural networks have recently been developed [Burgard et al., 2023].

On the other hand, the behavior of the sub-shelf melt has a much less ambiguous impact than that of the net mass accumulation rate. In fact, an increase of ocean temperatures in future climate scenarios has a clear destabilizing effect on ice sheets. There are several reasons for this. First, a rise in ocean temperatures leads to enhanced sub-shelf melting, since it is an increasing function of the temperature difference between the ice and the ocean [Jenkins et al., 2010, 2018; Burgard et al., 2022]. Secondly, rising temperatures could have a more structural effect by altering oceanographic currents. This could enhance the effect of sub-shelf melt at great depths, particularly near the grounding line, potentially destabilizing it [Hill et al., 2024]. Finally, by reducing the size of the ice shelves, the sub-shelf melt has the effect of destabilizing the ice sheets by removing or limiting their buttressing effect [Gudmundsson et al., 2019]. Conversely, evolving ice sheets can lead to a modification of the oceanographic currents because of the change in freshwater flux that is discharged in the oceans [Coulon et al., 2024a].

2.5.3 Ice-bedrock interactions

Marine ice sheets partly rest on the bedrock. This appears in the mechanical problem introduced above through the bedrock elevation field z_b. The simplest approach is to assume that this elevation is fixed in time. However, this is not strictly speaking the case: the bedrock (specifically, the lithosphere) has a viscoelastic behavior, so that it will react to any change in the geometry of the ice sheet. This modification, known as the 'glacial isostatic adjustment' (GIA) must be taken into account if the ice sheets are studied over relatively long periods, e.g., over several hundred years. In this case, it has been shown that GIA has a stabilizing effect on ice sheet, since it reduces their changes when they are subjected to external forcings [Gomez et al., 2010; Whitehouse, 2018].

In principle, changes in bedrock elevation should not be considered in an isolated fashion. They must be considered in conjunction with changes in ice-sheet thickness and sea-level elevation, as these three components interact through changes in gravitational loading. This led to the so-called 'sea-level equation', which relates changes in bedrock elevation, sea-level elevation, and ice-sheet thickness [Farrell and Clark, 1976]. However, solving this problem is costly, so a whole range of models of varying complexity have yet again been developed, from simple two-dimensional models which can be run efficiently in ice-sheet models [e.g., Le Meur and Huybrechts, 1996; Coulon et al., 2021] to full three-dimensional models [e.g., Zhong et al., 2022].

3

Stress approximations for ice flow

In this chapter, we review the main approximations for the models for ice flow. Starting from the original momentum-balance equations derived in the previous section, we motivate the use of simplifications based on scaling arguments (section 3.1). We then present approximations that were developed to simplify the stress state in the equations for the motion of ice, namely the Blatter–Pattyn model, the shallow-shelf approximation, and the shallow-ice approximation (section 3.2). We also present several approximations to the momentum balance that have been recently developed as a way to obtain a computationally cheap model that still contains the essential features for ice flow (section 3.3). Finally, we discuss a few practical aspects with respect to the use of ice-flow models (section 3.4). This chapter is mainly based on the references [Morlighem, 2011], [Perego et al., 2012], and [Pattyn, 2023].

3.1 Motivation

The motivation for developing approximate models for the equations of ice motion comes from the initial complexity of the governing equations. These are given in the following model, written here in their explicit form, which we call the 'full–Stokes model' to emphasize that it is the original, unsimplified model:

Full–Stokes model:

$$\frac{\partial}{\partial x}\left[2\eta\frac{\partial u}{\partial x}\right]+\frac{\partial}{\partial y}\left[\eta\left(\frac{\partial u}{\partial y}+\frac{\partial v}{\partial x}\right)\right]+\frac{\partial}{\partial z}\left[\eta\left(\frac{\partial u}{\partial z}+\frac{\partial w}{\partial x}\right)\right]-\frac{\partial p}{\partial x}=0, \tag{3.1a}$$

$$\frac{\partial}{\partial x}\left[\eta\left(\frac{\partial u}{\partial y}+\frac{\partial v}{\partial x}\right)\right]+\frac{\partial}{\partial y}\left[2\eta\frac{\partial v}{\partial y}\right]+\frac{\partial}{\partial z}\left[\eta\left(\frac{\partial v}{\partial z}+\frac{\partial w}{\partial y}\right)\right]-\frac{\partial p}{\partial y}=0, \tag{3.1b}$$

$$\frac{\partial}{\partial x}\left[\eta\left(\frac{\partial u}{\partial z}+\frac{\partial w}{\partial x}\right)\right]+\frac{\partial}{\partial y}\left[\eta\left(\frac{\partial v}{\partial z}+\frac{\partial w}{\partial y}\right)\right]+\frac{\partial}{\partial z}\left[2\eta\frac{\partial w}{\partial z}\right]-\frac{\partial p}{\partial z}=0, \tag{3.1c}$$

$$\frac{\partial u}{\partial x}+\frac{\partial v}{\partial y}+\frac{\partial w}{\partial z}=0. \tag{3.1d}$$

This system is made of the momentum-balance equations along the x,y,z directions as well as an incompressibility condition that corresponds to the mass-conservation equation. Together, those equations form a saddle-point problem for the velocity and pressure fields. Note that we here only focus on the differential equations governing the ice flow; for simplicity, we do not consider the kinematics (the evolution of the geometry), the thermal problem (the evolution of the temperature), or the boundary/initial conditions. As mentioned in section 2.4.2 of the previous chapter, the system of equations (3.1) is particularly

challenging to solve for several reasons; among others, it is a system of coupled non-linear differential equations that must be solved on a very large domain. As a consequence, obtaining a solution to the problem of ice flow is computationally expensive.

However, ice sheets heave specific features that can be exploited to simplify the system (3.1). The key point is that ice sheets are shallow, with a characteristic width $[x]$ of the order of thousands of kilometers and a characteristic thickness $[h]$ of the order of kilometers. It follows that the aspect ratio $\varepsilon := [h]/[x]$ is of the order $\mathcal{O}(10^{-3})$. One then expects certain spatial gradients to be smaller than others. Formally, let us denote by $[u]$ and $[w]$ the characteristic scales associated with the horizontal and vertical velocities. These two are constrained; according to the incompressibility condition (3.1d), we have

$$\frac{\partial u}{\partial x}, \frac{\partial v}{\partial y} \sim \frac{\partial w}{\partial z} \quad \Rightarrow \quad \frac{[u]}{[x]} \sim \frac{[w]}{[h]}. \tag{3.2}$$

It follows that

$$\frac{[w]}{[x]} \sim \varepsilon^2 \frac{[u]}{[z]} \quad \Rightarrow \quad \frac{\partial w}{\partial x}, \frac{\partial w}{\partial y} \sim \varepsilon^2 \frac{\partial u}{\partial z}, \varepsilon^2 \frac{\partial v}{\partial z}, \tag{3.3}$$

so that one expects $\partial_x w$ to be much smaller than $\partial_z u$ and $\partial_z v$. This observation will be exploited in the following sections.

3.2 Principal approximations

In this section, we derive the main approximations for ice flow. Here, we follow a physics-based approach in which some of the terms from the governing equations are neglected based on a priori assumptions on the flow geometry and regime. For a more formal derivation of these models based on an asymptotic treatment of the equations, we refer the interested reader to Hindmarsh [2004], Schoof [2006], and Schoof and Hindmarsh [2010]. For a derivation based on variational principles, we refer to Dukowicz et al. [2010, 2011] and Jouvet [2016].

3.2.1 Blatter–Pattyn model

Assumptions

We start with the so-called Blatter–Pattyn (BP) model. The model has been introduced by Herterich [1987], Blatter [1995], and Pattyn [2003]. It is sometimes referred to as a 'first-order approximation' as it is a model based on a rather limited set of assumptions. These are given by the following:

H1. The vertical equilibrium is quasi-cryostatic:

$$\partial_z \sigma_{zz} - \rho g \approx 0, \tag{3.4}$$

i.e., it is assumed that

$$|\partial_x \sigma_{xz}|, |\partial_y \sigma_{yz}| \ll |\partial_z \sigma_{zz}|. \tag{3.5}$$

H2. Ice sheets are shallow, in the sense that they are sufficiently thin so that:

$$|\partial_x w|, |\partial_y w| \ll |\partial_z u|, |\partial_z v|, \tag{3.6}$$

which is consistent with the estimation obtained in (3.3).

H3. The lower and upper ice-sheet surfaces are approximately horizontal, so that

$$n_x, n_y \approx 0 \quad \text{and} \quad |n_z| \approx 1. \tag{3.7}$$

Derivation

To derive the Blatter–Pattyn model, we need two elements: an expression for the pressure and a simplification of the strain-rate tensor. First, we integrate the simplified vertical equilibrium (3.4) (assumption H1). At the upper surface, $z = z_\mathrm{s}$ and we have a free-stress boundary condition $\boldsymbol{\sigma} \cdot \boldsymbol{n} = \boldsymbol{0}$, which here simplifies as $\sigma_{zz} = 0$ given that $n_z \approx 1$ (assumption H3). Hence,

$$\sigma_{zz} = \rho g (z - z_\mathrm{s}), \tag{3.8}$$

that is,

$$p = \rho g (z_\mathrm{s} - z) + 2\eta\, \partial_z w. \tag{3.9}$$

Uisng the incompressibility condition (3.1d), this equation becomes

$$p = \rho g (z_\mathrm{s} - z) - 2\eta (\partial_x u + \partial_y v), \tag{3.10}$$

which is the first key element of the Blatter–Pattyn model. To obtain the second element, we simplify the strain-rate tensor. According to assumption H2, the latter can be written as

$$\boldsymbol{D} = \begin{bmatrix} \partial_x u & \frac{1}{2}(\partial_x v + \partial_y u) & \frac{1}{2}\partial_z u \\ \frac{1}{2}(\partial_x v + \partial_y u) & \partial_y v & \frac{1}{2}\partial_z v \\ \frac{1}{2}\partial_z u & \frac{1}{2}\partial_z v & -\partial_x u - \partial_y v \end{bmatrix}. \tag{3.11}$$

These two results, namely, the simplified expression of the pressure and of the strain-rate tensor, can be exploited in order to simplify the momentum-balance equations (3.1a)–(3.1c). By construction, the vertical component (3.1c) is automatically satisfied. For the horizontal components, we get

$$\partial_x \left[2\eta\, \partial_x u\right] + \partial_y \left[\eta \left(\partial_y u + \partial_x u\right)\right] + \partial_z \left[\eta\, \partial_z u\right] - \rho g\, \partial_x z_\mathrm{s} + \partial_x \left[2\eta \left(\partial_x u + \partial_y v\right)\right] = 0, \tag{3.12a}$$

$$\partial_x \left[\eta \left(\partial_y u + \partial_x v\right)\right] + \partial_y \left[2\eta\, \partial_y v\right] + \partial_z \left[\eta\, \partial_z v\right] - \rho g\, \partial_y z_\mathrm{s} + \partial_y \left[2\eta \left(\partial_x u + \partial_y v\right)\right] = 0. \tag{3.12b}$$

Rearranging, we obtain the following system of equations for (u, v):

Blatter–Pattyn model:

$$-\frac{\partial}{\partial x}\left[2\eta\left(2\frac{\partial u}{\partial x} + \frac{\partial v}{\partial y}\right)\right] - \frac{\partial}{\partial y}\left[\eta\left(\frac{\partial u}{\partial y} + \frac{\partial v}{\partial x}\right)\right] - \frac{\partial}{\partial z}\left[\eta\frac{\partial u}{\partial z}\right] + \rho g \frac{\partial z_\mathrm{s}}{\partial x} = 0, \tag{3.13a}$$

$$-\frac{\partial}{\partial x}\left[\eta\left(\frac{\partial u}{\partial y} + \frac{\partial v}{\partial x}\right)\right] - \frac{\partial}{\partial y}\left[2\eta\left(\frac{\partial u}{\partial x} + 2\frac{\partial v}{\partial y}\right)\right] - \frac{\partial}{\partial z}\left[\eta\frac{\partial v}{\partial z}\right] + \rho g \frac{\partial z_\mathrm{s}}{\partial y} = 0. \tag{3.13b}$$

Discussion

The Blatter–Pattyn model has two significant advantages compared to the original full–Stokes model. Firstly, the number of equations and unknowns is reduced: we only need to solve two equations for (u, v), as the vertical velocity field w and the pressure field p do not appear anymore in the governing equations. The latter can in fact be obtained as by-products, once the u and v fields have been calculated; thanks to continuity equation (3.1d) and to (3.10), we have that

$$w = w|_{z=z_1} - \int_{z_1}^{z} \left(\partial_x u + \partial_y v\right) \mathrm{d}\tilde{z}, \tag{3.14a}$$

$$p = \rho g (z_\mathrm{s} - z) - 2\eta (\partial_x u + \partial_y v). \tag{3.14b}$$

Hence, we effectively have a semi-decoupling between the horizontal and vertical dynamics in the sense that the latter can entirely be determined based on the former. The second advantage is that the Blatter–Pattyn model forms an elliptic system of (non-linear) partial differential equations. Elliptic systems are particularly desirable from a numerical point of view, as standard finite elements or centered finite differences can be used to solve them. By contrast, the saddle-point form of the full–Stokes model requires special care when it is discretized numerically, e.g., mixed finite elements or stabilization methods. On top of that, there exists a large range of methods to accelerate the computation of the solution of equations of the form (3.13) [e.g., multigrids methods: Brown et al., 2013; Tuminaro et al., 2016].

3.2.2 Shallow-shelf approximation

The shallow-shelf approximation (SSA) is a model that further reduces the complexity of the ice flow by assuming that it takes the form of a sliding motion. It is therefore an appropriate model for ice streams (fast-flowing ice flows) and ice shelves. Introduced by Morland [1987], MacAyeal [1989], and Weis et al. [1999], it is sometimes also known as the shelfy-stream approximation.

Assumptions and derivation

In the SSA, the following additional assumption is assumed, on top of the ones used to derive the BP model:

H4a. There is negligible vertical shear in an ice column:

$$\partial_z u, \partial_z v \approx 0. \tag{3.15}$$

In other words, the horizontal velocity components are only functions of (x, y): $u(x, y)$ and $v = v(x, y)$.

To derive the SSA equations, the equations (3.13) are integrated over the ice column $z_\mathrm{l} \leq z \leq z_\mathrm{s}$. A small technical difficulty appears here in that when doing so, the two first terms in the equations (3.13) are integrals of the partial spatial derivative in the x and y axis. It would be convenient if these two operations –integration and derivation– could be exchanged. However, that is in principle not possible because the integration bounds, z_l and z_s, are themselves functions of x and y. Formally, we have

$$\partial_x \int_{z_\mathrm{l}}^{z_\mathrm{s}} f \,\mathrm{d}z = \int_{z_\mathrm{l}}^{z_\mathrm{s}} \partial_x f \,\mathrm{d}z + f|_{z=z_\mathrm{s}} \,\partial_x z_\mathrm{s} - f|_{z=z_\mathrm{l}} \,\partial_x z_\mathrm{l}, \tag{3.16a}$$

$$\partial_y \int_{z_\mathrm{l}}^{z_\mathrm{s}} f \,\mathrm{d}z = \int_{z_\mathrm{l}}^{z_\mathrm{s}} \partial_y f \,\mathrm{d}z + f|_{z=z_\mathrm{s}} \,\partial_y z_\mathrm{s} - f|_{z=z_\mathrm{l}} \,\partial_y z_\mathrm{l}, \tag{3.16b}$$

in which f represents the viscous terms in (3.13). Given the hypothesis of approximately horizontal lower and upper ice-sheet surfaces (assumption H3), we neglect the terms proportional to the spatial gradients of z_l and z_s. It follows that that we can effectively interchange the integration and differentiation operations. Then,

$$\partial_x \int_{z_\mathrm{l}}^{z_\mathrm{s}} \left[2\eta \left(2\partial_x u + \partial_y v\right)\right] \mathrm{d}z + \partial_y \int_{z_\mathrm{l}}^{z_\mathrm{s}} \left[\eta \left(\partial_y u + \partial_x u\right)\right] \mathrm{d}z + \left[\eta \,\partial_z u\right]_{z=z_\mathrm{l}}^{z=z_\mathrm{s}} - \rho g h \,\partial_x z_\mathrm{s} = 0, \tag{3.17a}$$

$$\partial_x \int_{z_\mathrm{l}}^{z_\mathrm{s}} \left[\eta \left(\partial_y u + \partial_x v\right)\right] \mathrm{d}z + \partial_y \int_{z_\mathrm{l}}^{z_\mathrm{s}} \left[2\eta \left(\partial_x u + 2\partial_y v\right)\right] \mathrm{d}z + \left[\eta \,\partial_z v\right]_{z=z_\mathrm{l}}^{z=z_\mathrm{s}} - \rho g h \,\partial_y z_\mathrm{s} = 0, \tag{3.17b}$$

Applying the dynamic boundary conditions (2.66d) and (2.65a), respectively representing the application of basal friction law at the bottom surface and free-slip at the top surface, we get

$$\partial_x \int_{z_\mathrm{l}}^{z_\mathrm{s}} \left[2\eta \left(2\partial_x u + \partial_y v\right)\right] \mathrm{d}z + \partial_y \int_{z_\mathrm{l}}^{z_\mathrm{s}} \left[\eta \left(\partial_y u + \partial_x u\right)\right] \mathrm{d}z + 1_\mathrm{g} \,\tau_{\mathrm{b},x} - \rho g h \,\partial_x z_\mathrm{s} = 0, \tag{3.18a}$$

$$\partial_x \int_{z_\mathrm{l}}^{z_\mathrm{s}} \left[\eta \left(\partial_y u + \partial_x v\right)\right] \mathrm{d}z + \partial_y \int_{z_\mathrm{l}}^{z_\mathrm{s}} \left[2\eta \left(\partial_x u + 2\partial_y v\right)\right] \mathrm{d}z + 1_\mathrm{g} \,\tau_{\mathrm{b},y} - \rho g h \,\partial_y z_\mathrm{s} = 0, \tag{3.18b}$$

in which 1_g is the indicator function for the grounded domain, over which there is basal friction, and $\tau_{\mathrm{b},y}, \tau_{\mathrm{b},y}$ are the x, y components of $\boldsymbol{\tau}_\mathrm{b}$. Finally, we evaluate the integrals of the viscous terms. Here, we rely on the assumption that u and v independent of z (assumption H4a) to get

$$\partial_x \left[2\bar{\eta}h \left(2\partial_x u + \partial_y v\right)\right] + \partial_y \left[\bar{\eta}h \left(\partial_y u + \partial_x u\right)\right] + 1_\mathrm{g}\, \tau_{\mathrm{b},x} - \rho g h\, \partial_x z_\mathrm{s} = 0, \tag{3.19a}$$

$$\partial_x \left[\bar{\eta}h \left(\partial_y u + \partial_x v\right)\right] + \partial_y \left[2\bar{\eta}h \left(\partial_x u + 2\partial_y v\right)\right] + 1_\mathrm{g}\, \tau_{\mathrm{b},y} - \rho g h\, \partial_y z_\mathrm{s} = 0, \tag{3.19b}$$

where $\bar{\eta}$ denotes the vertically-integrated effective viscosity defined as

$$\bar{\eta} := \frac{1}{h} \int_{z_\mathrm{l}}^{z_\mathrm{s}} \eta \, \mathrm{d}z = \frac{1}{h} \int_{z_\mathrm{l}}^{z_\mathrm{s}} \frac{1}{2} A^{-\frac{1}{n}} \|\boldsymbol{D}\|_*^{\frac{1-n}{n}} \, \mathrm{d}z, \tag{3.20}$$

and where $h := z_\mathrm{s} - z_\mathrm{l}$ is the ice thickness. This expression can be further simplified because of the simplified form of the strain-rate tensor (assumptions H3 and H4a). Indeed, we have

$$\|\boldsymbol{D}\|_*^2 = (\partial_x u)^2 + (\partial_y v)^2 + \partial_x u\, \partial_y v + \frac{1}{4} \partial_y u\, \partial_x v, \tag{3.21}$$

which does not depend on z. Hence,

$$\bar{\eta} = \frac{1}{2} \frac{\|\boldsymbol{D}\|_*^{\frac{1-n}{n}}}{h} \int_{z_\mathrm{l}}^{z_\mathrm{s}} A^{-\frac{1}{n}} \, \mathrm{d}z. \tag{3.22}$$

Overall, the following model is obtained:

Shallow-shelf approximation:

$$-\frac{\partial}{\partial x}\left[2\bar{\eta}h\left(2\frac{\partial u}{\partial x} + \frac{\partial v}{\partial y}\right)\right] - \frac{\partial}{\partial y}\left[\bar{\eta}h\left(\frac{\partial u}{\partial y} + \frac{\partial v}{\partial x}\right)\right] - 1_\mathrm{g}\, \tau_{\mathrm{b},x} + \rho g h \frac{\partial z_\mathrm{s}}{\partial x} = 0, \tag{3.23a}$$

$$-\frac{\partial}{\partial x}\left[\bar{\eta}h\left(\frac{\partial u}{\partial y} + \frac{\partial v}{\partial x}\right)\right] - \frac{\partial}{\partial y}\left[2\bar{\eta}h\left(\frac{\partial u}{\partial x} + 2\frac{\partial v}{\partial y}\right)\right] - 1_\mathrm{g}\, \tau_{\mathrm{b},y} + \rho g h \frac{\partial z_\mathrm{s}}{\partial y} = 0. \tag{3.23b}$$

Discussion

The main advantage of the shallow-shelf approximation over the Blatter–Pattyn model is that the equations governing u and v are defined on a two-dimensional set, whereas those of the Blatter–Pattyn model were defined on a three-dimensional set. This difference arises from assumption H4a, which removes the dependence of the equations on the vertical coordinate.

The system (3.23) has an interesting physical interpretation. It corresponds to a balance between three different forces: the divergence of viscous stresses, basal friction and gravitational driving stress. Rather than talking about viscous stresses, glaciologists generally speak of 'membrane stresses' or 'longitudinal stresses' to emphasize that in the SSA model, these are reduced to horizontal variations in velocity.

3.2.3 Shallow-ice approximation

Whereas the shallow-shelf approximation considers ice motion associated with a sliding motion, the shallow-ice approximation (SIA) considers ice motion associated with a vertical deformation, i.e., a shearing of the ice. It is appropriate for slow-flowing ice flow, e.g., the flow taking place inland of the ice sheet, far from the grounding line. This model was introduced by Fowler and Larson [1978], Morland and Johnson [1980], and Hutter [1983].

Assumptions and derivation

Here, on top of the assumptions of the BP model, the following assumption is added:

H4b. There is negligible horizontal straining in the ice:

$$\partial_x u, \partial_y u, \partial_x v, \partial_y v \approx 0. \tag{3.24}$$

With this assumption, the equations (3.13) of the BP model become

$$-\partial_z(\eta\,\partial_z u) + \rho g\,\partial_x z_\mathrm{s} = 0, \tag{3.25a}$$
$$-\partial_z(\eta\,\partial_z v) + \rho g\,\partial_y z_\mathrm{s} = 0. \tag{3.25b}$$

These can be integrated vertically. Because of the stress-free condition at $z = z_\mathrm{s}$, they become

$$\eta\,\partial_z u = \rho g(z - z_\mathrm{s})\partial_x z_\mathrm{s}, \tag{3.26a}$$
$$\eta\,\partial_z v = \rho g(z - z_\mathrm{s})\partial_y z_\mathrm{s}. \tag{3.26b}$$

The effective viscosity η greatly simplifies because of the hypotheses on the strain-rate tensor (assumptions H3 and H4b). It is given by

$$\eta = \frac{1}{2}A^{-\frac{1}{n}}\|\boldsymbol{D}\|^{\frac{1-n}{n}}, \quad \|\boldsymbol{D}\|^2 = \frac{1}{4}(\partial_z u)^2 + \frac{1}{4}(\partial_z v)^2. \tag{3.27}$$

Combining (3.26) with (3.27), it is possible to express the effective pressure η as follows:

$$\eta = \frac{1}{2}A^{-1}\left[\rho g(z - z_\mathrm{s})\|\bar{\nabla} z_\mathrm{s}\|\right]^{1-n}. \tag{3.28}$$

Combining this result with (3.26), on then gets

$$\partial_z u = 2(\rho g)^n A(z - z_\mathrm{s})^n \|\bar{\nabla} z_\mathrm{s}\|^n \partial_x z_\mathrm{s}, \tag{3.29a}$$
$$\partial_z v = 2(\rho g)^n A(z - z_\mathrm{s})^n \|\bar{\nabla} z_\mathrm{s}\|^n \partial_y z_\mathrm{s}. \tag{3.29b}$$

Finally, these equations can be integrated vertically yet again to obtain the shallow-ice approximation:

Shallow-ice approximation:

$$u = u|_{z=z_1} - 2(\rho g)^n \int_{z_1}^{z} A(z_\mathrm{s} - \tilde{z})^n \,\mathrm{d}\tilde{z}\, \|\bar{\nabla} z_\mathrm{s}\|^{n-1} \frac{\partial z_\mathrm{s}}{\partial x}, \tag{3.30a}$$
$$v = v|_{z=z_1} - 2(\rho g)^n \int_{z_1}^{z} A(z_\mathrm{s} - \tilde{z})^n \,\mathrm{d}\tilde{z}\, \|\bar{\nabla} z_\mathrm{s}\|^{n-1} \frac{\partial z_\mathrm{s}}{\partial y}. \tag{3.30b}$$

Discussion

The equations of the SIA model are such that the horizontal velocities u and v are simply obtained as analytical expressions which are functions of the slope of the upper-surface elevation z_s. It is necessary to perform a vertical integration, but this can be done independently at each position where the velocity is calculated; in that sense, the model is purely local.

It can be noted that this model can be coupled with an equation for the thickness h of the ice in order to obtain a parabolic equation for the latter [e.g., Schoof and Hewitt, 2013]. In view of the similarities with the theory of lubrication in fluid mechanics, this model is often refereed to as the 'lubrication model' for ice flow.

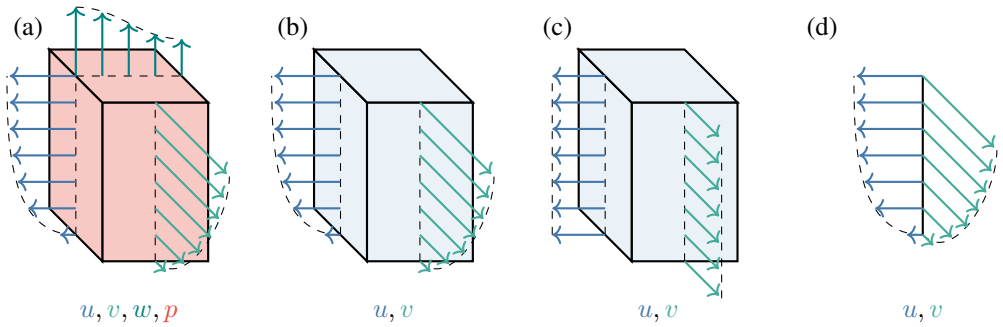

Figure 3.1: Schematic of the principal approximations of ice flow [adapted from Morlighem, 2011]: **(a)** Full–Stokes model; **(b)** Blatter–Pattyn model; **(c)** shallow-shelf approximation; **(d)** shallow-ice approximation. The variables below each drawing correspond to the unknowns in the approximate model for ice flow.

Name	L-classification	Type	Dimension	Unknowns
FS	-	Saddle point	3D	u, v, w, p
BP	LMLa	Elliptic	3D	u, v
SSA	L1L1	Elliptic	2D	u, v
SIA	S	Algebraic	0D	u, v

Table 3.1: Properties of the principal approximations for ice flow. The approximations are ordered by decreasing order of complexity. The L-classification is a systematic ordering for the approximations of ice flow, following Hindmarsh [2004].

3.2.4 Summary

The models presented in this subsection are summarized in figure 3.1 and in table 3.1.

3.3 Approximations to higher-order models

Here, we present models of ice flow that attempt to account for both membrane stresses (i.e., sliding behavior, similar to the SSA model) and vertical shear (i.e., vertical deformation behavior, similar to the SIA model), while maintaining low model complexity. In doing so, they provide approximations to the 'higher-order' BP model. While they are not formally of higher order themselves, these models yield errors comparable to those of the BP model in practice. Several approaches can be used to obtain such models, which we describe here.

3.3.1 Hybrid models

Hybrid models are the simplest models that allow to include both membrane and shear stresses. They simply consist in a linear combination of the velocity fields obtained by the SSA and SIA models. Bueler and Brown [2009] suggest to model the ice-flow velocity $\boldsymbol{u}$ as

$$\boldsymbol{u} = f\,\boldsymbol{u}_{\mathrm{sia}} + (1 - f)\,\boldsymbol{u}_{\mathrm{ssa}}, \tag{3.31}$$

in which $\boldsymbol{u}_{\mathrm{ssa}}$ and $\boldsymbol{u}_{\mathrm{sia}}$ are the velocity fields obtained with the SSA and SIA models, respectively, and $0 \leq f \leq 1$ is a weighing parameter. Given that the SSA is expected to hold in fast-flowing regions, while the SIA is expected to hold in slow-flowing regions, f can be parameterized as a function $f = f(\|\boldsymbol{u}_{\mathrm{ssa}}\|)$

that is such that

$$f(\|\boldsymbol{u}_{\mathrm{ssa}}\|) \sim 1 \quad \text{for } \|\boldsymbol{u}_{\mathrm{ssa}}\| \ll u_0, \tag{3.32a}$$
$$f(\|\boldsymbol{u}_{\mathrm{ssa}}\|) \sim 0 \quad \text{for } \|\boldsymbol{u}_{\mathrm{ssa}}\| \gg u_0, \tag{3.32b}$$

in which u_0 is a threshold velocity parameter separating slow-flowing from fast-flowing velocities, e.g., $u_0 = 100\,\mathrm{m/a}$. Alternatively, one can simply add both contributions [Winkelmann et al., 2011; Pollard and DeConto, 2012a; Pattyn, 2017], which results in

$$\boldsymbol{u} = \boldsymbol{u}_{\mathrm{sia}} + \boldsymbol{u}_{\mathrm{ssa}}. \tag{3.33}$$

Given that the SIA is dominant in the region where the SSA is not (and vice-versa), this provides an approximation scheme that is similar to (3.31) [Bernales et al., 2017]. Such a model is often refereed to as the 'SSA+SIA' model.

3.3.2 Depth-integrated models

Depth-integrated models arise from a vertical integration of the Blatter–Pattyn model. The depth-integrated equations are then simplified to obtain a model that can be used effectively in practice. It follows that depth-integrated models are very similar to the SSA model, since the latter was developed using this principle. However, the assumptions used to simplify the depth-integrated equations are weaker compared to that of the SSA, and in particular it is not assumed that there is no vertical shear in an ice column. In practical terms, depth-integrated models have a similar structure to the SSA equations, but the effective viscosity includes contributions associated with vertical shear stress. As a result, they provide a stronger coupling between sliding and shearing motions than hybrid models. Depth-integrated models include the L1L2 model of Schoof and Hindmarsh [2010], the DIVA model [Goldberg, 2011; Arthern et al., 2015], and the MOLHO model [Dias dos Santos et al., 2022].

3.3.3 Multilayer models

A third family of approximations to higher-order models are multi-layer models. Here, the idea is to have a series of a few horizontal models that can be solved very easily (in a similar way to an SSA model), and to combine them to obtain a vertical distribution of velocities. In this way, these models allow both sliding and shearing motion to be taken into account, but at a lower cost compared to the BP model. An example of such a model is the MSSA [Jouvet, 2014, 2015].

3.4 Practical aspects

3.4.1 Validity of the approximations

The choice of an ice-flow model depends on the conditions in which it is found and the computational resources available. The rule of thumb is that the SSA model is valid for flow in ice shelves or ice streams, whereas the SIA model is valid for regions where the ice flows slowly or where there are large slopes in the bed topography. In transition zones between SSA and SIA, it is preferable to use a higher-order model. Finally, the full–Stokes model is necessary where there is a particularly complex stress distribution (e.g., non-cryostatic vertical stress, Raymond effects at the ice divides).

In order to assess the validity of the different approximations, intercomparison studies have been developed within the glaciology community. These consider test cases with an imposed numerical set-up. Different ice-flow codes, associated with different model approximations, are then tested and compared on the same set-up. This makes it possible to compare both the validity of the approximations and the influence of numerical implementation details (type of discretization, resolution, etc). Intercomparative studies in the glaciological literature include the evaluation of higher-order models [ISMIP-HOM; Pattyn

Name	Model(s)	Discretization	Main reference
`Elmer/Ice`	FS	FE	Gagliardini et al. [2013]
`MALI`	BP	FE/FV	Hoffman et al. [2018]
`ISSM`	SSA, BP	FE	Larour et al. [2012]
`BISICLES`	L1L2	FV	Cornford et al. [2013]
`CISM`	DIVA	FE/FV	Lipscomb et al. [2019]
`f.ETISh/Kori-ULB`	SSA+SIA	FD	Pattyn [2017]
`PISM`	SSA+SIA	FD	Winkelmann et al. [2011]
`YELMO`	SSA+SIA	FD	Robinson et al. [2020]

Table 3.2: List including some of the main ice-flow codes. These codes are developed using different methods of spatial discretization: finite elements (FE), finite volumes (FV), or finite differences (FD). They generally include several model formulations that can be solved; here, we highlight only the models that are typically used with these codes [e.g., in intercomparison studies, as shown in Seroussi et al., 2020].

et al., 2008], of different models when applied to marine regions [MISMIPs; Pattyn et al., 2012, 2013; Asay-Davis et al., 2016; Cornford et al., 2020], and the evaluation of ice-sheet codes for predicting the evolution of the entire Antarctic ice sheet [ISMIP6; Seroussi et al., 2020].

3.4.2 Implementations

Examples of ice-flow codes are shown in table 3.2.

4

The subglacial environment

4.1 Introduction

Subglacial conditions, namely subglacial friction and basal hydrology, have a major influence on ice-sheet dynamics, but are currently poorly understood [Flowers, 2015; Bulthuis et al., 2019; Brondex et al., 2019; Dow, 2022b; Kazmierczak et al., 2022]. They are the subject of numerous studies which aim at modeling the processes that govern those conditions. These models are presented in sections 4.2 and 4.3. In the section dedicated to basal friction (section 4.2), we review friction laws, first on hard and then on soft beds. We conclude with friction laws that are thought to unify both hard and soft beds. Similarly, we start the section dedicated to subglacial hydrology (section 4.3) by first comparing the physics of subglacial water flow on hard and soft beds. Finally, we discuss the question of including multiple drainage systems in a unified model.

This chapter is based on the lecture notes Fowler and Ng [2021] and Hewitt [2023], as well as studies which are directly referred to in the text. For subglacial hydrology, a reference article on the subject is the review paper Flowers [2015]. A selected history of the earlier developments of basal friction can also be found in Fowler [2010c].

4.2 Basal friction

Numerous studies have shown that the surface velocities observed over ice sheets cannot be explained by the creep of ice alone [e.g., Rignot and Mouginot, 2012; Ryser et al., 2014; Maier et al., 2019]. In fact, there is an additional component to the ice motion which comes from the basal conditions: basal sliding. Physically, if the ice at the ice-sheet base is temperate, then there can be a small water film that allows ice to slide on the bedrock. This motion is not without resistance, as, among others, bumps in the bedrock create some drag that will slow down ice flow. Nevertheless, this sliding behavior is a major contributor to the motion of ice sheets.

Formally, basal mechanics are parametrized through a relation between the basal velocity $\boldsymbol{u}_\mathrm{b}$ and the basal traction or shear stress $\boldsymbol{\tau}_\mathrm{b}$, which are defined as the tangential components of the surface traction and of the velocity, respectively:

$$\boldsymbol{\tau}_\mathrm{b} := \boldsymbol{T}(\boldsymbol{\sigma} \cdot \boldsymbol{n}), \tag{4.1a}$$

$$\boldsymbol{u}_\mathrm{b} := \boldsymbol{T}(\boldsymbol{v}), \tag{4.1b}$$

where $\boldsymbol{T}$ is the tangential projection operator defined by

$$\boldsymbol{T} := (\boldsymbol{I} - \boldsymbol{n} \otimes \boldsymbol{n}), \tag{4.2}$$

with $\boldsymbol{I}$ the identity mapping and $\boldsymbol{n}$ the unit exterior normal to the ice-bed interface. While early developments in glaciology initially led to sliding relations of the form

$$\boldsymbol{u}_\mathrm{b} = \boldsymbol{u}_\mathrm{b}(\boldsymbol{\tau}_\mathrm{b}), \tag{4.3}$$

it is now a common practice to consider so-called friction laws, which are of the form

$$\boldsymbol{\tau}_\mathrm{b} = \boldsymbol{\tau}_\mathrm{b}(\boldsymbol{u}_\mathrm{b}). \tag{4.4}$$

Such a relation then takes the form of a (usually non-linear) boundary condition for the ice-flow problem (see section 2.4).

Importantly, friction laws parametrize unresolved sub-scale processes. Fundamentally speaking, the sliding behavior as previously described is nothing else than a form of ice creep that happens within a boundary layer close to the bed. However, there are many different phenomena in that region, which are both not well-known –direct measurements are very difficult– and at a very local scale (typically, sub-meter scale). Hence, when dealing with models for ice sheets, we encapsulate these small complex processes in a basal friction law of the form (4.4). Practically, this also means that parameters in the basal friction will be resolution-dependent [Kyrke-Smith et al., 2018]. A schematic of this concept of friction law, together with the main friction laws described later in this section, is shown in figure 4.1.

In what follows, we will not work with the vector relation (4.4) but, for convenience, with its scalar representation. Because friction at the bed is opposed to ice motion, we have

$$\boldsymbol{\tau}_\mathrm{b} = -\tau_\mathrm{b}\,\hat{\boldsymbol{u}}_\mathrm{b}, \tag{4.5}$$

in which $\tau_\mathrm{b} := \|\boldsymbol{\tau}_\mathrm{b}\|$ is the magnitude of the basal friction stress, and $\hat{\boldsymbol{u}}_\mathrm{b}$ is the direction of the basal velocity, defined as $\hat{\boldsymbol{u}}_\mathrm{b} = \boldsymbol{u}_\mathrm{b}/\|\boldsymbol{u}_\mathrm{b}\|$ if $\|\boldsymbol{u}_\mathrm{b}\| \neq 0$ and as $\hat{\boldsymbol{u}}_\mathrm{b} = \boldsymbol{0}$ otherwise. Writing $u_\mathrm{b} := \|\boldsymbol{u}_\mathrm{b}\|$, we will therefore describe friction laws in terms of relations of the form

$$\tau_\mathrm{b} = \tau_\mathrm{b}(u_\mathrm{b}). \tag{4.6}$$

4.2.1 Hard beds

Viscous sliding and regelation

The original study of sliding on hard beds is due to Weertman [1957]. They considered that sliding is influenced by two phenomena: viscous creep and regelation. Viscous creep simply corresponds to the influence of bedrock due to bumps (also called obstacles) in its geometry on ice flow. Because of Glen's flow law, a simple analysis suggests a non-linear relationship between τ_b and u_b of the following form:

$$\tau_\mathrm{b} = \nu^2 \left(2dA\right)^{-\frac{1}{n}} u_\mathrm{b}^{\frac{1}{n}}, \tag{4.7}$$

where A is the viscosity coefficient in Glen's flow law, n is the associated exponent, d is the scale of bumps in the bedrock, and $\nu := d/\lambda$ is a measure of bed roughness, where λ is the characteristic distance between the bumps. Regelation is a purely thermal effect. It can be explained as follows: upstream of a bed obstacle, the normal stress is relatively larger (because the bed offers resistance to the ice motion), which leads to a lower pressure melting point. By contrast, in the lee of the obstacle, the normal stress is relatively smaller, leading to a higher pressure melting point. This leads to a potential of melting upstream of the obstacle, and freezing downstream of it. This mechanism is made possible by a conductive heat flux that goes from downstream to upstream of the obstacle and gets converted to latent heat used for melting the ice. Balancing these two heat fluxes leads to the following relation:

$$\tau_\mathrm{b} = \nu^2 \left(\frac{\rho L d}{k_\mathrm{b} c_\mathrm{t}}\right) u_\mathrm{b}, \tag{4.8}$$

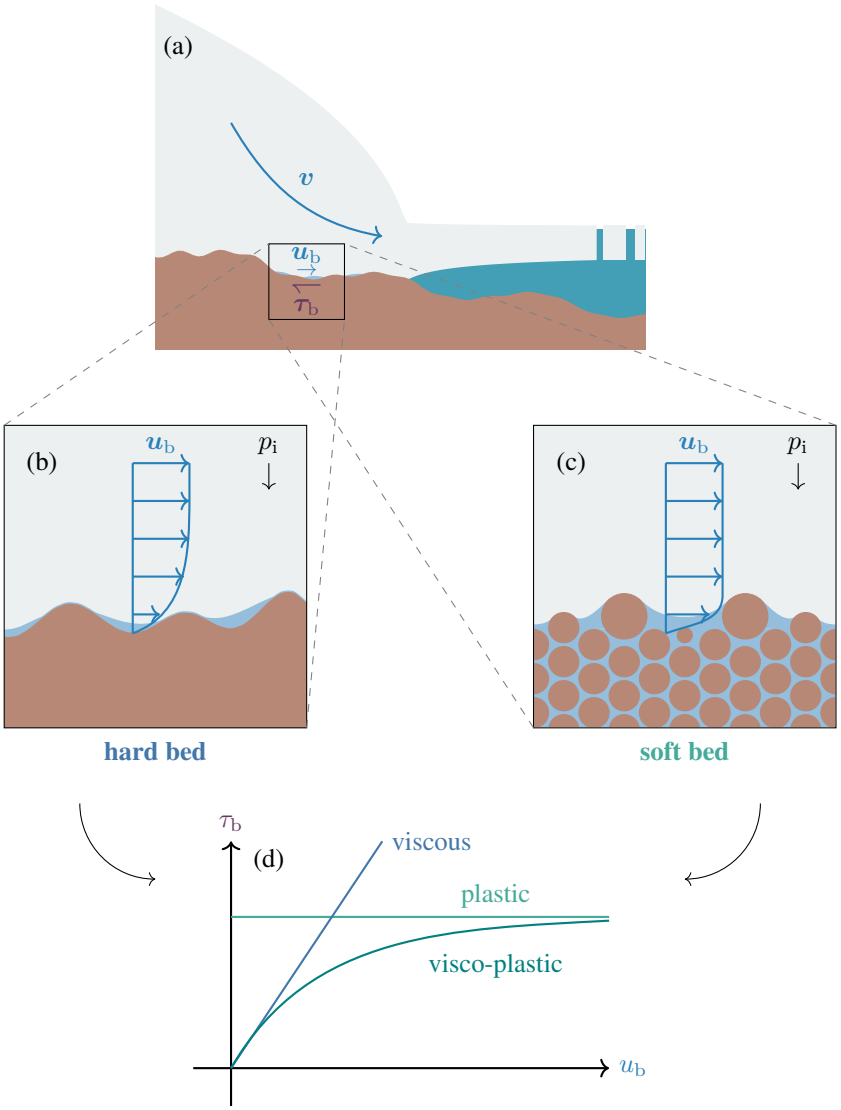

Figure 4.1: Schematics associated with the notion of friction law in ice-sheet modeling [adapted from Hewitt, 2023]. **(a)** Schematic of the concept of friction law: the macroscopic friction stress $\boldsymbol{\tau}_\mathrm{b}$ is related to the macroscopic basal velocity $\boldsymbol{u}_\mathrm{b}$ according to a relation of the form, in magnitude, $\tau_\mathrm{b} = \tau_\mathrm{b}(u_\mathrm{b})$. This relation models the physical phenomena that are not modelled in the large-scale model, e.g., sliding over small protrusions, regelation, or till deformation. **(b)** On hard beds, friction is caused by the resistance offered by the bed roughness, this resistance being modulated by the formation of water cavities. **(c)** On soft beds, friction is caused by the plow of particles at the ice-bed interface. **(d)** Models of subglacial friction in a log-log plot: viscous relation $\tau_\mathrm{b} \propto u_\mathrm{b}^p$ ('Weertman' friction law), plastic relation $\tau_\mathrm{b} \propto N$ ('Coulomb' friction law), and visco-plastic relation ('regularized Coulomb' friction law). The regularized Coulomb law has been proposed as way to unify several models of subglacial friction on both hard and soft beds [Minchew and Joughin, 2020]. A missing element in this schematic is the characterization of the effective pressure $N = p_\mathrm{i} - p_\mathrm{w}$, p_i being the ice overburden pressure and p_w the subglacial water pressure, which modulates the magnitude and regime of friction.

where L is the latent heat of water, k_b is the thermal conductivity of the bedrock, and c_t is the Clapeyron slope.

These two mechanisms are effective at different scales: the first one is dominant for large obstacles, while the second one is dominant for small obstacles. This suggests that there is a controlling obstacle size at which the stresses are comparable so that the sum of the friction stresses defined in (4.7) and (4.8) is minimized. This value is given by

$$d_0 := \left[\frac{k_\mathrm{b} c_\mathrm{t}}{n\rho L (2A)^{\frac{1}{n}}}\right]^{\frac{n}{n+1}} u_\mathrm{b}^{\frac{1-n}{1+n}} \tag{4.9}$$

and, for this obstacle size, we get

$$\tau_\mathrm{b} = \nu^2 \left(\frac{\rho L}{2\, n^n k_\mathrm{b} c_\mathrm{t} A}\right)^{\frac{1}{n+1}} u_\mathrm{b}^{\frac{2}{n+1}}. \tag{4.10}$$

This type of law, in which the basal friction stress takes the form of a power-law with respect to the basal velocity is then known as a Weertman friction law, which we denote as follows:

Weertman friction law

$$\tau_\mathrm{b} = C_\mathrm{w}\, u_\mathrm{b}^p, \tag{4.11}$$

in which $C_\mathrm{w} > 0$ is a friction coefficient that depends on the properties of the bed, and $p > 0$ is an exponent. In practice, the value $p = 1/3$ is often used [e.g., Pattyn et al., 2012].

A shortcoming of Weertman's derivation is that it is based on a scaling analysis, and not on a rigorous derivation. To circumvent this issue, Nye [1969, 1970] and Kamb [1970] solved the mathematical problem of sliding with regelation. They assumed that ice behaves as a Newtonian fluid, i.e., considered $n = 1$ in Glen's flow law, so that ice has a constant viscosity η. That is a major limitation of their work, as the shear-thinning behavior of ice is an essential component to the physics of ice flows. Nonetheless, this allows to obtain a system of linear equations for temperature and ice velocity, which can then be solved analytically for small perturbations in the bed profile. In particular, the following explicit expression for the friction law was obtained:

$$\tau_\mathrm{b} = \frac{\eta\, \kappa_0^2}{\pi} u_\mathrm{b} \int_0^{+\infty} \frac{\kappa^3}{\kappa^2 + \kappa_0^2} S_\mathrm{b}(\kappa)\, \mathrm{d}\kappa, \tag{4.12}$$

in which S_b denotes the power spectral density of the bedrock elevation z_b along a flowline. Here, κ_0 denotes the controlling wavenumber for the problem, and is defined as

$$\kappa_0^2 := \frac{\rho L}{4\, k_\mathrm{b} c_\mathrm{t} \eta}. \tag{4.13}$$

Several comments can be made with respect to this result. Firstly, bed roughness has a clear impact on the friction law, as can be seen to the influence of the power spectral density in the equation (4.12). Secondly, the obtained friction law is linear, which is expected as the equations of the problem are all linear. Thirdly, the controlling wavenumber is consistent with the earlier results of Weertman [1957] when considering the linear case $n = 1$. Indeed, for such a case, $\eta = (2A)^{-1}$, and comparison between (4.9) and (4.13) yields

$$\kappa_0 = \frac{1}{2} d_0^{-1}. \tag{4.14}$$

Sliding with cavitation

Early on, Lliboutry [1968] suggested that subglacial water could modify the sliding laws. The mechanism at play here is subglacial cavitation, in which cavities can be filled with water, depending on the subglacial water pressure and the basal velocity of ice. Following a series of measurements, Budd et al. [1979] introduced a generalization of the Weertman friction law (4.11) that includes the effect of subglacial water pressure:

Budd friction law

$$\tau_\mathrm{b} = C_\mathrm{b}\, u_\mathrm{b}^p N^q, \tag{4.15}$$

with $C_\mathrm{b} > 0$ a friction coefficient and p, q exponents that are typically such that $0 < p, q \leq 1$. Here, $N = p_\mathrm{i} - p_\mathrm{w}$ is the so-called effective pressure, with p_i the ice overburden pressure (i.e., the pressure that the ice applies on the bed, because of its thickness), and p_w the subglacial water pressure (i.e., the water pressure at the ice-bedrock interface). The rationale behind such a relation is that an increasing amount of water can further lubricate the bed by 'flooding' the obstacles, thereby easing sliding of the ice on it and reducing the basal friction. Importantly, the effective pressure should not be understood as the local difference between the normal ice stress and the subglacial water stress but, rather, as the average of such local difference over a characteristic region over which the friction law (4.15) is considered. Indeed, a friction law is used to parametrize unresolved physical phenomena through a parametrization between macroscopic quantities; here, the macroscopic basal friction stress, basal velocity, and effective pressure. The local friction stress, basal velocity, and effective pressure are unresolved in large-scale ice-sheet models and simulations.

One of the consequences of both the Weertman and the Budd friction laws is that basal friction is an unbounded function of the basal velocity. If cavitation is allowed, such a result should not hold. Indeed, the friction modeled by the friction law is associated with the resistance of the ice flow due to bumps in the bedrock. Quantitatively, this resistance is due to the unbalance of the normal stress applied to each side of the bumps. This normal stress upstream of the obstacle is larger the one downstream of it, which generates drag. However, these stresses are constrained: they should be consistent with the value of the effective pressure N. As a consequence, to increase drag, the normal stress applied to the lee of obstacle should be reduced, but that is not always possible as below a critical pressure value cavitation is initiated (see Fig. 4.2). Formally, one can show that the following bound, known as Iken's bound, holds [Iken, 1981; Schoof, 2005]:

$$\tau_\mathrm{b} \leq \sup(z_\mathrm{b}')\, N, \tag{4.16}$$

with $\sup(z_\mathrm{b}')$ the maximum up-slope of the bed in the direction of the ice flow.

A proper mathematical treatment of sliding with cavities was achieved by Fowler [1986a, 1987] after several years in which the quantification of the impact of subglacial cavities remained unsolved. They extended the Nye–Kamb theory with cavities by formulating the problem as a Hilbert problem so that tools from complex analysis can be used. A major difficulty here is that the problem is non-linear because of the free-boundary nature of the cavities, in contrast to the original Nye–Kamb theory. Assuming a single cavity per bed period, they obtained a sliding relation of the form

$$\tau_\mathrm{b} = f(u_\mathrm{b}/N)N, \tag{4.17}$$

in which f is a function that depends on the exact shape of the bedrock (see Fig. 4.3). However, the qualitative behavior of f is seemingly independent of the bedrock geometry: it consists of a first linear increasing part for small sliding velocities. Then, it reaches a maximum, after which it steadily decreases towards zero. The first ascending part can be explained by the fact that, originally, an increase in velocity leads to larger pressure differences on the sides of the bumps, thereby inducing more drag. This is

somewhat reminiscent of equation (4.12); actually, this first ascending part corresponds to sliding without cavitation; as such, it should be compatible with the particularization of equation (4.12) to the case where regelation is negligible. This happens if the spectral content of the bed is limited to relatively small wavenumbers $\kappa \ll \kappa_0$, and one can then formally derive a link between the first increasing behavior of f in (4.17) and the characteristics of the bed, similarly to (4.12) [Fowler, 1986a]. The decreasing part is associated with cavitation; for large velocities, cavities grow, taking more and more space in the lee of bumps and limiting the area of contact between the ice and the bed over which normal pressure can be applied. This leads to a decrease in drag. Eventually, all the bed becomes flooded and the drag becomes zero.

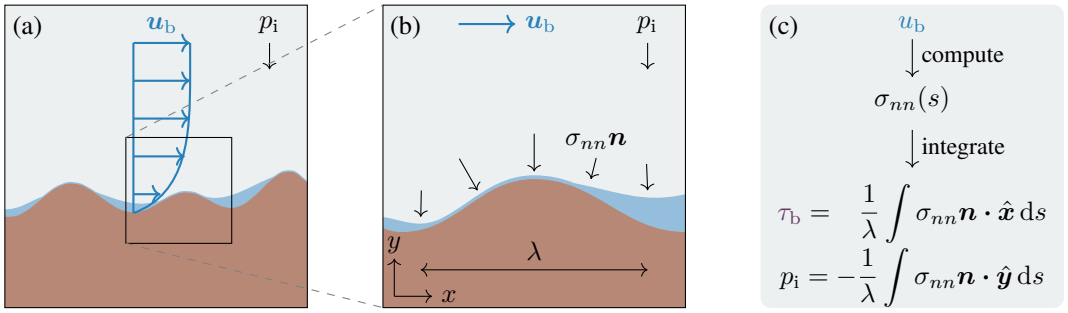

Figure 4.2: Schematic of sliding with cavitation on a hard bed [notations adapted from Schoof, 2005]. **(a)** For sufficiently large velocities or low effective pressures, cavities become filled with water. **(b)** Zoom on a single period of the bed. The ice flow creates an asymmetric distribution of the normal stress $\sigma_{nn} = (\boldsymbol{\sigma}\cdot\boldsymbol{n})\cdot\boldsymbol{n}$. Here, $\boldsymbol{n}$ is the upwards-facing normal to the ice-bed interface. Note that we assume a free-slip condition at the ice-bed interface, which leads to a zero tangential component of the traction vector, which is therefore parallel to $\boldsymbol{n}$. **(c)** Principle of the computation of a friction law for sliding with cavitation: the basal friction can be obtained by computing the mean horizontal normal pressure applied by the ice on the bed over a wavelength. A constraint here is that the far-field overburden pressure in the ice, p_i, should be consistent with the distribution of the vertical pressure applied by the ice on the bed.

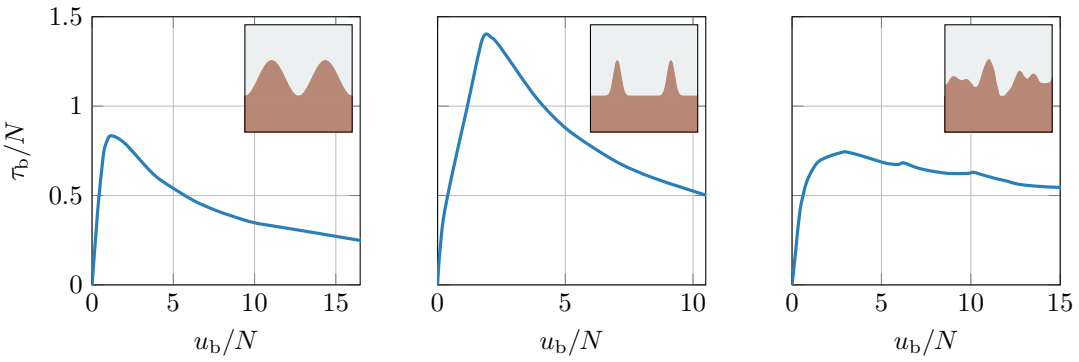

(a) Bed with sinusoidal bumps.

(b) Bed with Gaussian bumps.

(c) Bed with Fourier modes.

Figure 4.3: Examples of sliding relations $\tau_b/N = f(u_b/N)$ for various bed shapes [adapted from Fowler, 1986a; Schoof, 2005]. Here, the variables τ_b, u_b, and N must be understood as the dimensionless basal friction, basal velocity, and effective pressure, respectively.

Fowler's results have been extended by Schoof [2005] who considered sufficiently smooth but otherwise arbitrary periodic beds. This led to a relation similar to (4.17), in which f depends again on the

particular bed geometry considered. A difference compared to the earlier results of Fowler [1986a] is that the second part of f, associated with cavitation, decreases less rapidly and shows small local variations during this decrease. These changes are associated with water that gradually fill the smaller cavities, so that the normal pressure gets concentrated over the larger remaining bumps. Indeed, these changes in pressure distribution lead to a decreasing part of the f function that is less smooth compared to a bed with a single cavity per bump. Furthermore, the less sharp decrease can be explained by the variety of bump sizes over which friction can be exercised, even when a cavity becomes flooded, in contrast to a bed with one cavity per bed period. Note that the physical mechanism of cavitation somewhat validates the assumption of negligible regelation, at least for sufficiently large velocities: as cavitation is initiated, the smallest cavities get completely flooded. It follows that regelation can be neglected, as these small cavities were precisely the ones where regelation could take place.

Based on these results, Schoof [2005] suggested the following friction law:

Schoof friction law

$$\tau_\mathrm{b} = C_\mathrm{s} N \left(\frac{\Lambda}{\Lambda + \Lambda_0} \right)^{\frac{1}{n}}, \quad \Lambda := \frac{u_\mathrm{b}}{N^n}, \quad \Lambda_0 := \frac{\lambda_0 A}{m_0}. \tag{4.18}$$

Here, λ_0 is the wavelength for the dominant bumps, m_0 is a typical bed slope, and C_s is a constant that is smaller than the maximum bed slope. This friction law should not be understood as an exact analytical result, but, rather, as a law that is compatible with the results observed when considering the sliding of a Newtonian fluid over bed with cavitation. In particular, (4.18) was formally derived for the case $n = 1$. Schoof's friction law is such that the following limits hold:

$$\tau_\mathrm{b} \sim C_\mathrm{s} \Lambda_0^{-\frac{1}{n}} u_\mathrm{b}^{\frac{1}{n}}, \quad \text{for } \Lambda \ll \Lambda_0, \quad \text{i.e., for } u_\mathrm{b} \ll \Lambda_0 N^n, \tag{4.19a}$$

$$\tau_\mathrm{b} \sim C_\mathrm{s} N, \quad \text{for } \Lambda \gg \Lambda_0, \quad \text{i.e., for } u_\mathrm{b} \gg \Lambda_0 N^n. \tag{4.19b}$$

The first case case is associated with sliding over bed without cavitation; we recover a Weertman friction law. The second case is associated with the flooding of the dominant obstacles of the bed. In between, the friction law transitions from one state to the other, leading to a saturation curve. Importantly, Schoof's friction law obeys Iken's bound, and the bed cannot generate arbitrary large friction.

As previously mentioned, a limitation in Schoof's derivation is that it is assumed that ice follows a linear rheology. This hypothesis can be removed by relying on numerical methods to solve the problem of basal sliding, rather than mathematical analyses. Following this approach, Gagliardini et al. [2007] solved the Nye–Kamb problem, with cavitation, and with Glen's flow law. They used a finite-element method to simulate the ice flow, and tested several simple bed shapes. Their findings led them to suggest the following friction law:

Gagliardini friction law

$$\tau_\mathrm{b} = C_\mathrm{s} N \left(\frac{\chi}{1 + \alpha\, \chi^q} \right)^{\frac{1}{n}}, \quad \chi := \frac{u_\mathrm{b}}{C_\mathrm{s}^n N^n A_\mathrm{s}}, \quad \alpha := \frac{(q-1)^{q-1}}{q^q} \tag{4.20}$$

Here, χ is a dimensionless sliding velocity, A_s is the sliding parameter without cavitation, α is a scaling coefficient, and q is a free parameter that controls the shape of the friction law. The latter admits a

maximum for $\chi_0 := q/(q-1)$, at which $\tau_\mathrm{b} = C_\mathrm{s} N$. An important particular case is the limit $q \to 1$, for which Gagliardini's law becomes

$$\tau_\mathrm{b} = C_\mathrm{s} N \left(\frac{\chi}{1+\chi} \right)^{\frac{1}{n}}, \quad \chi := \frac{u_\mathrm{b}}{C_\mathrm{s}^n N^n A_\mathrm{s}}. \tag{4.21}$$

By definition, the sliding parameter A_s relates the basal velocity and stress in the absence of cavitation through the relation $u_\mathrm{b} = A_\mathrm{s} \tau_\mathrm{b}^n$. The absence of cavitation corresponds to the case of low velocities. Comparison with Schoof's friction law in that case, equation (4.19a), then leads to $C_\mathrm{s}^n A_\mathrm{s} = \Lambda_0$. It follows that

$$\chi = \frac{u_\mathrm{b}}{N^n \Lambda_0} = \frac{\Lambda}{\Lambda_0}, \tag{4.22}$$

so that

$$\tau_\mathrm{b} = C_\mathrm{s} N \left(\frac{\Lambda}{\Lambda + \Lambda_0} \right)^{\frac{1}{n}}, \tag{4.23}$$

and we recover Schoof's law (4.18).

Validation

While several field studies have found a positive correlation between the basal velocity and subglacial water pressure on hard beds [Bindschadler, 1983; Iken and Bindschadler, 1986], that is not always the case [e.g., Harper et al., 2007]. A difficulty is that basal properties vary over space and time, so that an assessment of sliding laws based on in-situ measurements is particularly challenging. Based on a controlled laboratory set-up, Zoet and Iverson [2015] managed to investigate hard-bed sliding. Their results suggest that the theory of sliding with cavitation is in good fit with experimental measurements, at least for sinusoidal beds.

4.2.2 Soft beds

Viscous vs. plastic sliding

The rheology of a soft bed or till is probably even more complex than that of ice. Indeed, subglacial till takes the form of a granular mass that is porous and deformable, its behavior depending both on the pressure exerted by the ice and on the local subglacial hydrology. A friction law can therefore be associated with several distinct modes of deformation: deformation of the till, slip motion at the ice-till interface or on slip planes within the till, and sliding over sediment reliefs. Compared to the hard-bed case, one still expects friction laws to be expressed as functions of basal friction and effective pressure, the latter representing the subglacial hydrology. Effective pressure is still defined as $N = p_\mathrm{i} - p_\mathrm{w}$, but p_w now represents the pore-water pressure at the ice-till interface.

Boulton and Hindmarsh [1987] modeled till as a viscous material with a power-law rheology:

$$\dot{\gamma} = A_\mathrm{t} \frac{\tau^a}{N_\mathrm{t}^b}, \tag{4.24}$$

with $a, b > 0$. Here, $\dot{\gamma}$ is the strain rate in the till, A_t is a viscosity coefficient, τ is the shear stress in the till, and N_t is the effective pressure within the till. Note that we use another notation for the effective pressure in the till (denoted by N_t) and the one at the ice-till interface (denoted by N), as both quantities are typically different due to the effect of gravity that leads to an increasing pressure with depth. Based on laboratory measurements, it was found that till rheology is consistent with that of a plastic material [Kamb, 1991; Iverson et al., 1998; Tulaczyk et al., 2000a,b]:

$$\begin{cases} \tau < \tau_\mathrm{y}, & \text{if } u = 0, \quad (4.25a) \\ \tau = \tau_\mathrm{y}, & \text{if } u > 0, \quad (4.25b) \end{cases}$$

in which τ_y is a yield stress and u is the shear velocity in the till. The yield stress follows a Coulomb relation:

$$\tau_y := c + \tan(\varphi)\, N_t, \tag{4.26}$$

with c the cohesion and φ the internal friction angle.

These two visions –the first representing till as a viscous material, the second representing it as a plastic material– have led to a bit of controversy within the geophysical community. These differences arose in part from criticism by experimentalists, who favored the plastic view, of the law (4.24), which was not very robust, having apparently been derived from seven data points. However, from a modeler's point of view, a law of the form (4.25) is incomplete, since it does not allow the deformation in the till to be determined [Fowler, 2002, 2003, 2018]. It seems that the approaches are in fact not totally incompatible: one way to combine a plastic approach with viscous behavior for the deformation of the till is, for example, to use a Herschel–Bulkley law (see next subsection). In this case, the till cannot deform if the stress does not exceed the yield stress. Above it, deformation is modeled by viscous behavior. Importantly, this viscous behavior is not necessarily a local characterization of the rheology of the till, but rather of its effective behavior on larger spatial or temporal scales. In particular, a till with a quasi-plastic behavior can be modeled by a viscous law, the latter being associated with behavior on larger spatial scales [Hindmarsh, 1997], plastic hardening [Fowler, 2003], local slip-stick events [Iverson and Iverson, 2001], or obstacles in the bed topography.

In practice, a convenient practical model for large-scale studies consists in modeling till with a perfectly-plastic friction law, and assuming that $\tau_b = \tau_y$. This leads to the following so-called Coulomb law:

Coulomb friction law

$$\tau_b = C_c N, \tag{4.27}$$

where $C_c > 0$ is a friction coefficient, and where we have neglected the cohesion c in (4.26) as it is quite small. Note the distinction from Coulomb's law in classical mechanics, where it typically describes a stick-slip behavior as in (4.25). In our case, however, we assume that the ice remains in a continuous sliding state with the basal stress consistently at its yield value.

Modern theories

Recent analytical and experimental studies suggest a visco-plastic behavior for dense granular material [Jop et al., 2006; Henann and Kamrin, 2013] and it is now standard to model till as a visco-plastic fluid [e.g., Schoof, 2007a,d; Fowler, 2009, 2010b; Damsgaard et al., 2020; Warburton et al., 2023]. For example, with a Herschel–Bulkley law that includes a dependence on effective pressure, one gets

$$\begin{cases} \dot\gamma = 0, & \text{if } \tau < \tau_y, \quad (4.28a) \\ \dot\gamma = A_t(\tau - \tau_y)^a N_t^{-b}, & \text{if } \tau \geq \tau_y, \quad (4.28b) \end{cases}$$

with a yield stress given by $\tau_y = \mu_t\, N_t$ where μ_t is a (static) friction coefficient for the till. Such a law can be written in its tensor form for general three-dimensional configurations.

Assume that, at the ice-till interface, the applied stress τ_b is above the yield-stress value τ_y. The till will then deform over a finite thickness (see Fig. 4.4). This can be explained by the fact that the shear stress at the ice-till interface can be assumed to be transmitted to the till so that $\tau = \tau_b$ within the till is a constant. However, that is not the case for the effective pressure that increases with depth. As a consequence, the yield stress τ_y increases with depth and, at a sufficiently large depth, it will get above

the applied shear stress τ_b so that the till will not deform beyond this limit.

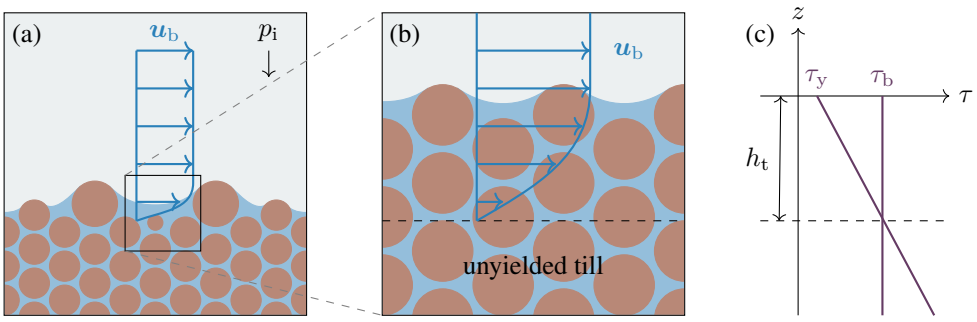

Figure 4.4: Schematic of sliding over a soft bed [adapted from Warburton et al., 2023]. **(a)** Depending on the applied stress and the hydrology, the till can be deformed by the motion of ice. **(b)** Zoom on the deformation of the till: for a visco-plastic rheology, the deformation is limited to a finite extent close to the ice-till interface. **(c)**. This extent h_t of the deformation horizon can be computed by comparing the applied stress $\tau = \tau_\mathrm{b}$ with the yield stress τ_y, the latter increasing with depth because of gravity.

The deformation horizon can be estimated quantitatively [Fowler, 2010a; Fowler and Ng, 2021; Warburton et al., 2023]. Assuming that the pressures within the solid and liquid part of the till follow a lithostatic and hydrostatic distribution, the effective pressure at an elevation $z \leq z_\mathrm{b}$ within the till can be written as

$$N_\mathrm{t}(z) = N + \int_z^{z_\mathrm{b}} \Delta\rho_\mathrm{t}\phi_\mathrm{t}(Z) g \,\mathrm{d}Z, \tag{4.29}$$

in which $\Delta\rho_\mathrm{t} = \rho_\mathrm{s} - \rho_\mathrm{w}$, ρ_s is the sediment density, and $\phi_\mathrm{t} = \phi_\mathrm{t}(z)$ is the porosity within the till. If that porosity does not vary much, then $N_\mathrm{t}(z) = N + \Delta\rho_\mathrm{t}\phi_\mathrm{t} g(z_\mathrm{b} - z)$ and the yield stress evolves according to

$$\tau_\mathrm{y}(z) = \mu_\mathrm{t}\left[N + \Delta\rho_\mathrm{t}\phi_\mathrm{t} g(z_\mathrm{b} - z)\right]. \tag{4.30}$$

The elevation where the till starts to deform is then characterized by $\tau_\mathrm{y} = \tau_\mathrm{b}$. This leads to the following deformation horizon:

$$h_\mathrm{t} = \frac{\tau_\mathrm{b} - \mu_\mathrm{t} N}{\Delta\rho_\mathrm{t}\phi_\mathrm{t} g \mu_\mathrm{t}}. \tag{4.31}$$

Interestingly, this estimation can be used to derive a friction law. Indeed, if there is no slip between the ice and the till, then $\dot\gamma \sim u_\mathrm{b}/h_\mathrm{t}$ in which u_b is the velocity in the ice near the ice-till interface. Using (4.28) and inverting for the basal friction then yields

$$\tau_\mathrm{b} = \mu_\mathrm{t} N + (A_\mathrm{t} h_\mathrm{t})^{-1} N^{1/b} u_\mathrm{b}^{a/b}. \tag{4.32}$$

This friction law can be seen a regularization of a perfectly-plastic friction law, thanks to the addition of a Budd-like component that stems from the deformation of the till. Warburton et al. [2023] obtained a similar result with a more elaborated model with a rheology $\dot\gamma = \dot\gamma(\tau, N_\mathrm{t})$ and a porosity $\phi_\mathrm{t} = \phi_\mathrm{t}(\dot\gamma, N_\mathrm{t})$ that are based on studies of flow in granular media.

Validation

Laboratory experiments of sliding ice over a soft bed suggest a friction law of the following form [Iverson and Zoet, 2015; Zoet and Iverson, 2020]:

$$\tau_\mathrm{b} = C_\mathrm{c}\, N \left(\frac{u_\mathrm{b}}{u_\mathrm{b} + u_0}\right)^p, \tag{4.33}$$

in which $u_0 = u_0(N)$ is a linear function of N that depends on properties of the till. The physical interpretation is that u_0 is a threshold velocity: below it, friction comes from the deformation of the ice flow around obstacles in the bed, so that we recover a Weertman-like friction law with $\tau_\mathrm{b} \propto u_\mathrm{b}^p$ (equation (4.11)). Above it, the bed deforms, and the friction is limited by the till shear strength, which yields a Coulomb-like friction law $\tau_\mathrm{b} \approx C_\mathrm{c} N$ (equation (4.27)).

Additional measurements have shown that a similar law can be obtained to model sliding over a till with a frozen fringe, i.e., a zone of layer of ice-rich debris at the ice-till interface [Hansen et al., 2024]. In that case, the Weertman-like part of the curve is actually associated with the deformation of the fringe (note the similarity with the rationale behind (4.32)), and u_0 is expected to depend on the rheological properties of the fringe.

4.2.3 Towards a unified friction law

The previously exposed developments in the field of subglacial friction have led researchers to postulate the existence of a so-called 'unified friction law' that would be able to model sliding on both hard and soft beds. Such a law can be constructed by combining a plastic component, represented by a Coulomb law, with a viscous component, represented by a Weertman law [Schoof, 2010a; Tsai et al., 2015]:

$$\tau_\mathrm{b} = \min(C_\mathrm{c} N, C_\mathrm{w} u_\mathrm{b}^p). \tag{4.34}$$

This expression then switches between the Coulomb and Weertman laws as a function of the conditions. To avoid a potential singularity associated with the transition between the two regimes, a smoothened version of this friction law has been introduced. It allows a smooth transition between these regimes [Joughin et al., 2019; Minchew and Joughin, 2020; Helanow et al., 2021]:

Unified friction law

$$\tau_\mathrm{b} = C_\mathrm{rc}\, N \left(\frac{u_\mathrm{b}}{u_\mathrm{b} + u_0} \right)^p. \tag{4.35}$$

Here, $C_\mathrm{rc} > 0$ is a friction coefficient and $u_0 > 0$ is a threshold velocity for the switch between the plastic and viscous regimes. Such an expression is effectively a regularized Coulomb friction law in which u_0 can be viewed as a regularization parameter. This friction law admits the following plastic and viscous limiting behaviors:

$$\tau_\mathrm{b} \sim C_\mathrm{rc} N, \qquad \text{for } u_\mathrm{b} \gg u_0, \tag{4.36a}$$

$$\tau_\mathrm{b} \sim C_\mathrm{rc} N u_0^{-p} u_\mathrm{b}^p, \qquad \text{for } u_\mathrm{b} \ll u_0. \tag{4.36b}$$

As such, it is consistent with the studies of sliding on hard and soft beds. For hard beds, we recover the dependency $\tau_\mathrm{b} \propto u_\mathrm{b}^p$ associated with sliding over bed obstacles at low velocities and the limiting behavior associated with the development of cavitation at large velocities. For soft beds, we also recover the dependency $\tau_\mathrm{b} \propto u_\mathrm{b}^p$ associated with sliding over bed obstacles at low velocities and the plastic behavior associated with the yield stress of the till. Such a friction law can also be viewed as a way to combine form drag (drag due to obstacles to the flow) and skin drag (drag due to local shear stress at interfaces), as described in figure 4.5.

The threshold velocity u_0 in (4.35) can be fixed to a constant value, for example to a characteristic velocity of ice streams: $u_0 \sim 300\,\mathrm{m/year}$ [Joughin et al., 2019]. Alternatively, it can be viewed as a parameter that depends on the effective pressure. This is in fact the view of the friction law (4.34) as it implicitly defines u_0 as

$$u_0(N) = (C_\mathrm{c}/C_\mathrm{w})^{1/p} N^{1/p}. \tag{4.37}$$

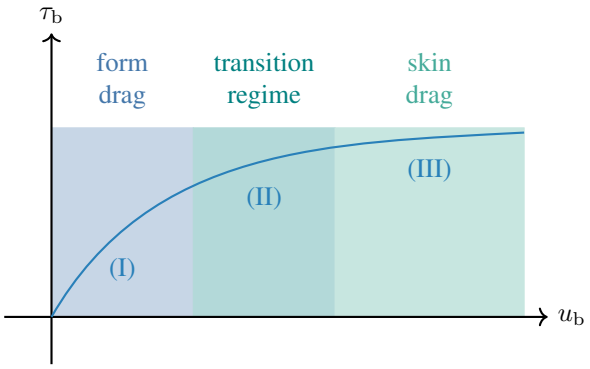

Figure 4.5: Schematic of a unified friction law [adapted from Minchew and Joughin, 2020]. For low velocities, basal friction mainly stems from form drag, i.e., from the effect of bed obstacles on the viscous flow of ice (I). For large velocities, basal friction mainly comes from skin drag (III). For hard beds, this corresponds to the filling of water cavities that leads to a slowdown in the increase of basal friction. For soft beds, this corresponds to the friction associated with the yield of the till. In between these two regimes, there is an intermediate region in which the system transitions from one regime to the other (II).

Similarly, the Schoof and Gagliardini friction laws (4.18) and (4.20) are equivalent to the unified friction law (4.35) with

$$u_0(N) = \Lambda_0 N^n. \tag{4.38}$$

The usual exponents values are $p = 1/3$ and $n = 3$, so that $u_0(N) \propto N^3$ for the two expressions above. Here, there is a slightly difference result with the soft-bed case, as Zoet and Iverson [2020] suggested that $u_0(N) \propto N$. Nonetheless, the qualitative behavior is similar, as u_0 increases with N.

Finally, it should be noted that the unified friction law (4.35) effectively corresponds to a Coulomb friction law at grounding lines, since such areas are characterized by high velocities and low effective pressures. Hence, basal friction will be proportional to the effective pressure near the grounding line. In many models of subglacial hydrology, the effective pressure actually vanishes at grounding lines, so that basal friction itself will vanish at grounding lines. This is in contrast to, for example, the Weertman friction law (4.11), which does not lead to vanishing basal friction at the grounding line.

4.3 Subglacial hydrology

A missing element from the previous section is the characterization of the effective pressure and of the physical processes that govern its evolution. This section is dedicated to such a discussion.

4.3.1 Effective pressure and hydraulic potentials

The effective pressure is defined as a difference between the pressure p_i associated with the weight of an ice column (often called overburden pressure) and p_w, associated with the pressure in water cavities at the ice-bed interface:

$$N = p_i - p_w. \tag{4.39}$$

Here, p_i must be understood as a 'far-field' value: this corresponds to the pressure in the ice outside the direct vicinity of the bed, in which local variations in the bed elevation and complex processes may modify this value. A typical assumption is that the ice pressure is cryostatic, which yields $p_i = \rho g h$ where ρ is the ice density and g is the acceleration of gravity: the ice pressure is simply proportional to its thickness. Similarly, and in a manner consistent with the concept of a friction law, both the effective

and the subglacial water pressures must be understood as local averages.

A first popular model of effective pressure consists in assuming that the subglacial water pressure p_w follows a hydrostatic distribution, as if the water system was perfectly connected to the ocean [e.g., Tsai et al., 2015]. In such a case, one gets the following parametrization over the grounded domain:

Height-above-buoyancy effective-pressure parametrization

$$N = \rho g h - \rho_\mathrm{w} g \max(0, -z_\mathrm{b}). \tag{4.40}$$

Such a model is suited for regions that are close to the grounding line, where the perfect connection assumption is plausible. However, such a simple model fails for regions that are further away from it, so that corrections [e.g., Downs and Johnson, 2022] or more sophisticated models, as described hereafter, must be used.

While the definition (4.39) is simple, it is not necessarily the most practical. Anticipating what follows, one expects that the subglacial hydrology will be described in terms potentials that drive subglacial water flows. Hence, we introduce the hydraulic potential ϕ and the geometric potential ϕ_0 as follows:

$$\phi := \rho_\mathrm{w} g z_\mathrm{b} + p_\mathrm{w}, \tag{4.41a}$$

$$\phi_0 := \rho g h + \rho_\mathrm{w} g z_\mathrm{b}. \tag{4.41b}$$

With these notations, the effective pressure is written as

$$N = \phi_0 - \phi. \tag{4.42}$$

The hydraulic potential ϕ drives subglacial water pressure: water flows from regions where ϕ is high towards regions where it is low. The hydraulic potential is defined so that this motion can be attributed to a change in basal elevation z_b or a change in pressure p_w. On the other hand, by construction, the geometric gradient does not depend on the subglacial hydrological system: it only depends on the geometry of the ice sheet. Furthermore, it corresponds to the value that the hydraulic potential would take if the effective pressure was zero.

4.3.2 Hard beds

We now proceed to the description of the main hydrological systems on hard beds: water films, linked-cavity systems, and channels (Fig. 4.6).

Water film (Fig. 4.6a)

One of the first models for subglacial water flow is due to Weertman [1972], who considered a water film that flows in between the bedrock and the ice (Fig. 4.6a). The water film is characterized by a thickness h_w that evolves over space and time. Mass balance of subglacial water yields the following equation:

$$\partial_t h_\mathrm{w} + \overline{\mathrm{div}}\, \boldsymbol{q}_\mathrm{w} = \frac{m_\mathrm{w}}{\rho_\mathrm{w}}, \tag{4.43}$$

in which $\overline{\mathrm{div}}\, \boldsymbol{q}_\mathrm{w}$ is the horizontal divergence of the subglacial water flux $\boldsymbol{q}_\mathrm{w}$ and m_w is the net water melt rate. If there is no other type of subglacial flow and no intrusion of water in the bed, then $m_\mathrm{w} = \rho_\mathrm{w} m_\mathrm{b}$, in which m_b is the basal melt rate introduced in section 2.3. Assuming that the water flow between the ice and bedrock takes the form a laminar flow leads to a Poiseuille law:

$$\boldsymbol{q}_\mathrm{w} = -\frac{h_\mathrm{w}^3}{12\eta_\mathrm{w}} \bar{\nabla}\phi, \tag{4.44}$$

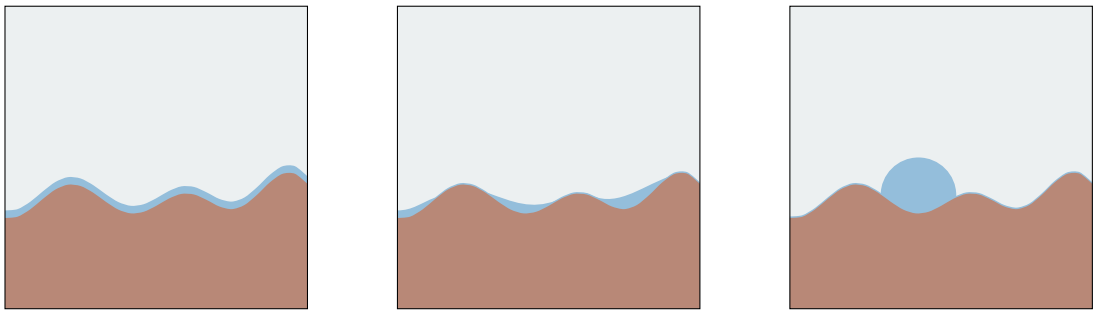

(a) Water film. (b) Linked-cavity system. (c) Channel.

Figure 4.6: Schematic of the main types of subglacial water flow over a hard bed **(a)** Water film that flows over the bedrock. **(b)** Linked-cavity system in which water fills the cavities that are in between bed protrusions. **(c)** Channel in which the water is conducted in localized conduits. While a water film and a linked-cavity system are distributed and inefficient water systems, channels are localized and efficient.

with η_w the dynamic viscosity of water.

It has been shown that such a water film cannot be stable, and necessarily leads to a channelization of the subglacial water flow [Walder, 1982]. The instability process is as follows: following a local increase in film thickness h_w, the subglacial water flow q_w increases. Thus, there will be an increase in melt water due to the energy dissipated by the water flow, which again leads to an increase in film thickness. Eventually, a series of channels is formed. This instability mechanism was later mitigated by Creyts and Schoof [2009] who showed that, in the presence of bed protrusions, regelation and ice creep can actually lead to a stabilization of the water film.

Nonetheless, Weertman's original water-film model can be used as a large-scale parametrization of the subglacial flow. Then, h_w must be understood as the spatial average of the water film thickness over a relatively large radius (say, hundreds of meters) that correspond to the resolution used in a large-scale ice-sheet model. This is the approach that was pursued in Le Brocq et al. [2009] and Kazmierczak et al. [2022]. These authors further simplified the models by assuming that (i) the water film was at equilibrium and (ii) the effective-pressure gradient was small compared to the geometric potential gradient, i.e., $\nabla\phi \approx \nabla\phi_0$. Under these assumptions, equations (4.43) and (4.44) become

$$\overline{\mathrm{div}}\,\boldsymbol{q}_\mathrm{w} = \frac{m_\mathrm{w}}{\rho_\mathrm{w}}, \tag{4.45a}$$

$$h_\mathrm{w} = \left(\frac{12\eta_\mathrm{w}\|\boldsymbol{q}_\mathrm{w}\|}{\|\nabla\phi_0\|}\right)^{\frac{1}{3}}. \tag{4.45b}$$

The structure of these equations allows for an efficient computation of the water-film thickness. Indeed, (4.45a) can first be solved for the subglacial water flux following a water-routing approach [Budd and Warner, 1996; Le Brocq et al., 2006]. Then, the water-film thickness can be computed thanks to (4.45b), which is an algebraic equation. It remains to link this thickness to the subglacial water pressure. This simplest model assumes a linear relation with respect to the overburden pressure, leading to

$$p_\mathrm{w} = \left(\frac{h_\mathrm{w}}{h_\mathrm{w}^0}\right)\rho g h, \tag{4.46}$$

in which h_w^0 is a scaling thickness that conceptually corresponds to the thickness for which all the bed is covered with water. This yields the following effective-pressure parametrization:

Subglacial-water-film effective-pressure parametrization

$$N = \left(1 - \frac{h_\mathrm{w}}{h_\mathrm{w}^0}\right) \rho g h. \tag{4.47}$$

A linear relation similar to (4.46) has also been used in Bueler and Brown [2009] and Martin et al. [2011]. An alternative to this relationship consists in replacing the dependence on the water-film thickness with a dependence on the subglacial water flux through a simple function [Pattyn et al., 2005; Goeller et al., 2013; Kazmierczak et al., 2022]. Finally, we note that algebraic relations of the form (4.46) have also been used in poroelastic models [Flowers and Clarke, 2002].

Linked-cavity systems (Fig. 4.6b)

The theory of linked-cavity systems was introduced by Walder [1986] and Kamb [1987]. The idea is that the subglacial water system takes the form of small patches of water that are connected between each other. These patches are formed in the lee of bed obstacles and persist as a result of a balance between sliding over these obstacles, which tends to open water cavities, and ice creep, which tends to close them. As we will see, from a modeling point of view, a linked-cavity system is similar to a Weertman film, since both systems obey similar mechanisms; the main difference is that in the former case there is a notion of localized patches, while in the latter one assumes a film that is more or less continuous. The theory of linked-cavity systems was revisited in Schoof [2010b], Hewitt [2011], and Schoof et al. [2012] and we here follow their model description.

As a proxy for the cavity size, we take the average cavity volume per unit area of the bed, which we note h_w. Here, the average is done over the bed roughness scale, and all the cavities are assumed to be filled for simplicity (see Schoof et al. [2012] for a discussion of the case where this assumption is not met). Mass conservation is then given by

$$\partial_t h_\mathrm{w} + \overline{\mathrm{div}}\, \boldsymbol{q}_\mathrm{w} = \frac{m_\mathrm{w}}{\rho_\mathrm{w}}, \tag{4.48}$$

with the same notations as before. An additional governing equation enforces the rate at which the cavity evolves over time:

$$\partial_t h_\mathrm{w} = v_\mathrm{o}(h_\mathrm{w}) - v_\mathrm{c}(h_\mathrm{w}, N). \tag{4.49}$$

Here, $v_\mathrm{o} = v_\mathrm{o}(h_\mathrm{w})$ and $v_\mathrm{c} = v_\mathrm{c}(h_\mathrm{w}, N)$ denote opening and closing rates that are associated with various physical phenomena, respectively. Usually, opening is assumed to be caused by sliding over bed protrusions, and is modeled as

$$v_\mathrm{o} = \frac{h_\mathrm{w} - h_\mathrm{b}}{l_\mathrm{b}} u_\mathrm{b} \quad \text{or} \quad v_\mathrm{o} = \frac{h_\mathrm{b}}{l_\mathrm{b}} u_\mathrm{b}, \tag{4.50}$$

with l_b the characteristic distance between bed protrusions and h_b their characteristic size. The first expression is probably more meaningful, as $v_\mathrm{o}(h_\mathrm{b}) = 0$. Note that this expression is only valid if $h_\mathrm{w} \leq h_\mathrm{b}$; for $h_\mathrm{w} > h_\mathrm{b}$, one should set $v_\mathrm{o} = 0$. The second expression is simpler, being independent of h_w. As such, it is particularly convenient for simulations over longer time scales and with interactions between the subglacial hydrology and the ice sheet, since the form of the opening rate and its dependence with respect to the ice-sheet basal velocity are preserved. The closing mechanisms is taken as ice viscous creep, with

$$v_\mathrm{c} = c_\mathrm{c} A h_\mathrm{w} |N|^{n-1} N, \tag{4.51}$$

where c_c is a factor that depends on the form of the conduit, oftentimes taken as unity, and A and n are the parameters in Glen's flow law [Nye, 1953].

Finally, a constitutive equation for the subglacial water flow is added to close the system of equations. We here consider a family of Darcy-like equations of the form

$$\boldsymbol{q}_{\mathrm{w}} = -k_{\mathrm{w}} h_{\mathrm{w}}^{\alpha} \|\bar{\nabla}\phi\|^{\beta-2} \bar{\nabla}\phi, \tag{4.52}$$

where k_{w} is a hydraulic conductivity and α, β are exponents that depend on the nature of the flow. A variety of values for α and β have been in considered in the glaciological literature as a function of the nature of the modeled flow. Hewitt [2011, 2013] assumed a laminar flow with $\alpha = 3$ and $\beta = 2$, which leads to a relation similar to the equation (4.44) used for Weertman film. For turbulent flows, one typically assumes $\beta = 3/2$, but several values for α have been considered. A frequent choice is the use of a Darcy–Weisbach relation, for which $\alpha = 5/4$ [Clarke, 1996; Schoof et al., 2012; Werder et al., 2013; Hoffman et al., 2018]. A Manning relation leads to $\alpha = 4/3$ [Hewitt, 2011; Fowler and Ng, 2021]. Finally, interpretation of the Darcy–Weisbach relation for a flow between parallel plates leads to $\alpha = 3/2$ [Creyts and Schoof, 2009; Sommers et al., 2018; Hill et al., 2023]. An overview of the constitutive equations for subglacial water flow, their limitations, and suggestions of improvements can be found in Clarke [2005] and, more recently, in Hill et al. [2023].

While a linked-cavity system is made of localized patches of water, the model is described by a thickness-like variable h_{w} that is an average over the bed roughness scale. As such, linked-cavity systems model in an effective way inhomogeneous flows that take place over multiple areas. Hence, they provide a basis for the modeling of distributed flows.

Distributed flow

$$\frac{\partial h_{\mathrm{w}}}{\partial t} + \overline{\mathrm{div}}\, \boldsymbol{q}_{\mathrm{w}} = \frac{m_{\mathrm{w}}}{\rho_{\mathrm{w}}}, \tag{4.53a}$$

$$\frac{\partial h_{\mathrm{w}}}{\partial t} = v_{\mathrm{o}}(h_{\mathrm{w}}) - v_{\mathrm{c}}(h_{\mathrm{w}}, N), \tag{4.53b}$$

$$\boldsymbol{q}_{\mathrm{w}} = -k h_{\mathrm{w}}^{\alpha} \|\bar{\nabla}\phi\|^{\beta-2} \bar{\nabla}\phi. \tag{4.53c}$$

Channels (Fig. 4.6c)

While linked-cavity systems are the archetypal models for distributed flows, channels are the standard models for localized, channelized flows. Their theory was initiated by Röthlisberger [1972] and Nye [1976]; as a consequence, the usual models of channels are known as models of Röthlisberger channels or R-channels. Channels are localized semi-circular conduits that are capable of transporting efficiently large amounts of water. This leads to large thermal dissipation, which allows for melt on the channels walls. This mechanisms is the primary means for channel growth. This is in contrast with linked-cavity systems in which the opening is mainly due to sliding over bed protrusions.

To model channels, we follow the modern theory as exposed in Schoof [2010b], Hewitt [2011], and Hewitt et al. [2012]. Channels are represented as infinitely small conduits and the position within the conduits is parameterized by the streamline coordinate s. Mass conservation for the water in the conduit is then given by

$$\partial_t S_{\mathrm{w}} + \partial_s Q_{\mathrm{w}} = \frac{M_{\mathrm{w}}}{\rho_{\mathrm{w}}}, \tag{4.54}$$

in which S_{w} is the conduit cross-sectional area, Q_{w} is the conduit (volumetric) water flux, and M_{w} is the effective input of water in the conduit. The channel geometry evolves according to

$$\partial_t S_{\mathrm{w}} = V_{\mathrm{o}}(Q_{\mathrm{w}}) - V_{\mathrm{c}}(S_{\mathrm{w}}, N), \tag{4.55}$$

in which $V_\mathrm{o} = V_\mathrm{o}(Q_\mathrm{w})$ and $V_\mathrm{c} = V_\mathrm{c}(S_\mathrm{w}, N)$ are opening and closing rates. As previously mentioned, opening is assumed to be due to the dissipated work of the water flow that allows melt at the conduit walls:

$$V_\mathrm{o} = \frac{\Xi - \Pi}{\rho L}, \quad \Xi := |Q_\mathrm{w} \partial_s \phi|, \quad \Pi := -c_\mathrm{t} c_\mathrm{w} \rho_\mathrm{w} Q_\mathrm{w} \partial_s p_\mathrm{w}. \tag{4.56}$$

Here, Ξ is the rate of dissipated energy by the water flow. The other term, Π, serves as a correction for the dependence of the pressure melting point with respect to temperature so that it can be interpreted as a change in sensible heat due to temperature variations. In its expression, c_t denotes the Clapeyron slope, and c_w represents the specific heat capacity of water. Closing is due to the ice viscous creep and is written as

$$V_\mathrm{c} = c_\mathrm{c} A S_\mathrm{w} |N|^{n-1} N. \tag{4.57}$$

The parameter c_c is in general different from the corresponding factor appearing in equation (4.51) as the geometry of a cavity is different from that of a channel. A common assumption is that channels are semi-circular, which yields $c_\mathrm{c} = 2\, n^{-n}$. Finally, a Darcy-like constitutive equation is again considered:

$$Q_\mathrm{w} = -K_\mathrm{w} S_\mathrm{w}^\alpha |\partial_s \phi|^{\beta-2} \partial_s \phi. \tag{4.58}$$

We refer to the previous discussion for the choice of parameters α and β as a function of the type of flow in the conduits. Note that channels typically feature relatively large water fluxes, so a turbulent parametrization is probably the most well-suited.

Physically, one expects that at low water fluxes, the hydrological system will be distributed as the opening mechanism in equation (4.56) is not large enough to allow channels to persist. However, at higher water fluxes, channelization becomes possible. A key feature of channels is that they tend to form an arterial network in which only a few channels persist. This behavior can be observed in numerical simulations but also in the equations of the model directly. Consider a steady-state channel with a known water flux Q_w and geometric potential gradient magnitude $\Psi := -\partial_s \phi_0$. The orientation of s is fixed so that Q_w and Ψ are non-negative. Furthermore, assume that the gradient in effective pressure is small with respect to the hydraulic potential gradient so that $\partial_s \phi \approx -\Psi$ and that the sensible heat due to thermal variations is small. Then, equations (4.55) and (4.58) become

$$\frac{Q_\mathrm{w} \Psi}{\rho L} = c_\mathrm{c} A S_\mathrm{w} N^n, \tag{4.59a}$$

$$Q_\mathrm{w} = -K_\mathrm{w} S_\mathrm{w}^\alpha \Psi^{\beta-1}. \tag{4.59b}$$

Combining these together yields

$$N = \left(\frac{\Psi}{\rho L c_\mathrm{c} A} \right)^{\frac{1}{n}} \left(K_\mathrm{w} \Psi^{\beta-1} \right)^{\frac{1}{\alpha n}} Q_\mathrm{w}^{\frac{\alpha-1}{\alpha n}}. \tag{4.60}$$

Hence, N is an increasing function of Q_w. If follows that larger channels, who have higher water fluxes, are also characterized by higher effective pressures. As high effective pressures correspond to low subglacial water pressures, those larger channels will be able to absorb more efficiently the neighboring melt water, thereby out-competing smaller channels.

The equations for channelized flow are summarized hereafter:

Channelized flow

$$\frac{\partial S_\mathrm{w}}{\partial t} + \frac{\partial Q_\mathrm{w}}{\partial s} = \frac{M_\mathrm{w}}{\rho_\mathrm{w}}, \tag{4.61a}$$

$$\frac{\partial S_\mathrm{w}}{\partial t} = V_\mathrm{o}(Q_\mathrm{w}) - V_\mathrm{c}(S_\mathrm{w}, N), \tag{4.61b}$$

$$Q_\mathrm{w} = -K_\mathrm{w} S_\mathrm{w}^\alpha \left|\frac{\partial \phi}{\partial s}\right|^{\beta-2} \frac{\partial \phi}{\partial s}. \tag{4.61c}$$

4.3.3 Soft beds

We continue with the description of the main hydrological systems on soft beds: Darcy flow, Creyts–Schoof film and canals (Fig. 4.7). Compared to the case of hard beds, a new component appears in the evolution of the till upper elevation, denoted by $z_\mathrm{b} = z_\mathrm{b}(x, y, t)$. It changes with time as the till is deformed, and this change depends on and influences subglacial hydrology.

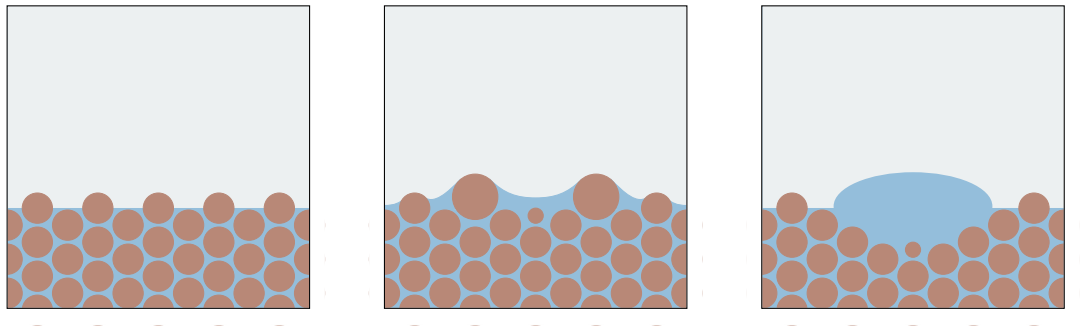

(a) Darcy flow. (b) Creyts–Schoof film. (c) Canal.

Figure 4.7: Schematic of the main types of subglacial water flow over a soft bed **(a)** Water film that flows in the till through a Darcy flow. **(b)** Creyts–Schoof film in which water flows between the clasts of the till, at the ice-till interface. **(c)** Canal in which the water is conducted in conduits incised in the ice and the till. Darcy flows and Creyts–Schoof films are inefficient water systems, while canals are efficient water systems.

Darcy flow (Fig. 4.7a)

If the meltwater input is limited, then the subglacial flow takes place within the till, below the ice-till interface. We here follow the model presented in Fowler [2010a,b]. Mass conservation of the water content in the till then yields

$$\partial_t \int_{z_\infty}^{z_\mathrm{b}} \phi_\mathrm{t} \, \mathrm{d}z + \overline{\mathrm{div}}\, \boldsymbol{q}_\mathrm{w} = \frac{m_\mathrm{w}}{\rho_\mathrm{w}}, \tag{4.62}$$

in which z_∞ is the minimum elevation of the till, ϕ_t is the porosity of the till, $\boldsymbol{q}_\mathrm{w}$ is the subglacial water flux in the porous medium, and m_w is the net melt water input. Water flow in porous media is typically modeled as a Darcy flow, leading to

$$\boldsymbol{q}_\mathrm{w} = -\int_{z_\infty}^{z_\mathrm{b}} \phi_\mathrm{t} \frac{k_\mathrm{t}}{\eta_\mathrm{w}} \bar{\nabla}\phi \, \mathrm{d}z, \tag{4.63}$$

with k_t the till permeability and η_w the water viscosity. Here, $\phi = p_\mathrm{w} + \rho_\mathrm{w} g z$ is the hydraulic potential within the till, and it should not be confused with the till porosity ϕ_t. On top of these equations, we also prescribe equations for the evolution of the till elevation z_b. This takes the form of a conservation of the sediment material:

$$\partial_t \int_{z_\infty}^{z_\mathrm{b}} (1 - \phi_\mathrm{t}) \, \mathrm{d}z + \overline{\mathrm{div}} \, \boldsymbol{q}_\mathrm{s} = \frac{m_\mathrm{s}}{\rho_\mathrm{s}}, \tag{4.64}$$

with $\boldsymbol{q}_\mathrm{s}$ the sediment flux in the till and m_s the net deposition rate of sediment material. Note that for a constant and uniform porosity, the previous equation becomes a classical Exner equation:

$$(1 - \phi_\mathrm{t}) \, \partial_t z_\mathrm{b} + \overline{\mathrm{div}} \, \boldsymbol{q}_\mathrm{s} = \frac{m_\mathrm{s}}{\rho_\mathrm{s}}. \tag{4.65}$$

For the sediment flux, we follow Kyrke-Smith and Fowler [2014] by estimating it as

$$\boldsymbol{q}_\mathrm{s} = \frac{1}{2} h_\mathrm{t} \boldsymbol{u}_\mathrm{b} - \frac{h_\mathrm{t}^3}{12 \eta_\mathrm{t}} \bar{\nabla} N, \tag{4.66}$$

with h_t the thickness of deformable till and η_t its viscosity. Such a model attempts to model the sediment flow as the sum of a Couette-like flow, due to the ice motion at the till-ice interface, and of a Poiseuille-like flow, due to horizontal gradients in effective pressure [Fowler, 2009, 2010a].

To close the system, it remains to specify the behavior of the till as a function of the effective pressure through a relation of the form $\phi_\mathrm{t} = \phi_\mathrm{t}(N_\mathrm{t})$. Such a relation can be found based on soil mechanics, as described hereafter. This results in the following model:

Darcy flow

$$\frac{\partial}{\partial t} \int_{z_\infty}^{z_\mathrm{b}} \phi_\mathrm{t} \, \mathrm{d}z + \overline{\mathrm{div}} \, \boldsymbol{q}_\mathrm{w} = \frac{m_\mathrm{w}}{\rho_\mathrm{w}}, \tag{4.67a}$$

$$\frac{\partial}{\partial t} \int_{z_\infty}^{z_\mathrm{b}} (1 - \phi_\mathrm{t}) \, \mathrm{d}z + \overline{\mathrm{div}} \, \boldsymbol{q}_\mathrm{s} = \frac{m_\mathrm{s}}{\rho_\mathrm{s}}, \tag{4.67b}$$

$$\boldsymbol{q}_\mathrm{w} = - \int_{z_\infty}^{z_\mathrm{b}} \frac{k_\mathrm{t} \phi_\mathrm{t}}{\eta_\mathrm{w}} \bar{\nabla} \phi \, \mathrm{d}z, \tag{4.67c}$$

$$\boldsymbol{q}_\mathrm{s} = \frac{1}{2} h_\mathrm{t} \boldsymbol{u}_\mathrm{b} - \frac{h_\mathrm{t}^3}{12 \eta_\mathrm{t}} \bar{\nabla} N, \tag{4.67d}$$

$$\phi_\mathrm{t} = \phi_\mathrm{t}(N_\mathrm{t}). \tag{4.67e}$$

A simplified model of till hydrology has been proposed by Bueler and van Pelt [2015]. It is based on the observation that the permeability in the till is typically small, so that the horizontal transport due to the flux $\boldsymbol{q}_\mathrm{w}$ is expected to be relatively small. It follows that the mass-balance equation (4.67a) can be simplified as

$$\partial_t h_\mathrm{w} = \frac{m_\mathrm{w}}{\rho_\mathrm{w}}, \tag{4.68}$$

in which $h_\mathrm{w} := \int_{z_\infty}^{z_\mathrm{b}} \phi_\mathrm{t} \, \mathrm{d}z$ is the equivalent thickness of water content in the till. Assuming that the till is homogeneous, the porosity ϕ_t and the effective pressure N_t are then uniform within it. In particular, the latter is equal to N. It follows that the porosity can be written as

$$\phi_\mathrm{t} = \frac{h_\mathrm{w}}{h_\mathrm{w} + h_\mathrm{s}}, \tag{4.69}$$

in which h_s is the equivalent thickness of sediment content in the till. Experiments in till [Tulaczyk et al., 2000a] suggest a linear relation between the till void-ratio $e_\mathrm{t} := h_\mathrm{w}/h_\mathrm{s}$ and the logarithm of the effective pressure:

$$e_\mathrm{t} - e_\mathrm{t}^0 = C_\mathrm{t} \log_{10}\left(\frac{N}{N_0}\right), \tag{4.70}$$

with C_t the coefficient of compressibility of the till and where e_t^0 is the void-ratio at the effective-pressure reference value N_0 [van der Wel et al., 2013]. The void ratio e_t contains the same information as the porosity as both are related to

$$e_\mathrm{t} = \frac{\phi_\mathrm{t}}{1-\phi_\mathrm{t}}. \tag{4.71}$$

In particular, it follows that equation (4.70) is an example of a model of the form $\phi_\mathrm{t} = \phi_\mathrm{t}(N_\mathrm{t})$ (equation (4.67e)). Combining the previous equations together, we have the following model, which we call 'till storage model' because of its local behavior.

Till storage model

$$\frac{\partial h_\mathrm{w}}{\partial t} = \frac{m_\mathrm{w}}{\rho_\mathrm{w}}, \tag{4.72a}$$

$$e_\mathrm{t} = \frac{h_\mathrm{w}}{h_\mathrm{s}}, \tag{4.72b}$$

$$e_\mathrm{t} - e_\mathrm{t}^0 = C_\mathrm{t} \log_{10}\left(\frac{N}{N_0}\right). \tag{4.72c}$$

To avoid having to determine h_s, Bueler and van Pelt [2015] assumed that the equivalent water thickness h_w could not go beyond a maximum value h_w^0 at which the effective pressure reaches a minimal value N_min. From this, they obtained the following expression for the effective pressure:

$$N = N_0 \left(\frac{N_\mathrm{min}}{N_0}\right)^{h_\mathrm{w}/h_\mathrm{w}^0} 10^{[e_\mathrm{t}^0(h_\mathrm{w}^0 - h_\mathrm{w})]/(C_\mathrm{t} h_\mathrm{w}^0)}. \tag{4.73}$$

While convenient –this is an explicit algebraic expression for effective pressure– such an expression has a rather limited range of application. Indeed, melt rates under ice sheets are such that the till would be rapidly totally filled in such a model. This is what has been observed in numerical simulations over Antarctica and Greenland, in which the above model resulted in a saturated till over the temperate regions [Bueler and van Pelt, 2015; Kazmierczak et al., 2022]. For such a saturated till, $N = N_\mathrm{min}$ uniformly over the temperate regions. Given that this limiting behavior does not correspond to the conditions for which the model has been designed, we conclude that it cannot be used for such cases. Form a modeling perspective, the inability of subglacial till to transport large amounts of water suggests that an efficient way capable of doing so must be present at the ice-till interface [Fountain and Walder, 1998; Fowler, 2010a].

Creyts–Schoof film (Fig. 4.7b)

One possibility for water flow at the ice-till interface is that it takes the form of a film that moves between the various obstacles formed by the different bed protrusions and clasts. Such drainage system is known as an inter-clastic or Creyts–Schoof film [Creyts and Schoof, 2009; Kyrke-Smith and Fowler, 2014]. Conceptually, such a film is a distributed drainage system and, as such, we can rely on the description of a distributed flow as introduced for the case of hard beds, i.e., the system of equations (4.53). However, two changes/clarifications need to be made, in that the closure rate now depends on the distribution of

clasts. In addition, a model for sediment flow must be added. These two additions are described now.

For the determination of the closure rate v_c, we follow the model presented in Creyts and Schoof [2009]. We consider the flow of a water film of thickness h_w between the ice and the till. The latter is covered by a collection of clasts, the smallest ones being fully drowned by the film, while the largest ones are in contact with the ice (Fig. 4.8). The clasts are separated by size, and we assume that there are J types of clasts, which are indexed by $j = 1, ..., J$. We note r_j and l_j the radius and the distance between the centers of the nearest neighbors of the clasts in the class j, respectively. The classes are assumed to be sorted by size so that $r_1 \gg r_2 \gg ... \gg r_J$ and $l_1 \gg l_2 \gg ... \gg l_J$. To determine the closure rate of such a system, we first consider the simple case of a single clasts class. In that case, the closing rate is given by

$$v_c = c_c A l |N|^{n-1} N + \frac{c_t k_b}{\rho L r} \frac{N}{\zeta}, \tag{4.74}$$

where l is the distance between neighboring clasts, c_t is the Clapeyron slope, k_b is the thermal conductivity of the bed, ρ is the ice density, L is the latent heat of water, r is the radius of the bed protrusions, and ζ is the proportion of ice that is in contact with these protrusions. The second term in the right-hand side of (4.74) accounts for regelation, which acts as mechanism for closing of water cavities by the melting of ice around the bed protrusions. Such a term is expected to be an important contribution to the total closing rate if the thickness of the water film is small so that smallest clasts are not immersed. To generalize equation (4.74) to the case of multiple classes of clasts, Creyts and Schoof [2009] suggested to attribute to each class j an effective pressure $N_j := p_j - p_{j+1}$, in which p_j and p_{j+1} are respectively the far-field normal stress applied on the clasts and on the ice roof of the clasts j. Hence, by construction, the normal stress applied on the ice roof of class j corresponds to the far-field normal stress applied on the clasts in the class $j + 1$. For the largest and smallest clasts, we have $p_1 = p_i$ and $p_{J+1} = p_w$. As a consequence,

$$\sum_{j=1}^{J} N_j = N, \tag{4.75}$$

so that the effective pressure is partitioned into the N_j. The closing rate v_c^j of clast size j is then given by the following generalization of (4.74):

$$v_c^j = c_c A \tilde{l}_j |N_j|^{n-1} N_j + \frac{c_t k_b}{\rho L \tilde{r}_j} \frac{N_j}{\zeta_j}, \quad j = 1, ..., J. \tag{4.76}$$

Here, $\tilde{l}_j$ and $\tilde{r}_j$ are the effective distance for ice creep and bed protrusions radius, taking into account the effect of the subglacial water thickness h_w (see Fig. 4.8):

$$\tilde{r}_j := \sqrt{r_j^2 - h_w^2}, \tag{4.77a}$$

$$\tilde{l}_j := \sqrt{l_j^2 - \pi \tilde{r}_j^2}. \tag{4.77b}$$

Similarly, the proportion ζ_j can be expressed as a function of the thickness of the film and of the size and spacing between the clasts. Now, we assume that the closing rates v_c^j are all the same, so that they can be denoted by v_c. We also assume that the effective pressure N and the water film thickness h_w are known. In that case, the system of equations formed by (4.75) and (4.76) consists in $(J + 1)$ equations for $(J + 1)$ unknowns: $N_1, N_2, ..., N_J$ and v_c. Note that the clasts are here all assumed to be unsubmerged, i.e., $r_j > h_w$ for all $j = 1, ..., J$. This implicitly determines the number of clast classes J in this model: if the water film gets thicker so that the smallest clasts, which are in the class J, get submerged with $r_J \leq h_w$, then they should be removed from the calculation. The model then becomes a system of $(J - 1)$ equations for $(J - 1)$ unknowns, and so on.

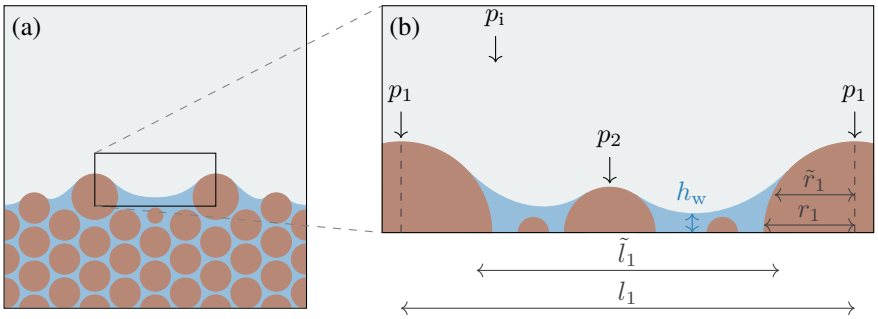

Figure 4.8: Notations for the model of a Creyts–Schoof film [adapted from Creyts and Schoof, 2009]. **(a)** A Creyts–Schoof film takes the form of a film that flows in between clasts that are at the ice-till interface. **(b)** Zoom on the ice-till interface. The ice is in contact with a series of clasts that are sorted by classes of decreasing size. The clasts in the class j have a radius r_j and the distance between neighboring clasts is denoted by l_j. The effective radius $\tilde{r}_j$ and distance $\tilde{l}_j$ correspond to modifications of r_j and l_j that include the effect of the thickness of the water film h_w (see equations (4.77)). The effective pressure N is distributed into the effective pressures $N_j := p_j - p_{j+1}$, in which p_j denotes the far-field normal pressure applied by the ice on the clasts of class j (see equation (4.75)).

Overall, it follows from this discussion that one can, in principle, determine the closing rate v_c as a sole function of the effective pressure N and of the water film thickness h_w:

$$v_\mathrm{c} = v_\mathrm{c}(h_\mathrm{w}, N). \tag{4.78}$$

However, this requires the knowledge of the distribution of the clast size and of the clast spacing, as well as the solution of a system of equations. An alternative consists in prescribing an effective closing rate that contains the qualitative features associated with a distribution of clasts:

$$v_\mathrm{c} = c_\mathrm{c} A \tilde{l} |N|^{n-1} N, \tag{4.79}$$

in which $\tilde{l} = \tilde{l}(h_\mathrm{w})$ is a function that represents an effective distance between the clasts over the soft bed [Kyrke-Smith and Fowler, 2014; Kyrke-Smith et al., 2014, 2015]. A reasonable assumption for $\tilde{l}$ is that it is an increasing function of h_w, with $\tilde{l}(0) = l_0$ in which l_0 represents the distance between the clasts in the absence of water.

In terms of the till evolution, the model presented in (4.67) has to be modified. The driving force for sediment motion is now the motion of water rather than ice. The effective shear stress $\boldsymbol{\tau}_\mathrm{s}$ applied by the water on the till can be estimated as

$$\boldsymbol{\tau}_\mathrm{s} = -\frac{1}{2} h_\mathrm{w} \bar{\nabla}\phi - \Delta\rho_\mathrm{t} g d_\mathrm{s} \bar{\nabla} z_\mathrm{b}, \tag{4.80}$$

in which $\Delta\rho_\mathrm{t} = \rho_\mathrm{s} - \rho_\mathrm{w}$ is the difference of densities between the sediment and the water and d_s is the characteristic diameter of particles in the till [Fowler, 2010a; Kyrke-Smith and Fowler, 2014]. The first term accounts for the motion of the water, while the second one accounts for the downward force on the till particles due to the local bed slope. The (bed-load) sediment flux $\boldsymbol{q}_\mathrm{s}$ can then be modeled using a Meyer-Peter and Mueller [1948] law:

$$\boldsymbol{q}_\mathrm{s} = K_\mathrm{s} \left(\frac{\Delta\rho_\mathrm{t} g d_\mathrm{s}^3}{\rho_\mathrm{w}} \right)^{1/2} \left\langle \frac{\|\boldsymbol{\tau}_\mathrm{s}\|}{\Delta\rho_\mathrm{t} g d_\mathrm{s}} - \tau_0 \right\rangle^{3/2} \frac{\boldsymbol{\tau}_\mathrm{s}}{\|\boldsymbol{\tau}_\mathrm{s}\|}, \tag{4.81}$$

where K_s is a dimensionless flux factor, τ_0 is the (dimensionless) critical Shields stress, and $\langle\cdot\rangle := \max(\cdot, 0)$ denote the Macaulay brackets [Ng, 2000; Fowler, 2010a; Damsgaard et al., 2017].

Canals (Fig. 4.7c)

Canals are the efficient drainage systems on soft beds. They can be studied in a framework that is similar to that of channelized drainage systems (see system (4.61)). However, there are two main differences compared to the hard-bed case: firstly, canals do not take the form of semi-circular conduits but, rather, as shallow, wide conduits that are incised in both the ice and the till. Secondly, there is a complication in that both water and sediment are drained through canals, so appropriate laws have to be added for the transport of sediment. Here, we describe a canal model following Walder and Fowler [1994].

We first fix the notations (Fig. 4.9). The total (volumetric) flux in a canal is denoted by $Q_\mathrm{c} = Q_\mathrm{w} + Q_\mathrm{s}$, in which Q_w denotes the water flux and Q_s the flux of suspended sediments. We also introduce the proportions of water and sediment content π_w and π_s, such that $Q_\mathrm{w} = \pi_\mathrm{w} Q_\mathrm{c}$ and $Q_\mathrm{s} = \pi_\mathrm{s} Q_\mathrm{c}$. By construction, we have $\pi_\mathrm{w} + \pi_\mathrm{s} = 1$, and we can further assume that $\pi_\mathrm{s} \ll \pi_\mathrm{w}$, so $Q_\mathrm{c} \approx Q_\mathrm{w}$. The cross-sectional area of canals is denoted by $S = S_\mathrm{i} + S_\mathrm{s}$, in which S_i is the part that is incised in the ice and S_s is the part that is incised in the till. We also denote by l_i the value of the portion of the canal perimeter that is incised in the ice and l_s the value of the portion incised in the till. Finally, the canal width is denoted by l_c, and the mean canal thickness is denoted by h_c. With these notations, conservation of mass for water and sediment can written as

$$\partial_t(\pi_\mathrm{w} S) + \partial_s Q_\mathrm{w} = \frac{m_\mathrm{w} l_\mathrm{i}}{\rho_\mathrm{w}} + \frac{M_\mathrm{w}}{\rho_\mathrm{w}}, \tag{4.82a}$$

$$\partial_t(\pi_\mathrm{s} S) + \partial_s(Q_\mathrm{s} + Q_\mathrm{b}) = \frac{m_\mathrm{s} l_\mathrm{s}}{\rho_\mathrm{s}} + \frac{M_\mathrm{s}}{\rho_\mathrm{s}}, \tag{4.82b}$$

where m_w is the melt rate of ice at the ice-canal interface and m_s is the net erosion sediment rate at the till-canal interface. Here, M_w and M_s correspond to water and sediment input that might come from neighboring tributaries. The flux Q_b corresponds to the bed-load sediment flux, which is different from the suspended sediment flux Q_s.

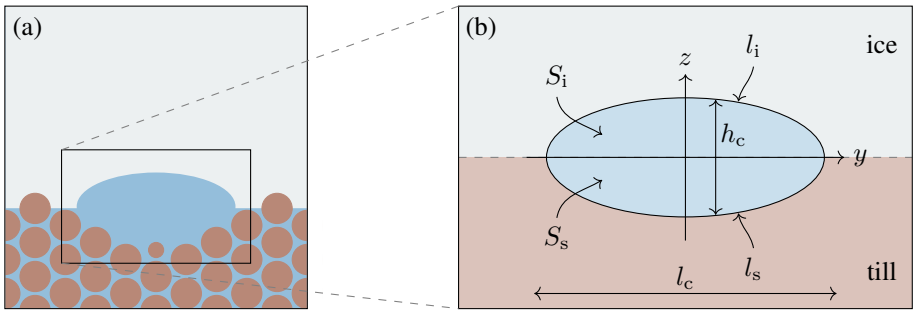

Figure 4.9: Schematic of a canal. **(a)** Canals are drainage systems that are both incised in the ice and the till. They open due to ice melt and sediment erosion, and close due to ice creep, till creep, and sediment deposition. **(b)** Geometry of a canal [adapted from Walder and Fowler, 1994; Ng, 2000]. The cross-sectional area of a canal is denoted by $S = S_\mathrm{i} + S_\mathrm{s}$ in which S_i is the area incised in the ice and S_s is the area incised in the till. The lengths l_i and l_s are the contact areas at the ice/water and till/water interfaces, per unit of canal length, respectively. The thickness of the canal is denoted by h_c. The width of the canal is denoted by l_c. Note that, in general, the canal is not equally incised in the ice and the till so that $S_\mathrm{i} \neq S_\mathrm{s}$ and $l_\mathrm{i} \neq l_\mathrm{s}$.

Equations have to be added for the evolution of the sections S_i and S_s incised in the ice and the till, respectively. The mechanisms over both sections are similar: opening is due to melt/erosion, and closing is due to creep. Assuming the viscous till rheology of Boulton and Hindmarsh [1987] (see

equation (4.24)), Fowler and Walder [1993] derived the following creep rate of the till:

$$\dot{\varepsilon} = c_{\mathrm{c,t}} A_{\mathrm{t}} N_{\mathrm{c}}^{a} N^{-b}, \tag{4.83}$$

in which, in which A_{t} is a viscosity coefficient of the till a, b are exponents in the till rheology (taken as $a = 1.33$ and $b = 1.8$), and $c_{\mathrm{c,t}}$ is a prefactor that depends on the exact shape of the canal and on a, b. Here, $N_{\mathrm{c}} = p_{\mathrm{i}} - p_{\mathrm{c}}$ denotes the effective pressure in the canal, with p_{c} the water pressure in the conduit, and $N = p_{\mathrm{i}} - p_{\mathrm{w}}$ denotes the effective pressure in the till, with p_{w} the pore-water pressure far from the canal. In general, both effective pressures are different; however, an analysis suggests that $N_{\mathrm{c}} = aN \approx N$, so as a first approximation we assume that both are equal to each other [Fowler and Walder, 1993; Walder and Fowler, 1994]. The equations for the opening of S_{i} and S_{s} are then given by

$$\partial_t S_{\mathrm{i}} = \frac{m_{\mathrm{w}} l_{\mathrm{i}}}{\rho_{\mathrm{i}}} - c_{\mathrm{c,i}} A_{\mathrm{i}}\, l_{\mathrm{i}}^2 N^n, \tag{4.84a}$$

$$\partial_t S_{\mathrm{s}} = \frac{m_{\mathrm{s}} l_{\mathrm{s}}}{\rho_{\mathrm{s}}} - c_{\mathrm{c,t}} A_{\mathrm{t}}\, l_{\mathrm{s}}^2 N^{a-b}. \tag{4.84b}$$

We have written the $\rho_{\mathrm{i}} := \rho$ and $A_{\mathrm{i}} := A$ to emphasize that these values correspond to properties of ice and not of water or sediment. A constitutive equation, linking the changes in hydraulic gradient ϕ and the flux Q_{c}, must be added to form a model for canals. Given that canals are shallow, an appropriate constitutive equation is given by

$$q_{\mathrm{c}} = -k_{\mathrm{c}}\, h_{\mathrm{c}}^{3/2} |\partial_s \phi|^{-1/2} \partial_s \phi, \tag{4.85}$$

in which q_{c} is the flux per unit width and $k_{\mathrm{c}} = \sqrt{8/(\rho_{\mathrm{w}} f_{\mathrm{w}})}$ is the hydraulic conductivity with $f_{\mathrm{w}} \sim 0.1$ a friction coefficient [Walder and Fowler, 1994; Ng, 2000]. Note that such equation effectively corresponds to a turbulent Darcy–Weisbach equation with $\alpha = 3/2$ and $\beta = 3/2$ (see equation (4.52)). Hence, the volumetric water flux in the canal is given by

$$Q_{\mathrm{c}} = -k_{\mathrm{c}}\, l_{\mathrm{c}} h_{\mathrm{c}}^{3/2} |\partial_s \phi|^{-1/2} \partial_s \phi. \tag{4.86}$$

Overall, the following model for canal flow is obtained:

Canal flow

$$\frac{\partial}{\partial t}(\pi_{\mathrm{w}} S) + \frac{\partial Q_{\mathrm{w}}}{\partial s} = \frac{m_{\mathrm{w}} l_{\mathrm{i}}}{\rho_{\mathrm{w}}} + \frac{M_{\mathrm{w}}}{\rho_{\mathrm{w}}}, \tag{4.87a}$$

$$\frac{\partial}{\partial t}(\pi_{\mathrm{s}} S) + \frac{\partial}{\partial s}(Q_{\mathrm{s}} + Q_{\mathrm{b}}) = \frac{m_{\mathrm{s}} l_{\mathrm{s}}}{\rho_{\mathrm{s}}} + \frac{M_{\mathrm{s}}}{\rho_{\mathrm{s}}}, \tag{4.87b}$$

$$\frac{\partial S_{\mathrm{i}}}{\partial t} = \frac{m_{\mathrm{w}} l_{\mathrm{i}}}{\rho_{\mathrm{i}}} - c_{\mathrm{c,i}} A_{\mathrm{i}}\, l_{\mathrm{i}}^2 N^n, \tag{4.87c}$$

$$\frac{\partial S_{\mathrm{s}}}{\partial t} = \frac{m_{\mathrm{s}} l_{\mathrm{s}}}{\rho_{\mathrm{s}}} - c_{\mathrm{c,t}} A_{\mathrm{t}}\, l_{\mathrm{s}}^2 N^{a-b}, \tag{4.87d}$$

$$Q_{\mathrm{c}} = -k_{\mathrm{c}}\, l_{\mathrm{c}} h_{\mathrm{c}}^{3/2} \left|\frac{\partial \phi}{\partial s}\right|^{-1/2} \frac{\partial \phi}{\partial s}. \tag{4.87e}$$

The system of equations (4.87) must be accompanied by a characterization of M_{w}, M_{s}, m_{w}, m_{s}, and Q_{b}. The rates M_{w} and M_{s} are considered to be inputs of the model and are therefore assumed to be known. The melt rate m_{w} at the ice-canal interface can be computed by assuming that all the dissipated energy is used to melt ice at that interface, given that the work done by erosion and associated with the transport of sediment is negligible. Then,

$$\frac{m_{\mathrm{w}} l_{\mathrm{i}}}{\rho_{\mathrm{i}}} = \frac{|Q_{\mathrm{c}} \partial_s \phi|}{\rho_{\mathrm{i}} L}. \tag{4.88}$$

The net erosion rate m_s at the till-canal interface can be computed by subtracting the sedimentation rate from the erosion rate. Following Parker [1978], these rates are parametrized as follows:

$$m_\mathrm{s} l_\mathrm{s} = E_\mathrm{s} v_\mathrm{s} \left\langle \frac{\tau}{\Delta \rho_\mathrm{t} g d_\mathrm{s}} - \tau_0 \right\rangle^{3/2} - \frac{v_\mathrm{s}^2}{\epsilon} \pi_\mathrm{s} h_\mathrm{c}, \tag{4.89}$$

where $E_\mathrm{s} \sim 0.1$ is a constant of proportionality for erosion, v_s is the sediment grain-settling velocity, and ϵ is an eddy diffusivity that characterizes the turbulence of the water flow. The stress τ corresponds to the shear stress exerted at the roof and at the bed, which can be estimated based on the Darcy–Weisbach relation $\tau = f \rho_\mathrm{w} u_\mathrm{w}^2 / 8$ with $u_\mathrm{w} = Q_\mathrm{w}/S$ the mean velocity of the water flow in the canal. Finally, the bed-load flux Q_b is written using a Meyer–Peter–Mueller law (see equation (4.81)):

$$Q_\mathrm{b} = K_\mathrm{s} l_\mathrm{s} \left(\frac{\Delta \rho_\mathrm{t} g d_\mathrm{s}^3}{\rho_\mathrm{w}} \right)^{1/2} \left\langle \frac{\tau}{\Delta \rho_\mathrm{t} g d_\mathrm{s}} - \tau_0 \right\rangle^{3/2}. \tag{4.90}$$

We note that other parametrizations for sediment rate, erosion rate, and bed-load flux can be found in the literature [e.g., Brinkerhoff et al., 2017; Delaney et al., 2019, 2023; Aitken et al., 2024]. Additionally, the model presented assumes transport-limited conditions, where sediment flux reaches its carrying capacity. However, canals may also experience supply-limited conditions [e.g., Delaney et al., 2019; Hewitt and Creyts, 2019].

Despite its complexity, the model (4.87) can be used to obtain interesting insights relative to the characteristics of canals. To simplify the analysis, consider a steady-state canal that is such that the gradient in effective pressure is small with respect to the hydraulic potential gradient so that $\partial_s \phi \approx -\Psi$. Given the steady-state assumption, the ratio of the melt rate in the ice over the net erosion rate in the till can then be estimated thanks to a ratio between (4.87c) and (4.87d):

$$\frac{m_\mathrm{w} l_\mathrm{i}}{m_\mathrm{s} l_\mathrm{s}} = \left(\frac{N}{N_0} \right)^{n+b-a}, \quad N_0 := \left(\frac{\rho_\mathrm{s} l_\mathrm{s}^2 c_{\mathrm{c,t}} A_\mathrm{t}}{\rho_\mathrm{i} l_\mathrm{i}^2 c_{\mathrm{c,i}} A_\mathrm{i}} \right)^{1/(n+b-a)}. \tag{4.91}$$

It follows that if $N > N_0$, the canal will be be mainly incised in the ice, while for $N < N_0$, it will be mainly incised in the till. A numerical estimation of the critical effective pressure value N_0 reveals that $N_0 \approx 8 \times 10^5$ Pa. We suppose that we are in the case $N < N_0$, as this is the case associated with canals. Then, $l_\mathrm{c} \approx l_\mathrm{i}$. This, together with equations (4.87c), (4.87e), and (4.88) allows to obtain an explicit algebraic expression for the effective pressure, expressed as a function of the water flux:

$$N = \left(\frac{k_\mathrm{c}^2}{\rho_\mathrm{i} c_{\mathrm{c,i}} A_\mathrm{i}} \right)^{\frac{1}{n}} h_\mathrm{c}^{\frac{3}{n}} \Psi^{\frac{2}{n}} Q_\mathrm{w}^{-\frac{1}{n}}. \tag{4.92}$$

Importantly, the effective pressure in a canal is a decreasing function of the subglacial water flux. This is a rather unexepected result, as channels have been found to have the opposite behavior, their effective pressures increasing with increasing water fluxes (see equation (4.60)). In particular, this means that, in contrast to channels, canals do not tend to isolate themselves from each other, and rather organize themselves in a relatively distributed way, co-existing next to other canals. The key difference between channels and canals is their shapes (circular vs. shallow) and it follows that the geometry of subglacial conduits is a key driver for their dynamics and the spatial pattern they take.

The model of Walder and Fowler [1994] has been surpassed by the more sophisticated model of Ng [1998, 2000]. They key difference is that in this new model, an expression for the canal thickness $h_\mathrm{c} = h_\mathrm{c}(y)$ is derived (see Fig. 4.9), while Walder and Fowler's original model assumed a mean thickness value. Ng [2000] obtained the following expression:

$$N \propto \Psi^{-\frac{1}{n}} Q_\mathrm{s}^{\frac{3}{2n}} Q_\mathrm{w}^{-\frac{5}{2n}}, \tag{4.93}$$

thereby including the effect of sediment flux in the expression for the effective pressure. Compared to (4.92), the exponent of the water flux and the geometric potential gradient are different. However, the same intriguing canal behavior is kept in that N decreases if Q_w increases. A limitation in (4.93) is that it requires the sediment flux to be known, while (4.92) does not depend on it. van der Wel et al. [2013] suggest to overcome this issue by assuming that Q_s is equal to a fixed small proportion of Q_w, e.g., $Q_\mathrm{s} = Q_\mathrm{w}/500$. Then, (4.93) becomes

$$N \propto \Psi^{-\frac{1}{n}} Q_\mathrm{w}^{-\frac{1}{n}}, \tag{4.94}$$

leading to the same dependency with respect to the subglacial water flux as (4.92). Note that, within our system of notations, the fraction $Q_\mathrm{s}/Q_\mathrm{w}$, here taken as $1/500$, corresponds to $\pi_\mathrm{s}/\pi_\mathrm{w}$.

4.3.4 Multi-drainage models

The models presented above each involve the study of a single type of drainage on a clearly identified type of bed. However, in practice, several types of drainage are expected to co-exist and evolve as a function of subglacial conditions. In order to develop a multi-drainage model, the following questions need to be addressed:

1. How to couple different localized and distributed drainage systems?
2. How to distribute subglacial melt to different types of drainage systems?
3. How to handle multiple bed types?

We note that existing multi-drainage models usually only tackle the first and second questions. Indeed, they typically consider a system that is entirely made of a hard bed. An englacial storage term is sometimes added to allow for storage in some kind of underlying aquifer [e.g., Werder et al., 2013], but such term has a limited impact for simulations of the hydrological system over long time scales as it disappears when the system is in a steady state. The inclusion of both hard and soft beds in a hydrological model is a motivation for the second original contribution of this thesis, which is presented in chapter 6.

We now present three frameworks for modeling multi-drainage systems: a lumped-element approach, a continuous-discrete approach, and a fully continuous approach.

Lumped-element approach

In the lumped-element approach, we consider prototype models, called ‘elements’, that represent one or more particular types of drainage with identified dynamics [Clarke, 1996]. Several elements can then be linked together to form a network [Schoof, 2010b], or attributed to each grid cell of a large-scale mesh to represent the hydrology on that cell [Gowan et al., 2023]. In the approach of Schoof [2010b], each element of the hydrological system is supposed to be channel, a cavity filled with water, or something in between these two cases. Formally, each element is characterized by a cross-sectional area S_w, a volumetric water flux Q_w, and an effective pressure N. The equations governing these quantities are given by the following:

$$\partial_t S = V_\mathrm{o}(Q_\mathrm{w}) - V_\mathrm{c}(S_\mathrm{w}, N), \tag{4.95a}$$
$$Q_\mathrm{w} = -K_\mathrm{w} S_\mathrm{w}^\alpha |\partial_s \phi|^{\beta-2} \partial_s \phi, \tag{4.95b}$$

with opening and closing rates $V_\mathrm{o} = V_\mathrm{o}(Q_\mathrm{w})$ and $V_\mathrm{c} = V_\mathrm{c}(S_\mathrm{w}, N)$ given by

$$V_\mathrm{o} = h_\mathrm{b} u_\mathrm{b} + |Q_\mathrm{w} \partial_s \phi|/\rho L, \tag{4.96a}$$
$$V_\mathrm{c} = c_\mathrm{c} A S_\mathrm{w} |N|^{n-1} N. \tag{4.96b}$$

Such a model is very similar to the model of localized flow as introduced for channels in the hard-bed section (system of equations (4.61)), and we use the same notations. The main difference is the addition of the additional term $h_\mathrm{b} u_\mathrm{b}$ in the expression of the opening rate (4.96a). This term is reminiscent of the opening term in linked cavities; see equation (4.50). The rationale behind such an approach is the following. For low water fluxes, the hydrology system is supposed to be inefficient, i.e., similar to a linked-cavity system. In that case, the first term $h_\mathrm{b} u_\mathrm{b}$, which corresponds to opening by sliding over bed protrusions, is dominant in (4.96a), so the element indeed mimics a cavity. For large water fluxes, the hydrology system is supposed to take the form of a channel. This is again what the model does as the second term $|Q_\mathrm{w} \partial_s \phi| / \rho L$, which corresponds to opening by melting of the conduit walls, becomes dominant in the opening rate in that case. Overall, we thus see that taking a simple sum of the opening rates associated with cavities and channels allows us to obtain a hydrological element that covers both behaviors.

Further analysis is possible thanks to the simplicity of the model. Consider a steady-state element with a known water flux Q_w and geometric potential gradient magnitude $\Psi := -\partial_s \phi_0$. If there are relatively small spatial variations in the effective pressure, then $\partial_s \phi \approx -\Psi$. It follows that the effective pressure is given by

$$N = \left(\frac{\rho L h_\mathrm{b} u_\mathrm{b} + Q_\mathrm{w} \Psi}{\rho L c_\mathrm{c} A K_\mathrm{w}^{-\frac{1}{\alpha}} \Psi^{\frac{1-\beta}{\alpha}} Q_\mathrm{w}^{\frac{1}{\alpha}}} \right)^{\frac{1}{n}}, \tag{4.97}$$

which is a generalization of the result (4.60) which has been obtained for channels alone. In particular, the effective pressure is no longer an increasing function of the water flux, as it was the case for channels. Now, there is a threshold water flux Q_w^0 at which the element switches between a cavity and a channel. It can be estimated by matching the opening rates associated with each type (cavity/channel); this yields

$$Q_\mathrm{w}^0 \sim \frac{\rho L h_\mathrm{b} u_\mathrm{b}}{\Psi}. \tag{4.98}$$

The following limiting behaviors can then be obtained as for water fluxes far smaller or greater than Q_w^0, which are respectively associated with cavities and channels:

$$N \propto Q_\mathrm{w}^{-\frac{1}{\alpha n}}, \quad \text{for } Q_\mathrm{w} \ll Q_\mathrm{w}^0, \tag{4.99a}$$

$$N \propto Q_\mathrm{w}^{\frac{\alpha-1}{\alpha n}}, \quad \text{for } Q_\mathrm{w} \gg Q_\mathrm{w}^0. \tag{4.99b}$$

We observe two strikingly different behavior as the effective pressure in cavities decreases with increasing water flux, while it increases in the case of channels (Fig. 4.10). Typical values of the exponents are $n = 3$ and $\alpha = 5/4$, for which one gets $-1/(\alpha n) = -4/15 \approx -0.27$ and $(\alpha - 1)/(\alpha n) = 1/15 \approx 0.07$. This difference also explains the different spatial organization of cavities and channels: channels tend to be 'on their own' as they will out-compete any smaller neighboring channels, leading to a localized pattern. However, cavities will form a distributed system in which cavities co-exist close to each other.

Continuous-discrete approach

In the continuous-discrete approach, a (finite-element) triangulation of the domain is used to include both localized and distributed drainage systems. Within each element of the triangulation, the system is assumed to be made of linked cavities. By contrast, channels are localized on the edges of the elements. Hence, the distributed drainage systems (linked cavities) are simulated in a continuous fashion, while the localized ones (channels) are simulated on the network created by the set of element edges.

The evolution of the distributed component is driven by cavity opening through sliding and closing via ice creep, as described by the system of equations (4.61). By contrast, the localized component evolves through opening due to melting at the ice-channel interface and closing caused by ice creep, as described by the system of equations (4.53). We note that the melt generated over the distributed drainage system is not used as a possible mechanism for cavities opening. The reason behind this choice is practical:

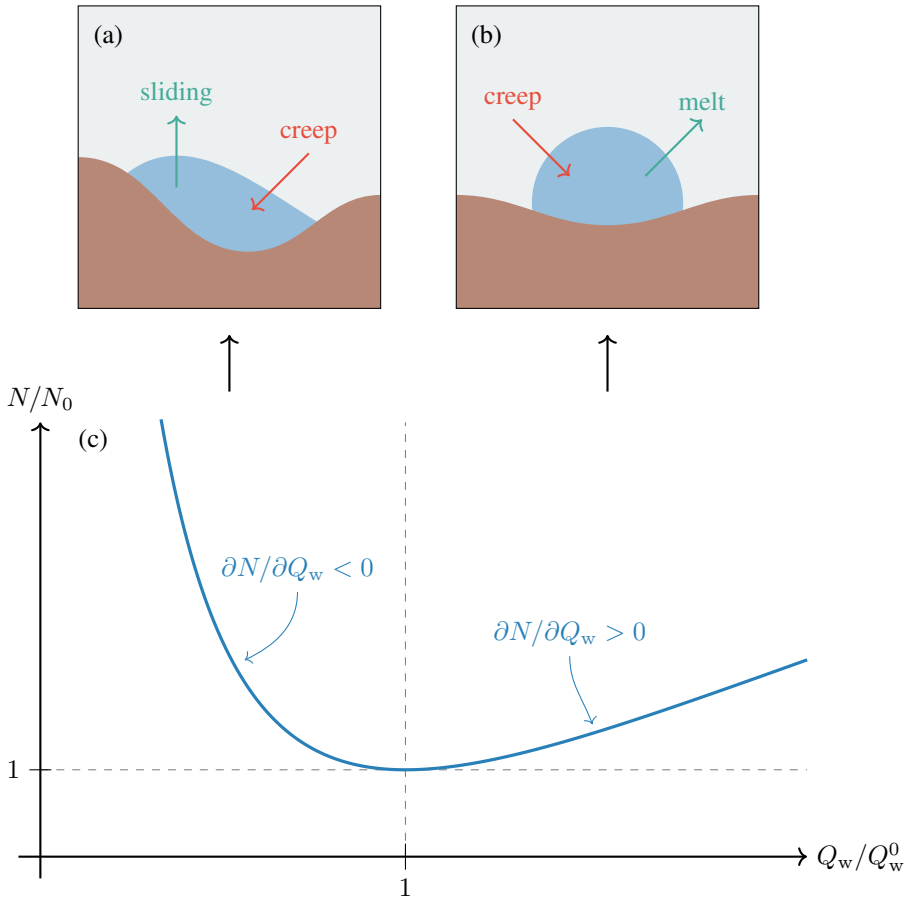

Figure 4.10: Schematic of the main physical drivers for the opening and closing of conduits on hard beds [adapted from Schoof, 2010b]. **(a)** Cavities open thanks to sliding over bed protrusions and close due to viscous creep of ice. **(b)** Channels open thanks to water melt at its boundaries and close due to viscous creep of ice. **(c)** Relation between the steady-state effective pressure N and the subglacial water flux Q_w, following equation (4.97). Here, N_0 and Q_w^0 are scaling values that allow to adimentionalize the system [see Schoof, 2010b].

it was found that including such a component in a distributed drainage system leads to an instability in which the system becomes unstable. Such instability has been identified in Hewitt [2009] and discussed in greater details in the appendix of Schoof et al. [2012]. To link the channels between each other, the channel flux going into each node of the mesh is constrained to be equal to the channel flux going outside of it. This creates a constraint that effectively couples the channels of all the edges with each other (analogously to Kirchhoff's current law for electric circuits). The distributed and localized systems are coupled with each other by attributing the net distributed water flux that goes into each edge as a source term for the channels in these edges.

Such a model has been implemented in the hydrological model `GlADS` [Werder et al., 2013] and in the hydrological component of the ice-sheet model `MALI` [Hoffman et al., 2018] which are quite popular within the glaciological community [e.g., Dow et al., 2022; Hager et al., 2022]. It represents a quite practical approach for including both distributed and localized components. However, there are several limitations associated with it [Werder et al., 2013; Warburton et al., 2024]:

- Channels are a priori assumed to be located at the location of the edges of the elements of the triangulation. In other words, their positions is not solely a result of the hydrological model (while it should be).
- There is a dependence of the results on both the mesh and the mesh resolution, so that the results do not actually converge when the mesh is refined.
- As previously mentioned, the opening due to melt is not included as a component for conduit opening in the distributed system.

Fully continuous approach

In a fully continuous approach, the location of channels is not prescribed a priori, so channels are expected to emerge spontaneously as a consequence of conditions in the hydrological system. In the hydrological component of the `PISM` model, Bueler and van Pelt [2015] removed any localized component (i.e., the model only consists of equations similar to (4.53)), effectively leading to a fully continuous approach. However, such a model is incapable of producing channels, as channelization is made possible by melt opening, which is not included in such a model. As channels are thought to play an important role in the dynamics of subglacial hydrology, such an approach must be put aside.

In the `SHAKTI` hydrological model, Sommers et al. [2018] also adopted a fully continuous approach, but included opening terms associated to melt in their formulation. Another change compared to the previous hydrological models is that they adopted a constitutive equation for the subglacial water flux $\boldsymbol{q}_\mathrm{w}$ that should be better at modeling both laminar and turbulent flows (the former being typically associated with distributed, inefficient systems, and the latter being associated with localized, efficient systems). Following studies of fluid flow in rock fractures [Zimmerman et al., 2004], they introduced the following equation:

$$\boldsymbol{q}_\mathrm{w} = -\frac{h_\mathrm{w}^3}{12\eta_\mathrm{w}(1+\mathrm{Re}/\mathrm{Re}_\mathrm{c})}\bar{\nabla}\phi, \tag{4.100}$$

where $\mathrm{Re} = \rho_\mathrm{w}\|\boldsymbol{q}_\mathrm{w}\|/\eta_\mathrm{w}$ is the Reynolds number of subglacial water flux and in which $\mathrm{Re}_\mathrm{c} \sim 10^3$ is a critical value associated with the laminar-turbulent transition. The main advantage of such constitutive equation is that it admits the following limit cases,

$$\boldsymbol{q}_\mathrm{w} = -\frac{h_\mathrm{w}^3}{12\eta_\mathrm{w}}\bar{\nabla}\phi, \qquad \text{for } \mathrm{Re}/\mathrm{Re}_\mathrm{c} \ll 1, \tag{4.101a}$$

$$\boldsymbol{q}_\mathrm{w} = -\frac{h_\mathrm{w}^{3/2}}{\sqrt{12\rho_\mathrm{w}/\mathrm{Re}_\mathrm{c}}}\|\bar{\nabla}\phi\|^{-1/2}\bar{\nabla}\phi, \qquad \text{for } \mathrm{Re}/\mathrm{Re}_\mathrm{c} \gg 1, \tag{4.101b}$$

which effectively corresponds to a laminar behavior ($\alpha = 3$, $\beta = 2$ in the Darcy equation (4.52)) and a turbulent behavior ($\alpha = 3/2$, $\beta = 3/2$ in the Darcy equation (4.52)).

With these modifications, channels do appear in numerical simulations. This is not unexpected, as the inclusion of the melt-opening term is known to trigger an instability in the flow, leading to channelization. However, said channels are found to be infinitely small, practically always being one 'pixel' wide in simulations [Warburton et al., 2024]. Their locations were also found to be model dependent [Sommers et al., 2018]. To solve this issue, Felden et al. [2023] added a diffusive term in the opening-closing equation for the film thickness evolution h_w. This allowed to obtain channels with a finite width. Nonetheless, this diffusive term can seen as somewhat artificial, given that it does not rely on a physical mechanism. Recently, Warburton et al. [2024] showed that there was in fact a missing piece in continuous hydrological models that led to infinitely small channels. They showed that this missing component was a non-local diffusive term within the equation (2.56) for melt rate :

$$m_\mathrm{w} = \frac{q_\mathrm{t} + q_\mathrm{geo} + |\boldsymbol{\tau}_\mathrm{b} \cdot \boldsymbol{u}_\mathrm{b}| + |\boldsymbol{q}_\mathrm{w} \cdot \bar{\nabla}\phi|}{\rho L} + \overline{\mathrm{div}} \left(\frac{h_\mathrm{w} m_\mathrm{w} \bar{\nabla} h_\mathrm{w}}{1 + \|\bar{\nabla} h_\mathrm{w}\|^2} \right). \tag{4.102}$$

This new term is the last one and comes from the horizontal variations in the heat flux within the water conduit. With this term, channels appear to have a finite width, and their shape actually correspond to the one that is expected for such localized systems. This corresponds to a major improvement in subglacial hydrological modeling. However, given the small size of the appearing channels –they have a width of the order of meters– the applicability of such approach in large-scale ice-sheet simulations might be limited, so further research efforts are needed in order to obtain computationally cheap models.

List of symbols

Greek symbols

α	Exponent in the Darcy–Weisbach equation	-
β	Exponent in the Darcy–Weisbach equation	-
γ, γ_0	Deformation angle	-
$\dot{\gamma}$	Shear rate	s^{-1}
$\boldsymbol{\gamma}$	True gravity	$\mathrm{kg\,m\,s}^{-2}$
ϵ	Eddy diffusivity	$\mathrm{m}^2\,\mathrm{s}^{-1}$
ε	Aspect ratio	-
$\dot{\varepsilon}$	Creep rate	s^{-1}
ζ, ζ_j	Proportion of ice in contact with bed protrusions	-
η	Ice viscosity	$\mathrm{Pa\,s}$
η_t	Till viscosity	$\mathrm{Pa\,s}$
η_w	Water viscosity	$\mathrm{Pa\,s}$
θ, θ_0	Ice temperature	K
θ'	Pressure-corrected ice temperature	K
θ_cf	Ice temperature at the calving front	K
θ_m	Ice temperature at pressure melting point	K
θ_s	Ice temperature at the upper ice-sheet surface	K
θ_w	Ocean water temperature	K
κ, κ_0	Wavenumber of the bedrock elevation	m^{-1}
λ, λ_0	Wavelength of the bedrock elevation	m
μ_t	Friction coefficient in the till	-
ν	Measure of bed roughness	-
π_s	Proportion of sediment content in a conduit	-

π_{w}	Proportion of water content in a conduit	-
ρ, ρ_{i}	Ice density	$\mathrm{kg\,m^{-3}}$
ρ_{s}	Sediment density	$\mathrm{kg\,m^{-3}}$
ρ_{w}	Water density	$\mathrm{kg\,m^{-3}}$
$\Delta\rho_{\mathrm{t}}$	Difference of sediment/water density in the till	$\mathrm{kg\,m^{-3}}$
σ	Compression stress	Pa
$\boldsymbol{\sigma}$	Cauchy stress tensor	Pa
σ_{nn}	Normal stress	Pa
σ_{zz}	Vertical stress	Pa
τ	Shear stress	Pa
τ_0	Critical Shields stress	-
τ_{y}	Yield stress	Pa
τ_{b}, $\boldsymbol{\tau}_{\mathrm{b}}$	Basal friction stress	Pa
$\boldsymbol{\tau}_{\mathrm{s}}$	Shear stress applied on the till	Pa
ϕ	Hydraulic potential	Pa
ϕ_0	Geometric potential	Pa
ϕ_{t}	Till porosity	-
φ	Internal friction angle	-
$\boldsymbol{\varphi}$	Mapping of the motion of a body	m
$\boldsymbol{\varphi}_t^{-1}$	Inverse mapping of the motion of a body	m
χ	Friction coefficient in Gagliardini's friction law	-
$\boldsymbol{\omega}$	Vorticity	$\mathrm{s^{-1}}$
Γ	Boundary of a domain	m
Γ_{cf}	Calving-front boundary	m
Γ_{f}	Floating lower-surface boundary	m
Γ_{g}	Grounded lower-surface boundary	m
Γ_{gl}	Grounding line	m
Γ_{s}	Upper-surface boundary	m
Λ, Λ_0	Friction coefficient in Schoof's friction law	$\mathrm{Pa^{-n}\,m\,s^{-1}}$
Ξ	Power per unit length dissipated by the water flow	$\mathrm{Pa\,m^2\,s^{-1}}$
Π	Rate of change of sensible heat per unit length	$\mathrm{Pa\,m^2\,s^{-1}}$
Ψ	Geometric potential gradient	$\mathrm{Pa\,m^{-1}}$

Ω	Domain	m
Ω_t, Ω_0	Ice-sheet domain	m
$\bar{\Omega}_t$	Projection of the ice-sheet domain on a plane	m
$\partial\Omega_t$	Boundary of the Ice-sheet domain	m
$\boldsymbol{\Omega}$	Earth's Poisson vector	s^{-1}

Latin symbols

a	Exponent in the till rheology	-
$\boldsymbol{a}$	Spatial acceleration	$\mathrm{m\,s}^{-2}$
a_s	Net mass accumulation rate	$\mathrm{m\,s}^{-1}$
b	Exponent in the till rheology	-
c	Specific heat capacity of ice	$\mathrm{J\,kg}^{-1}\,\mathrm{K}^{-1}$
c_c, $c_\mathrm{c,i}$	Prefactor in the closing rate of ice creep	$\mathrm{m\,s}^{-1}$
$c_\mathrm{c,t}$	Prefactor in the closing rate of till creep	$\mathrm{m\,s}^{-1}$
c_t	Clapeyron slope	$\mathrm{K\,Pa}^{-1}$
c_w	Specific heat capacity of water	$\mathrm{J\,kg}^{-1}\,\mathrm{K}^{-1}$
d, d_0	Scale of bumps in the bedrock	m
d_s	Scale of sediment particles	m
e	Internal energy density	$\mathrm{J\,kg}^{-1}$
e_t, e_t^0	Till void ratio	-
f	Function	-
$\boldsymbol{f}$	Volumetric forces	$\mathrm{m\,s}^{-2}$
f_cf	Equation of calving-front position	m
f_s	Equation of upper-surface elevation	m
f_w	Friction coefficient	-
g, $\boldsymbol{g}$	Gravitational acceleration	$\mathrm{m\,s}^{-2}$
h	Ice thickness	m
h_b	Characteristic size of bed protrusions	m
h_c	Thickness of a canal	m
h_s	Equivalent thickness of sediment content in a till	m
h_t	Thickness of deformable till	m
h_w, h_w^0	Effective thickness of water	m

k	Thermal heat conductivity of ice	$\mathrm{W\,m^{-1}\,K^{-1}}$
k_b	Thermal heat conductivity of the bedrock	$\mathrm{W\,m^{-1}\,K^{-1}}$
k_c	Hydraulic conductivity of a canal	$\mathrm{Pa^{-1/2}\,m\,s^{-1}}$
k_t	Till permeability	$\mathrm{m^2}$
k_w	Hydraulic conductivity of a distributed drainage system	$\mathrm{Pa^{1-\beta}\,m^{1+\beta-\alpha}\,s^{-1}}$
$l, l_j, \tilde{l}, \tilde{l}_j$	Effective distance between neighboring clasts	m
l_b	Characteristic distance between bed protrusions	m
l_c	Width of canal	m
l_i	Contact area of the canal with the ice per unit length	m
l_s	Contact area of the canal with the till per unit length	m
m_0	Typical bed slope	-
m_b	Basal melt rate	$\mathrm{m\,s^{-1}}$
m_s	Net deposition rate of sediment material	$\mathrm{kg\,m^{-2}\,s^{-1}}$
m_w	Net melt rate of water	$\mathrm{kg\,m^{-2}\,s^{-1}}$
n	Exponent in Glen's flow law	-
$\boldsymbol{n}$	Normal to a boundary	-
n_x	Component of a normal along the x axis	-
n_y	Component of a normal along the y axis	-
n_z	Component of a normal along the z axis	-
p	Exponent in the friction law	-
p, p_i, p_j	Pressure in ice	Pa
p_atm	Atmospheric pressure	Pa
p_c	Water pressure in a canal	Pa
p_cf	Pressure at the calving front	Pa
p_w	Water pressure	Pa
q	Exponent in the friction law	-
$\boldsymbol{q}$	Heat flux in the ice	$\mathrm{W\,m^{-2}}$
q_b	Heat dissipation associated with basal processes	$\mathrm{W\,m^{-2}}$
q_c	Flux per unit length in a canal	$\mathrm{m^2\,s^{-1}}$
q_geo	Geothermal heat flux	$\mathrm{W\,m^{-2}}$
$\boldsymbol{q}_\mathrm{s}$	Subglacial sediment flux	$\mathrm{m^2\,s^{-1}}$
q_t	Conductive heat flux in the ice	$\mathrm{W\,m^{-2}}$

$\boldsymbol{q}_{\mathrm{w}}$	Subglacial water flux	$\mathrm{m}^2\,\mathrm{s}^{-1}$
r	Heat production source term	$\mathrm{W\,kg}^{-1}$
r, r_j, $\tilde{r}_j$	Effective radius of bed protrusions	m
t	Time	s
$\boldsymbol{t}$	Surface forces	Pa
u	Velocity component along the x axis	$\mathrm{m\,s}^{-1}$
$\boldsymbol{u}$	Horizontal velocity	$\mathrm{m\,s}^{-1}$
u_0	Characteristic velocity	$\mathrm{m\,s}^{-1}$
u_{b}, $\boldsymbol{u}_{\mathrm{b}}$	Basal velocity	$\mathrm{m\,s}^{-1}$
u_{cf}	Calving-front velocity	$\mathrm{m\,s}^{-1}$
$\boldsymbol{u}_{\mathrm{sia}}$	SIA velocity	$\mathrm{m\,s}^{-1}$
$\boldsymbol{u}_{\mathrm{ssa}}$	SSA velocity	$\mathrm{m\,s}^{-1}$
u_{w}	Mean water velocity in a conduit	$\mathrm{m\,s}^{-1}$
v	Velocity component along the y axis	$\mathrm{m\,s}^{-1}$
$\boldsymbol{v}$	Spatial velocity	$\mathrm{m\,s}^{-1}$
v_{c}, v_{c}^j	Closing rate in a distributed drainage system	$\mathrm{m\,s}^{-1}$
$\boldsymbol{v}_{\mathrm{i}}$	Interface velocity	$\mathrm{m\,s}^{-1}$
v_{o}, v_{o}^j	Opening rate in a distributed drainage system	$\mathrm{m\,s}^{-1}$
v_{s}	Sediment grain-settling velocity	$\mathrm{m\,s}^{-1}$
w	Velocity component along the z axis	$\mathrm{m\,s}^{-1}$
$\boldsymbol{w}$	Vector associated with the spin-rate tensor	s^{-1}
x	Spatial position component along the x axis	m
$\boldsymbol{x}$, $\boldsymbol{x}_0$	Position vector	m
$\mathrm{d}\boldsymbol{x}$	Infinitesimal vector in the current configuration	m
y	Spatial position component along the y axis	m
z	Spatial position component along the z axis	m
z_{b}	Bedrock elevation	m
z_{l}	Lower-surface elevation	m
z_{s}	Upper-surface elevation	m
z_{sl}	Sea-level elevation	m
A, A_{i}, A_0	Ice viscosity coefficient	$\mathrm{Pa}^{-n}\,\mathrm{s}^{-1}$
$\boldsymbol{A}$	Material acceleration	$\mathrm{m\,s}^{-2}$

A_s	Sliding parameter without cavitation	$\mathrm{Pa}^{-n}\,\mathrm{m\,s}^{-1}$
A_t	Till viscosity coefficient	$\mathrm{Pa}^{b-a}\,\mathrm{s}^{-1}$
C_b	Friction coefficient in the Budd friction law	$\mathrm{Pa}^{1-q}\,\mathrm{m}^{-p}\,\mathrm{s}^{p}$
C_rc	Friction coefficient in the regularized Coulomb friction law	-
C_s	Friction coefficient in the Schoof friction law	-
C_t	Till compressibility coefficient	-
C_w	Friction coefficient in the Weertman friction law	$\mathrm{Pa\,m}^{-p}\,\mathrm{s}^{p}$
E_s	Constant of proportionality for sedimentation	-
$\boldsymbol{D}$	Strain-rate tensor	s^{-1}
$\boldsymbol{F}$	Deformation gradient	-
$\boldsymbol{I}$	Identity tensor	-
K_w	Hydraulic conductivity in conduit	$\mathrm{Pa}^{1-\beta}\,\mathrm{m}^{2-2\alpha+\beta}\,\mathrm{s}^{-1}$
K_s	Dimensionless flux factor	-
L	Latent heat of fusion of ice	$\mathrm{J\,kg}^{-1}$
$\boldsymbol{L}$	Velocity gradient	s^{-1}
M_w	Effective melt rate in a localized conduit	$\mathrm{kg\,m}^{-1}\,\mathrm{s}^{-1}$
N, N_0	Effective pressure	Pa
N_c	Effective pressure in canals	Pa
N_min	Minimal effective pressure	Pa
N_t	Effective pressure in the till	Pa
Q	Activation energy for creep	J
Q_c	Volumetric flux in a canal	$\mathrm{m}^3\,\mathrm{s}^{-1}$
Q_s	Suspended sediment flux in a canal	$\mathrm{m}^3\,\mathrm{s}^{-1}$
Q_w, Q_w^0	Volumetric water flux	$\mathrm{m}^3\,\mathrm{s}^{-1}$
R	Universal gas constant	$\mathrm{J\,K}^{-1}$
Re, Re_c	Reynolds number	-
S	Cross-sectional canal area	m^2
S_b	Power spectral density of the bedrock elevation	m^3
S_i	Cross-sectional canal area incised in ice	m^2
S_s	Cross-sectional canal area incised in till	m^2
S_w	Cross-sectional area of a conduit	m^2
T	Length of the interval of time of interest	s

$\boldsymbol{T}$	Tangential projection operator	-
$\boldsymbol{V}$	Material velocity	$\mathrm{m\,s^{-1}}$
V_c	Closing rate of a conduit	$\mathrm{m^2\,s^{-1}}$
V_o	Opening rate of a conduit	$\mathrm{m^2\,s^{-1}}$
$\boldsymbol{W}$	Spin-rate tensor	$\mathrm{s^{-1}}$
$\boldsymbol{X}$	Material point	m
$\mathrm{d}\boldsymbol{X}$	Infinitesimal vector in the reference configuration	m

Mathematical symbols

$\mathbb{R}$	Set of real numbers	-
$f \sim g$	f is of the order of g, f is asymptotic to g	-
$f \approx g$	f is approximately equal to g	-
$f := g$	f is defined as g	-
$f \ll g$	f is much smaller than g	-
$f \propto g$	f is proportional to g	-
$\mathcal{O}(f)$	Order of f	units of f
$\langle f \rangle$	Macaulay brackets of f	units of f
$[f]$	Order of magnitude of f	units of f
$[\![f]\!]$	Variation of f across the interface	units of f
$]f, g[$	Open interval: $\{x \in \mathbb{R} : f < x < g\}$	units of f, g
$\hat{\boldsymbol{f}}$	Direction of $\boldsymbol{f}$	-
$\|\boldsymbol{f}\|$	Euclidean norm of $\boldsymbol{f}$	units of $\boldsymbol{f}$
$\boldsymbol{f} \cdot \boldsymbol{g}$	Inner product of $\boldsymbol{f}$ and $\boldsymbol{g}$	units of $\boldsymbol{f}, \boldsymbol{g}$
$\boldsymbol{f} \times \boldsymbol{g}$	Vector product of $\boldsymbol{f}$ and $\boldsymbol{g}$	units of $\boldsymbol{f}, \boldsymbol{g}$
$\boldsymbol{f} \otimes \boldsymbol{g}$	Outer product of $\boldsymbol{f}$ and $\boldsymbol{g}$	units of $\boldsymbol{f}, \boldsymbol{g}$
$\boldsymbol{F}^\mathrm{T}$	Transpose of $\boldsymbol{F}$	units of $\boldsymbol{F}$
$\|\boldsymbol{F}\|_*$	Norm of $\boldsymbol{F}$	units of $\boldsymbol{F}$
$\boldsymbol{F} : \boldsymbol{G}$	Tensor contraction of $\boldsymbol{F}$ and $\boldsymbol{G}$	units of $\boldsymbol{F}, \boldsymbol{G}$
$\mathrm{I}_{\boldsymbol{F}}$	First principal invariant of $\boldsymbol{F}$	units of $\boldsymbol{F}$
$\mathrm{II}_{\boldsymbol{F}}$	Second principal invariant of $\boldsymbol{F}$	(units of $\boldsymbol{F}$)^2
$\mathrm{III}_{\boldsymbol{F}}$	Third principal invariant of $\boldsymbol{F}$	(units of $\boldsymbol{F}$)^3
$\mathrm{tr}(\boldsymbol{F})$	Trace of $\boldsymbol{F}$	units of $\boldsymbol{F}$

$\det(\boldsymbol{F})$	Determinant of $\boldsymbol{F}$	(units of $\boldsymbol{F}$)^3
$\mathrm{cl}(\mathcal{F})$	Closure of the set $\mathcal{F}$	units of $\mathcal{F}$
$\mathrm{d}_t f$, $\mathrm{d}f/\mathrm{d}t$	Material time derivative of f	units of $f \times \mathrm{s}^{-1}$
$\partial_t f$, $\partial f/\partial t$	Partial time derivative of f	units of $f \times \mathrm{s}^{-1}$
$\partial_s f$, $\partial f/\partial s$	Spatial derivative of f along a streamline	units of $f \times \mathrm{m}^{-1}$
$\partial_x f$, $\partial f/\partial x$	Spatial derivative of f along the x axis	units of $f \times \mathrm{m}^{-1}$
$\partial_y f$, $\partial f/\partial y$	Spatial derivative of f along the y axis	units of $f \times \mathrm{m}^{-1}$
$\partial_z f$, $\partial f/\partial z$	Spatial derivative of f along the z axis	units of $f \times \mathrm{m}^{-1}$
∇f, $\nabla_{\boldsymbol{x}} f$	Spatial gradient of the scalar field f	units of $f \times \mathrm{m}^{-1}$
$\bar{\nabla} f$	Horizontal spatial gradient of scalar field f	units of $f \times \mathrm{m}^{-1}$
$\boldsymbol{\nabla f}$, $\boldsymbol{\nabla}_{\boldsymbol{x}} \boldsymbol{f}$	Spatial gradient of the vector field $\boldsymbol{f}$	units of $\boldsymbol{f} \times \mathrm{m}^{-1}$
$\boldsymbol{\nabla}_{\boldsymbol{X}} \boldsymbol{f}$	Spatial gradient of the vector field $\boldsymbol{f}$ in the reference configuration	units of $\boldsymbol{f} \times \mathrm{m}^{-1}$
$\mathrm{div}\, \boldsymbol{f}$	Divergence of the vector field $\boldsymbol{f}$	units of $\boldsymbol{f} \times \mathrm{m}^{-1}$
$\overline{\mathrm{div}}\, \boldsymbol{f}$	Horizontal divergence of the vector field $\boldsymbol{f}$	units of $\boldsymbol{f} \times \mathrm{m}^{-1}$
$\mathbf{div}\, \boldsymbol{F}$	Divergence of the tensor field $\boldsymbol{F}$	units of $\boldsymbol{F} \times \mathrm{m}^{-1}$

Part II

Original contributions

5

Extension of grounding-line flux conditions

T. Gregov, F. Pattyn, and M. Arnst
Grounding-line flux conditions for marine ice-sheet systems under effective-pressure-dependent and hybrid friction laws
Journal of Fluid Mechanics, 975, 2023

Flux conditions are semi-analytical expressions that can be used to determine the flux at the grounding line of marine ice sheets. In the glaciology literature, such flux conditions have initially been established for the Weertman and Coulomb friction laws. However, the extension to more general and complex friction laws, such as the Budd friction law for which basal friction depends on both the basal velocity and the effective pressure, is a topic of recent research. Several studies have also shown that hybrid friction laws, which consider a transition between a power-law friction far from the grounding line and a plastic behavior close to it, were good candidates for improved modeling of marine ice sheets. In this article, we show that the flux conditions previously derived for the Weertman and Coulomb friction laws can be generalized to flux conditions for the Budd friction law with two different effective-pressure models. In doing so, we build a bridge between the results obtained for these two friction laws. We provide a justification for the existence and uniqueness of a solution to the boundary-layer problem based on asymptotic developments. We also generalize our results to hybrid friction laws, based on a parametrization of the flux condition. Finally, we discuss the validity of the assumptions made during the derivation, and we provide additional explicit expressions for the flux that stay valid when the bedrock slopes are important or when the friction coefficients are relatively small.

5.1 Introduction

Marine ice sheets, such as the West Antarctic ice sheet, are continental ice masses which possess both a grounded and a floating part. These two regions are separated by the so-called *grounding line* where ice starts floating. There have been several studies in the recent literature aimed at understanding the grounding-line behavior using numerical simulations, analytical methods, or a combination of both. In particular, Schoof [2007c] and Tsai et al. [2015] have derived, based on simplified mechanical models for marine ice sheets and asymptotic expansions, so-called *flux conditions* which allow the flux at the grounding line, i.e., the amount of ice that crosses the grounding line per unit time, to be determined as a function of grounding-line thickness. The stability of marine ice-sheet systems can then be studied, and it has been found that, under certain assumptions, their dynamical behavior in these simplified mechanical

models can be described in terms of saddle-node bifurcations and hysteresis [Schoof, 2007b, 2012].

Schoof [2007c] and Tsai et al. [2015] considered two friction laws: the Weertman friction law, in which the magnitude of basal friction is proportional to a power of the basal velocity, and the Coulomb friction law, in which basal friction depends on a yield stress proportional to an effective pressure between the ice sheet and the underlying bedrock. Their work has been extended to more complex configurations including the impact of buttressing, which appears for three-dimensional ice sheets [Schoof et al., 2017; Pegler, 2018a,b; Haseloff and Sergienko, 2018, 2022; Sergienko, 2022a], the regime of low driving and basal stress [Sergienko and Wingham, 2019], and the impact of non-negligeable bed gradients [Sergienko and Wingham, 2022]. A current research topic is the study of more complex friction laws [Sergienko and Haseloff, 2023]. This research is motivated by the observation that the behavior of marine ice sheets in long-term numerical simulations is significantly influenced by the friction law that is used, even if the starting configuration can be similar if one tunes adequately the friction coefficients [Brondex et al., 2017].

In this paper, we derive flux conditions for a general class of friction models related to the Budd friction law, which includes dependence on basal velocity and on effective pressure. Modeling effective pressure is a challenging topic, and complex hydrology models can be coupled to the ice-sheet model [Hewitt, 2013; Werder et al., 2013; Bueler and van Pelt, 2015]. Here, we consider two different effective-pressure models that are elementary. The first one is associated with a perfectly-permeable bed, similar to the effective-pressure model used in Tsai et al. [2015]. The second one considers a linear dependence between the effective pressure and the ice thickness, which is frequent in numerical simulations of ice sheets [Bueler and Brown, 2009; Martin et al., 2011]. The derivation of the flux conditions leads to a problem that is formulated in terms of a dynamical system. We provide insight into the existence and uniqueness of a solution to this problem. We propose a numerical solving strategy for obtaining the value of a numerical factor appearing in this system. We also consider *hybrid* friction laws that are similar to the ones considered in Schoof [2005, 2010a], Gagliardini et al. [2007], and Zoet and Iverson [2020]. Instead of allowing only friction coefficients to be tuned, these friction laws can represent different regimes which can be triggered where certain physical conditions are met, e.g., friction has a plastic behavior near the grounding line. The derivation of flux conditions for hybrid friction laws is challenging because they introduce additional parameters whose magnitude is not necessarily small.

This paper is structured as follows. First, in section 5.2, the mathematical problem associated with the mechanical behavior of marine ice sheets is described. Then, in section 5.3, we show that the approach adopted in Schoof [2007c] and Tsai et al. [2015] can be generalized to the Budd friction law in combination with two different effective-pressure models. Using asymptotic developments, we also provide a justification for the existence and uniqueness of a solution to the resulting leading-order dynamical system. In section 5.4, we generalize our results to hybrid friction laws similar to the one described in Schoof [2005] based on a parametrization of the flux condition. In section 5.5, we discuss the validity of the assumptions made to derive the flux conditions, and we propose explicit expressions that can be used to take into account effects that have been neglected in the initial derivation. In section 5.6, the flux conditions are compared with numerical simulations. Finally, in section 5.7, we discuss our results.

5.2 Problem formulation

We consider the evolution of an isothermal marine ice sheet using a flowline model known as the shallow-shelf approximation [Morland, 1987; MacAyeal, 1989]. Such a model is suited for rapidly sliding ice sheets. Vertical shear in the ice is then neglected, and the vertical normal stress is cryostatic. We assume that the ice sheet is in a steady state. For a two-dimensional geometry, the solution to the flowline model consists of two functions defined over an interval $\Omega =]0, x_c[$: the thickness $h : \Omega \to \mathbb{R}^+$ and the horizontal velocity $u : \Omega \to \mathbb{R}$. The position $x = x_c$ corresponds to a calving front, where icebergs

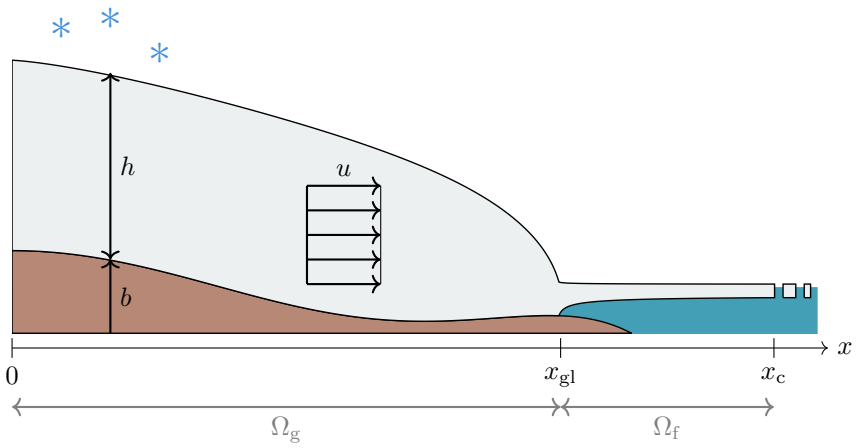

Figure 5.1: Schematic representation of the ice-sheet geometry. The unknowns are the grounding-line position x_{gl}, the ice thickness $h = h(x)$, and the horizontal velocity $u = u(x)$. The bed is characterized by a prescribed elevation $b = b(x)$. We also assume that the calving-front position x_c is known.

detach from the marine ice sheet. For simplicity, we consider a fixed calving-front position. In general, the domain Ω contains both a grounded and a floating portion, denoted respectively by Ω_g and Ω_f. If it exists and is unique, the point where the ice transitions from a grounded to a floating configuration is known as the grounding line and is denoted here by x_{gl}. This position is itself an unknown of the problem. A schematic representation of such an ice-sheet geometry is shown in figure 5.1.

5.2.1 Governing equations

Multi-domain formulation

Let us denote by (h_g, u_g) and (h_f, u_f) the values taken by the functions (h, u) on the grounded portion Ω_g and the floating portion Ω_f of the domain Ω, respectively. With these notations, the governing equations read as follows in the grounded portion:

$$\frac{\mathrm{d}}{\mathrm{d}x}(u_g\, h_g) = a, \quad \text{in } \Omega_g, \tag{5.1a}$$

$$2A^{-\frac{1}{n}}\frac{\mathrm{d}}{\mathrm{d}x}\left(h_g \left|\frac{\mathrm{d}u_g}{\mathrm{d}x}\right|^{\frac{1}{n}-1}\frac{\mathrm{d}u_g}{\mathrm{d}x}\right) - \tau_b - \Lambda\, h_g |u_g|^{\frac{1}{n}-1}u_g = \rho g h_g \frac{\mathrm{d}}{\mathrm{d}x}(b + h_g), \quad \text{in } \Omega_g. \tag{5.1b}$$

Equation (5.1a) is a mass-conservation equation, stating that the flux variation of the ice flow must be exactly compensated by the net mass accumulation rate a. Equation (5.1b) is a momentum-conservation equation and establishes a balance between the divergence of membrane stress, the friction stress, the lateral-drag stress, and the gravitational stress. The factor A and the exponent n are ice viscosity parameters associated with the Glen flow law (usually, $n = 3$), Λ is a lateral-drag coefficient, ρ is the ice density, ρ_w is the water density, g is the gravity acceleration, and $b = b(x)$ is the prescribed elevation of the underlying bedrock. The models used for the friction stress $\tau_b = \tau_b(h, u)$ are described in the next section. While we do not explicitly consider lateral drag in the present study, we do include it in the problem formulation, as it allows for an easier comparison with the other results from the literature.

In the floating portion, friction with the ocean and the air is neglected, leading to the following:

$$\frac{\mathrm{d}}{\mathrm{d}x}(u_\mathrm{f}\, h_\mathrm{f}) = a, \quad \text{in } \Omega_\mathrm{f}, \tag{5.2a}$$

$$2A^{-\frac{1}{n}}\frac{\mathrm{d}}{\mathrm{d}x}\left(h_\mathrm{f}\left|\frac{\mathrm{d}u_\mathrm{f}}{\mathrm{d}x}\right|^{\frac{1}{n}-1}\frac{\mathrm{d}u_\mathrm{f}}{\mathrm{d}x}\right) - \Lambda\, h_\mathrm{f}|u_\mathrm{f}|^{m-1}u_\mathrm{f} = \rho\left(1-\frac{\rho}{\rho_\mathrm{w}}\right)gh_\mathrm{f}\frac{\mathrm{d}h_\mathrm{f}}{\mathrm{d}x}, \quad \text{in } \Omega_\mathrm{f}. \tag{5.2b}$$

Finally, continuity conditions are added at the interface between the regions:

$$h_\mathrm{g} = h_\mathrm{f}, \quad u_\mathrm{g} = u_\mathrm{f}, \quad 2A^{-\frac{1}{n}}h_\mathrm{g}\left|\frac{\mathrm{d}u_\mathrm{g}}{\mathrm{d}x}\right|^{\frac{1}{n}-1}\frac{\mathrm{d}u_\mathrm{g}}{\mathrm{d}x} = 2A^{-\frac{1}{n}}h_\mathrm{f}\left|\frac{\mathrm{d}u_\mathrm{f}}{\mathrm{d}x}\right|^{\frac{1}{n}-1}\frac{\mathrm{d}u_\mathrm{f}}{\mathrm{d}x} \quad \text{on } \Sigma, \tag{5.3}$$

The portions Ω_g and Ω_f and their interface Σ are defined by a flotation condition:

$$\Omega_\mathrm{g} = \{x \in \Omega :\ \rho g h > \rho_\mathrm{w} g \langle -b\rangle\}, \tag{5.4a}$$

$$\Omega_\mathrm{f} = \{x \in \Omega :\ \rho g h < \rho_\mathrm{w} g \langle -b\rangle\}, \tag{5.4b}$$

$$\Sigma = \overline{\Omega}_\mathrm{g} \cap \overline{\Omega}_\mathrm{f}. \tag{5.4c}$$

The symbol $\langle\cdot\rangle = \max(\cdot, 0)$ corresponds to the Macaulay brackets. Hence, the grounded portion includes both the parts where the bedrock lies above the sea level (i.e., where $\langle -b\rangle = 0$), as well as the parts where the bedrock lies below the sea level, but where there is too much ice for it to be floating (i.e., where $\rho g h > -\rho_\mathrm{w} g b$).

In the simplest configuration, such as the one shown in figure 5.1, the grounded and floating portions can be written as open sets $\Omega_\mathrm{g} =]0, x_\mathrm{gl}[$ and $\Omega_\mathrm{g} =]x_\mathrm{gl}, x_\mathrm{c}[$, so that the grounded-line position can be properly defined as the unique element of Σ: $\Sigma = \{x_\mathrm{gl}\}$. We note that in general, the geometry might be more complex. For example, there could be several isolated points on which the ice sheet switches from a grounded to a floating position and vice-versa, leading to multiple grounding lines. A more exotic configuration, not considered here, is the one described by Pegler [2018a] with the so-called marginal-flotation zones. In that case, the interface Σ becomes a set of its own, i.e., the grounding-line width becomes finite.

Boundary conditions

At $x = 0$, we assume the ice to be sufficiently slow so that it is virtually motionless (this could also correspond to a symmetry condition):

$$u = 0, \quad \text{at } x = 0. \tag{5.5}$$

At the calving front, equilibrium between the horizontal stress in the ice and the ocean water pressure yields the following Neumann boundary condition:

$$2A^{-\frac{1}{n}}\left|\frac{\mathrm{d}u}{\mathrm{d}x}\right|^{\frac{1}{n}-1}\frac{\mathrm{d}u}{\mathrm{d}x} = \frac{1}{2}\rho\left(1-\frac{\rho}{\rho_\mathrm{w}}\right)gh, \quad \text{at } x = x_\mathrm{c}. \tag{5.6}$$

Actually, if one considers an ice shelf without lateral drag and restricts the domain to the grounded part Ω_g only, which we will do in this study, then this boundary condition can still be used, i.e.,

$$2A^{-\frac{1}{n}}\left|\frac{\mathrm{d}u}{\mathrm{d}x}\right|^{\frac{1}{n}-1}\frac{\mathrm{d}u}{\mathrm{d}x} = \frac{1}{2}\rho\left(1-\frac{\rho}{\rho_\mathrm{w}}\right)gh, \quad \text{at } x = x_\mathrm{gl}. \tag{5.7}$$

Indeed, the equation (5.2b) with $\Lambda = 0$ implies that the quantity

$$\left[2A^{-\frac{1}{n}}h\left|\frac{\mathrm{d}u}{\mathrm{d}x}\right|^{\frac{1}{n}-1}\frac{\mathrm{d}u}{\mathrm{d}x} - \frac{1}{2}\rho\left(1-\frac{\rho}{\rho_\mathrm{w}}\right)gh^2\right] \tag{5.8}$$

is conserved through the ice shelf.

5.2.2 Friction laws

Power-law friction laws

The simplest friction law is the Weertman friction law, for which τ_b is proportional to $|u|^p$ with $p > 0$ [Weertman, 1957]. Usually, $p = 1/3$ is chosen. To take into account effective pressure, one can use the so-called Budd friction law [Budd et al., 1979] for which

$$\tau_\mathrm{b} = CN^q\,|u|^{p-1}u, \tag{5.9}$$

with C a friction coefficient, N an effective pressure, and $p, q \geq 0$. Two elementary effective-pressure models are presented in subsection 5.2.2. The Budd friction law can be rewritten as a sliding law, i.e., the velocity can be written as a function of the basal friction stress:

$$u = C^{-\frac{1}{p}}N^{-\frac{q}{p}}|\tau_\mathrm{b}|^{\frac{1}{p}-1}\tau_\mathrm{b}. \tag{5.10}$$

It can also be noted that the law in (5.9) includes as a particular case the Weertman friction law if one sets $p = 1/3$ and $q = 0$.

Coulomb friction law

A Coulomb behavior assumes that there is a yield stress $\tau_\mathrm{y} = CN$ that must be reached for ice to be sliding:

$$\begin{cases} \tau_\mathrm{b} = CN\mathrm{sgn}(u), & \text{if } |u| > 0, \quad (5.11a) \\ |\tau_\mathrm{b}| \leq CN, & \text{if } u = 0. \quad (5.11b) \end{cases}$$

If the ice velocity is non-zero everywhere, then $\tau_\mathrm{b} = CN\mathrm{sgn}(u)$, which formally corresponds to a Budd friction law with $p = 0$ and $q = 1$. In the rest of this paper, we will always consider this case.

Hybrid friction laws

Tsai et al. [2015] have considered a hybrid law that combines the Weertman and Coulomb friction laws:

$$\tau_\mathrm{b} = \min(A_s^{-p}|u|^p, CN)\,\mathrm{sgn}(u), \tag{5.12}$$

with A_s a friction coefficient that controls the onset of the plastic behavior. Such a law was originally introduced in Schoof [2010a]. Smoothed versions have already been studied analytically and numerically [Schoof, 2005, 2010a; Gagliardini et al., 2007]. They take the following form:

$$\tau_\mathrm{b} = C\left(\frac{|u|}{|u| + A_sC^{\frac{1}{p}}N^{\frac{1}{p}}}\right)^p N\,\mathrm{sgn}(u), \tag{5.13}$$

or, by introducing $u_0 = A_sC^{\frac{1}{p}}N^{\frac{1}{p}}$,

$$\tau_\mathrm{b} = C\left(\frac{|u|}{|u| + u_0}\right)^p N\,\mathrm{sgn}(u). \tag{5.14}$$

This type of law, which exhibits viscoplastic behavior, is interesting from a modeling perspective because it can be used to include both form and skin drag, even if these are distinct mechanisms [Minchew and Joughin, 2020]. Form drag is associated with friction induced by ice deformation around obstacles and can be modeled with a power-law friction law, while skin drag is associated with friction induced by shear stress at the ice-bedrock interface, and can be modeled with a Coulomb friction law. Recently, Zoet and Iverson [2015, 2020] have shown that such laws are in good agreement with experimental results.

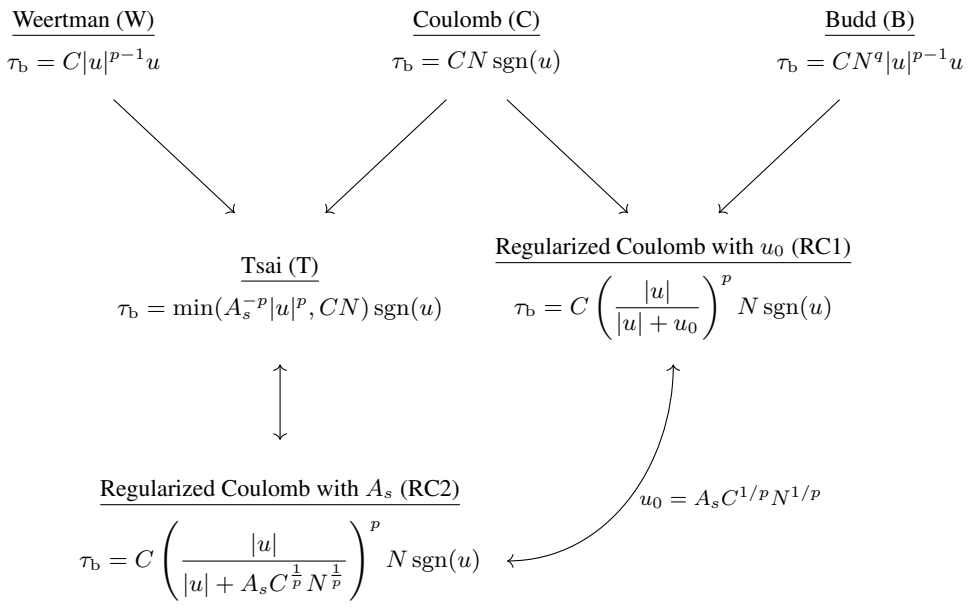

Figure 5.2: The considered friction models. The same notation C is used for the friction coefficient in every friction law although those coefficients are not necessarily comparable to one another.

Summary

The friction laws that we will consider in this article are shown in figure 5.2.

Effective pressure

Modeling effective pressure is complex. The effective pressure can be expected to depend on both the subglacial interface and the subglacial hydrology whose description is an active area of research [Flowers, 2015]. State-of-the-art hydrology models typically involve sets of partial differential equations that must be coupled with the ice-sheet model itself [Hewitt, 2013; Werder et al., 2013; Bueler and van Pelt, 2015]. Here, we will limit ourselves to very simple hydrology models that provide an explicit equation for the effective pressure $N = \rho g h - p_w$.

The first elementary effective-pressure model we consider consists in assuming that the bedrock below the ice sheet is perfectly permeable and connected to the nearby ocean, so that $N = \rho g h - p_w$ with p_w following a hydrostatic distribution: $p_w = \rho_w g \langle -b \rangle$. The second elementary effective-pressure model we consider consists in assuming a dependence of p_w on the ice-sheet thickness h, such as through a linear relation $p_w = c\,\rho g h$, with c a coefficient close to, but smaller than, one. We choose this model for its simplicity, and because similar parametrizations are common in ice-sheet models. For example, Bueler and Brown [2009] consider $p_w = 0.95\,\rho g h\,(w/w_c)$, with w the thickness of a subglacial water film and w_c a critical value of that thickness. Martin et al. [2011] consider $p_w = 0.96\,\lambda \rho g h$, with λ a parameter depending on the bedrock elevation that is such that $0 \leq \lambda \leq 1$. We acknowledge that such relations are usually used as parametrizations to close models, and they do not necessarily rely on the modeling of a physical phenomenon. For convenience, we name the first type of elementary effective-pressure model $\mathrm{N_A}$ and the second one $\mathrm{N_B}$.

5.2.3 Dimensionless formulation

We introduce scales $[x]$, $[h]$, $[u]$, and $[\tau_\mathrm{b}]$, leading to the following dimensionless variables:

$$\hat{x} = \frac{x}{[x]}, \quad \hat{h} = \frac{h}{[h]}, \quad \hat{b} = \frac{b}{[h]}, \quad \hat{u} = \frac{u}{[u]}, \quad \hat{\tau}_\mathrm{b} = \frac{\tau_\mathrm{b}}{[\tau_\mathrm{b}]}, \tag{5.15}$$

and to the following dimensionless ratios:

$$\alpha = \frac{a}{([u]/[x])[h]}, \quad \beta = \left(\frac{\mathrm{d}b}{\mathrm{d}x}\right)\frac{[x]}{[h]}, \quad \gamma = \frac{[\tau_\mathrm{b}][x]}{\rho g [h]^2}, \tag{5.16a}$$

$$\delta = \frac{\rho_\mathrm{w} - \rho}{\rho_\mathrm{w}}. \quad \varepsilon = \frac{A^{-\frac{1}{n}}[u]^{\frac{1}{n}}}{2\rho g [x]^{\frac{1}{n}}[h]}, \quad \lambda = \frac{\Lambda [u]^m [x]}{\rho g [h]^2}. \tag{5.16b}$$

These scales and ratios should be characteristic of ice streams. The problem can be further simplified by choosing the scales so that additional constraints on the dimensionless ratios are enforced, e.g., by setting some of them to a unit value. However, we postpone these assumptions to a later stage, where the context will provide justification for them. We also introduce the dimensionless flotation thickness $\hat{h}_\mathrm{b}$ as $\hat{h}_\mathrm{b} = (1-\delta)^{-1}\hat{b}$. With these notations, the governing equations become

$$\frac{\mathrm{d}}{\mathrm{d}\hat{x}}(\hat{u}_\mathrm{g}\,\hat{h}_\mathrm{g}) = \alpha, \tag{5.17a}$$

$$4\,\varepsilon\,\frac{\mathrm{d}}{\mathrm{d}\hat{x}}\left(\hat{h}_\mathrm{g}\left|\frac{\mathrm{d}\hat{u}_\mathrm{g}}{\mathrm{d}\hat{x}}\right|^{\frac{1}{n}-1}\frac{\mathrm{d}\hat{u}_\mathrm{g}}{\mathrm{d}\hat{x}}\right) - \gamma\,\hat{\tau}_\mathrm{b} - \lambda\,\hat{h}_\mathrm{g}|\hat{u}_\mathrm{g}|^{m-1}\hat{u}_\mathrm{g} = \hat{h}_\mathrm{g}\left(\frac{\mathrm{d}\hat{h}_\mathrm{g}}{\mathrm{d}\hat{x}} + \beta\right), \tag{5.17b}$$

for $0 < \hat{x} < \hat{x}_\mathrm{gl}$,

$$\hat{h}_\mathrm{g} = \hat{h}_\mathrm{f}, \quad \hat{u}_\mathrm{g} = \hat{u}_\mathrm{f}, \quad \hat{h}_\mathrm{g}\left|\frac{\mathrm{d}\hat{u}_\mathrm{g}}{\mathrm{d}x}\right|^{\frac{1}{n}-1}\frac{\mathrm{d}\hat{u}_\mathrm{g}}{\mathrm{d}x} = \hat{h}_\mathrm{f}\left|\frac{\mathrm{d}\hat{u}_\mathrm{f}}{\mathrm{d}x}\right|^{\frac{1}{n}-1}\frac{\mathrm{d}\hat{u}_\mathrm{f}}{\mathrm{d}x}, \tag{5.18}$$

at $\hat{x} = \hat{x}_\mathrm{gl}$,

$$\frac{\mathrm{d}}{\mathrm{d}\hat{x}}(\hat{u}_\mathrm{f}\,\hat{h}_\mathrm{f}) = \alpha, \tag{5.19a}$$

$$4\,\varepsilon\,\frac{\mathrm{d}}{\mathrm{d}\hat{x}}\left(\hat{h}_\mathrm{f}\left|\frac{\mathrm{d}\hat{u}_\mathrm{f}}{\mathrm{d}\hat{x}}\right|^{\frac{1}{n}-1}\frac{\mathrm{d}\hat{u}_\mathrm{f}}{\mathrm{d}\hat{x}}\right) - \lambda\,\hat{h}_\mathrm{f}|\hat{u}_\mathrm{f}|^{m-1}\hat{u}_\mathrm{f} = \delta\,\hat{h}_\mathrm{f}\frac{\mathrm{d}\hat{h}_\mathrm{f}}{\mathrm{d}\hat{x}}, \tag{5.19b}$$

for $\hat{x}_\mathrm{gl} < \hat{x} < \hat{x}_\mathrm{c}$, with the following boundary conditions:

$$\hat{u} = 0, \quad at \hat{x} = 0, \tag{5.20a}$$

$$\left|\frac{\mathrm{d}\hat{u}}{\mathrm{d}\hat{x}}\right|^{\frac{1}{n}-1}\frac{\mathrm{d}\hat{u}}{\mathrm{d}\hat{x}} = \frac{\delta\hat{h}}{8\,\varepsilon}, \quad \text{at } \hat{x} = \hat{x}_\mathrm{gl}, \tag{5.20b}$$

$$\hat{h} = \hat{h}_\mathrm{b}, \quad \text{at } \hat{x} = \hat{x}_\mathrm{gl}. \tag{5.20c}$$

5.2.4 Flux conditions

A flux condition is an expression of the grounding-line flux $q_\mathrm{gl} \equiv h(x_\mathrm{gl})u(x_\mathrm{gl})$ as a function of the different physical parameters A, C, ... that appear in the problem formulation. Such an expression usually takes the form of an approximation that is valid within an asymptotic regime associated with the magnitude of the previously introduced dimensionless ratios. Historically, the first flux condition was derived by Schoof [2007c] for the Weertman friction law. They considered an unbuttressed ice sheet, i.e., $\lambda = 0$,

a scaling and a bed geometry such that $\alpha \sim 1$, $\gamma \sim 1$, and $|\beta| \lesssim 1$, and they assumed that $\varepsilon \ll 1$ and $\delta \ll 1$. Tsai et al. [2015] derived a flux condition under the same assumptions, but for the Coulomb friction law. They showed that the resulting flux condition was more sensitive compared to one derived by Schoof [2007c]. The importance of buttressing, i.e., the case $\lambda \neq 0$, was discussed by Pegler [2016, 2018a,b], Schoof et al. [2017], and Haseloff and Sergienko [2018, 2022]. They showed that taking into account lateral drag could significantly change the dynamics of ice sheets, in particular by modifying the stability criterion that was previously derived for unbuttressed ice sheets [Schoof, 2012]. The regime of low basal stress, $\gamma \ll 1$, was covered by Sergienko and Wingham [2019]. The same authors also discussed the importance of α and β, showing that the so-called marine-ice sheet instability hypothesis was not applicable in general [Sergienko and Wingham, 2022; Sergienko, 2022b]. Schoof et al. [2017] studied the impact that calving laws have on the flux conditions. All these authors, except Tsai et al. [2015], have considered the Weertman friction law in their studies. Recently, Sergienko and Haseloff [2023] studied the notion of stability of marine ice sheets submitted to a climate forcing for a broad class of friction laws. However, they did not derive flux conditions for the configuration studied in the present paper, which we describe hereafter.

In this paper, we derive flux conditions for the Budd friction law with two elementary effective-pressure models, and show how they can be extended to hybrid friction laws. We will use the same assumptions that were done by Schoof [2007c] and Tsai et al. [2015], namely, we consider an unbuttressed ice sheet ($\lambda = 0$), scales that are such that α, β, and γ are at most of order $\mathcal{O}(1)$, and consider the asymptotic regimes $\varepsilon \ll 1$ and $\delta \ll 1$. We will discuss in a later section the validity of these hypotheses, and we will show how the flux conditions can be modified to remain valid in the event that α, β, and γ are not small or moderate.

5.3 Generalization to the Budd friction law

We now proceed to the derivation of a flux condition for the Budd friction law, that is, we consider a friction law belonging to the family of friction laws $\tau_\mathrm{b} = CN^q|u|^{p-1}u$, where the effective pressure N obeys one of the two elementary models previously introduced. We assume that $n = 3$, $0 \leq p \leq 1/3$, and $0 \leq q \leq 1$, which holds for commonly used values. We assume that all the variables that appear are constant, except x and the functions b, h, u, and N, which depend on this coordinate. We base our derivation on the ideas that Schoof [2007c] and Tsai et al. [2015] have developed for the Weertman and the Coulomb friction laws, and we show that they can be extended to the present context.

We introduce the dimensionless effective pressure as $\hat{N} = N/[N]$ where the scale $[N]$ is related to the scales $[h]$ and $[\tau_\mathrm{b}]$ as follows:

$$[N] = \begin{cases} \rho g[h] & (\mathrm{N_A}\text{ model}), \\ (1-c)\rho g[h] & (\mathrm{N_B}\text{ model}), \end{cases} \quad \text{and} \quad [\tau_\mathrm{b}] = C[u]^p[N]^q. \tag{5.21}$$

We neglect lateral drag ($\lambda = 0$) and consider scales that are such that

$$\alpha = 1, \quad \gamma = 1, \quad \text{and} \quad |\beta| \lesssim 1. \tag{5.22}$$

With these considerations, the following problem is obtained:

$$\frac{\mathrm{d}}{\mathrm{d}\hat{x}}(\hat{u}\,\hat{h}) = 1, \quad \text{for } 0 < \hat{x} < \hat{x}_{\mathrm{gl}}, \tag{5.23a}$$

$$4\,\varepsilon\,\frac{\mathrm{d}}{\mathrm{d}\hat{x}}\left(\hat{h}\left|\frac{\mathrm{d}\hat{u}}{\mathrm{d}\hat{x}}\right|^{\frac{1}{n}-1}\frac{\mathrm{d}\hat{u}}{\mathrm{d}\hat{x}}\right) - (\hat{h} - 1_{\mathrm{A}}\langle\hat{h}_{\mathrm{b}}\rangle)^{q}|\hat{u}|^{p-1}\hat{u} - \hat{h}\left(\frac{\mathrm{d}\hat{h}}{\mathrm{d}\hat{x}} + \beta\right) = 0, \quad \text{for } 0 < \hat{x} < \hat{x}_{\mathrm{gl}}, \tag{5.23b}$$

$$\hat{u} = 0, \quad \text{at } \hat{x} = 0, \tag{5.23c}$$

$$\left|\frac{\mathrm{d}\hat{u}}{\mathrm{d}\hat{x}}\right|^{\frac{1}{n}-1}\frac{\mathrm{d}\hat{u}}{\mathrm{d}\hat{x}} = \frac{\delta\hat{h}}{8\,\varepsilon}, \quad \text{at } \hat{x} = \hat{x}_{\mathrm{gl}}, \tag{5.23d}$$

$$\hat{h} = \hat{h}_{\mathrm{b}}, \quad \text{at } \hat{x} = \hat{x}_{\mathrm{gl}}, \tag{5.23e}$$

in which $1_{\mathrm{A}} = 1$ for the $\mathrm{N_A}$ model, and $1_{\mathrm{A}} = 0$ for the $\mathrm{N_B}$ model.

5.3.1 Derivation of the flux condition

Equivalent dynamical system for the boundary-layer problem

One can expand the unknown fields as powers of ε and keep the leading-order terms because ε is typically very small – about 10^{-3} for commonly used values of the physical parameters. One then expects an equilibrium between the friction and gravity terms in (5.23b), with the divergence of membrane stress which can be neglected. However, this balance fails in two cases. If δ is such that $\varepsilon \ll \delta$, then the Neumann boundary condition (5.23d) at the grounding line cannot be fulfilled. This hints at the existence of a boundary layer near the grounding line, in which the membrane-stress divergence becomes relatively important. Furthermore, if the friction stress reaches a zero value at the grounding line (e.g., if $1_{\mathrm{A}} = 1$ and $q \neq 0$), then all the terms appearing in (5.23b) must become very small close to the grounding line, leading again to a boundary layer. In what follows, we place ourselves in one of these two cases so that we expect the presence of a boundary layer close to the grounding line.

To solve a very similar problem, Schoof [2007c] and Tsai et al. [2015] used the method of matched asymptotics: the solution inland, known as *outer solution* was matched with the so-called *inner solution* associated with the boundary layer. To obtain this inner solution, they introduced a scaling of the form

$$\hat{x}_{\mathrm{gl}} - \hat{x} = \varepsilon^{\kappa_x} X, \quad \hat{h} = \varepsilon^{\kappa_h} H, \quad \hat{h}_{\mathrm{b}} = \varepsilon^{\kappa_h} H_{\mathrm{b}}, \quad \hat{b} = \varepsilon^{\kappa_h} B, \quad \hat{u} = \varepsilon^{\kappa_u} U, \tag{5.24}$$

where κ_x, κ_h, and κ_u are chosen in a such way that the divergence of membrane stress, the friction stress, and the gravity stress are of the same order of magnitude near the grounding line; in other words, they are of all of order $\mathcal{O}(\varepsilon^{\kappa})$ for a same exponent κ. Furthermore, they are chosen such that the flux $Q = HU$ is $\mathcal{O}(1)$ at the grounding line. This leads in the current context to the following exponent values:

$$\kappa_x = \frac{n(p-q+2)}{n+(p-q)+3}, \quad \kappa_u = -\frac{n}{n+(p-q)+3}, \quad \kappa_h = \frac{n}{n+(p-q)+3}. \tag{5.25}$$

We remark that with the assumed values for n, p, and q, we have $\kappa_x > 0$, $\kappa_u < 0$, and $\kappa_h > 0$. At leading order, the flux Q is then constant within the boundary layer, and we replace it by the grounding-line flux Q_{gl}.

The inner problem can be further transformed. As in Schoof [2007c] and Tsai et al. [2015], the solution to the inner problem is written as a trajectory of a 2D dynamical system of the form $\tilde{X} \mapsto (\tilde{U}, \tilde{W})$, where $\tilde{X}$, $\tilde{U}$, and $\tilde{W}$ are respectively a scaled spatial coordinate, a scaled velocity, and a scaled

membrane stress, thus allowing the dynamics of the system to be interpreted in the phase plane $(\tilde{U}, \tilde{W})$. To obtain this dynamical system, the following change of variables is introduced:

$$X = H_{\mathrm{gl}}{}^{\frac{2-q-np}{p+1}}\tilde{X},\quad U = H_{\mathrm{gl}}{}^{\frac{2-q+n}{p+1}}\tilde{U},\quad -|U_X|^{\frac{1}{n}-1}U_X = H_{\mathrm{gl}}\tilde{W},\quad Q_{\mathrm{gl}} = H_{\mathrm{gl}}{}^{\frac{n+(p-q)+3}{p+1}}\tilde{Q}_{\mathrm{gl}}. \tag{5.26}$$

At leading order, the following leading-order system is then obtained:

$$\frac{\mathrm{d}\tilde{U}}{\mathrm{d}\tilde{X}} = -|\tilde{W}|^{n-1}\tilde{W}, \quad \text{for } \tilde{X} > 0, \tag{5.27a}$$

$$\frac{\mathrm{d}\tilde{W}}{\mathrm{d}\tilde{X}} = -\frac{|\tilde{W}|^{n+1}}{\tilde{U}} - \frac{1}{4}\frac{\tilde{U}}{\tilde{Q}_{\mathrm{gl}}}\left(\frac{\tilde{Q}_{\mathrm{gl}}}{\tilde{U}} - 1_{\mathrm{A}}\right)^{q}|\tilde{U}|^{p-1}\tilde{U} + \frac{\tilde{Q}_{\mathrm{gl}}|\tilde{W}|^{n-1}\tilde{W}}{4\,\tilde{U}^2}, \quad \text{for } \tilde{X} > 0, \tag{5.27b}$$

$$(\tilde{U}, \tilde{W}) = (\tilde{Q}_{\mathrm{gl}}, \delta/8), \quad \text{at } \tilde{X} = 0, \tag{5.27c}$$

$$(\tilde{U}, \tilde{W}) \to (0, 0), \quad \text{as } \tilde{X} \to +\infty. \tag{5.27d}$$

Equation (5.27d) is a matching condition and follows from the the fact that the inner and outer solution must be of the same order in an intermediate region. Because $U = \hat{u}\,\varepsilon^{-\kappa_u}$ and the outer solution is such that $\hat{u} \sim 1$, we must enforce $U \to 0$, and therefore $\tilde{U} \to 0$, outside of the boundary layer. Similarly, $U_X = \mathcal{O}(\varepsilon^{\kappa_x - \kappa_u})$, and thus $\tilde{W} \to 0$ outside of it.

Flux condition

The rescaled flux at the grounding line, $\tilde{Q}_{\mathrm{gl}}$, appears as a free parameter in (5.27). In the following section we will provide a justification for the existence of a trajectory that follows the flow defined by (5.27a)–(5.27b) and satisfies the boundary condition (5.27c) for a unique value of $\tilde{Q}_{\mathrm{gl}}$ dependent on the effective-pressure model and the parameters n, p, q, and δ. Then,

$$\tilde{Q}_{\mathrm{gl}} \equiv \tilde{Q}_{\mathrm{gl}}(1_{\mathrm{A}}, n, p, q, \delta). \tag{5.28}$$

This numerical value can be computed using the numerical method described in the appendix B. Using (5.26), it is possible to switch back to the original variables. The flux at the grounding line is then given by the following expressions, for the $\mathrm{N_A}$ and $\mathrm{N_B}$ effective-pressure models, respectively:

$$q_{\mathrm{gl}} = \tilde{Q}_{\mathrm{gl}}\,(\rho g)^{-\frac{q-1}{p+1}}(2\rho g)^{\frac{n}{p+1}}C^{-\frac{1}{p+1}}A^{\frac{1}{p+1}}h_{\mathrm{gl}}^{\frac{n+(p-q)+3}{p+1}}, \tag{5.29a}$$

$$q_{\mathrm{gl}} = \tilde{Q}_{\mathrm{gl}}\,(\rho g)^{-\frac{q-1}{p+1}}(2\rho g)^{\frac{n}{p+1}}[C(1-c)^q]^{-\frac{1}{p+1}}A^{\frac{1}{p+1}}h_{\mathrm{gl}}^{\frac{n+(p-q)+3}{p+1}}. \tag{5.29b}$$

Impact of the relative ice-water density difference

Tsai et al. [2015] also showed a way to derive the approximate dependence of $\tilde{Q}_{\mathrm{gl}}$ on δ. The idea is to remark that if δ is treated as a small parameter in (5.27), then $\tilde{U}_{\tilde{X}} \approx 0$ within the boundary layer. This observation supports the introduction of a new scaling so that this term becomes $\mathcal{O}(1)$ at the grounding line. With

$$\tilde{X} = (\delta/8)^{r_1}\check{X},\quad \tilde{Q}_{\mathrm{gl}} = (\delta/8)^{r_2}\check{Q}_{\mathrm{gl}},\quad \tilde{U} = (\delta/8)^{r_2}[\check{Q} - (\delta/8)\check{U}],\quad \tilde{W} = (\delta/8)\check{W}, \tag{5.30}$$

a distinguished limit can be obtained, in which the dominant powers of δ balance each other. For the $\mathrm{N_A}$ model, a distinguished limit is achieved for

$$r_1 = [(p-q+1) - np]/(p+1) \quad \text{and} \quad r_2 = (n-q)/(p+1). \tag{5.31}$$

For the $\mathrm{N_B}$ model, a distinguished limit is obtained for

$$r_1 = [(p+1) - np]/(p+1) \quad \text{and} \quad r_2 = n/(p+1). \tag{5.32}$$

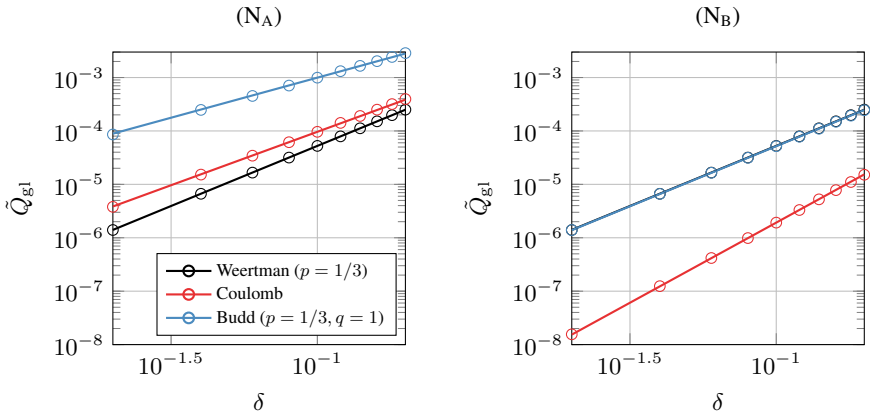

Figure 5.3: Comparison between values of $\tilde{Q}_{\mathrm{gl}}$ obtained numerically (circles) and the scaling $\tilde{Q}_{\mathrm{gl}} \propto (\delta/8)^{r_2}$ (lines) for several friction laws and effective-pressure models. The lines obey the equation $\tilde{Q}_{\mathrm{gl}} = \tilde{Q}_{\mathrm{gl}}|_{\delta=0.1}\,(\delta/0.1)^{r_2}$ with $r_2 = (n - 1_{\mathrm{A}}q)/(p+1)$. In the right plot, the Weertman and the Budd results coincide, as expected.

Finally, the following flux at the grounding line is obtained for the $\mathrm{N_A}$ and $\mathrm{N_B}$ effective-pressure models:

$$q_{\mathrm{gl}} = \check{Q}_{\mathrm{gl}} \left(\frac{1-\rho/\rho_{\mathrm{w}}}{8}\right)^{\frac{n-q}{p+1}} (\rho g)^{-\frac{q-1}{p+1}} (2\rho g)^{\frac{n}{p+1}} C^{-\frac{1}{p+1}} A^{\frac{1}{p+1}} h_{\mathrm{gl}}^{\frac{n+(p-q)+3}{p+1}}, \tag{5.33a}$$

$$q_{\mathrm{gl}} = \check{Q}_{\mathrm{gl}} \left(\frac{1-\rho/\rho_{\mathrm{w}}}{8}\right)^{\frac{n}{p+1}} (\rho g)^{-\frac{q-1}{p+1}} (2\rho g)^{\frac{n}{p+1}} [C(1-c)^q]^{-\frac{1}{p+1}} A^{\frac{1}{p+1}} h_{\mathrm{gl}}^{\frac{n+(p-q)+3}{p+1}}. \tag{5.33b}$$

This scaling $\tilde{Q}_{\mathrm{gl}} = (\delta/8)^{r_2}\check{Q}_{\mathrm{gl}}$, that is, the way in which $\tilde{Q}_{\mathrm{gl}}$ depends on δ, is verified numerically in figure 5.3.

5.3.2 Analysis of the leading-order dynamical system

We now consider the analysis of the dynamical system governed by the system of equations (5.27). More precisely, we motivate the existence of a solution for a unique value of the grounding-line flux $\tilde{Q}_{\mathrm{gl}}$ by considering separately the case where the friction stress vanishes, or not, at the grounding line.

Strategy

To study the leading-order dynamical system, we first rewrite the system of equations in a way that allows the dynamics close to the origin in the $(\tilde{U}, \tilde{W})$ phase plane, i.e., for $\tilde{X} \to +\infty$, to be studied. To this end, we rewrite this system in terms of new variables $\mathcal{X}$, ξ, Ψ, and $\mathcal{Q}_{\mathrm{gl}}$. The interpretation of these variables is the following: $\mathcal{X}$ plays the role of a spatial coordinate, ξ is a rescaled velocity, Ψ is a measure of the ratio of friction stress over gravity stress, and $\mathcal{Q}_{\mathrm{gl}}$ is a rescaled grounding-line flux. The specific form that these variables take will be described separately for the case in which friction vanishes at the grounding

line, and the case in which it does not. A problem of the following form is then be obtained:

$$\frac{\mathrm{d}\xi}{\mathrm{d}\mathcal{X}} = F_\xi(\xi, \Psi, \mathcal{X}; \mathcal{Q}_{\mathrm{gl}}), \quad \text{for } \mathcal{X} > 0, \tag{5.34a}$$

$$\frac{\mathrm{d}\Psi}{\mathrm{d}\mathcal{X}} = F_\Psi(\xi, \Psi, \mathcal{X}; \mathcal{Q}_{\mathrm{gl}}), \quad \text{for } \mathcal{X} > 0, \tag{5.34b}$$

$$(\xi, \Psi) = (G_\xi(\mathcal{Q}_{\mathrm{gl}}), G_\Psi(\mathcal{Q}_{\mathrm{gl}})), \quad \text{at } \mathcal{X} = 0, \tag{5.34c}$$

$$(\xi, \Psi) \to (0, 1), \quad \text{as } \mathcal{X} \to +\infty. \tag{5.34d}$$

We then identify the point $(\xi, \Psi) = (0, 1)$ as a fixed point, and study the dynamics of the flow defined by (5.34a) and (5.34b) close to that point. It turns out that the only way to reach the fixed point is through a center manifold that is unique. Therefore, if a solution to the problem defined by (5.34) exists, it necessarily goes through this center manifold. The question then amounts to finding whether an orbit that reaches this center manifold, i.e., that obeys (5.34a), (5.34b), and (5.34d), can satisfy the boundary condition (5.34c). This last condition is in fact satisfied for exactly one value of the grounding-line flux $\mathcal{Q}_{\mathrm{gl}}$. To show this, we introduce a mapping D as follows:

$$D : \ ]0, +\infty[\to \mathbb{R} : \quad \mathcal{Q}_{\mathrm{gl}} \mapsto D(\mathcal{Q}_{\mathrm{gl}}) \equiv f(\mathcal{Q}_{\mathrm{gl}}) \left[\Psi^{\mathrm{c}}(G_\xi(\mathcal{Q}_{\mathrm{gl}}); \mathcal{Q}_{\mathrm{gl}}) - G_\Psi(\mathcal{Q}_{\mathrm{gl}})\right], \tag{5.35}$$

in which f is a strictly positive or a strictly negative function and $\Psi^{\mathrm{c}}(\xi, \mathcal{Q}_{\mathrm{gl}})$ is the Ψ coordinate of the center manifold at position ξ. To satisfy (5.34c), it is then necessary and sufficient that $D(\mathcal{Q}_{\mathrm{gl}}) = 0$ for some $\mathcal{Q}_{\mathrm{gl}}$. If, in addition, D is a strictly monotonic function, then this root is unique. Overall, this means that there is exactly one value of $\mathcal{Q}_{\mathrm{gl}}$ that leads to a solution of (5.34), and the solution to the leading-order dynamical system exists and is unique.

To simplify the notations in what follows, we define c_1 and c_2 by

$$c_1 = 1 + (p - q + 3)/n \quad \text{and} \quad c_2 = 1 - (p - q + 3)/n. \tag{5.36}$$

We note that for the assumed ranges of values of n, p, and q, the following inequalities hold:

$$c_1 > 1 \quad \text{and} \quad -1 < c_2 < 1. \tag{5.37}$$

Non-vanishing friction at the grounding line

We first consider the case of a non-vanishing friction stress at the grounding line, that is, a friction model with either an exponent $q = 0$, so that there is no dependence with respect to the effective pressure, or with the $\mathrm{N_B}$ effective-pressure model. We note that this case shares similarities with the study considered in Schoof et al. [2017], where the authors have included a lateral drag term in their momentum balance. This term is of the form $\Lambda\, h\, |u|^{m-1} u$, which is analogous to a Budd friction law with $p = m$, $q = 1$, and the $\mathrm{N_B}$ effective-pressure model. In fact, it can be noted that the Budd friction law taken with the $\mathrm{N_B}$ effective-pressure model is effectively equivalent to considering a friction term dominated by lateral drag.

We introduce ξ, Ψ and $\mathcal{Q}_{\mathrm{gl}}$ as

$$\xi = \tilde{Q}_{\mathrm{gl}}^{\frac{q-2}{n}-1} \tilde{U}^{c_1}, \quad \Psi = \tilde{Q}_{\mathrm{gl}}^{-\frac{q-2}{n}} \tilde{W}\, \tilde{U}^{1-c_1}, \quad \mathcal{Q}_{\mathrm{gl}} = \tilde{Q}_{\mathrm{gl}}^{\frac{p+1}{n}}, \tag{5.38}$$

and $\mathcal{X}$ as

$$\mathcal{X} = \int_0^{\tilde{X}} s\left(\xi(X), \Psi(X)\right) \mathrm{d}X, \quad s(\xi, \Psi) = \tilde{Q}_{\mathrm{gl}}^{\frac{q-2+np}{n\, c_1}} \xi^{\frac{n(p-q)-(p-q+3)+n}{(p-q+3)+n}} |\Psi|^{n-1} \Psi. \tag{5.39}$$

The system (5.27) then becomes

$$\frac{\mathrm{d}\xi}{\mathrm{d}\mathcal{X}} = -c_1\,\xi^2, \quad \text{for } \mathcal{X} > 0, \tag{5.40a}$$

$$\frac{\mathrm{d}\Psi}{\mathrm{d}\mathcal{X}} = -c_2\,\xi\Psi - \frac{1}{4}|\Psi|^{-n-1}\Psi + \frac{1}{4}, \quad \text{for } \mathcal{X} > 0, \tag{5.40b}$$

$$(\xi, \Psi) = (\mathcal{Q}_{\mathrm{gl}}, \mathcal{Q}_{\mathrm{gl}}^{-1}\delta/8), \quad \text{at } \mathcal{X} = 0, \tag{5.40c}$$

$$(\xi, \Psi) \to (0, 1), \quad \text{as } \mathcal{X} \to +\infty. \tag{5.40d}$$

It can be remarked that $\mathcal{Q}_{\mathrm{gl}}$ completely disappears from the differential equations and is only present in the boundary conditions. This system is similar to the system considered by Schoof [2011], where they considered the Weertman friction law. The only differences are the values of the parameters c_1 and c_2 which, in our case, could depend on q if we consider the $\mathrm{N_B}$ effective-pressure model. The method used in Schoof [2011] to show the existence and uniqueness of a solution can still be applied. We briefly describe it, the calculations being analogous.

The idea of Schoof [2011] to show existence and uniqueness properties of a similar system is to consider the characterization of $(\xi, \Psi) = (0, 1)$ as a fixed point that can only be reached through a center manifold that is unique, as well as the evolution of the product $\Psi\,\xi$ along that manifold. They showed that this product was equal to zero at the fixed point, and increasing without bound for increasing values of ξ along that orbit. It then follows that there is exactly one value of $\mathcal{Q}_{\mathrm{gl}}$ that satisfies (5.40c), which shows the existence and uniqueness of a solution. These ideas can still be applied to the more general case that is considered here.

The reasoning can also be made with respect to the mapping D defined in (5.35) by choosing $f(\mathcal{Q}_{\mathrm{gl}}) = \mathcal{Q}_{\mathrm{gl}}$. Indeed, the center manifold is independent of $\mathcal{Q}_{\mathrm{gl}}$, so $\Psi^{\mathrm{c}}(\xi; \mathcal{Q}_{\mathrm{gl}}) \equiv \Psi^{\mathrm{c}}(\xi)$. Furthermore, the mapping $\xi \mapsto \xi\,\Psi^{\mathrm{c}}(\xi)$ increases without bound with ξ. Therefore, the mapping

$$\mathcal{Q}_{\mathrm{gl}} \quad \mapsto \quad D(\mathcal{Q}_{\mathrm{gl}}) = \mathcal{Q}_{\mathrm{gl}}\Psi^{\mathrm{c}}(\mathcal{Q}_{\mathrm{gl}}) - (\delta/8) \tag{5.41}$$

also increases without bound with $\mathcal{Q}_{\mathrm{gl}}$. Because $\xi\,\Psi^{\mathrm{c}}(\xi) = 0$ for $\xi = 0$, we also have $D(0) = -\delta/8 < 0$. Hence, D has exactly one root, which concludes the discussion.

Vanishing friction at the grounding line

We now consider friction laws that vanish at the grounding line, namely friction laws that involve the $\mathrm{N_A}$ effective-pressure model (in particular, we consider that $q \neq 0$). In that case, it cannot be shown that the product $\Psi\,\xi$ increases monotonically with ξ along an orbit that reaches the center manifold. Geometrically, the hyperbola $\Psi = (\delta/8)/\xi$ will not necessarily intersect the solution trajectory at a single location.

We propose another strategy. Specifically, we consider another change of variables for ξ, namely, $\xi = (\tilde{U}/\tilde{Q}_{\mathrm{gl}})^{\frac{1}{2}}$, and we take $f(\mathcal{Q}_{\mathrm{gl}}) = 1$ in (5.35). This change of variables is similar to the one described in the supplementary material of Schoof et al. [2017]. We will also limit ourselves to the Budd friction law with a linear dependence with respect to the effective pressure, that is, $q = 1$. For that value,

we note that $c_2 > 0$. The system (5.27) then becomes

$$\frac{\mathrm{d}\xi}{\mathrm{d}\mathcal{X}} = -\frac{1}{2}\mathcal{Q}_{\mathrm{gl}}\,\xi^{2c_1+1}, \quad \text{for } \mathcal{X} > 0, \tag{5.42a}$$

$$\frac{\mathrm{d}\Psi}{\mathrm{d}\mathcal{X}} = -c_2\,\mathcal{Q}_{\mathrm{gl}}\xi^{2c_1}\Psi - \frac{1}{4}|\Psi|^{-n-1}\Psi\left(1-\xi^2\right) + \frac{1}{4}, \quad \text{for } \mathcal{X} > 0, \tag{5.42b}$$

$$(\xi, \Psi) = (1, \mathcal{Q}_{\mathrm{gl}}^{-1}\delta/8), \quad \text{at } \mathcal{X} = 0, \tag{5.42c}$$

$$(\xi, \Psi) \to (0, 1), \quad \text{as } \mathcal{X} \to +\infty, \tag{5.42d}$$

and the mapping D becomes

$$\mathcal{Q}_{\mathrm{gl}} \quad \mapsto \quad D(\mathcal{Q}_{\mathrm{gl}}) = \Psi^{\mathrm{c}}(1; \mathcal{Q}_{\mathrm{gl}}) - (\delta/8)\mathcal{Q}_{\mathrm{gl}}^{-1}. \tag{5.43}$$

As before, the only fixed point in the system is the point $(\xi, \Psi) = (0, 1)$, which corresponds to the boundary condition (5.42d). We can again determine that the only way to reach this point is through a center manifold. In contrast to the previous case, $\mathcal{Q}_{\mathrm{gl}}$ appears in the definition of the flow defined by (5.42a) and (5.42b), so the center manifold depends on $\mathcal{Q}_{\mathrm{gl}}$. To demonstrate that D possesses exactly one root, we then show, based on asymptotic expansions, that the following properties hold: (i) D is a continuous mapping, (ii) $\mathrm{d}D/\mathrm{d}\mathcal{Q}_{\mathrm{gl}} > 0$ for all $\mathcal{Q}_{\mathrm{gl}} > 0$, (iii) $\lim_{\mathcal{Q}_{\mathrm{gl}}\to+\infty} D(\mathcal{Q}_{\mathrm{gl}}) > 0$, and (iv) $D(\delta/8) < 0$. The details of this analysis can be found in the appendix A.

5.3.3 Existence of a boundary layer

It can be remarked that, for some configurations, we obtain $\check{Q}_{\mathrm{gl}} \approx 1$. In fact, these configurations are those that are such that friction at the grounding line does not vanish, i.e., they correspond to a friction law with $q = 0$, or with $q > 0$ but with the effective-pressure model $\mathrm{N_B}$. In that case, no boundary layer is needed close to the grounding line, and the membrane-stress divergence can be neglected. Indeed, the flux condition can be obtained by simply combining a balance between the friction and the gravity stresses and the boundary conditions at the grounding line. For the Budd friction law, that approach yields

$$CN^q u^p \approx -\rho g h \frac{\mathrm{d}}{\mathrm{d}x}(b+h)\,. \tag{5.44}$$

With the assumption that the bedrock slope $\mathrm{d}b/\mathrm{d}x$ is negligible ($|\beta| \lesssim 1$) and that the flux divergence $\mathrm{d}q_{\mathrm{adv}}/\mathrm{d}x$ is not too large ($\alpha = 1$), and in particular much smaller than $q_{\mathrm{adv}}(\mathrm{d}u/\mathrm{d}x)/u$, we have

$$\frac{\mathrm{d}}{\mathrm{d}x}(b+h) \approx \frac{\mathrm{d}h}{\mathrm{d}x} \approx q_{\mathrm{adv}}\frac{\mathrm{d}}{\mathrm{d}x}\left(\frac{1}{u}\right). \tag{5.45}$$

Using this relation in (5.44) and combining it with the grounding-line boundary condition (5.7) leads to the following relation at the grounding line:

$$CN^q\left(\frac{q_{\mathrm{gl}}}{h_{\mathrm{gl}}}\right)^p \approx \rho g \frac{h_{\mathrm{gl}}^3}{q_{\mathrm{gl}}}\left(\frac{1}{4}\rho\left(1-\frac{\rho}{\rho_{\mathrm{w}}}\right)g\right)^n h_{\mathrm{gl}}^n\,A, \tag{5.46}$$

that is,

$$q_{\mathrm{gl}} \approx \left(\frac{\rho g}{C}\right)^{\frac{1}{p+1}} N^{-\frac{q}{p+1}}\left(\frac{1}{4}\rho\left(1-\frac{\rho}{\rho_{\mathrm{w}}}\right)g\right)^{\frac{n}{p+1}} A^{\frac{1}{p+1}} h_{\mathrm{gl}}^{\frac{n+p+3}{p+1}}. \tag{5.47}$$

This relation corresponds to our flux condition (5.33b) with $\check{Q}_{\mathrm{gl}} \approx 1$, as announced. In fact, the observation that the membrane-stress divergence can be neglected to derive the flux condition has been remarked by Schoof [2007c, 2011] in their derivation for the Weertman friction law, and later by Sergienko and Wingham [2022] who revisited their boundary-layer analysis. In particular, Sergienko and Wingham

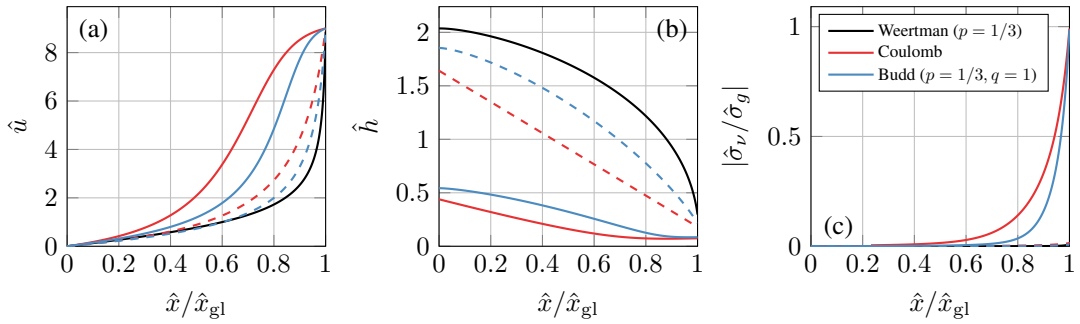

Figure 5.4: Solutions to the dimensionless problem for various friction laws, with the $\mathrm{N_A}$ (continuous lines) and the $\mathrm{N_B}$ effective pressure-model (dashed lines): **(a)** velocity, **(b)** thickness, and **(c)** ratio of the membrane-stress divergence and the gravity stress.

[2022] have shown that for $\varepsilon \ll \delta$, which is what is assumed here, the boundary layer is very weak, and this observation can be explained by the non-linearity of the governing equations. Furthermore, the boundary layer will become increasingly weak as δ becomes smaller.

However, this analysis is not valid for a combination of friction law and effective-pressure model that are such that friction stress vanishes at the grounding line. For these configurations, there is another stress regime in the vicinity of the grounding line. In our analysis, this takes the form of a boundary layer, which is necessary to obtain the correct flux condition. If it was not the case, then one would obtain $\check{Q}_{\mathrm{gl}} = 1$. It follows that the fact that $\check{Q}_{\mathrm{gl}}$ takes a value distinct from unity reflects the importance of membrane-stress divergence in the boundary layer. This key observation was already made by Tsai et al. [2015] for the Coulomb law, and is here confirmed for the more general Budd friction law.

The distinction between these two distinct behaviors can be observed in solutions to the different formulations of the problem that arise in the derivation of the flux conditions. First, let us consider the solutions to the problem written in its dimensionless form, namely to the system (5.23). We consider the Weertman law with $p = 1/3$, the Coulomb law, and the Budd law with $p = 1/3$ and $q = 1$, with both the $\mathrm{N_A}$ and $\mathrm{N_B}$ hydrological models. We take $\beta = -10^{-1}$, $\varepsilon = 6 \times 10^{-4}$, and $\delta = 10^{-1}$. The solutions of the problem are shown in figure 5.4. The most striking difference concerns the ratio of the membrane-stress divergence and the gravity stress: this ratio is almost equal to zero in the entire grounded domain for the Weertman friction law, as well as for the Coulomb and Budd friction laws with the $\mathrm{N_B}$ model. On the other hand, it becomes significant close to the grounding line for the Coulomb and Budd friction laws when they are coupled with the $\mathrm{N_A}$ model, i.e., when the friction stress vanishes at the grounding line.

A similar observation can be made if the problem is formulated in terms of $(\tilde{U}, \tilde{W})$, i.e., by considering the system (5.27). The solutions are shown in figure 5.5. Qualitatively, the solutions associated with vanishing grounding-line friction exhibit a stronger curvature in their trajectories. Importantly, the far-field solutions, shown in dotted lines and corresponding to a simple friction/gravity balance, do not represent well the dynamics close to the grounding line located at $\tilde{U} = \tilde{Q}_{\mathrm{gl}}$.

Finally, this observation is also present in the version of the problem used in the analysis presented in the previous subsection, namely (5.40). Indeed, the solution is then obtained as a portion of an orbit that reaches the fixed point located at $(\xi, \Psi) = (0, 1)$ through its center manifold. The solution trajectory can be parametrized by $\xi \in [0, \mathcal{Q}_{\mathrm{gl}}]$, where $\mathcal{Q}_{\mathrm{gl}}$ is the ξ coordinate of the intersection of the center manifold with the hyperbola whose equation is $\xi\Psi = \delta/8$. An asymptotic analysis reveals that the center manifold is such that $\Psi \sim 1$ for small ξ. It thus follows that, for small values of $\delta/8$, the solution trajectory is included in the region which is such that $\Psi \sim 1$. Because Ψ is a scaled version of the ratio between

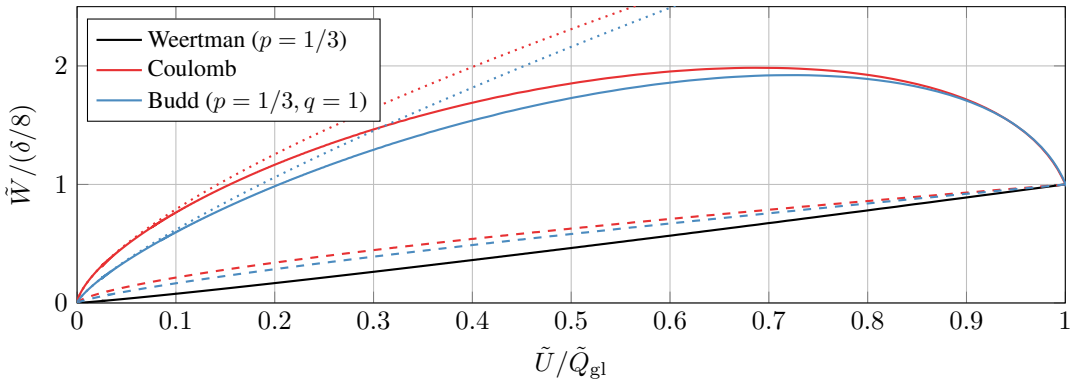

Figure 5.5: Solutions to the problem formulated in terms of $(\tilde{U}, \tilde{W})$, for various friction laws, with the $\mathrm{N_A}$ (continuous lines) and the $\mathrm{N_B}$ effective pressure-model (dashed lines). The dotted lines correspond to the far-field solutions associated with the coupling of the Coulomb and Budd friction laws with the $\mathrm{N_A}$ model.

friction and gravity stresses, the divergence of membrane stress can be neglected over the whole domain, even close to the grounding line. This argument is similar to the one developed in Schoof [2011] for the Weertman friction law.

5.4 Generalization to hybrid friction laws

The derivation of the flux condition for the Budd friction law can be generalized to more general friction laws of the form

$$\tau_{\mathrm{b}} = C\Phi(|u|, N)\, N^q |u|^{p-1} u. \tag{5.48}$$

In this equation, Φ denotes a general function of $|u|$ and N which is dimensionless.

We illustrate the derivation of flux conditions for hybrid flux conditions with the (RC1) friction law. The derivation of flux conditions for the (RC2) and (T) friction laws is similar, and the details can be found in the supplementary material. For the (RC1) friction law,

$$\tau_{\mathrm{b}} = C\left(\frac{|u|}{|u| + u_0}\right)^{p'} N \operatorname{sgn}(u), \quad \text{i.e.,} \quad \Phi(|u|, N) = \left(\frac{|u|}{|u| + u_0}\right)^{p'}, \quad \text{with } (p, q) = (0, 1). \tag{5.49}$$

As compared with figure 5.2, we use an exponent p' instead of p so as to distinguish this exponent from the one in $|u|^{p-1}$ in (5.48). Following the same steps as the ones described in the context of the Budd friction law, the system (5.27) becomes

$$\frac{\mathrm{d}\tilde{U}}{\mathrm{d}\tilde{X}} = -|\tilde{W}|^{n-1}\tilde{W}, \quad \text{for } \tilde{X} > 0, \tag{5.50a}$$

$$\frac{\mathrm{d}\tilde{W}}{\mathrm{d}\tilde{X}} = -\frac{|\tilde{W}|^{n+1}}{\tilde{U}} - \frac{1}{4}\left(\frac{|\tilde{U}|}{|\tilde{U}| + \tilde{v}}\right)^{p'} \left(1 - 1_{\mathrm{A}}\frac{\tilde{U}}{\tilde{Q}_{\mathrm{gl}}}\right)\frac{\tilde{U}}{|\tilde{U}|} + \frac{\tilde{Q}_{\mathrm{gl}}|\tilde{W}|^{n-1}\tilde{W}}{4\,\tilde{U}^2}, \quad \text{for } \tilde{X} > 0, \tag{5.50b}$$

$$(\tilde{U}, \tilde{W}) = (\tilde{Q}_{\mathrm{gl}}, \delta/8), \quad \text{at } \tilde{X} = 0, \tag{5.50c}$$

$$(\tilde{U}, \tilde{W}) \to (0, 0), \quad \text{as } \tilde{X} \to +\infty, \tag{5.50d}$$

with $\tilde{\upsilon}$ defined such that $\tilde{\upsilon} = \upsilon/\upsilon_c$ with $\upsilon \equiv u_0/[u]$ and

$$\upsilon_c \equiv \begin{cases} (2\rho g)^n C^{-1} A h_{gl}^{n+1} [u]^{-1} & (\mathrm{N_A\ model}), \\ (2\rho g)^n [C(1-c)]^{-1} A h_{gl}^{n+1} [u]^{-1} & (\mathrm{N_B\ model}). \end{cases} \tag{5.51}$$

The difference with the system in (5.27) is that the system in (5.50) depends on an additional parameter, namely, $\tilde{\upsilon}$. This new parameter is a scaled version of u_0. We interpret υ as the dimensionless version of the reference velocity in the (RC1) friction law and υ_c as the proper variable to which υ must be compared to in order to assess its importance on the system. The previous derivation cannot be applied as it assumes that $\tilde{Q}_{gl}$ is the only parameter left in the system (provided n, p', and δ are fixed). Furthermore, we cannot consider that $\tilde{\upsilon}$ is a small parameter and rescale the system accordingly, mirroring what has been done with δ, because u_0 could be large.

We propose the following strategy. If the value of the parameter $\tilde{\upsilon}$ is fixed, then $\tilde{Q}_{gl}$ can be found using the numerical approach presented in appendix B. Repeating this process for a collection of parameter values $\tilde{\upsilon}^{(1)}, ..., \tilde{\upsilon}^{(N)}$, a collection of corresponding values $\tilde{Q}_{gl}^{(1)}, ..., \tilde{Q}_{gl}^{(N)}$, solutions of (5.50), is obtained. A parametric representation of the mapping $\tilde{\upsilon} \mapsto \tilde{Q}_{gl}(\tilde{\upsilon})$ can then be fitted to the obtained dataset. The flux conditions for the two effective-pressure models are then expressed as

$$q_{gl} = \tilde{Q}_{gl}(\tilde{\upsilon})\, (2\rho g)^n C^{-1} A\, h_{gl}^{n+2}, \tag{5.52a}$$

$$q_{gl} = \tilde{Q}_{gl}(\tilde{\upsilon})\, (2\rho g)^n\, [C(1-c)]^{-1}\, A\, h_{gl}^{n+2}. \tag{5.52b}$$

The form of the function that approximates the relation $\tilde{\upsilon} \mapsto \tilde{Q}_{gl}(\tilde{\upsilon})$ can be constrained. The friction law presented in (5.49) is such that it tends towards a Coulomb-like friction law for small values of u_0 and a Budd-like friction law for large values of u_0. Assuming that this behavior is also present in the flux condition, we expect the following relations to hold:

$$\tilde{Q}_{gl}(\tilde{\upsilon}) \sim \tilde{Q}_{gl}^{(C)}, \qquad \text{for } \tilde{\upsilon} \ll 1, \tag{5.53a}$$

$$\tilde{Q}_{gl}(\tilde{\upsilon}) \sim \frac{\tilde{Q}_{gl}^{(B)}}{\tilde{Q}_{gl}^{(C)}}\, \tilde{\upsilon}^{\frac{p'}{p'+1}}, \qquad \text{for } \tilde{\upsilon} \gg 1. \tag{5.53b}$$

with

$$\tilde{Q}_{gl}^{(C)} \equiv \tilde{Q}_{gl}(1_A, n, 0, 1, \delta) \quad \text{and} \quad \tilde{Q}_{gl}^{(B)} \equiv \tilde{Q}_{gl}(1_A, n, p', 1, \delta), \tag{5.54}$$

that is, the values of $\tilde{Q}_{gl}$ for the Coulomb and Budd friction laws.

The transition between the limit cases $\tilde{\upsilon} \ll 1$ and $\tilde{\upsilon} \gg 1$ can be observed numerically (figure 5.6b, circles). These considerations justify the use of the following function as the fitted curve:

$$\tilde{Q}_{gl}(\tilde{\upsilon}) \approx m_\epsilon \left(\tilde{Q}_{gl}^{(B)},\, \tilde{Q}_{gl}^{(C)},\, \tilde{\upsilon}^{p'/(p'+1)} \right), \tag{5.55}$$

see figure 5.6a, where $x \mapsto m_\epsilon(a, b, x)$ is a smoothed version of the $x \mapsto \max(a\, x, b)$ function defined by

$$m_\epsilon(a, b, x) = (a/\epsilon)\, \log[\exp(\epsilon\, (x - b/a)) + 1] + b. \tag{5.56}$$

The free parameter ϵ can be tuned to get the best fit, using for example a least-square fit to the dataset $\{(\tilde{\upsilon}^{(1)}, \tilde{Q}_{gl}^{(1)}), ..., (\tilde{\upsilon}^{(N)}, \tilde{Q}_{gl}^{(N)})\}$. As shown in figure 5.6b, this approximation gives satisfactory results.

The dependency of $\tilde{Q}_{gl}$ on δ can also be obtained. As before, because we expect the flux condition to be similar to the Coulomb and Budd cases for $\tilde{\upsilon} \ll 1$ and $\tilde{\upsilon} \gg 1$ respectively, we expect that the flux

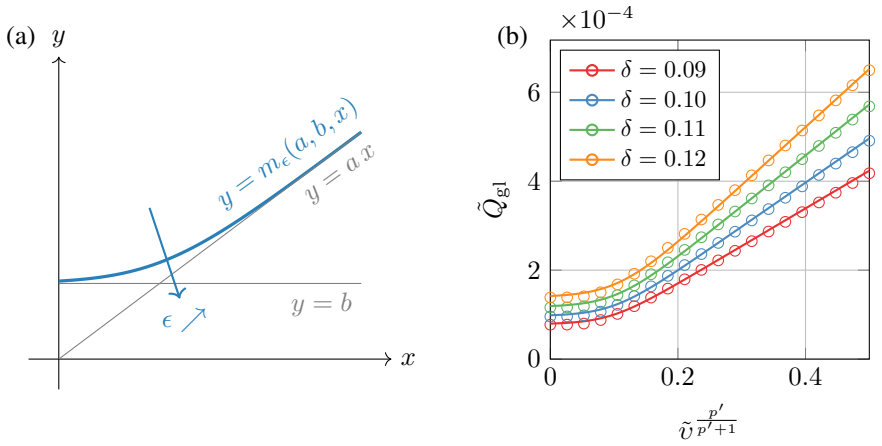

Figure 5.6: Approximation of the relation $\tilde{v} \mapsto \tilde{Q}_{\mathrm{gl}}(\tilde{v})$ for the (RC1) friction law combined with the $\mathrm{N_A}$ model. **(a)** Smooth version of the $x \mapsto \max(a\,x, b)$ function. The free parameter ϵ controls the sharpness of the transition between the lines $y = b$ and $y = a\,x$. **(b)** Relation between $\tilde{v}$ and $\tilde{Q}_{\mathrm{gl}}$ for the $\mathrm{N_A}$ effective-pressure model. The circles correspond to the values of $\tilde{Q}_{\mathrm{gl}}$ obtained numerically, and the lines correspond to (5.55) with $\epsilon = 3.383$.

Friction law	Effective pressure	$\check{Q}_{\mathrm{gl}}(\check{v})$	Free parameter
(RC1)	$\mathrm{N_A}$ ($1_{\mathrm{A}} = 1$)	$m_\epsilon(\check{Q}_{\mathrm{gl}}^{(\mathrm{B})}, \check{Q}_{\mathrm{gl}}^{(\mathrm{C})}, \check{v}^{p'/(p'+1)})$	$\epsilon = 3.383$
	$\mathrm{N_B}$ ($1_{\mathrm{A}} = 0$)	$m_\epsilon(\check{Q}_{\mathrm{gl}}^{(\mathrm{B})}, \check{Q}_{\mathrm{gl}}^{(\mathrm{C})}, \check{v}^{p'/(p'+1)})$	$\epsilon = 3.043$

Table 5.1: Functions $\check{v} \mapsto \check{Q}_{\mathrm{gl}}(\check{v})$ used in the flux condition of the (RC1) friction law.

conditions depend on δ in the following way:

$$q_{\mathrm{gl}} = \check{Q}_{\mathrm{gl}}(\check{v})\ (\delta/8)^{n-1}\,(2\rho g)^n C^{-1} A\, h_{\mathrm{gl}}^{n+2}, \qquad \check{v} \equiv (\delta/8)^{1-n}\,\tilde{v}, \tag{5.57a}$$

$$q_{\mathrm{gl}} = \check{Q}_{\mathrm{gl}}(\check{v})\ (\delta/8)^{n}\,(2\rho g)^n [C(1-c)]^{-1} A\, h_{\mathrm{gl}}^{n+2}, \qquad \check{v} \equiv (\delta/8)^{-n}\,\tilde{v}, \tag{5.57b}$$

for the $\mathrm{N_A}$ and $\mathrm{N_B}$ models, respectively. Approximating the relation $\check{v} \mapsto \check{Q}_{\mathrm{gl}}(\check{v})$ with the same function as before, i.e., considering

$$\check{Q}_{\mathrm{gl}}(\check{v}) \approx m_\epsilon\left(\check{Q}_{\mathrm{gl}}^{(\mathrm{B})}, \check{Q}_{\mathrm{gl}}^{(\mathrm{C})}, \check{v}^{p'/(p'+1)}\right), \tag{5.58}$$

with

$$\check{Q}_{\mathrm{gl}}^{(\mathrm{C})} \equiv \check{Q}_{\mathrm{gl}}(1_{\mathrm{A}}, n, 0, 1) \quad \text{and} \quad \check{Q}_{\mathrm{gl}}^{(\mathrm{B})} \equiv \check{Q}_{\mathrm{gl}}(1_{\mathrm{A}}, n, p', 1), \tag{5.59}$$

we obtain satisfactory results compared to the original dataset (figure 5.7). Table 5.1 summarizes the approximation used to include the dependency with respect to the parameter u_0.

5.5 Effect of α, β, and γ

In the derivation of flux conditions for the Budd friction law, as well as hybrid friction laws, we considered an unbuttressed marine ice sheet with scales that are such that $\alpha = 1$, $\gamma = 1$, and $|\beta| \lesssim 1$. Those assumptions have proved useful, as they allowed to simplify the problem, leading to explicit expressions for the flux conditions. In particular, they lead to a constant flux in the boundary layer and a negligible bedrock slope in the momentum-balance equation. Originally, these assumptions were made

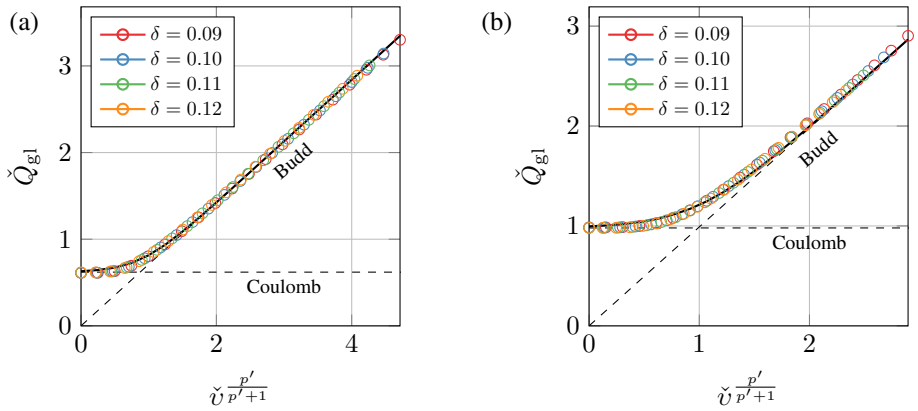

Figure 5.7: Relation between $\check{\upsilon}$ and $\check{Q}_{\mathrm{gl}}$ for the (RC1) friction law combined with **(a)** the $\mathrm{N_A}$ effective-pressure model and **(b)** the $\mathrm{N_B}$ effective-pressure model. The circles correspond to values obtained numerically, and the continuous lines correspond to the approximations described in table 5.1.

for marine ice-sheet systems, in particular by Schoof [2007c] and Tsai et al. [2015], whose work is the starting point of this article. Nonetheless, recent studies have challenged these hypotheses. Specifically, Sergienko and Wingham [2022] have shown that considering other scales, in which previously neglected terms are included, leads to a more complex relation between the grounding-line flux and the ice thickness at the grounding line. A corollary is that the marine ice-sheet instability, which amounts to say that grounding lines which are located on regions with up-sloping beds are unstable, does not generally apply.

The role of this section is not to repeat the same analysis as the one presented in Sergienko and Wingham [2022], but rather to see how, starting from our original flux conditions that follow the scaling presented in Schoof [2007c] and Tsai et al. [2015], we can derive correction factors. These factors allow to quantify the impact of a deviation from the original scaling (i.e., the effect of our hypotheses), and to correct the flux conditions accordingly. Eventually, we will still obtain similar results as the ones presented in Sergienko and Wingham [2022], although we here focus on explicit expressions of the flux conditions.

To discuss these hypotheses, we consider the Budd friction law, and we structure this section in several stages. First, we consider the case of a Budd friction law which is such that the divergence of membrane stress can be neglected. This is the case if the friction stress does not vanish at the grounding line and if $\gamma \sim 1$ so that essentially friction balances gravity. The analysis is then simplified because we obtain an algebraic equation for the grounding-line flux q_{gl}. We identify two dimensionless groups, denoted $\alpha/\alpha_{\mathrm{c}}$ and β/β_{c}, which allow to quantify the effect of the neglected terms in the derivation of the flux condition on the ratio $q_{\mathrm{gl}}/q_{\mathrm{gl,c}}$, where $q_{\mathrm{gl,c}}$ is a reference flux, corresponding to the flux derived in section 5.3. We also provide new explicit expressions for the flux conditions which are valid in the cases where $\alpha/\alpha_{\mathrm{c}}$ and β/β_{c} are not small. Then, we consider the case of a Budd friction law which is such that the friction stress does vanish at the grounding line. The previous developments can no longer be used, as the divergence of membrane stress plays an important role near the grounding line. Instead, we rely on solutions of a problem involving a dynamical system and an unknown parameter $\tilde{Q}_{\mathrm{gl}}$, similarly to what was done in section 5.3 and in section 5.4, to extend the validity of the flux conditions. We also comment on the case of a friction stress which does not vanish at the grounding line, but for which $\gamma \ll 1$ so that we do not expect a simple balance between friction stress and gravity stress.

5.5.1 Non-vanishing friction law with $\gamma \sim 1$: negligible membrane-stress divergence

Let us consider a general Budd friction law $\tau_\mathrm{b} = CN^q|u|^{p-1}u$ for which the divergence of membrane stress can be neglected in the momentum-balance equation, so that no boundary layer is needed close to the grounding line to obtain the flux condition (i.e., for which $\check{Q}_\mathrm{gl} \approx 1$ in the flux conditions that have been derived). To fulfill this condition, we consider a case where the effective pressure at the grounding line, N_gl, is non-zero, so that the friction stress does not vanish, and where we have $\gamma \sim 1$, so that the friction stress indeed balances the gravity stress. The $\mathrm{N_B}$ effective-pressure model falls into the category of effective-pressure models that are such that $N_\mathrm{gl} \neq 0$. In that case, the combination of the mass-balance equation, the momentum-balance equation, and the grounding-line boundary condition yields the following algebraic equation at the grounding line:

$$CN_\mathrm{gl}^q q_\mathrm{gl}^{p+1} + \rho g q_\mathrm{gl} h_\mathrm{gl}^{p+1} \left(\frac{\mathrm{d}b}{\mathrm{d}x}\right)_\mathrm{gl} = \rho g \left(\frac{1}{4}\rho\left(1-\frac{\rho}{\rho_\mathrm{w}}\right)g\right)^n A h_\mathrm{gl}^{n+p+3} - \rho g h_\mathrm{gl}^{p+2} a. \tag{5.60}$$

A similar expression can be found in Schoof [2007b,c] and in Sergienko and Wingham [2022]. If a and $(\mathrm{d}b/\mathrm{d}x)_\mathrm{gl}$ cannot be neglected, then no expression relating the grounding-line flux q_gl to the grounding-line thickness h_gl that is both exact and explicit can be obtained. We note that (5.60) can be written as

$$\frac{q_\mathrm{gl}}{q_\mathrm{gl,c}}\left(\left(\frac{q_\mathrm{gl}}{q_\mathrm{gl,c}}\right)^p + \frac{\beta}{\beta_\mathrm{c}}\right) = 1 - \frac{\alpha}{\alpha_\mathrm{c}}, \tag{5.61}$$

in which $q_\mathrm{gl,c}$ is a reference flux, given by

$$q_\mathrm{gl,c} = \left(\frac{\rho g}{C}\right)^{\frac{1}{p+1}} N_\mathrm{gl}^{-\frac{q}{p+1}} \left(\frac{1}{4}\rho\left(1-\frac{\rho}{\rho_\mathrm{w}}\right)g\right)^{\frac{n}{p+1}} A^{\frac{1}{p+1}} h_\mathrm{gl}^{\frac{n+p+3}{p+1}}. \tag{5.62}$$

In the case where the friction stress is non-zero at the grounding line, this reference flux is equal to the flux that would be obtained if a and $(\mathrm{d}b/\mathrm{d}x)_\mathrm{gl}$ could be neglected in (5.60), i.e., this is the expression of the flux that we have derived in section 5.3. The ratios α/α_c and β/β_c are defined as

$$\frac{\alpha}{\alpha_\mathrm{c}} = \frac{a}{\left(\frac{1}{4}\rho\left(1-\frac{\rho}{\rho_\mathrm{w}}\right)g\right)^n A\, h_\mathrm{gl}^{n+1}} \quad \text{and} \quad \frac{\beta}{\beta_\mathrm{c}} = \frac{(\mathrm{d}b/\mathrm{d}x)_\mathrm{gl}\, q_\mathrm{gl,c} h_\mathrm{gl}^{-1}}{\left(\frac{1}{4}\rho\left(1-\frac{\rho}{\rho_\mathrm{w}}\right)g\right)^n A\, h_\mathrm{gl}^{n+1}}. \tag{5.63}$$

These ratios provide a way to quantify the impact of the hypotheses made to derive the flux conditions on these flux expressions, more precisely the discrepancy with respect to the reference flux value $q_\mathrm{gl,c}$. This difference will be small if α/α_c and β/β_c are both small. We note that the denominators in (5.63) are proportional to the strain rate at the grounding line, so α/α_c and β/β_c can respectively be interpreted as a normalized measure of the variation of ice velocity associated with the net mass accumulation rate and the bedrock slope. These ratios can also be written with respect to the dimensionless numbers introduced in section 5.2: we have

$$\frac{\alpha}{\alpha_\mathrm{c}} = \alpha\left(\frac{\varepsilon}{\delta/8}\right)^n \left(\frac{h_\mathrm{gl}}{[h]}\right)^{-n} \quad \text{and} \quad \frac{\beta}{\beta_\mathrm{c}} = \beta\,\gamma^{-\frac{1}{p+1}} \left(\frac{\varepsilon}{\delta/8}\right)^{\frac{np}{p+1}} \left(\frac{h_\mathrm{gl}}{[h]}\right)^{-\frac{(p+q-np+1)}{p+1}}, \tag{5.64}$$

so in the limit of $\varepsilon \to 0$, the ratios α/α_c and β/β_c must tend towards zero. However, that limit is never reached in practice. Equation (5.63) then allows to compute, quantitatively, the importance of a, $(\mathrm{d}b/\mathrm{d}x)_\mathrm{gl}$, and C on the derivation of flux conditions, as a function of the original dimensional variables. Analogously, equation (5.64) allows to assess the importance of α, β, and γ on the validity of our flux conditions.

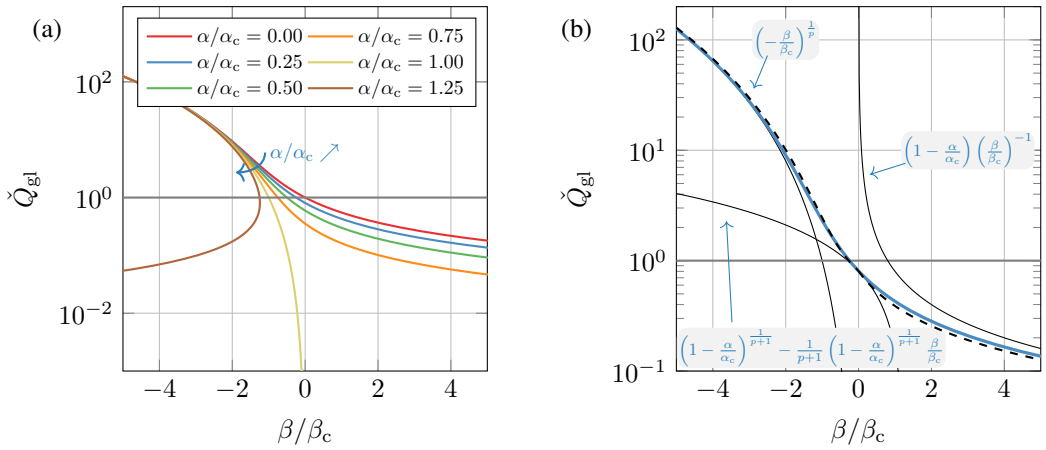

Figure 5.8: Effect of α/α_c and β/β_c on $\check{Q}_{gl}$, for a non-vanishing Budd friction law with $p = 1/3$. **(a)** Various values of α/α_c. **(b)** Zoom on the case $\alpha/\alpha_c = 0.25$. The colored continuous lines are obtained by solving numerically equation (5.61). The dashed black line is obtained using equation (5.72).

The dimensionless ratios α/α_c and β/β_c can also be used to derive new flux conditions which are approximately valid in the case where those ratios are not small. Indeed, we can formally write that

$$q_{gl} = \check{Q}_{gl} \left(\frac{\rho g}{C}\right)^{\frac{1}{p+1}} N_{gl}^{-\frac{q}{p+1}} \left(\frac{1}{4}\rho\left(1-\frac{\rho}{\rho_w}\right)g\right)^{\frac{n}{p+1}} A^{\frac{1}{p+1}} h_{gl}^{\frac{n+p+3}{p+1}}, \tag{5.65}$$

where $\check{Q}_{gl} = \check{Q}_{gl}(\alpha/\alpha_c, \beta/\beta_c)$ is a correction factor. Note that, by construction, $\check{Q}_{gl} = q_{gl}/q_{gl,c}$. The expression of $\check{Q}_{gl}$ can be approximated by considering the algebraic equation (5.61). On the one hand, this equation can be solved numerically for several fixed values of α/α_c and β/β_c (figure 5.8a). The number of acceptable solutions of (5.61), i.e., of real and strictly positive solutions values for $\check{Q}_{gl}$, depends on the value of α/α_c. In fact, $\alpha/\alpha_c = 1$ plays the role of a bifurcation point. Indeed, for $\alpha/\alpha_c < 1$, there is exactly one acceptable solution $\check{Q}_{gl}$. It is also found that in that case, $\check{Q}_{gl}$ decreases with both α/α_c and β/β_c. For $\alpha/\alpha_c = 1$, there is exactly one acceptable solution, provided that $\beta/\beta_c < 0$; otherwise, there is no solution. For $\alpha/\alpha_c > 1$, we observe a folding of the solution branch $\beta/\beta_c \mapsto \check{Q}_{gl}(\alpha/\alpha_c, \beta/\beta_c)$, which becomes multi-valued for $\beta/\beta_c < (\beta/\beta_c)_*$, and for which there is no solution for $\beta/\beta_c > (\beta/\beta_c)_*$. The critical value $(\beta/\beta_c)_*$ is given by

$$\left(\frac{\beta}{\beta_c}\right)_* = -(p+1)p^{-\frac{p}{p+1}}\left(\frac{\alpha}{\alpha_c}-1\right)^{\frac{p}{p+1}}. \tag{5.66}$$

On the other hand, the equation (5.61) can be solved approximately based on asymptotic analysis. Specifically, the following asymptotic expressions hold. For $\alpha/\alpha_c < 1$,

$$\check{Q}_{gl} \sim \left(1-\frac{\alpha}{\alpha_c}\right)^{\frac{1}{p+1}} - \frac{1}{p+1}\left(1-\frac{\alpha}{\alpha_c}\right)^{\frac{p-1}{p+1}}\frac{\beta}{\beta_c}, \qquad \text{for } \left|\frac{\beta}{\beta_c}\right| \ll 1, \tag{5.67}$$

$$\check{Q}_{gl} \sim \left(-\frac{\beta}{\beta_c}\right)^{\frac{1}{p}}, \qquad \text{for } \frac{\beta}{\beta_c} < 0 \text{ and } \left|\frac{\beta}{\beta_c}\right| \gg 1, \tag{5.68}$$

$$\check{Q}_{gl} \sim \left(1-\frac{\alpha}{\alpha_c}\right)\left(\frac{\beta}{\beta_c}\right)^{-1}, \qquad \text{for } \frac{\beta}{\beta_c} > 0 \text{ and } \left|\frac{\beta}{\beta_c}\right| \gg 1. \tag{5.69}$$

For $\alpha/\alpha_c = 1$, $\check{Q}_{gl} = (-\beta/\beta_c)^{1/p}$, provided that $\beta/\beta_c < 0$. For $\alpha/\alpha_c > 1$, the upper and lower solution

branches obey the following relations:

$$\breve{Q}_{\mathrm{gl}} \sim \left(-\frac{\beta}{\beta_{\mathrm{c}}}\right)^{\frac{1}{p}}, \qquad \text{for } \frac{\beta}{\beta_{\mathrm{c}}} < 0 \text{ and } \left|\frac{\beta}{\beta_{\mathrm{c}}}\right| \gg 1, \tag{5.70}$$

$$\breve{Q}_{\mathrm{gl}} \sim \left(1-\frac{\alpha}{\alpha_{\mathrm{c}}}\right)\left(\frac{\beta}{\beta_{\mathrm{c}}}\right)^{-1}, \qquad \text{for } \frac{\beta}{\beta_{\mathrm{c}}} < 0 \text{ and } \left|\frac{\beta}{\beta_{\mathrm{c}}}\right| \gg 1. \tag{5.71}$$

It can be expected that the lower solution branch is seldom reached in practice as it corresponds to relatively large values of a (as $\alpha/\alpha_{\mathrm{c}} > 1$) but to relatively small values of the flux q_{gl} (as $\breve{Q}_{\mathrm{gl}} \lesssim 1$). Combining these expressions together, a closed-form formula can be obtained to approximate the value of $\breve{Q}_{\mathrm{gl}}$. Assuming that we are in the case where there is a least one solution for $\breve{Q}_{\mathrm{gl}}$, i.e., considering the case $\alpha/\alpha_{\mathrm{c}} < 1$ or $\beta/\beta_{\mathrm{c}} < (\beta/\beta_{\mathrm{c}})_*$, we suggest the following expression (figure 5.8b, dashed line):

$$\breve{Q}_{\mathrm{gl}} \approx \begin{cases} (1-\alpha/\alpha_{\mathrm{c}})^{\frac{1}{p+1}} - \frac{1}{p+1}(1-\alpha/\alpha_{\mathrm{c}})^{\frac{p-1}{p+1}}\,\beta/\beta_{\mathrm{c}} + (-\beta/\beta_{\mathrm{c}})^{\frac{1}{p}}, & \text{for } \beta/\beta_{\mathrm{c}} < 0, \\ (1-\alpha/\alpha_{\mathrm{c}})^{\frac{1}{p+1}}\left[1+(1-\alpha/\alpha_{\mathrm{c}})^{-\frac{p}{p+1}}\,\beta/\beta_{\mathrm{c}}\right]^{-1}, & \text{for } \beta/\beta_{\mathrm{c}} \geq 0. \end{cases} \tag{5.72}$$

This expression can then be used to obtain the new flux condition (5.65), which is still approximately valid for values of $\alpha/\alpha_{\mathrm{c}}$ and β/β_{c} which are not small.

5.5.2 Vanishing friction law: non-negligible membrane-stress divergence

We now consider the case where the divergence of membrane stress cannot be neglected in the momentum-balance equation. Specifically, we consider the Budd friction law combined with the $\mathrm{N_A}$ effective-pressure model. In that case $N_{\mathrm{gl}} = 0$, so it does not make sense to use the reference flux $q_{\mathrm{gl,c}}$ defined in (5.62). Instead, we define it as

$$q_{\mathrm{gl,c}} = \left(\frac{1-\rho/\rho_{\mathrm{w}}}{8}\right)^{\frac{n}{p+1}} (\rho g)^{-\frac{q-1}{p+1}} (2\rho g)^{\frac{n}{p+1}} C^{-\frac{1}{p+1}} A^{\frac{1}{p+1}} h_{\mathrm{gl}}^{\frac{n+(p-q)+3}{p+1}}. \tag{5.73}$$

Note that, in contrast to the previous subsection, this is not the expression of the flux that was derived in section 5.3. It is rather a reference flux that is used to define β/β_{c}, without any specific physical interpretation. Again, we include the effect of the assumptions into a prefactor $\breve{Q}_{\mathrm{gl}}$ such that

$$q_{\mathrm{gl}} = \breve{Q}_{\mathrm{gl}} \left(\frac{1-\rho/\rho_{\mathrm{w}}}{8}\right)^{\frac{n-q}{p+1}} (\rho g)^{-\frac{q-1}{p+1}} (2\rho g)^{\frac{n}{p+1}} C^{-\frac{1}{p+1}} A^{\frac{1}{p+1}} h_{\mathrm{gl}}^{\frac{n+(p-q)+3}{p+1}}. \tag{5.74}$$

with $\breve{Q}_{\mathrm{gl}} = \breve{Q}_{\mathrm{gl}}(\alpha/\alpha_{\mathrm{c}}, \beta/\beta_{\mathrm{c}})$. The previous discussion holds if the divergence of membrane stress can be neglected in the momentum-balance equation. In general, and in particular for the Budd friction law with the $\mathrm{N_A}$ effective-pressure model, that is not the case. Still, we can follow a strategy similar to the one used in section 5.4 to derive the flux conditions of hybrid friction laws to take into account the effect of $\alpha/\alpha_{\mathrm{c}}$ and β/β_{c}: we can treat these ratios as parameters of the problem, and consider a mapping of the form $(\tilde{\alpha}, \tilde{\beta}) \mapsto \tilde{Q}_{\mathrm{gl}}(\tilde{\alpha}, \tilde{\beta})$. More precisely, if we keep the terms associated with the net mass accumulation rate and the bedrock slope in the derivation of the flux condition described in section 5.3,

we obtain the following system of equations, in place of (5.27):

$$\frac{\mathrm{d}\tilde{U}}{\mathrm{d}\tilde{X}} = -|\tilde{W}|^{n-1}\tilde{W}, \quad \text{for } 0 < \tilde{X} < \tilde{Q}_{\mathrm{gl}}/\tilde{\alpha}, \tag{5.75a}$$

$$\begin{aligned}\frac{\mathrm{d}\tilde{W}}{\mathrm{d}\tilde{X}} = -\frac{1}{4}\frac{\tilde{U}}{\tilde{Q}_{\mathrm{gl}} - \tilde{\alpha}\tilde{X}} \left(\frac{\tilde{Q}_{\mathrm{gl}} - \tilde{\alpha}\tilde{X}}{\tilde{U}} - 1_{\mathrm{A}}\left\langle 1 + \frac{\tilde{\beta}}{1-\delta}\tilde{X}\right\rangle\right)^{q} \\ \times |\tilde{U}|^{p-1}\tilde{U} - \frac{|\tilde{W}|^{n+1}}{\tilde{U}} + \tilde{\alpha}\frac{\tilde{W}}{\tilde{Q}_{\mathrm{gl}} - \tilde{\alpha}\tilde{X}} \\ -\frac{1}{4}\frac{\tilde{\alpha}}{\tilde{U}} + \frac{(\tilde{Q}_{\mathrm{gl}} - \tilde{\alpha}\tilde{X})|\tilde{W}|^{n-1}\tilde{W}}{4\,\tilde{U}^2} - \frac{\tilde{\beta}}{4}, \quad \text{for } 0 < \tilde{X} < \tilde{Q}_{\mathrm{gl}}/\tilde{\alpha},\end{aligned} \tag{5.75b}$$

$$(\tilde{U}, \tilde{W}) = (\tilde{Q}_{\mathrm{gl}}, \delta/8), \quad \text{at } \tilde{X} = 0, \tag{5.75c}$$

$$\tilde{U} = 0, \quad \text{at } \tilde{X} = \tilde{Q}_{\mathrm{gl}}/\tilde{\alpha}, \tag{5.75d}$$

with

$$\tilde{\alpha} = \left(\frac{\delta}{8}\right)^{n}\frac{\alpha}{\alpha_{\mathrm{c}}} \quad \text{and} \quad \tilde{\beta} = \left(\frac{\delta}{8}\right)^{\frac{np}{p+1}}\frac{\beta}{\beta_{\mathrm{c}}}. \tag{5.76}$$

This system of equations is fundamentally different from (5.27). Indeed, it is is formally equivalent to the initial system of equations presented in section 5.2, for unbuttressed ice sheets, since no additional assumption has been made. By contrast, the system of equations (5.27) used in section 5.3 to obtain the flux conditions was only valid within the boundary layer near the grounding line and in the limit of $\varepsilon \to 0$. The system (5.75) is also more complex in two respects. On the one hand, the dynamical system defined by (5.75a) and (5.75b) is non-autonomous, since $\tilde{X}$ appears in the definition of $\mathrm{d}\tilde{W}/\mathrm{d}\tilde{X}$. On the other hand, this system depends on the additional parameters $\tilde{\alpha}$ and $\tilde{\beta}$. Because $\tilde{\beta}$ is proportional to the bedrock slope $\mathrm{d}b/\mathrm{d}x$ which depends on the x coordinate, in general, $\tilde{\beta} = \tilde{\beta}(\tilde{X})$.

However, the analysis can be simplified by considering linear bed geometries, so that $\tilde{\beta}$ is constant. Let us fix the values of both $\tilde{\alpha}$ and $\tilde{\beta}$. The system of equations (5.75) is then a parametric system which only possesses solutions for specific values of $\tilde{Q}_{\mathrm{gl}}$. Despite the differences that have been mentioned, we have found that the shooting method introduced in section 5.3 and described in appendix B was still applicable to the system (5.75). We can thus obtain these particular values $\tilde{Q}_{\mathrm{gl}}$. Then, we convert the mapping $(\tilde{\alpha}, \tilde{\beta}) \mapsto \tilde{Q}_{\mathrm{gl}}(\tilde{\alpha}, \tilde{\beta})$ back the mapping $(\alpha/\alpha_{\mathrm{c}}, \beta/\beta_{\mathrm{c}}) \mapsto \breve{Q}_{\mathrm{gl}}(\alpha/\alpha_{\mathrm{c}}, \beta/\beta_{\mathrm{c}})$ by using (5.76) and $\tilde{Q}_{\mathrm{gl}} = (\delta/8)^{(n-q)/(p+1)}\breve{Q}_{\mathrm{gl}}$, which was derived in section 5.3. We have represented the effect of $\alpha/\alpha_{\mathrm{c}}$ and β/β_{c} on $\breve{Q}_{\mathrm{gl}}$ in figure 5.9a using the aforementioned numerical method.

In contrast to the case of non-vanishing friction laws, it is not easy to derive asymptotic expressions for $\breve{Q}_{\mathrm{gl}}$ for large or small values of β/β_{c}, as one has to solve (5.75), which is significantly more complex than an algebraic equation. Instead, we parametrize $\breve{Q}_{\mathrm{gl}}$ using a curve-fitting approach with simple expressions. We suggest the following expression (5.9b, dashed line):

$$\breve{Q}_{\mathrm{gl}} \approx \begin{cases} \breve{Q}^0_{\mathrm{gl}}\left(1 - 3.72\,\beta/\beta_{\mathrm{c}}\right), & \text{for } \beta/\beta_{\mathrm{c}} < 0, \\ \breve{Q}^0_{\mathrm{gl}}\left[1 + 17.76\left(1 - \alpha/\alpha_{\mathrm{c}}\right)^{-1}\beta/\beta_{\mathrm{c}}\right]^{-1}, & \text{for } \beta/\beta_{\mathrm{c}} \geq 0, \end{cases} \tag{5.77}$$

with $\breve{Q}^0_{\mathrm{gl}} \equiv \breve{Q}_{\mathrm{gl}}|_{(\alpha/\alpha_{\mathrm{c}}, \beta/\beta_{\mathrm{c}}) = (0,0)} = 0.71$.

5.5.3 Non-vanishing friction law with $\gamma \ll 1$

Sergienko and Wingham [2019] have considered flux conditions for the Weertman friction law in a regime of low basal and gravity stress. Specifically, they considered $\varepsilon \sim \delta \sim \gamma \ll 1$, leading to the divergence

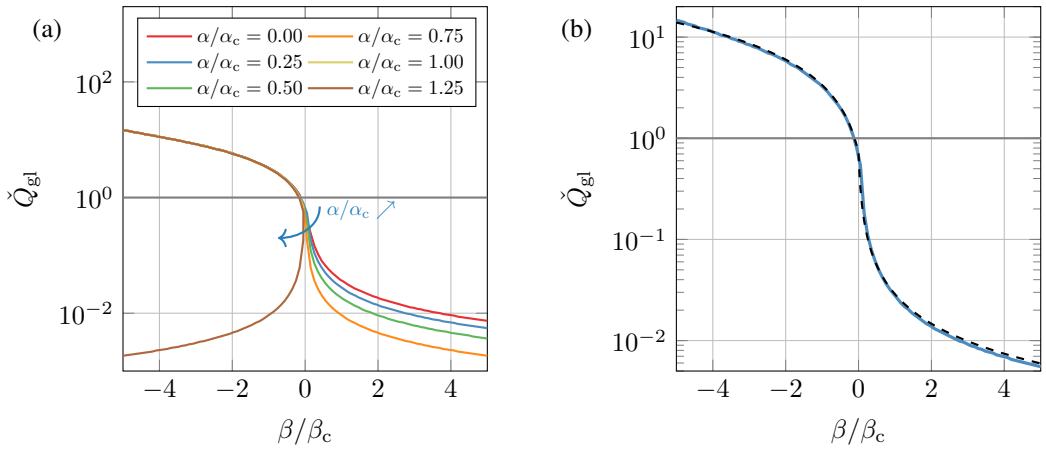

Figure 5.9: Effect of α/α_c and β/β_c on $\check{Q}_{gl}$, for the Budd friction law with the effective-pressure model N_A, $n = 1/3$, $p = 1/3$, $q = 1$, and $\delta = 0.1$. **(a)** Various values of α/α_c. **(b)** Zoom on the case $\alpha/\alpha_c = 0.25$. The colored continuous lines are obtained by finding the values of $\check{Q}_{gl}$ that yield a solution to (5.75). The dashed black line is obtained using equation (5.77).

of membrane stress being of the same order as the friction stress, but much smaller than the gravity stress. This is a different regime from ours: in section 5.3 we have assumed that $\gamma \sim 1$ and considered a scaling that is such that the divergence of membrane stress, the friction stress, and the gravity stress have the same order of magnitude.

They have obtained, as a zeroth-order solution, the following expression:

$$q_{gl}\left(\frac{\mathrm{d}b}{\mathrm{d}x}\right)_{gl} + a(1-\delta)h_{gl} = \left(\frac{1}{4}\rho g\left(1-\frac{\rho}{\rho_w}\right)\right)^n A\left[(1-\delta)h_{gl}\right]^{n+2}. \tag{5.78}$$

In the limit $\delta \ll 1$, this equation becomes

$$q_{gl} = \left[1 - \frac{a}{\left(\frac{1}{4}\rho\left(1-\frac{\rho}{\rho_w}\right)g\right)^n A\, h_{gl}^{n+1}}\right]\left[\frac{(\mathrm{d}b/\mathrm{d}x)_{gl}}{\left(\frac{1}{4}\rho\left(1-\frac{\rho}{\rho_w}\right)g\right)^n A\, h_{gl}^{n+2}}\right]^{-1}. \tag{5.79}$$

This is exactly our equations (5.69) and (5.71), i.e., this flux condition can be associated with the regime $|\beta/\beta_c| \gg 1$ of a Budd friction law which does not vanish at the grounding line and in which the membrane-stress divergence is negligible. This scaling can be motivated by equation (5.64): $|\beta/\beta_c| \propto \gamma^{-1/(p+1)}$.

5.6 Verification with numerical experiments

In this section, we verify the obtained flux conditions. First, we present the set-up used for the numerical experiments. Then, we verify the flux conditions derived in section 5.3 and 5.4. Finally, we investigate numerically the effect of α, β, and γ, and we confirm the results obtained in section 5.5.

5.6.1 Set-up

The values chosen for the physical parameters are typical for numerical experiments with marine ice sheets, and are similar to the ones presented in Pattyn et al. [2012]. We take $n = 3$, $\rho = 900\,\mathrm{kg\,m^{-3}}$, $\rho_w = 1000\,\mathrm{kg\,m^{-3}}$, and $g = 9.8\,\mathrm{m\,s^{-2}}$. Glen's viscosity parameter is set to $A = 4.9 \times 10^{-25}\,\mathrm{Pa^{-3}s^{-2}}$,

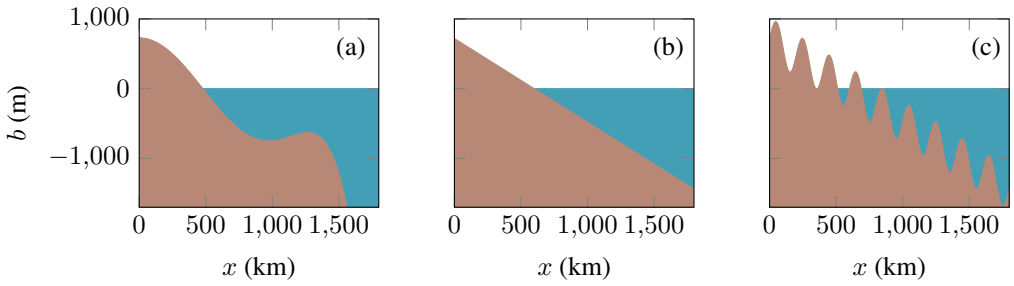

Figure 5.10: Bed profiles considered in the numerical experiments: **(a)** polynomial bed; **(b)** linear bed; **(c)** linear bed with oscillations.

and the net mass accumulation rate is set to $a = 9.51 \times 10^{-9}\,\mathrm{m\,s^{-1}}$. In terms of the friction laws, we consider the (W), (C), (B), (T), (RC1), and (RC2) friction laws with $p = 1/3$ and $q = 1$, and with both the $\mathrm{N_A}$ and the $\mathrm{N_B}$ effective-pressure models. The friction coefficient for the (W) friction law is set to $C = 7.624 \times 10^6\,\mathrm{Pa\,m^{-1/3}\,s^{1/3}}$. For the other friction laws, the friction coefficient will be specified for each specific numerical experiment. The hydrology parameter c is set to 0.96. Three bed elevation profiles are considered (figure 5.10). The first one is a polynomial bed that will be used to compare the flux conditions in an idealized configuration. The second one depends linearly on x and will be used to check the effect of the bed slope (and thus of β) on the flux conditions. The third one is similar to the linear one, but an oscillatory signal has been added on top of it. It will be used to investigate the effect of local variability in the bedrock profile.

Results are obtained either from the flux conditions themselves, or from the numerical solution of the initial problem (equations (5.1)–(5.6)). For the spatial discretization, we use an in-house finite-element code. The mesh is uniform with a constant element size of 180 m.

5.6.2 Flux conditions for the Budd and hybrid friction laws

The first experiment compares the flux conditions obtained in sections 5.3 and 5.4 with results of numerical simulations. It mimics the experiment 3 of the Marine Ice Sheet Model Intercomparison Project [Pattyn et al., 2012] which is a benchmark for the comparison of marine ice-sheet flowline models. We considered the polynomial bed profile (figure 5.10a), fixed all the parameters to their reference values, except for the ice rheology parameter A which is varied. For each particular value of A, a steady-state ice-sheet solution was obtained and the grounding-line position was retrieved. On the one hand, this position was obtained numerically, thanks to the finite-element solution. On the other hand, we computed the grounding-line position from the flux conditions: from the mass-conservation equation, we have the global balance

$$q_{\mathrm{gl}}(h_{\mathrm{gl}}) = a\,x_{\mathrm{gl}}, \tag{5.80}$$

where we have written $q_{\mathrm{gl}} = q_{\mathrm{gl}}(h_{\mathrm{gl}})$ to emphasize the dependency on the grounding-line ice thickness. The flotation condition $h_{\mathrm{gl}} = -(\rho_{\mathrm{w}}/\rho)b(x_{\mathrm{gl}})$ then allowed to obtain an algebraic equation for x_{gl}:

$$q_{\mathrm{gl}}\left(-(\rho_{\mathrm{w}}/\rho)b(x_{\mathrm{gl}})\right) = a\,x_{\mathrm{gl}}. \tag{5.81}$$

We solved this non-linear equation using a Newton–Raphson procedure.

It remains to choose the values of the friction coefficients for all the friction laws except for the Weertman one. This is quite delicate, because the friction coefficients associated with different friction laws are not necessarily comparable to one another; in particular, they do not have the same dimensions. For the Weertman friction law, equation (5.81) has a solution $x_{\mathrm{gl}} \approx 800\,\mathrm{km}$ for $A = 10^{-25}\,\mathrm{Pa^{-3}\,s^{-1}}$. We then chose the friction coefficients C for the Coulomb friction law and the Budd friction law so as

Friction law		Effective pressure	C	
(W)	$(p = 1/3)$	/	7.624×10^6	$\mathrm{Pa\,m^{-1/3}\,s^{1/3}}$
(C)		$\mathrm{N_A}$ $(1_\mathrm{A} = 1)$	1.316×10^0	-
(C)		$\mathrm{N_B}$ $(1_\mathrm{A} = 0)$	6.634×10^{-1}	-
(B)	$(p = 1/3, q = 1)$	$\mathrm{N_A}$ $(1_\mathrm{A} = 1)$	6.116×10^1	$\mathrm{m^{-1/3}\,s^{1/3}}$
(B)	$(p = 1/3, q = 1)$	$\mathrm{N_B}$ $(1_\mathrm{A} = 0)$	3.018×10^1	$\mathrm{m^{-1/3}\,s^{1/3}}$
(RC1)	$(p = 1/3)$	$\mathrm{N_A}$ $(1_\mathrm{A} = 1)$	1.316×10^0	-
(RC1)	$(p = 1/3)$	$\mathrm{N_B}$ $(1_\mathrm{A} = 0)$	6.634×10^{-1}	-
(RC2)	$(p = 1/3)$	$\mathrm{N_A}$ $(1_\mathrm{A} = 1)$	1.316×10^0	-
(RC2)	$(p = 1/3)$	$\mathrm{N_B}$ $(1_\mathrm{A} = 0)$	6.634×10^{-1}	-
(T)	$(p = 1/3)$	$\mathrm{N_A}$ $(1_\mathrm{A} = 1)$	1.316×10^0	-
(T)	$(p = 1/3)$	$\mathrm{N_B}$ $(1_\mathrm{A} = 0)$	6.634×10^{-1}	-

Table 5.2: Numerical values of the friction coefficients used for the verification of the flux conditions.

Friction law		Effective pressure	Additional parameter	
(RC1)	$(p = 1/3)$	$\mathrm{N_A}$ $(1_\mathrm{A} = 1)$ & $\mathrm{N_B}$ $(1_\mathrm{A} = 0)$	$u_0 = 10^{-5}$	$\mathrm{m\,s^{-1}}$
(RC2)	$(p = 1/3)$	$\mathrm{N_A}$ $(1_\mathrm{A} = 1)$ & $\mathrm{N_B}$ $(1_\mathrm{A} = 0)$	$A_s^{-p} = 7.624 \times 10^6$	$\mathrm{Pa\,m^{-1/3}\,s^{1/3}}$
(T)	$(p = 1/3)$	$\mathrm{N_A}$ $(1_\mathrm{A} = 1)$ & $\mathrm{N_B}$ $(1_\mathrm{A} = 0)$	$A_s^{-p} = 7.624 \times 10^6$	$\mathrm{Pa\,m^{-1/3}\,s^{1/3}}$

Table 5.3: Numerical values of the additional friction parameters A_s and u_0 used for the verification of the flux conditions.

to obtain this solution as well. The obtained friction parameters are shown in table 5.2. For the hybrid friction laws, we considered the same friction coefficient C as the one obtained for the Coulomb friction law because the Coulomb friction law is a limit case of the hybrid friction laws. The coefficient A_s was chosen such that A_s^{-p} had the same value as the Weertman friction coefficient, again by identification of the hybrid friction law as a Weertman friction law. Finally, we considered $u_0 = 10^{-5}\,\mathrm{m\,s^{-1}}$, which is a typical value for the velocity in marine ice sheets. All these values are summarized in table 5.2 and in table 5.3.

The results are shown in figure 5.11. The grounding-line positions obtained using the flux conditions match the results from the numerical simulations. We note that the physical parameters and the bed profile considered in this numerical experiment are consistent with the assumptions made during the derivation of the flux conditions, namely, the net mass accumulation rate and the bedrock slopes are not too large, and the friction coefficient is not too small. With respect to the discussion of section 5.5, the experiments have been conducted in a regime for which α/α_c and β/β_c are small.

As a side note, it can be observed that the curves all have the same shape, which could suggest that the choice of friction laws actually has little impact on the mechanical equilibrium of marine ice sheets, and in particular on flux conditions. However, this similarity is not the result of the impact of friction laws but rather stems from the methodology used. The flux conditions associated with different friction laws differ in two aspects: the exponent on the grounding-line thickness, and the dependence of the factor that multiplies this thickness with respect to the physical parameters (A, C, ...). The considered bedrock does not show a strong variability, so that the exponent on top of the grounding-line thickness has a limited effect. Moreover, by construction, the friction coefficients were chosen uniformly and in such a way that the curves pass through the same point, which effectively leads to a similar factor in front of the grounding-line thickness. This explains the similarity between the curves shown in figure 5.11. In practice, however, the friction coefficients are not uniform, but, rather, are tuned spatially so as to obtain a similar thickness and velocity profile compared to some observations. This results in very different

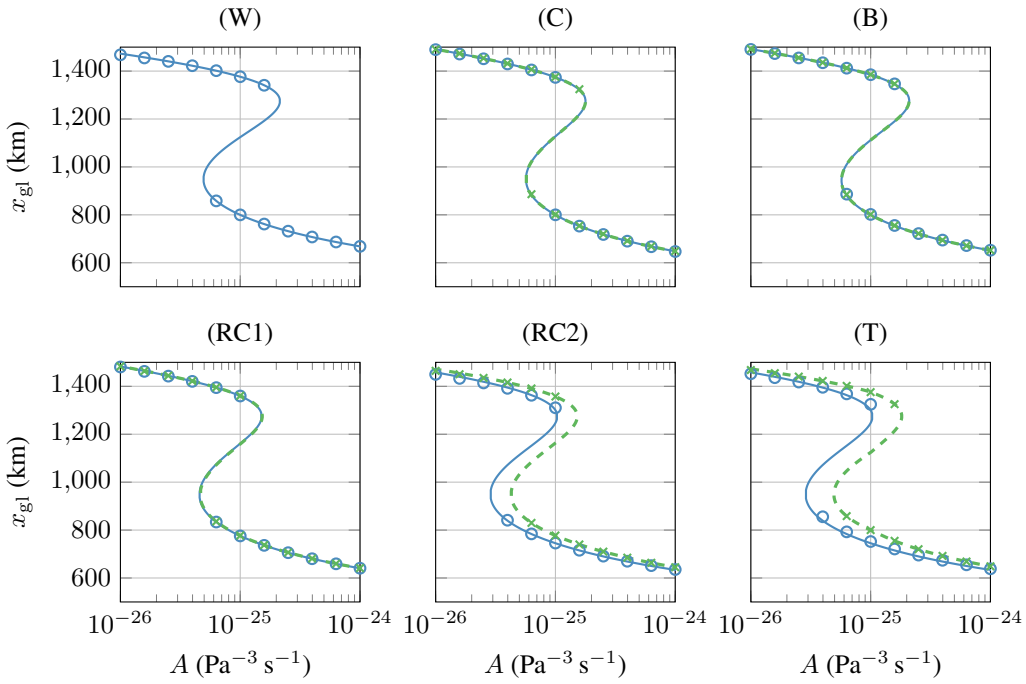

Figure 5.11: Comparison of the evolution of the grounding-line position with respect to A for the different friction laws and effective-pressure models, using the flux condition (lines) and results of a finite-element discretization of the original problem (circles, crosses). The results for the $\mathrm{N_A}$ and $\mathrm{N_B}$ effective pressure models are respectively shown in blue and in green.

dynamics. We refer interested readers to Brondex et al. [2017] where these differences are discussed.

5.6.3 Effect of α, β, and γ

We now conduct a series of numerical experiments to determine numerically the situations in which the assumptions made to derive the flux conditions in section 5.3 are not valid, and to confirm that the new expressions, namely equations (5.65) and (5.74) combined respectively with the corrections factors defined in (5.72) and (5.77), can be applied to correct these flux conditions. Practically, we check that they lead to the same grounding-line flux value as the numerical results. We call the flux conditions derived in section 5.5 'enriched' flux conditions. First, we consider the linear bed profile (figure 5.10b), whose elevation is given by $b(x) = b_0 + b_1(x/L)$ with $b_0 = 720\,\mathrm{m}$, $b_1 = -900\,\mathrm{m}$, and $L = 750\,\mathrm{km}$. We vary three physical parameters: the net mass accumulation rate a, the bedrock slope $\mathrm{d}b/\mathrm{d}x$, and the friction coefficient C. The goal is to reach a regime in which $\alpha/\alpha_{\mathrm{c}}$ and β/β_{c} are not small so that the flux conditions derived in section 5.3 are not valid anymore. Then, we consider the more realistic 'rough' bedrock profile, as well as different values for the friction coefficient. We always consider the Budd friction law with both the $\mathrm{N_A}$ and $\mathrm{N_B}$ effective-pressure models. We choose a reference friction coefficient of $C_0^{\mathrm{A}} = 1.73\,\mathrm{m}^{-1/3}\mathrm{s}^{1/3}$ in the first case, and $C_0^{\mathrm{B}} = 43.22\,\mathrm{m}^{-1/3}\mathrm{s}^{1/3}$ in the second case. These values where chosen such that $C_0^{\mathrm{A}}\rho g h_{\mathrm{gl}} \approx C_0^{\mathrm{B}}(1-c)\rho g h_{\mathrm{gl}} \approx 7.624\times10^6\,\mathrm{Pa\,m}^{-1/3}\mathrm{s}^{1/3}$ for $h_{\mathrm{gl}} = 500\,\mathrm{m}$.

First, we consider the reference physical parameters previously introduced, and we modify the values of a, $\mathrm{d}b/\mathrm{d}x$, and C in the following way. We first consider a, and vary its value within the interval $a_0 \leq a \leq 10\,a_0$, where a_0 is the reference value introduced in the set-up subsection. For each fixed value of a, we let the ice sheet evolve until it reaches a steady state. This leads to a collection of grounding-line fluxes, which are compared to the grounding-line fluxes that would have been obtained thanks to our

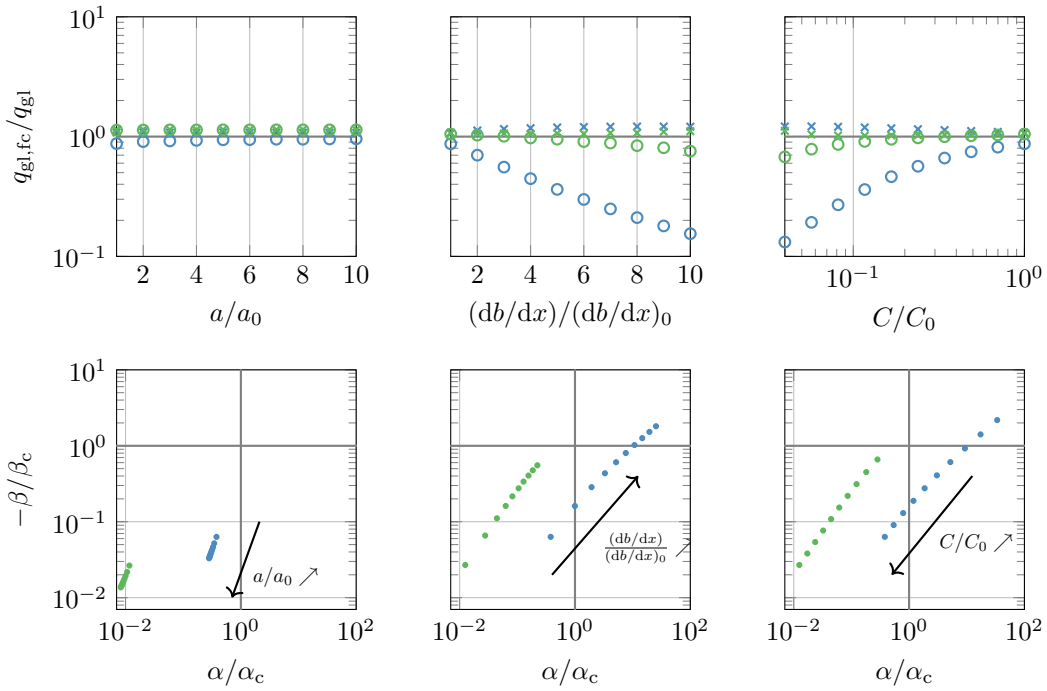

Figure 5.12: First line: comparison between the fluxes $q_{\mathrm{gl,fc}}$ obtained thanks to the flux conditions derived in section 5.3 (circles) and thanks to the enriched flux conditions (crosses), and the grounding-line fluxes q_{gl} obtained numerically, when a/a_0, $(\mathrm{d}b/\mathrm{d}x)/(\mathrm{d}b/\mathrm{d}x)_0$, and C/C_0 are varied. Second line: ratios $\alpha/\alpha_{\mathrm{c}}$ and β/β_{c} corresponding to each numerical solution. We have considered the Budd friction law with the $\mathrm{N_A}$ (blue) and the $\mathrm{N_B}$ (green) effective-pressure models.

flux conditions. For the $\mathrm{N_A}$ effective-pressure model, we use (5.74) combined with (5.77), while for the $\mathrm{N_B}$ effective-pressure model, we use (5.65) combined with (5.72). We then perform a similar procedure for $\mathrm{d}b/\mathrm{d}x$ and C, which are respectively varied in the ranges $10\,(\mathrm{d}b/\mathrm{d}x)_0 \leq \mathrm{d}b/\mathrm{d}x \leq (\mathrm{d}b/\mathrm{d}x)_0$ and $0.5 \times 10^{-1} C_0 \leq C \leq C_0$, with $(\mathrm{d}b/\mathrm{d}x)_0 = b_1/L$. In this former case, only the slope of the linear bed is varied; the value $b(0) = b_0$ is left unchanged. By increasing the value of a, of $|\mathrm{d}b/\mathrm{d}x|$, and reducing the value of C, we attempt to reach a regime in which $\alpha/\alpha_{\mathrm{c}}$ and β/β_{c} cannot be neglected. The results are shown in figure 5.12. It can be observed that, for the parameters considered, the ratio $q_{\mathrm{gl,fc}}/q_{\mathrm{gl}}$ stays close to one when the $\mathrm{N_B}$ effective-pressure model is used, even when we use the flux condition derived in section 5.3. By contrast, this ratio departs significantly from one when the slope or the friction parameter are varied in a simulation in which the $\mathrm{N_A}$ effective-pressure model is considered. That is not the case if we use the enriched flux conditions, as those lead to a ratio that is always close to one.

In practice, we expect a relatively variable bedrock elevation; hence, a linear configuration might not be appropriate. To investigate the impact of this bedrock variability, we consider the bedrock profile shown in figure 5.10c. Its elevation is given by $b(x) = b_0 + b_1(x/L) + b_2 \sin(2\pi x/L_{\mathrm{o}})$, where b_0, b_1, and L have the same values as before, $b_2 = 300\,\mathrm{m}$, and where L_{o} is varied between 100 km and 300 km. The physical parameters are the same as the ones used previously when varying the net mass accumulation rate a. We observe in figure 5.13 similar findings compared to the previous numerical experiment. Firstly, the ratio $q_{\mathrm{gl,fc}}/q_{\mathrm{gl}}$ calculated using the flux conditions derived in section 5.3 deviates further from a unit value as the bedrock has a larger slope variation. Secondly, the effect is much more pronounced in the case of the $\mathrm{N_A}$ effective-pressure model. Lastly, the use of corrective factors in flux conditions enables satisfactory results, namely a $q_{\mathrm{gl,fc}}/q_{\mathrm{gl}}$ ratio that remains close to unity.

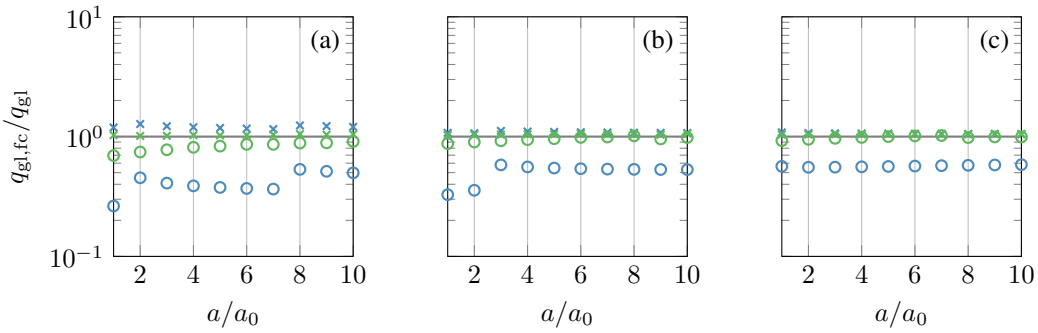

Figure 5.13: Effect of local variability in the geometry profile on the ratio between the fluxes $q_{\mathrm{gl,fc}}$ obtained based on the flux conditions derived in section 5.3 (circles) and on the enriched flux conditions (crosses), and the flux q_{gl} obtained numerically, with **(a)** $L_{\mathrm{o}} = 100\,\mathrm{km}$; **(b)** $L_{\mathrm{o}} = 200\,\mathrm{km}$; and **(c)** $L_{\mathrm{o}} = 300\,\mathrm{km}$. We have considered the Budd friction law with the $\mathrm{N_A}$ (blue) and the $\mathrm{N_B}$ (green) effective-pressure models.

5.7 Discussion

In this section, we briefly discuss the flux conditions that we have derived in section 5.3 and in section 5.4. Then, we comment on the limitations of these conditions by addressing both the analysis provided in section 5.5 and some modeling assumptions.

5.7.1 Specifications of the obtained flux conditions

Dependence on the effective-pressure model

The flux conditions associated with the two effective-pressure models that we have considered are similar. Their only differences concern the coefficient c, which only appears with the effective-pressure model $\mathrm{N_B}$, the dependency with respect to δ, and the value of the numerical prefactor $\breve{Q}_{\mathrm{gl}}$. In particular, for the friction laws covered in this article, we found that $\breve{Q}_{\mathrm{gl}}$ is generally smaller for the $\mathrm{N_A}$ model, compared to the $\mathrm{N_B}$ model.

Dependence on the physical parameters for the Budd friction law

The grounding-line flux depends on A and C in the following way: $q_{\mathrm{gl}} \propto (A/C)^{1/(p+1)}$. We remark that the exponent q, which is associated with the effective pressure, does not intervene. In particular, this leads to the same dependency with respect to these parameters for the Weertman friction law ($p = 1/3$) and the Budd friction law ($p = 1/3$, $q = 1$). For the $\mathrm{N_B}$ effective-pressure model, the grounding-line flux depends on c through $q_{\mathrm{gl}} \propto (1-c)^{q/(p+1)}$. This time, both p and q impact this dependency.

Dependence on the additional parameter for hybrid friction laws

In a similar way to the hybrid friction laws which allow to switch from one friction law to another depending on an additional parameter, the associated flux conditions allow to transition between different states. For example, the (RC1) friction law is an intermediate friction law between the (C) and (B) friction law, and the additional parameter u_0 controls the tendency of that law (figure 5.14).

Another point concerns the behavior close to the grounding line. Let us consider a friction law that vanishes at the grounding line but that is different from the Coulomb friction law, for example the (RC1) friction law. Close to the grounding line, both friction laws will be similar so that one could consider the flux condition derived by Tsai et al. [2015] for the Coulomb friction law, even if it was not developed

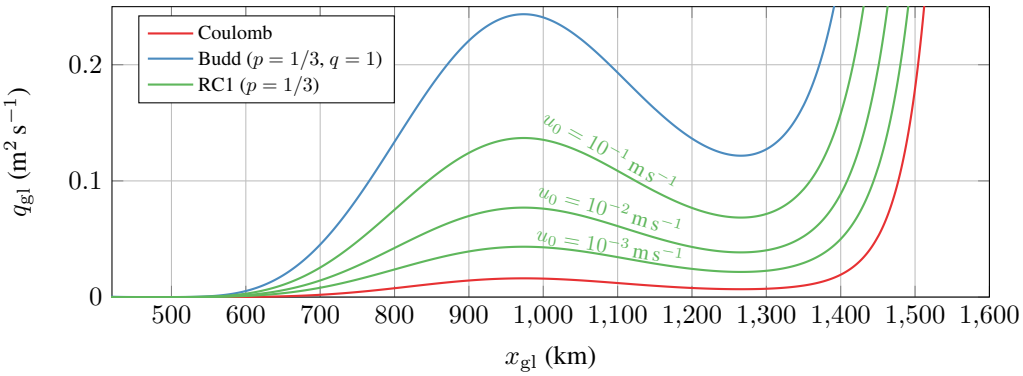

Figure 5.14: Grounding-line flux expressed as a function of the grounding-line position, using the flux conditions derived in section 5.3 and 5.4. The grounding-line thickness was linked to the grounding-line position thanks to the flotation condition $h_{\mathrm{gl}} = -(\rho_{\mathrm{w}}/\rho)b(x_{\mathrm{gl}})$. The results are displayed for the (C), (B), and (RC1) friction laws using similar physical parameters and the bedrock profile of figure 5.10a.

for this particular friction law. Our approach allows to assess this idea quantitatively. As shown in figure 5.7, there is a transition in the plots, from a constant value of $\check{Q}_{\mathrm{gl}}$ to an approximately linear curve. The Coulomb behavior precisely corresponds to this first constant part. We therefore deduce that the Coulomb flux condition can be considered if the additional parameter, $\check{\upsilon}$, is sufficiently small. For example, for the $\mathrm{N_A}$ effective-pressure model, it is necessary that

$$\check{\upsilon}^{p'/(p'+1)} \lesssim 0.1. \tag{5.82}$$

Physically, this means that the viscous boundary layer is included inside the region in which the friction law essentially behaves like a Coulomb friction law. It must be noted that the parameter u_0 is critical in that context because it controls the width of the region in which friction has a Coulomb-like behavior.

Dependence on the grounding-line thickness

Another result of our derivation concerns the stability of marine ice sheets. It is often assumed that if q_{g} depends on h_{g} with a relatively large exponent κ, then the stable equilibrium positions will be more stable with respect to external perturbations while the unstable ones will be more unstable with respect to external perturbations [Schoof, 2012; Tsai et al., 2015]. This exponent can be computed for the friction laws covered in this article. If $n = 3$, $p = 1/3$, and $q = 1$, then κ varies within $[4, 5]$, depending on the friction law considered (figure 5.15). Furthermore, the hybrid friction laws effectively behave as power laws for limiting values of the additional parameter, u_0 or A_s, so that the exponent κ transitions between multiple values. For instance, κ switches from 4.75 to 5 for the (RC2) and (T) friction laws.

5.7.2 Limitations

Effect of α, β, and γ

From the mathematical analyses and the numerical simulations described in section 5.5 and 5.6, we conclude that accounting for the net mass accumulation rate and the bedrock slope can have a significant impact on the flux conditions, so that correction factors may be necessary. The impact is more significant when using a friction law such that friction stress vanishes at the grounding line than when using a friction law such that friction stress does not vanish at the grounding line. For both types of friction laws, the impact of the net mass accumulation rate and the bedrock slope on the flux condition increases with a decrease in the friction coefficient.

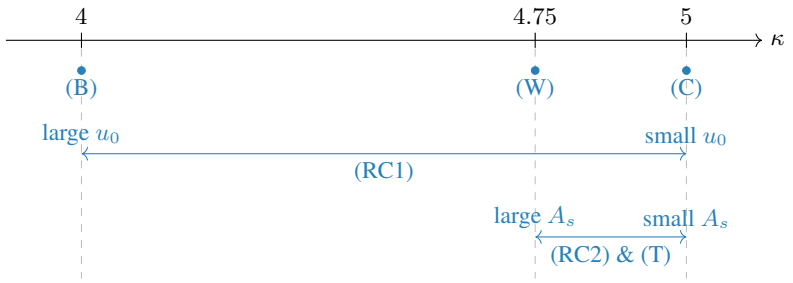

Figure 5.15: Effective exponent κ associated to a flux condition of the form $q_g \propto h_g^\kappa$ for the friction laws covered in this article with $n = 3$, $p = 1/3$, and $q = 1$. For hybrid friction laws the exponent κ takes different values whether u_0 and A_s are either very small or very large.

2D geometry and steady-state assumptions

Another important assumption that was made concerns the geometry: in our derivation, we have used a 1D flowline model that is in a steady state. This leads to modeling errors associated to (i) the effect of lateral drag and (ii) the conservation of the flux along a streamline and over time. As described in section 5.2, lateral drag can only be taken into account in a flowline model by a parametrization. The effect of this parametrization on grounding-line flux conditions has been studied in Schoof et al. [2017], Haseloff and Sergienko [2018], and Reese et al. [2018b]. We also refer the interested reader to Gudmundsson et al. [2012], Gudmundsson [2013], and Pegler [2016, 2018a,b] for numerical and theoretical studies of the stability of buttressed ice sheets. The flowline assumption is important, as it leads to an invariant flux near the grounding line, i.e., the flux is spatially constant in that area. In practice, that will not be the case for channels that are widening or narrowing. Furthermore, it is unrealistic to assume that ice streams are independent of the transverse bed variability [Sergienko, 2012]; it can be expected that streamlines are condensed in areas where the friction induced by the bed roughness is limited.

In parallel, the steady-state assumption guarantees that all the unknown fields, and in particular the grounding-line flux, are constant over time. If the ice sheet was not in a stationary configuration, then the only equation that would need to be modified is the mass balance equation. It would be changed to

$$\frac{\partial h}{\partial t} + \frac{\partial}{\partial x}(uh) = a, \tag{5.83}$$

that is, the same equation as the one we have used, provided we replace the net mass accumulation by an effective accumulation rate given by $a_{\text{eff}} = a - \partial h/\partial t$. It follows that if the geometry is changing sufficiently slowly such that $\partial h/\partial t$ is much lower than a, then flux conditions still make sense. Clearly, this conclusion also assumes that the physical parameters, which were previously regarded as constant, evolve over time scales that are sufficiently large compared to the dynamics of the problem under consideration here. In general, however, that is not the case, and the time dynamics requires an analysis of its own, see e.g. Schoof [2007b,c], Haseloff and Sergienko [2022], Sergienko and Wingham [2022], and Sergienko and Haseloff [2023]. Nonetheless, we speculate that flux conditions can still be applied with an effective accumulation rate as defined above when there is no grounding-line boundary layer, similarly to what is observed, e.g., in Sergienko and Wingham [2022].

5.8 Conclusion

In this article, we generalized the flux conditions of marine ice-sheet systems. We showed that the methodology of Schoof [2007c] and Tsai et al. [2015] can be extended to the general Budd friction law

and for two different effective-pressure models, leading to the following expressions:

$$q_{\mathrm{gl}} = \check{Q}_{\mathrm{gl}} \left(\frac{1-\rho/\rho_{\mathrm{w}}}{8} \right)^{\frac{n-q}{p+1}} (\rho g)^{-\frac{q-1}{p+1}} (2\rho g)^{\frac{n}{p+1}} C^{-\frac{1}{p+1}} A^{\frac{1}{p+1}} h_{\mathrm{gl}}^{\frac{n+(p-q)+3}{p+1}},$$

$$q_{\mathrm{gl}} = \check{Q}_{\mathrm{gl}} \left(\frac{1-\rho/\rho_{\mathrm{w}}}{8} \right)^{\frac{n}{p+1}} (\rho g)^{-\frac{q-1}{p+1}} (2\rho g)^{\frac{n}{p+1}} [C(1-c)^q]^{-\frac{1}{p+1}} A^{\frac{1}{p+1}} h_{\mathrm{gl}}^{\frac{n+(p-q)+3}{p+1}}.$$

Our flux conditions generalize and reconcile these previous works as we recover their flux conditions as special cases. We also extended the flux conditions to hybrid friction laws. This was achieved through the use of regularized functions which depend on a limited number of parameters that can be tuned easily. Furthermore, we provided justifications for several properties of an equivalent dynamical system associated with the leading-order solution to our problem. A numerical strategy was proposed for the computation of a numerical factor appearing in the flux condition. Finally, the validity of the assumptions made during the derivation was discussed, and a correction factor was proposed to extend the domain of validity of the flux conditions, in particular in the context of rough bedrocks and low friction coefficients.

The flux conditions can be separated in two classes, depending on the combination of friction and effective-pressure models. The first class is associated with a non-vanishing friction stress at the grounding line, and the dynamical behavior of the ice sheet near the grounding line is then qualitatively similar to the one obtained with a Weertman friction law. Therefore, the derivation of the flux condition is simpler because the divergence of membrane stress can be neglected. On the other hand, the second class is more complex, with a combination of friction stress, gravity stress, and membrane-stress divergence contributing significantly to the mechanical equilibrium near the grounding line. The effective-pressure model considered is also important because for a fixed friction law a system could be categorized depending on the effective-pressure model used.

The present work could be pursued in several directions. Firstly, the effective-pressure models considered are very simple. More realistically, a dynamic hydrology model should be coupled to the ice-sheet model, similar to, e.g., Hewitt [2013]. The study of a flux condition associated with a steady state may no longer be adequate in this case, since recent research has shown the presence of oscillatory phenomena for such systems [Robel et al., 2013, 2016]. Still, a boundary-layer analysis that includes the time evolution for such systems would be interesting.

Another direction for future work concerns the use of flux conditions. While they have allowed to improve our theoretical understanding of marine ice sheets, they are also typically used in ice-sheet codes with coarse meshes that do not allow for resolving the fine details near the grounding line. Assessing their usage, with regards to the latest developments in flux conditions, is a possible research direction. Jointly, it is possible to view this problem through another viewpoint. In a coarse mesh, the unknowns of the problem are macroscopic variables, which represent in a certain sense a local average of phenomena not explicitly solved. The governing equations, and in particular any potential flux condition, must then obey modified equations that take this averaging process into account. To the best of our knowledge, such a multiscale approach has been little applied in glaciology –a notable exception being Schoof [2003]– and the standard rather consists in adding ad-hoc parametrizations.

Finally, it would be interesting to investigate the mechanical behavior of ice sheets near their grounding line with models that are more involved than the shallow-shelf approximation, e.g., the Blatter–Pattyn model [Pattyn, 2003] or the L1L2 model [Schoof and Hindmarsh, 2010].

5.9 Appendix A: Analysis of the leading-order dynamical system: vanishing friction at the grounding line

5.9.1 Problem formulation

The problem consists in finding $\mathcal{X} \mapsto (\xi(\mathcal{X}), \Psi(\mathcal{X}))$ and $\mathcal{Q}_{\rm gl}$ such that

$$\frac{\mathrm{d}\xi}{\mathrm{d}\mathcal{X}} = -\frac{1}{2}\mathcal{Q}_{\rm gl}\,\xi^{2c_1+1}, \quad \text{for } \mathcal{X} > 0, \tag{5.85a}$$

$$\frac{\mathrm{d}\Psi}{\mathrm{d}\mathcal{X}} = -c_2\,\mathcal{Q}_{\rm gl}\xi^{2c_1}\Psi - \frac{1}{4}|\Psi|^{-n-1}\Psi\left(1-\xi^2\right) + \frac{1}{4}, \quad \text{for } \mathcal{X} > 0, \tag{5.85b}$$

$$(\xi, \Psi) = (1, \mathcal{Q}_{\rm gl}^{-1}\delta/8), \quad \text{at } \mathcal{X} = 0, \tag{5.85c}$$

$$(\xi, \Psi) \to (0, 1), \quad \text{as } \mathcal{X} \to +\infty, \tag{5.85d}$$

We consider the Budd friction law with a linear dependence with respect to the effective pressure ($q = 1$), so that $c_1 > 0$ and $0 < c_2 < 1$.

5.9.2 Principle of the analysis

Compared to the case of non-vanishing friction at the grounding line, we remark that the dynamical system defined by (5.85a) and (5.85b) depends on $\mathcal{Q}_{\rm gl}$. It is characterized by the following differential equation:

$$\frac{\mathrm{d}\Psi}{\mathrm{d}\xi} = 2\,c_2\frac{\Psi}{\xi} + \frac{1}{2}\frac{1}{\mathcal{Q}_{\rm gl}}\frac{1}{\xi^{2c_1+1}}\left(|\Psi|^{-n-1}\Psi(1-\xi^2) - 1\right). \tag{5.86}$$

The only fixed point of this dynamical system is the point $(\xi, \Psi) = (0, 1)$. A linearization close to this point reveals the presence of an unstable manifold associated with the vertical axis $\xi = 0$, and a center manifold. A solution to the system of equations (5.85) must therefore go through this manifold, which is unique (similarly to what is described in the appendix of Schoof [2011]). It is characterized by the following behavior, close to the fixed point:

$$\Psi^{\rm c} \sim 1 - \frac{1}{n}\xi^2, \quad \text{as } \xi \to 0, \quad \forall\, \mathcal{Q}_{\rm gl} > 0, \tag{5.87}$$

in which $\Psi^{\rm c} = \Psi^{\rm c}(\xi; \mathcal{Q}_{\rm gl})$ is the Ψ coordinate of the center manifold at position ξ and for a value $\mathcal{Q}_{\rm gl}$.

To show the existence and uniqueness of the system of equations (5.85), the mapping D is defined as follows:

$$\mathcal{Q}_{\rm gl} \quad \mapsto \quad D(\mathcal{Q}_{\rm gl}) = \Psi^{\rm c}(1; \mathcal{Q}_{\rm gl}) - (\delta/8)\mathcal{Q}^{-1}. \tag{5.88}$$

The problem then consists in showing that D admits exactly one root. To do so, we rely on a series of intermediary properties associated with the center manifold as well as the dynamical system defined by (5.85a) and (5.85b):

$$\Psi^{\rm c} \geq (1-\xi^2)^{\frac{1}{n}}, \quad \text{for } \xi \in [0,1], \quad \forall\, \mathcal{Q}_{\rm gl} > 0, \tag{5.89a}$$

$$\partial\Psi^{\rm c}/\partial\mathcal{Q}_{\rm gl} \geq 0, \quad \text{for } \xi \in [0,1], \quad \forall\, \mathcal{Q}_{\rm gl} > 0, \tag{5.89b}$$

$$\Psi^{\rm c} > 0, \quad \text{for } \xi \in [0,1], \quad \forall\, \mathcal{Q}_{\rm gl} > 0, \tag{5.89c}$$

$$\mathrm{d}\Psi/\mathrm{d}\xi|_{\Psi=1} < 0, \quad \text{for } \xi \in]0,1], \quad \text{for } \mathcal{Q}_{\rm gl} = \delta/8. \tag{5.89d}$$

These properties allow to show that D has the desired behavior: it is a continuous, strictly monotonous function which takes both positive and negative values. Indeed, D is a continuous mapping, because the

flow of the dynamical system defined by (5.85a) and (5.85b) is continuous over $(\xi, \Psi) \in]0,1]\times]0,+\infty[$, and $\mathcal{Q}_{\rm gl}$ impacts these equations in a smooth manner. Furthermore, from (5.89b),

$$\frac{\mathrm{d}D}{\mathrm{d}\mathcal{Q}_{\rm gl}}(\mathcal{Q}_{\rm gl}) = \frac{\partial \overline{\Psi}^{\rm c}}{\partial \mathcal{Q}_{\rm gl}}(1;\mathcal{Q}_{\rm gl}) + \frac{\delta}{8}\frac{1}{\mathcal{Q}_{\rm gl}^2} \geq \frac{\delta}{8}\frac{1}{\mathcal{Q}_{\rm gl}} > 0, \quad \forall\, \mathcal{Q}_{\rm gl} > 0. \tag{5.90}$$

From (5.89b) and (5.89c),

$$\Psi^{\rm c}(1;\mathcal{Q}_{\rm gl}) > 0 \quad \text{and} \quad \frac{\partial \Psi^{\rm c}}{\partial \mathcal{Q}_{\rm gl}}(1;\mathcal{Q}_{\rm gl}) \geq 0, \quad \forall\, \mathcal{Q}_{\rm gl} > 0. \tag{5.91}$$

In particular, this implies that $\lim_{\mathcal{Q}_{\rm gl}\to+\infty} \Psi^{\rm c}(1;\mathcal{Q}_{\rm gl}) > 0$; hence, $\lim_{\mathcal{Q}_{\rm gl}\to+\infty} D(\mathcal{Q}_{\rm gl}) > 0$. Finally, fix $\mathcal{Q}_{\rm gl} = \delta/8$. From (5.87), an orbit associated with the center manifold is below the $\Psi = 1$ line for sufficiently small values of ξ. Furthermore, it cannot cross this line because (5.89d) prevents it. Therefore, $\Psi^{\rm c}(1;\delta/8) < 1$, which yields $D(\delta/8) < 0$.

5.9.3 Derivation of the intermediary properties

The form of the center manifold close to the fixed point is obtained with an ansatz of the form $\Psi^{\rm c}(\xi) = 1 + C\,\xi^{\eta}$. Balancing the leading powers in ξ closed to the fixed point leads to $C = -1/n$ and $\eta = 2$, as announced. In can be deduced from (5.87) that

$$\frac{\partial \Psi^{\rm c}}{\partial \xi} \sim -\frac{2}{n}\xi \quad \text{and} \quad \frac{\partial \Psi^{\rm c}}{\partial \mathcal{Q}_{\rm gl}} \to 0, \quad \text{as } \xi \to 0, \quad \forall\, \mathcal{Q}_{\rm gl} > 0. \tag{5.92}$$

Furthermore, close to the fixed point, $\Psi^{\rm c} > 0$. From (5.86), $\mathrm{d}\Psi/\mathrm{d}\xi \to +\infty$ as $\Psi \to 0$ for any fixed $\xi \in]0,1[$ and $\mathcal{Q}_{\rm gl} > 0$. Therefore, the center manifold cannot cross the $\Psi = 0$ line, and

$$\Psi^{\rm c} \geq 0, \quad \xi \in [0,1], \quad \forall\, \mathcal{Q}_{\rm gl} > 0. \tag{5.93}$$

We now derive the properties (5.89a)–(5.89d). Fix $\mathcal{Q}_{\rm gl} > 0$. Using (5.92), $\partial\Psi^{\rm c}/\partial\xi < 0$ for sufficiently small values of ξ. Then, (5.86) yields $(\Psi^{\rm c})^{-n}(1-\xi^2) - 1 < 0$, sufficiently close to the fixed point. Furthermore,

$$\left.\frac{\mathrm{d}\Psi}{\mathrm{d}\xi}\right|_{\Psi=(1-\xi^2)^{\frac{1}{n}}} = 2\,c_2\frac{\Psi}{\xi} > 0, \quad \text{for } \xi \in]0,1]. \tag{5.94}$$

This implies that the center manifold, which is initially above the curve $\Psi = (1-\xi^2)^{1/n}$, cannot cross it, hence (5.89a) is verified.

Using (5.86), we compute

$$\frac{\partial}{\partial\xi}\frac{\partial\Psi^{\rm c}}{\partial\mathcal{Q}_{\rm gl}} = -\frac{1}{2}\frac{1}{\mathcal{Q}_{\rm gl}^2}\frac{|\Psi^{\rm c}|^{-n-1}\Psi^{\rm c}(1-\xi^2)-1}{\xi^{2c_1+1}} + \left[\frac{2\,c_2}{\xi} - \frac{1}{2}\frac{n}{\mathcal{Q}_{\rm gl}}\frac{|\Psi^{\rm c}|^{-n-2}\Psi^{\rm c}(1-\xi^2)}{\xi^{2c_1+1}}\right]\frac{\partial\Psi^{\rm c}}{\partial\mathcal{Q}_{\rm gl}}, \tag{5.95}$$

where we have assumed that we can interchange the partial derivatives. For $\xi \to 0$, $\partial\Psi^{\rm c}/\partial\mathcal{Q}_{\rm gl} \to 0$ using (5.92). Based on (5.89a), this implies that $\partial(\partial\Psi^{\rm c}/\partial\mathcal{Q}_{\rm gl})/\partial\xi \geq 0$ as $\xi \to 0$. Hence, $\partial\Psi^{\rm c}/\partial\mathcal{Q}_{\rm gl}$ is initially equal to zero, and does not decrease with ξ for sufficiently small values of ξ. Furthermore, it will always be non-negative because if $\partial\Psi^{\rm c}/\partial\mathcal{Q}_{\rm gl} = 0$, then $\partial(\partial\Psi^{\rm c}/\partial\mathcal{Q}_{\rm gl})/\partial\xi \geq 0$ from (5.95). This yields (5.89b).

From (5.93), $\Psi^{\rm c} \geq 0$ for $\xi \in [0,1]$. From the previous discussion, the center manifold cannot cross the $\Psi = 0$ line for $\xi \in (0,1)$. Therefore, to show that $\Psi^{\rm c} > 0$ for $\xi \in [0,1]$, we only have to discuss the case $\Psi^{\rm c} = 0$ at $\xi = 1$. To do so, we show that the point $(\xi,\Psi) = (1,0)$ is not accessible. Because $\mathrm{d}\Psi/\mathrm{d}\xi$ is ill-defined if $\Psi = 0$, we switch back to the $(\tilde{U},\tilde{W})$ variables, and to the system of equations (5.27). The point $(\xi,\Psi) = (1,0)$ corresponds to the point $(\tilde{U},\tilde{W}) = (\tilde{Q}_{\rm gl},0)$. By looking at the flow

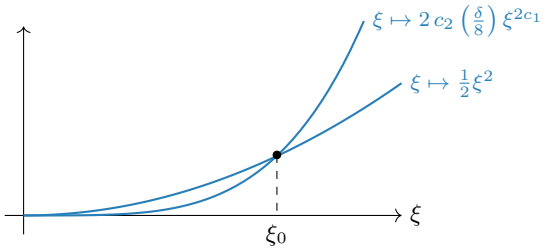

Figure 5.16: Schematic representation of functions of ξ in order to determine the sign of $f(\xi)$. Note that $c_1 > 1$ and $0 < c_2 < 1$.

near that point, we conclude that this point is a degenerate spiral. Hence, it cannot be reached from an orbit that comes from the domain $(\tilde{U}, \tilde{W}) \in [0, \tilde{Q}_{\mathrm{gl}}[\times]0, +\infty[$. This point is not accessible by the orbit that we consider, and $\Psi^{\mathrm{c}} > 0$ for $\xi = 1$. This leads to (5.89c).

Finally, evaluating (5.86) at $\Psi = 1$ and for $\mathcal{Q}_{\mathrm{gl}} = \delta/8$ yields

$$\left.\frac{\mathrm{d}\Psi}{\mathrm{d}\xi}\right|_{\Psi=1} = \frac{1}{\xi^{1+c_1}}\left(\frac{\delta}{8}\right)^{-1}\left[2\,c_2\left(\frac{\delta}{8}\right)\xi^{2c_1} - \frac{1}{2}\xi^2\right] \equiv \frac{1}{\xi^{1+c_1}}\left(\frac{\delta}{8}\right)^{-1} f(\xi). \tag{5.96a}$$

The terms defining the function f depends on ξ as in figure 5.16. We have

$$f(1) = 2\,c_2\left(\frac{\delta}{8}\right) - \frac{1}{2} < \frac{\delta}{4} - \frac{1}{2} < 0 \tag{5.97}$$

because $\delta \leq 1$ as $\rho, \rho_{\mathrm{w}} > 0$. This means that ξ_0, the strictly-positive point where $f(\xi_0) = 0$, is such that $\xi_0 > 1$. Therefore, $f(\xi) < 0$ for $\xi \in]0, 1]$, and $\mathrm{d}\Psi/\mathrm{d}\xi|_{\Psi=1} < 0$ for $\xi \in]0, 1]$. This corresponds to (5.89d).

5.10 Appendix B: Numerical solving strategy for finding $\tilde{Q}_{\mathrm{gl}}$

To determine the numerical prefactor $\tilde{Q}_{\mathrm{gl}}$ (or, equivalently, $\check{Q}_{\mathrm{gl}}$) appearing in the system of equations (5.27) and in the flux conditions (5.29a) and (5.29b), we propose the following numerical strategy. Consider the phase plane associated with the dynamical system defined by equations (5.27a) and (5.27b) (figure 5.17). For any $\tilde{Q}_{\mathrm{gl}}$, the first quadrant of the phase plane is split into two regions that are separated by an orbit that goes towards the origin; one region above it and the other one below it. The solution sought is the trajectory that, starting from the boundary condition at $\tilde{X} = 0$, that is, equation (5.27c), reaches the origin for $\tilde{X} \to +\infty$ when following the flow defined by equations (5.27a) and (5.27b).

If $\tilde{Q}_{\mathrm{gl}}$ is too large, then a trajectory that starts from the boundary condition at $\tilde{X} = 0$ is in the lower region of the phase-plane and never reaches the origin; on the other hand, if $\tilde{Q}_{\mathrm{gl}}$ is too small, then the trajectory stays in the upper part of the phase plane. The numerical approach to find a solution can then be described. Let us assume that we have two values $\tilde{Q}_{\mathrm{gl},-}$ and $\tilde{Q}_{\mathrm{gl},+}$, associated respectively to a trajectory that stays in the lower part and in the upper part of the phase plane, similarly to figure 5.17a and figure 5.17c. A bisection-like method can then be applied: the trajectory associated with $\tilde{Q}_{\mathrm{gl}} = (\tilde{Q}_{\mathrm{gl},-} + \tilde{Q}_{\mathrm{gl},+})/2$ can be computed, and if it is in the lower part (resp. upper part) of the phase plane, then it replaces $\tilde{Q}_{\mathrm{gl},-}$ (resp. $\tilde{Q}_{\mathrm{gl},+}$). Eventually, $\tilde{Q}_{\mathrm{gl}}$ will converge towards the correct value $\tilde{Q}_{\mathrm{gl},*}$ which is associated with the solution to (5.27). It follows that the corresponding trajectory is the one that separates the phase plane in two (figure 5.17b). We note that a similar approach has been used in Hindmarsh [2012], to tackle a different but related problem. Table 5.4 shows results, i.e., the values of $\tilde{Q}_{\mathrm{gl}}$, for combinations of the parameters $(1_{\mathrm{A}}, n, p, q, \delta)$ that correspond to several friction laws of interest.

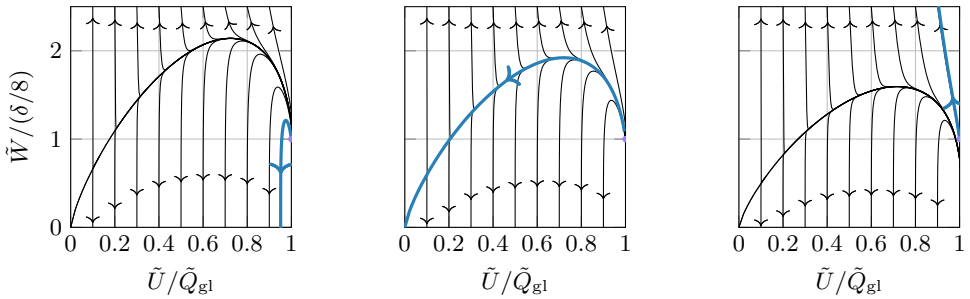

(a) $\tilde{Q}_{\mathrm{gl}} > \tilde{Q}_{\mathrm{gl},*}$. (b) $\tilde{Q}_{\mathrm{gl}} = \tilde{Q}_{\mathrm{gl},*}$. (c) $\tilde{Q}_{\mathrm{gl}} < \tilde{Q}_{\mathrm{gl},*}$.

Figure 5.17: Form of the phase plane associated with the dynamical system defined by (5.27a)–(5.27b), for different values of $\tilde{Q}_{\mathrm{gl}}$, where $\tilde{Q}_{\mathrm{gl},*}$ is associated with a solution to (5.27). The blue curves represent the trajectories that go through $(\tilde{U}, \tilde{W}) = (\tilde{Q}_{\mathrm{gl}}, \delta/8)$.

Friction law		Effective pressure	n	δ	$\tilde{Q}_{\mathrm{gl}}$	$\check{Q}_{\mathrm{gl}}$
Weertman	$(p = 1/3)$	/	3	0.1	5.25×10^{-5}	1.00
Coulomb		$\mathrm{N_A}$ $(1_{\mathrm{A}} = 1)$	3	0.1	9.63×10^{-5}	0.62
Coulomb		$\mathrm{N_B}$ $(1_{\mathrm{A}} = 0)$	3	0.1	1.92×10^{-6}	0.98
Budd	$(p = 1/3, q = 1)$	$\mathrm{N_A}$ $(1_{\mathrm{A}} = 1)$	3	0.1	9.95×10^{-4}	0.71
Budd	$(p = 1/3, q = 1)$	$\mathrm{N_B}$ $(1_{\mathrm{A}} = 0)$	3	0.1	5.18×10^{-5}	0.99

Table 5.4: Examples of values of $\tilde{Q}_{\mathrm{gl}}$ and $\check{Q}_{\mathrm{gl}}$ for combinations of $(1_{\mathrm{A}}, n, p, q, \delta)$ associated with several friction laws of interest. The values of $\tilde{Q}_{\mathrm{gl}}$ have been computed using the described numerical method. The values of $\check{Q}_{\mathrm{gl}}$ have been computed according to $\check{Q}_{\mathrm{gl}} = \Delta^{-r}\tilde{Q}_{\mathrm{gl}}$ with $r = (n - 1_{\mathrm{A}}q)/(p + 1)$. Because $q = 0$ for the Weertman friction law, the associated problem does not depend on the type of effective-pressure model.

6

A fast and simplified subglacial hydrological model

*E. Kazmierczak**, *T. Gregov**, *V. Coulon, and F. Pattyn*
A fast and simplified subglacial hydrological model for the Antarctic Ice Sheet and outlet glaciers
The Cryosphere, 2024

**Equal contribution*

We present a novel and computationally efficient subglacial hydrological model that represents in a simplified way both hard and soft bed rheologies as well as an automatic switch between efficient and inefficient subglacial discharge, designed for the Antarctic Ice Sheet. The subglacial model is dynamically linked to a regularized Coulomb friction law, allowing for a coupled evolution of the ice sheet on decadal to centennial time scales. It does not explicitly simulate the details of water conduits at the local scale and assumes that subglacial hydrology is in quasi-static equilibrium with the ice sheet, which makes the computations very fast. The hydrological model is tested on an idealized marine ice sheet and subsequently applied to the drainage basin of Thwaites Glacier, West Antarctica, that is composed of a heterogeneous (hard/soft) bed. We find that accounting for subglacial hydrology in the sliding law accelerates the grounding-line retreat of Thwaites Glacier under present-day climatic conditions. Highest retreat rates are obtained for hard bed configurations and/or inefficient drainage systems. We show that the sensitivity is particularly driven by large gradients in effective pressure, more so than the value of effective pressure itself, in the vicinity of the grounding line. Therefore, we advocate for a better understanding of the subglacial system with respect to both the spatial and temporal variability in effective pressure and the rheological conditions/properties of the bed.

6.1 Introduction

Due to the ubiquitous and permanent ice cover, subglacial environments in Antarctica are hard to observe. The lack of direct observations results in major uncertainties in ice-dynamical behavior, especially since the ice-bed interface is one of the main boundary layers that influence the overall dynamics of the ice sheet. In ice-sheet models, basal processes are generally translated in a basal sliding law, that, for the sake of simplicity, is largely parameterized. However, recent studies have shown that the level of plasticity of basal sliding, which mainly depends on the bed rheology, is a highly controlling factor in terms of mass change of the Antarctic Ice Sheet [Brondex et al., 2019; Bulthuis et al., 2019; Sun et al., 2020;

Kazmierczak et al., 2022]. The rheology of the bed broadly covers two categories, i.e., (i) hard beds, composed of bedrock and whose rigidity is greater than the ice, and also considered as non-deformable and (ii) soft beds, or a subglacial till cover, whose rigidity is lower than the ice, and which can easily be deformed [Muto et al., 2019]. The rheology is further influenced by the presence of subglacial water, which is present underneath more than 50% of the ice sheet due to the thick ice cover [Robin et al., 1970; Smith et al., 2009; Pattyn, 2010]. The spatial organization of the subglacial drainage system remains poorly known, although recent attempts led to improvements regarding the modeling of subglacial water flow [Livingstone et al., 2013; Willis et al., 2016; Dow et al., 2022; Dow, 2022a; Hager et al., 2022].

The nature of drainage systems and their tendency to organize into channels depend on subglacial water flow as well as bed rheology. The morphology of subglacial water drainage systems influences basal sliding by modifying the basal boundary conditions [Hewitt, 2011]. Furthermore, within drainage systems, water flow and water pressure also vary greatly. Physically, the presence of subglacial water directly influences basal sliding by lubricating the bedrock or by weakening the till strength. Budd et al. [1979] proposed to link subglacial water to basal sliding through the effective pressure (which is the ice overburden pressure, i.e., the downward pressure due to the weight of overlying ice, minus the subglacial water pressure). The link between basal sliding and subglacial hydrology through the effective pressure is used in most glacier and ice-sheet studies [Pattyn, 1996; Hoffman and Price, 2014; Beyer et al., 2018; Gagliardini and Werder, 2018]. Other approaches are the use of subglacial water thickness [Weertman and Birchfield, 1982; Budd and Jenssen, 1987; Alley et al., 1989; Johnson and Fastook, 2002] or subglacial water flux [Pattyn et al., 2005; Goeller et al., 2013] as a control on basal sliding. In this study, we consider basal sliding a function of effective pressure at the base of the ice sheet.

Generally, bed areas characterized by a low effective pressure correspond to regions of faster ice flow [Iken and Bindschadler, 1986; Iverson et al., 1999] and consequently may become more sensitive (react much faster and/or exhibit more ice change) to climate forcing [Kazmierczak et al., 2022]. However, the effective pressure at the base of the ice sheet is difficult to determine as it depends on bed rheology, the presence and distribution of subglacial water, the distribution of subglacial till and its thickness, etc. Furthermore, subglacial processes occur on time scales that can be as small as a few hours [e.g., Clarke, 2005]. Such time scales are several orders of magnitude smaller than the typical response times of glaciers and ice sheets, which are at least of the order of years. This discrepancy hampers numerical coupling between subglacial hydrology and the ice dynamical response. Another limiting factor is the spatial resolution on which these processes occur, hence the computational demand it entails. For instance, state-of-the-art hydrological models such as `GlaDS` [Werder et al., 2013] are –due to their high spatial and temporal resolution– extremely computationally demanding, and their applications to evolving ice sheets are often limited to the initialization of the ice-sheet system [e.g., McArthur et al., 2023; Pelle et al., 2023]. Although there have been recent attempts to reduce their computational cost using data-driven methods [Verjans and Robel, 2024], physics-based approaches have not yet been widely explored to achieve this goal.

In this paper, we propose a simplified model of the complex subglacial system that allows us to dynamically link subglacial hydrology to basal sliding for various bed types (hard and soft). The model considers different spatially- and temporally-varying subglacial water drainage systems. Their morphologies depend both on the subglacial water flux (distributed or channelized) and the rheology of the bed. The approach allows us to evaluate the impact of the subglacial hydrological system and its evolution on the ice-sheet response in a hard and a soft bed environment in large-scale models and with reasonable computational times. By large-scale models, we mean models that have a spatial grid size that is orders of magnitude larger than that of the hydrological system. The model also allows us to deal with mixed beds, composed of zones of different rigidity.

In section 6.2, we describe the hydrological model and its implementation. We first evaluate our model for an idealized marine ice sheet in section 6.3, to evaluate the implementation and robustness

of the method. Subsequently, we apply our methodology to Thwaites Glacier, West Antarctica (section 6.4), generally characterized by a heterogeneous bed composed of soft and hard bed zones [Joughin et al., 2009; Schroeder et al., 2014; Muto et al., 2019]. We discuss the impact of the dynamic subglacial hydrology linked to basal sliding as well as the limitations of the model in section 6.5. Finally, we conclude on the relevance of our findings in section 6.6.

6.2 Model description

6.2.1 Ice-flow model

We employ the Kori-ULB ice-sheet model [previously called f.ETISh; Pattyn, 2017; Seroussi et al., 2019, 2020; Sun et al., 2020; Coulon et al., 2024b], which is a vertically integrated thermomechanically-coupled, hybrid ice-sheet/ice-shelf model. It combines the shallow-ice approximation for ice deformation with the shallow-shelf approximation for basal sliding in a similar way as in Winkelmann et al. [2011]. To account for sliding on both a hard and soft bed [Cuffey and Paterson, 2010; Beaud et al., 2022], we employ a regularized Coulomb friction law [Joughin et al., 2019; Zoet and Iverson, 2020]. Such law allows for a smooth transition between a power-law behavior at low velocity and a plastic Coulomb behavior at high velocity, and takes the following form:

$$\boldsymbol{\tau}_\mathrm{b} = CN \left(\frac{\|\boldsymbol{v}_\mathrm{b}\|}{\|\boldsymbol{v}_\mathrm{b}\| + v_0} \right)^{\frac{1}{m}} \frac{\boldsymbol{v}_\mathrm{b}}{\|\boldsymbol{v}_\mathrm{b}\|}, \tag{6.1}$$

where $\boldsymbol{\tau}_\mathrm{b}$ is the basal shear or friction stress, N is the effective pressure, C is a friction coefficient limiting the shear stress to a maximum plastic value CN, and $\boldsymbol{v}_\mathrm{b}$ is the basal sliding velocity. The velocity threshold v_0 is a parameter that controls the onset of plasticity in the friction law. A value of $m = 3$ and $v_0 = 300\,\mathrm{m\,a^{-1}}$ are taken as in Joughin et al. [2019]. A complete list of symbols, and their corresponding values and units, can be found in appendix A.

6.2.2 Hydrological model

Subglacial water in Antarctica essentially stems from basal melting of areas of the ice sheet that are at the pressure melting point [Pattyn et al., 2005; Pattyn, 2010; Beyer et al., 2018; Dow, 2022a], due to dissipative phenomena at the ice-bedrock interface. It is absent when the basal ice is at a temperature below the pressure melting point [Pattyn, 2010; Livingstone et al., 2013]. Limited surface water infiltration towards the bed has been observed in Antarctica, contrary to the Greenland Ice Sheet [Bell et al., 2018]. The presence of subglacial water will lead to a reduction of the contact between the ice and the subglacial substrate, i.e., it will decrease the value of the effective pressure $N = p_\mathrm{o} - p_\mathrm{w}$, with p_o the ice overburden pressure and p_w the subglacial water pressure. It is generally assumed that the ice overburden pressure is cryostatic, so that $p_\mathrm{o} = \rho_\mathrm{i} g h$ where ρ_i is the ice density, g is the gravitational acceleration, and h is the ice thickness. For a given ice-sheet geometry, the effective pressure is therefore fully characterized by the subglacial water pressure.

Alternatively, one can consider a description based on potentials. Introducing the hydraulic potential $\phi = \rho_\mathrm{w} g b + p_\mathrm{w}$ and the geometric potential $\phi_0 = \rho_\mathrm{i} g h + \rho_\mathrm{w} g b$, ρ_w being the density of fresh water and b the bedrock elevation with respect to the local sea-level height, the effective pressure is then the difference between both, i.e., $N = \phi_0 - \phi$. The rationale behind this description is that water flows from regions where the hydraulic potential is high to regions where the potential is low [Shreve, 1972].

In this paper, we attempt to model together efficient and inefficient water flow over both hard and soft beds. Generally, efficient systems transport large water fluxes and are characterized by localized channelized flow, while inefficient systems take the form of distributed water flow. We define two spatial scales: a global scale, which is the same as the one used for the ice-sheet model and that is typically of

the order of kilometers, and a local scale, associated with a water conduit, and that is much smaller than the global one (observations suggest that channels are meters to at most a few hundreds meters wide, that maximal width being reached close to the grounding line [Drews et al., 2017]). The computation of the water flow is done at the global scale, while the computation of the effective pressure is done at the local scale. For the latter, we consider a single element of the hydrological system, which we refer generically to as 'conduit'. The term conduit is used for localized drainage systems (such as cavities, channels, canals), as opposed to diffuse drainage systems (such as continuous films, diffuse water flow within sediments). This applies to efficient flow (channel or canal), or to elements of an inefficient system (cavity or patchy film between clasts), applicable to both a hard or a soft bed. In particular, we do not use 'conduit' as a synonym for 'channel', as a conduit can correspond to other types of hydrological elements. Such approach can be seen as a sub-grid parametrization of the effective pressure; a similar procedure was described in Gowan et al. [2023]. The idea of unifying both inefficient and efficient water flow has been previously explored in Arnold and Sharp [2002], in Schoof [2010b], and in Sommers et al. [2018]. Our approach is shown schematically in figure 6.1 and described in detail in the next subsections.

Simplifying assumptions

Our model is constructed from multiple approximations that simplify the physics describing subglacial hydrology. It differs from recent studies aiming to develop high-resolution models, such as `GlaDS` [Werder et al., 2013], `SHAKTI` [Sommers et al., 2018], `CUAS` [Beyer et al., 2018], and the subglacial hydrology components within `PISM` [Bueler and van Pelt, 2015] and `MALI` [Hoffman et al., 2018]. These models typically take the form of a series of coupled partial differential equations that are computationally challenging to solve. Furthermore, these models involve a large number of parameters, many being poorly constrained. Finally, due to their high spatial and temporal resolution they are often computationally demanding. The latter may limit their application to drainage basins or single glaciers on time scales of a few years. By contrast, our model is computationally cheap, with the computational time associated with the subglacial hydrology calculation representing only a small fraction of the computational time associated with the ice-sheet model. This allows us to study the impact of subglacial hydrology on ice dynamics on a large scale and at a limited computational cost, while at the same time keeping the essential features of complex subglacial hydrology models.

The key simplifying assumptions are given by the following:

1. There is limited temporal melt variability so that the hydrological system is in a quasi-static equilibrium with respect to the ice-sheet geometry. Therefore, changes in ice geometry will be the main driver for changes in subglacial water variability (both spatial and temporal).

2. A few kilometers upstream of the grounding line, the hydraulic gradient is approximated by the geometrical gradient.

3. The drainage density, that is, the number of conduits per grid cell, is uniform.

4. The effective-pressure distribution is not calculated at the sub-grid (local) level.

The first assumption is based on several studies of subglacial hydrology in Antarctica [Le Brocq et al., 2009; Pattyn, 2010; Kazmierczak et al., 2022], among others, that demonstrate that –contrary to the Greenland Ice Sheet– there is limited surface meltwater infiltration. Hence, changes in hydrology are primarily due to changes in ice geometry. Since the time scales associated with water flow are much smaller than those associated with ice flow, subglacial hydrology automatically adapts to any change in ice geometry and reaches the associated equilibrium. The second assumption is motivated by a scaling analysis through an estimation of the dimensionless ratio $\eta := [\nabla N]/[\nabla \phi_0]$, where $[\nabla N]$ is the scale of the spatial gradients for the effective pressure and $[\nabla \phi_0]$ is the characteristic scale for the geometric potential gradient. For the former we take $[\nabla N] = [N]/[x]$, with $[N] = 1\,\text{MPa}$ and $[x] = 10^3\,\text{km}$. For the latter we take $[\nabla \phi_0] = 5 \times 10^{-2}\,\text{MPa}\,\text{km}^{-1}$, which is a plausible value for ice sheets [Hewitt, 2011].

This results in $\eta = 2 \times 10^{-2} \ll 1$, suggesting that $\|\nabla N\| \ll \|\nabla \phi_0\|$ and $\nabla \phi \approx \nabla \phi_0$. We further note that profiles obtained with a high-resolution subglacial hydrology model suggest that $\nabla \phi$ and $\nabla \phi_0$ have a correlation of at least $\sim 80\%$ for a region that is several kilometers upstream of the grounding line (see Supplementary Material S1). Finally, the third and fourth assumptions follow from our modeling approach, where we do not describe the effective pressure at the sub-grid scale and where we assume the same number of conduits in each grid cell, similar to Gowan et al. [2023]. However, the effective pressure within a channel may well differ from its value away from the channel, which is something that is not taken into account. Consequently, these last assumptions are the most likely to be debatable.

Subglacial water routing

Let us denote by Ω the grounded ice-sheet domain where subglacial water is routed. This domain evolves over time according to both internal conditions (e.g., changes in ice velocity) and external conditions (e.g., changes in sub-shelf melt). Its boundary is partitioned into non-overlapping subsets Γ_d and Γ_gl, representing the divides of the considered basin and the grounding line, respectively. The subglacial water flux, $\boldsymbol{q}_\mathrm{w}$ ($\mathrm{m}^2\ \mathrm{s}^{-1}$), is determined from a mass balance equation that takes the form of a steady-state continuity equation:

$$\nabla \cdot \boldsymbol{q}_\mathrm{w} = \frac{\dot{m}}{\rho_\mathrm{w}}, \quad \text{in } \Omega, \tag{6.2a}$$

$$\boldsymbol{q}_\mathrm{w} \cdot \boldsymbol{n} = 0, \quad \text{on } \Gamma_\mathrm{d}, \tag{6.2b}$$

in which ∇ is the horizontal spatial gradient, $\boldsymbol{n}$ is the outward normal to the boundary Γ_d, and $\dot{m}$ is the melt rate ($\mathrm{kg\ m}^{-2}\ \mathrm{s}^{-1}$). The latter is computed from the energy balance within the ice sheet and includes effects of geothermal heat flux, frictional heating due to the motion of both ice and subglacial water, and thermal conduction, i.e.,

$$\dot{m} = \frac{G + \boldsymbol{\tau}_\mathrm{b} \cdot \boldsymbol{v}_\mathrm{b} - q_T}{\mathcal{L}_\mathrm{w}} + \dot{m}_\mathrm{w}, \tag{6.3}$$

where G is the geothermal heat flux, q_T is the thermal conduction flux, L_w is the latent heat for ice, and $\dot{m}_\mathrm{w} = |\boldsymbol{q}_\mathrm{w} \cdot \nabla \phi| / L_\mathrm{w}$ is the water melt rate due to the dissipated energy from the subglacial water conduits. However, we do not include this last term in the computation of the subglacial water in our simulations as it was found to be negligible compared to the other terms. Note that by writing the system of equations (6.2), we have assumed that the subglacial water system is in steady state with respect to a given ice-sheet geometry. As previously mentioned, we justify this assumption by the observation that the time scales associated with subglacial water flow are much smaller than the ones associated with ice flow. By construction, this inhibits oscillations in the coupled system formed by the ice sheet and the subglacial hydrology, which are known to exist for ice streams on time scales of thousands of years [Robel et al., 2013], well beyond the time scales considered here.

Equation (6.2) is solved at the global scale, using the water routing of Le Brocq et al. [2009] to compute the water flux based on the geometric potential gradient $\nabla \phi_0$. As the subglacial water flux $\boldsymbol{q}_\mathrm{w}$ is in fact proportional to $\nabla \phi$ instead of $\nabla \phi_0$, we should use the potential gradient $\nabla \phi$ itself. Nonetheless, in view of the assumption that $\nabla \phi \approx \nabla \phi_0$ over most of the domain,we choose not to do so as this allows us to decouple the water routing solver from the effective-pressure calculation.

Subglacial effective pressure

The distributed water flux $\boldsymbol{q}_\mathrm{w}$ needs to be converted to the local volumetric water flux Q_w ($\mathrm{m}^3\ \mathrm{s}^{-1}$) within the water conduits. Since the distance between the conduits is given by l_c, it follows that there are $\Delta x / l_\mathrm{c}$ conduits within each square grid cell of size $\Delta x \times \Delta x$ of the ice-sheet mesh. Hence, the local water flux is given by [Gowan et al., 2023]:

$$Q_\mathrm{w} = \frac{\|\boldsymbol{q}_\mathrm{w}\|\, \Delta x}{\Delta x / l_\mathrm{c}} = \|\boldsymbol{q}_\mathrm{w}\|\, l_\mathrm{c}. \tag{6.4}$$

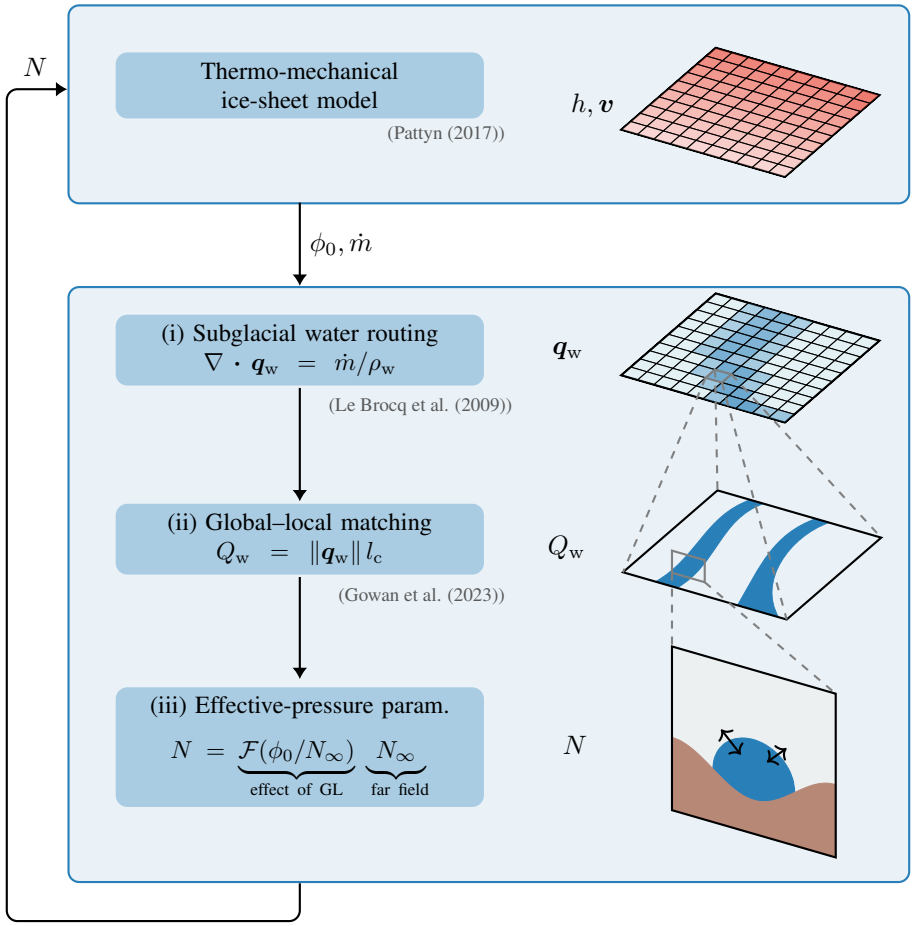

Figure 6.1: Flowchart of the dynamical linkage between the ice sheet and the subglacial hydrology. At each time step, the ice-sheet model provides the basal melt rate $\dot{m}$ and the geometrical potential ϕ_0. Based on these, the effective pressure is computed in three steps: (i) The globally distributed subglacial water flux $\boldsymbol{q}_\mathrm{w}$ is computed according to Le Brocq et al. [2009]; (ii) a connection between both global and local (conduit) scale is obtained by specifying the distance l_c between the conduits [Gowan et al., 2023], yielding a volumetric water flux Q_w in each conduit; (iii) the effective pressure N is computed for each conduit via a parametrization where $\mathcal{F}(\phi_0/N_\infty) = \mathrm{erf}[(\sqrt{\pi}/2)\phi_0/N_\infty]$ serves as a correction factor for the impact of the grounding line (GL), and where N_∞ is the effective pressure far upstream of the grounding line. This effective pressure is then used by the large-scale ice-sheet model and is the same for all conduits that belong to the same grid cell.

We take $l_c = 10\,\text{km}$, which is similar to the value considered in Gowan et al. [2023] based on observations of distances between eskers formed under the Laurentide Ice Sheet [Storrar et al., 2014]. However, we acknowledge that this distance is likely to be a function of the drainage system, but leave this to be investigated in future work.

While the water mass balance is defined at the global scale, conduits must evolve at the local scale, which requires water flow to be resolved at this scale, irrespective of whether it is associated with a distributed or a localized flow pattern, similarly to what is done in Arnold and Sharp [2002], Schoof [2010b], and Gowan et al. [2023]. Let us denote by S the cross-section area in a conduit, with characteristic width and thickness L and H (Figure 6.2), so that $S = H\,L$. The equations governing the geometry of the conduits and the flow of water within them in a quasi-static regime are given by the following:

$$Q_\text{w} = K\,S^\alpha \|\nabla\phi\|^{\beta-1}, \text{ in } \Omega, \tag{6.5a}$$

$$\|\boldsymbol{v}_\text{b}\| h_\text{b} + \frac{Q_\text{w}\|\nabla\phi\|}{\rho_\text{i} L_\text{w}} = 2\,n^{-n} A L^2 |N|^{n-1} N, \text{ in } \Omega, \tag{6.5b}$$

$$N = 0, \text{ on } \Gamma_\text{gl}, \tag{6.5c}$$

where h_b is the characteristic height of bed obstacles, and A and n are the viscosity parameters in Glen's flow law [Glen, 1955; Paterson, 1994], respectively. The first equation is a Darcy–Weisbach constitutive equation for the water flow with K a conductivity coefficient, and α and β exponents. Following Schoof [2010b], we assume a turbulent flow, with $\alpha = 5/4$, $\beta = 3/2$, and $K = (2/\pi)^{1/4}\sqrt{(\pi+2)/(\rho_\text{w} f)}$, where f is a friction coefficient [e.g., Clarke, 1996]. The choice of a turbulent flow is justified for large water fluxes, which is the case for converging subglacial channels near the grounding line. Other choices have been considered for subglacial hydrology in the literature; we refer to Hewitt [2011] and Werder et al. [2013] for laminar parametrizations, and to Hill et al. [2023] for a discussion of the transition between laminar and turbulent flow and their range of validity. The second equation describes the equilibrium between opening and closure rates of the conduits, assuming that the hydrological system is at equilibrium. In general, opening and closing of subglacial water systems are due to various mechanisms depending on the drainage system and bed type involved. These mechanisms include, amongst others, melt of the subglacial conduit walls, sliding over bed protrusions, erosion of sediments, regelation, creep of ice, and creep of sediments [Hewitt, 2011; Bueler and van Pelt, 2015]. Here, we consider opening rates associated with sliding over bed obstacles, melting of the conduit walls, and a closure rate due to ice creep [Nye, 1953]. The bed obstacles correspond to bed protrusions if the bed is hard, and to clasts if the bed is soft, and our model treats these cases the same. Note that the first type of opening rate is associated with an inefficient drainage system, while the second one is associated with an efficient one. Finally, the third equation comes from the equality between the subglacial water pressure and the sea-water pressure at the grounding line [Drews et al., 2017], which holds because we are considering marine-terminated ice sheets.

The above model (6.5) is similar to the one that was used by Schoof [2010b] to describe both linked-cavity systems (i.e., inefficient systems) and channels (i.e., efficient systems). Linked cavities have first been described by Kamb [1987], following earlier theoretical developments related to sliding with cavitation [Lliboutry, 1968; Kamb, 1970; Lliboutry, 1979; Iken, 1981; Fowler, 1986a, 1987]. For larger water fluxes, the flow in cavities localizes into channels and the system becomes efficient, forming so-called R-channels [Röthlisberger, 1972], defined as semi-circular tunnels formed within the ice of the glacier. Such conduits allow water to flow rapidly and more efficiently [Kamb et al., 1985; Iken et al., 1993; Hubbard et al., 1995; Lappegard et al., 2006].

Our model is also analogous to those that describe ice flow over soft beds. In a soft-bed system, water can infiltrate the till and weaken its strength, hence increasing basal motion. In Antarctica, till properties indicate a low porosity and hydraulic conductivity, obstructing the water circulation in the till itself and leading to water saturation [Tulaczyk et al., 2000a,b]. Indeed, as the drainage rate from the

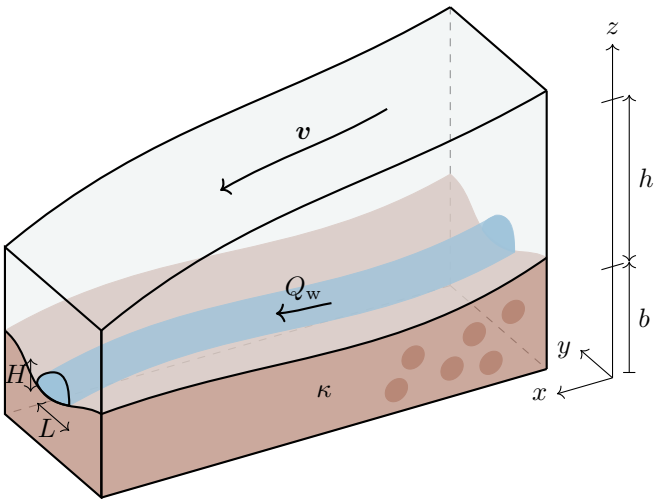

Figure 6.2: Schematic representation of a conduit (here, of a channel) in the subglacial hydrological system, characterized by a cross-sectional width L and thickness H and by a water flux Q_w. The ice sheet has a thickness h, is moving at a velocity $\boldsymbol{v}$, and overlays the bedrock whose upper surface is located at $z = b$. The bedrock type is parameterized by κ, with $\kappa = 1$ corresponding to a soft bed, $\kappa = 0$ corresponding to a hard bed, and $0 < \kappa < 1$ corresponding to a mixed bed.

till towards a subglacial aquifer is much smaller than the basal melt rate, subglacial till is supposed to be water-saturated [Bueler and van Pelt, 2015; Kazmierczak et al., 2022]. Water that cannot infiltrate the till will take the form of a water film that flows around clasts higher than the water thickness [Creyts and Schoof, 2009; Kyrke-Smith et al., 2014]. For large subglacial water fluxes, the film becomes unstable and conduits form a channelized network [Walder, 1982]. For ice sheets, efficient conduits on a soft bed take the form of canals, which are incised in the till. They are typically much wider and shallower compared to hard-bed channels [Walder and Fowler, 1994]. These different types of drainage systems, following (6.5), are schematized in figure 6.3. Despite the qualitative differences between soft and hard bed hydrology, the governing equations are quite similar and mainly differ in their geometry, i.e., how width L and thickness H of the conduits are related to their cross-sectional area S.

To compute the effective pressure within each conduit, we combine the Darcy–Weisbach equation (6.5a) with the opening-closing equation (6.5b). This allows us to eliminate S and obtain an equation for N only. However, the resulting equation takes the form of a non-linear differential equation, which is not easy to solve. The complexity stems from the fact that $\nabla\phi$ depends on N through $\nabla\phi = \nabla\phi_0 - \nabla N$. However, given our second simplifying assumption, we have $\nabla\phi \approx \nabla\phi_0$ outside the vicinity of the grounding line. We then obtain algebraic equations for the effective pressure and the cross-sectional area far from the grounding line, N_∞ and S_∞:

$$N_\infty = \left[\left(\frac{H(S_\infty)}{S_\infty} \right)^2 \frac{\rho_i L_w \|\boldsymbol{v}_b\| h_b + Q_w \|\nabla\phi_0\|}{2n^{-n} \rho_i L_w A S_\infty} \right]^{\frac{1}{n}}, \tag{6.6a}$$

$$S_\infty = K^{-\frac{1}{\alpha}} \|\nabla\phi_0\|^{\frac{1-\beta}{\alpha}} Q_w^{\frac{1}{\alpha}}. \tag{6.6b}$$

Here, we have written $H(S)/S$ instead of $1/L$ to emphasize that N_∞ depends on the way that H depends on S, which is a function of the bed type.

The assumption that $\nabla\phi \approx \nabla\phi_0$ breaks down close to the grounding line because N must reach a zero value there for water to be connected to the ocean, as given by (6.5c). Hence, the effective pressure decreases significantly in that area, leading to strong gradients in N. A boundary-layer analysis

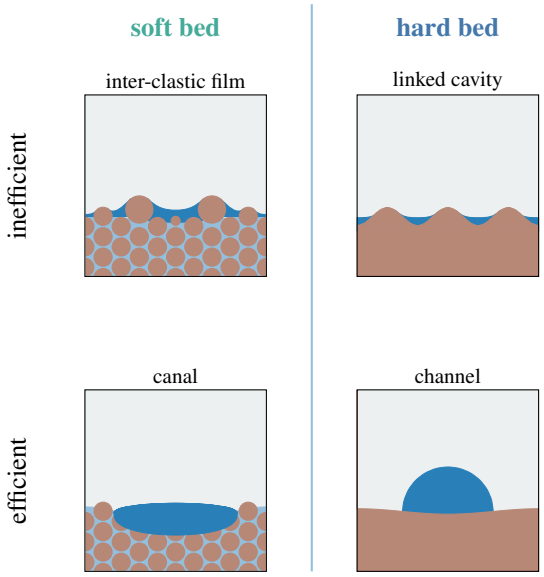

Figure 6.3: Schematic representation of the different types of drainage systems considered in this study: efficient and inefficient drainage systems on soft and hard beds.

actually reveals that $N \approx \phi_0$ close to the grounding line, and suggests that the effective pressure can be approximated over the whole domain by

$$N = \mathrm{erf}\left[\frac{\sqrt{\pi}}{2}\frac{\phi_0}{N_\infty}\right] N_\infty, \tag{6.7}$$

where $\mathrm{erf}(x)$ is the Gauss error function (see appendix B for more details). This approximation has been verified by comparing it with numerical solutions of the differential equation for the effective pressure. This equation reveals that the assumption that $N \approx N_\infty$ becomes valid when ϕ_0 becomes of the order of N_∞, which for Thwaites Glacier is typically a few kilometres from the grounding line.

Bed rheology

One element that is lacking from the equations describing conduits is the definition of their geometry, e.g., through a relation between their thicknesses and their cross-sectional areas, $H = H(S)$. For **hard-bed** systems, we follow Schoof [2010b] by assuming that $L = H = \sqrt{S}$, i.e., we consider conduits that are equally wide and thick, even though we acknowledge that the theory of linked cavities by Kamb [1987] was initially developed in the context of shallow cavities. For **soft-bed** systems, the geometry of conduits is more challenging. For small subglacial water fluxes, water takes the form of a patchy film. When the film gets thicker due to an increased water flux, its height will exceed the thickness of the smallest clasts, so that the film will be flowing in between larger clasts that are separated by a larger distance [Kyrke-Smith and Fowler, 2014; Kyrke-Smith et al., 2014]. This means that L increases with H. The relation between both depends on the spatial distribution of the clasts, as well as their thickness [Creyts and Schoof, 2009]. Here, we assume $L \sim \sqrt{S}$, which is not implausible, as this corresponds to the parametrization used for cavities on a hard bed. However, a soft bed is qualitatively different from a hard bed, as the till can be deformed. To take into account this difference, we introduce a factor F_{till}, defined as

$$L = F_{\mathrm{till}}\sqrt{S}. \tag{6.8}$$

This deformation factor depends on the difference between ice and till viscosity, as well as the till thickness, and increases with the ability of the till to deform, provided it is sufficiently thick. For a factor

$F_{\text{till}} > 1$, the effective pressure is lower compared to hard-bed systems [Beaud et al., 2022]. For this reason, we here consider $F_{\text{till}} = 1.1$. For larger subglacial water fluxes, water flow channelizes into canals, for which we prescribe a thickness $H = H_0$. Here, we take $H_0 = 0.1\,\text{m}$ as prescribed in Walder and Fowler [1994] for a sand/silt sediment type located under an ice sheet. For both inefficient and efficient cases, we then set

$$H(S) = H_0 + \left(\sqrt{S}/F_{\text{till}} - H_0\right) \exp\left(-Q_{\text{w}}/Q_{\text{c}}\right), \tag{6.9}$$

with Q_{c} a critical water flux value. Then $H \approx \sqrt{S}/F_{\text{till}}$ if $Q_{\text{w}} \ll Q_{\text{c}}$ and $H \approx H_0$ if $Q_{\text{w}} \gg Q_{\text{c}}$. In our simulations, we take $Q_{\text{c}} = 1\,\text{m}^3\,\text{s}^{-1}$ which corresponds to the scale of the water flux considered in Walder and Fowler [1994].

Finally, a **mixed bed** is composed of regions of various stiffness. We define the state of the bed through a spatial field $\kappa = \kappa(\boldsymbol{x})$ that describes the proportion of hard ($\kappa = 0$) and soft ($\kappa = 1$) bed. An intermediate value of $0 < \kappa < 1$ corresponds to a variation of the till thickness or stiffness, granting it possesses intermediate rigidity compared to those attributed to the hard and soft cases. For a mixed bed, the conduit-evolution relation is the same as the one used for the hard and soft cases, where we set $H = (1-\kappa)H_{\text{hard}} + \kappa\, H_{\text{soft}}$, with H_{hard} (resp. H_{soft}) the thickness associated with a hard (resp. soft) bed. A mixed-bed system is therefore able to cover the case of linked-cavities, channels, inter-clastic films, and canals, depending on the value of κ and of the subglacial water flow intensity. A summary of the differences between these cases can be found in table 6.1.

Type of bed	Scaling	$H = H(S)$
Hard	$L \sim H$	$H = \sqrt{S}$
Soft (inter-clastic film)	$L/H \sim F_{\text{till}}^2$	$H = \sqrt{S}/F_{\text{till}}$
Soft (canal)	$H \sim H_0$	$H = H_0$

Table 6.1: Scaling for the geometry of the conduits of the hydrology system.

The dependence of the far-field effective pressure N_∞ with respect to the magnitude of the conduit water flux Q_{w} is shown in figure 6.4 for hard and soft-bed systems. It clearly shows that the effective pressure decreases with water flux for inefficient systems. For efficient systems, hard and soft-bed systems differ, where channels lead to an increase in the effective pressure, contrary to canals. Note that this last distinction can be explained as follows. For large flux values, the opening-closing relation (6.5b) essentially becomes a balance between the opening due to melt, which is proportional to the water flux, and ice creep. Therefore, if the flux further increases, the ice-creep term must also increase. For channels, the factor L^2 in the ice-creep term of (6.5b) increases with the water flux, but at an insufficient rate; hence, the effective-pressure factor must also increase. By contrast, canals, because of their shallower form, are such that this factor increases at a much faster rate. As a consequence, the effective pressure must decrease in that case.

Besides soft, hard, and mixed beds, we also consider entirely efficient and inefficient drainage systems to gauge the sensitivity of both separately, independent of the subglacial water flux. By default, our model is such that the subglacial system naturally transitions from one to another depending on the subglacial water flux. This transition happens because the melting term, which is proportional to the water flux, becomes dominant over the sliding term in the left-hand side of (5a) as the water flux increases. By removing the opening term associated with the sliding over obstacles, $\|\boldsymbol{v}_{\text{b}}\|h_{\text{b}}$, from equations (6.5b) and (6.6a), it is possible to force the model to produce an entirely efficient drainage system. In this case, we also set $Q_{\text{c}} = \infty$, which guarantees that the conduit geometry is the one of an inefficient system for soft beds. Similarly, to force an entirely inefficient system, the efficient component, $Q_{\text{w}}\|\nabla\phi\|/\rho_{\text{i}}L_{\text{w}}$, can be removed from (6.5b), together with the condition that $Q_{\text{c}} = 0$.

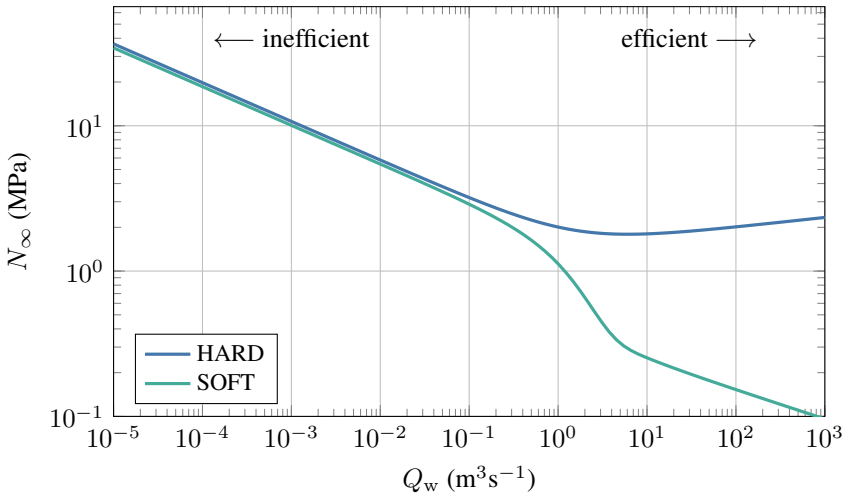

Figure 6.4: Relation between the value of the effective pressure N_∞ far from the grounding line and the magnitude of the conduit water flux Q_w, for hard (in blue) and soft (in green) beds. The curves correspond to equation (6.6a) coupled with the geometric relations shown in table 6.1. The physical parameters are the ones displayed in the appendix A, with $A = 2.4 \times 10^{-24}\,\mathrm{Pa}^{-3}\,\mathrm{s}^{-1}$, $\|\boldsymbol{v}_b\| = 0.5 \times 10^{-5}\,\mathrm{m\,s}^{-1}$, and $\|\nabla\phi_0\| = 100\,\mathrm{Pa\,m}^{-1}$.

6.3 Idealized experiments

6.3.1 Experimental setup

As a first test of the hydrological model, we consider a flowband geometry for a marine ice sheet, taken from the benchmark projects MISMIP and MISMIP3d [Pattyn et al., 2012, 2013], and which consists of a linearly downward-sloping bed towards the ocean (Figure 6.5a). On this bed topography a marine ice sheet is developed with a spatial resolution of 500 m, following the set-up described in the EXP1 of the MISMIP experiments [Pattyn et al., 2012, see figure 6.5a]. The steady state obtained with these conditions is considered to be the 'reference state'.

In our experiments, we use a regularized Coulomb friction law combined with hydrological models, while the reference state from the MISMIP set-up has been obtained with a Weertman friction law. To guarantee that the thickness and velocity fields obtained in the reference state are still compatible with a steady state, we modify the friction coefficient at each position, following the method of Brondex et al. [2017, 2019]. In practice, an iterative nudging method is used so that the basal friction matches the basal friction obtained in the reference state. Here, the subglacial hydrologies are generated with a uniform basal melt rate underneath the grounded ice sheet of $\dot{m}/\rho_w = 5 \times 10^{-3}\,\mathrm{m\,a}^{-1}$, which corresponds to the mean basal melt rate of the Antarctic Ice Sheet [Pattyn, 2010]. By construction, this method yields initial states that are steady states and in which both the geometry and the velocity field are identical for each type of hydrology, allowing a direct comparison between them. The initial ice-sheet effective-pressure profiles are shown in figure 6.5b.

We consider a uniform hard and soft bed and compare these to an experiment where (i) the effective pressure is determined according to the HAB model (for 'height-above-buoyancy'), which assumes a perfect connection with the ocean, and (ii) basal sliding being independent of subglacial pressure or bed rheology (NON). The effective pressure in the HAB model is therefore simply defined by

$$N = \rho_i g h - \rho_s g \max(0, -b)\,, \tag{6.10}$$

where ρ_s is the density of sea water. It is the most common parametrization of N used [e.g., Tsai et al.,

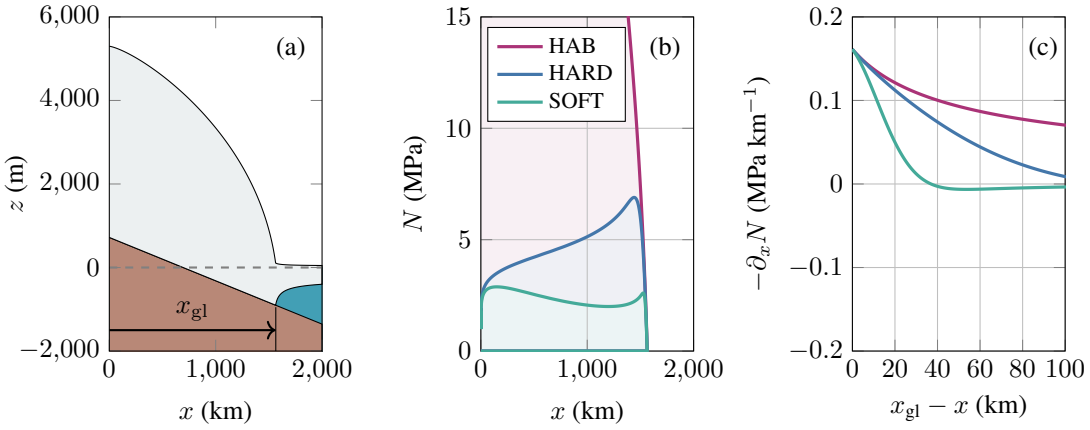

Figure 6.5: Initial state for the experiments on idealized conditions, based on the MISMIP geometry [Pattyn et al., 2012]. **(a)** The initial MISMIP steady-state ice-sheet geometry; x_{gl} corresponds to the distance to the grounding line. **(b)** Flowband profiles of the subglacial effective pressure for HAB (in purple), HARD (in blue), and SOFT (in green) hydrological models. **(c)** Gradient of the subglacial effective pressure near the grounding line for HAB (in purple), HARD (in blue), and SOFT (in green) hydrological models.

2015].

For all models, the effective pressure is high in the interior and decreases towards the grounding line, where it becomes zero by definition. For the HAB model, the horizontal gradient of the effective pressure is the highest, mainly governed by the geometry of the bedrock and surface slopes. For HARD and SOFT, representing the hard-bed and soft-bed systems, respectively, the effective pressure varies due to variations in both the subglacial water flux and the cross-sectional size of the conduits, according to equation (6.6a) (figure 6.5b).

Besides, we also compare the impact of the drainage efficiency, by comparing the cases where only efficient (eff) or inefficient (ineff) systems are allowed to develop. Note that, by default, the switch between both systems (efficient/inefficient) is determined based on the subglacial water flux magnitude.

6.3.2 Results: the efficient to inefficient switch

A first experiment aims at understanding the switch between efficient and inefficient drainage systems. We force the MISMIP flowband setup with a sinusoidal variation in subglacial meltwater that is then routed across a hard bed (figure 6.6a). The response in effective pressure and sliding velocity do not simply follow the same sinusoidal pattern, but the ice velocity accelerates and decelerates as a function of whether the system evolves into an efficient or inefficient drainage system (figure 6.6b and c). Sudden speedups correspond to sudden drops in the effective pressure and occur when either the amount of meltwater diminishes or increases. Note that these sudden changes do not appear if the model is entirely efficient or entirely inefficient. Similar characteristics of the subglacial hard-bed system have been described by Schoof [2010b] and are shown in figure 6.6d. Although our model is a relatively crude parametrization of the subglacial system, the intrinsic instability related to the switch between efficient and inefficient drainage systems is captured.

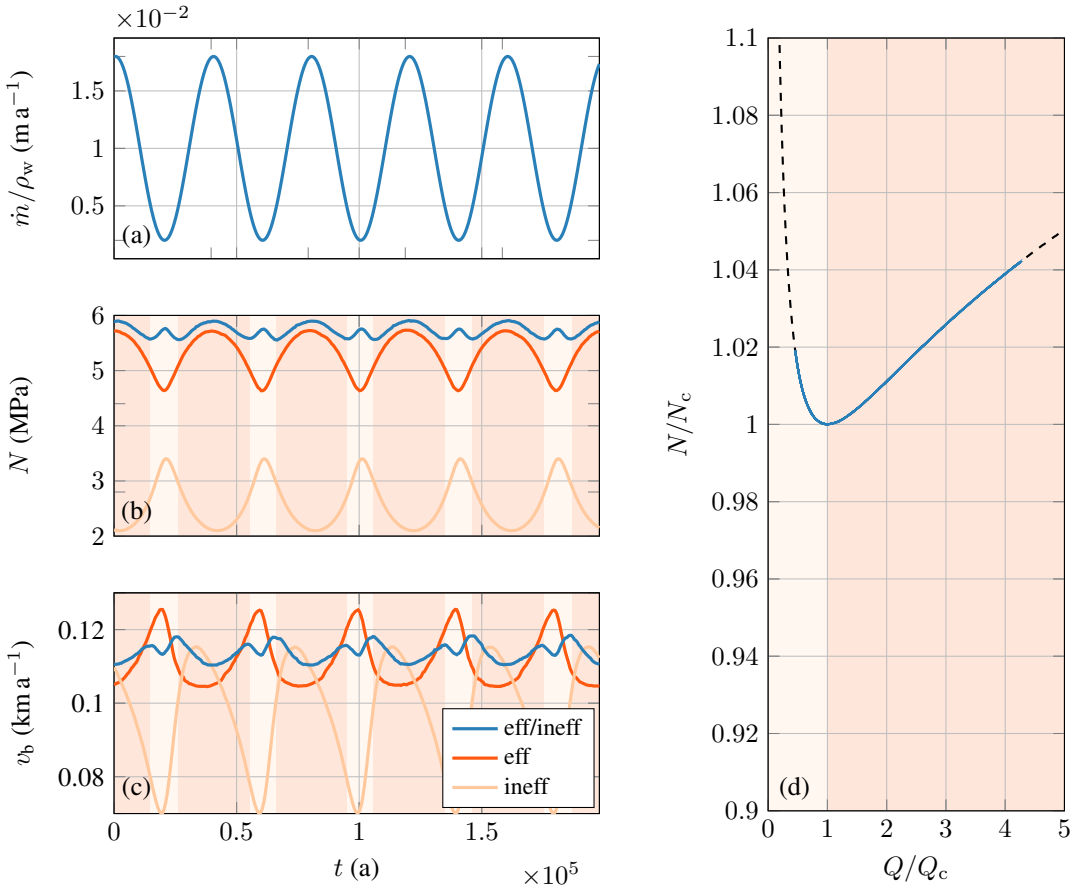

Figure 6.6: **(a)** Forcing of the MISMIP geometry with a sinusoidal variation in subglacial meltwater, for a hard-bed system. **(b)** Response to the forcing in effective pressure, and **(c)** basal sliding velocity (blue: efficient/inefficient; red: entirely efficient; beige: entirely inefficient). **(d)** Relationship between subglacial water flux and effective pressure for both the efficient/inefficient drainage system. All quantities have been evaluated at $x = 1000\,\mathrm{km}$, away from the vicinity of the grounding line. The dashed line corresponds to equation (6.6a), and N_c and Q_c are critical values for a hard-bed system as defined in Schoof [2010b]. The light pink (resp. dark pink) areas correspond to regions in which the efficient/inefficient system is an inefficient (resp. efficient) regime.

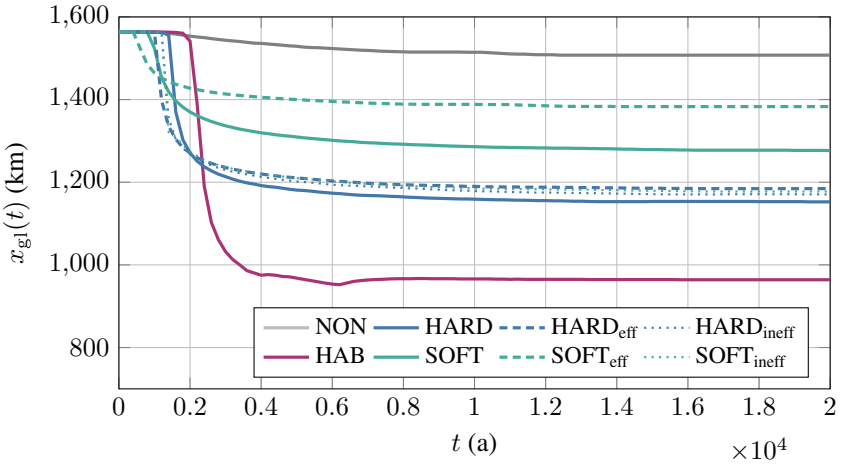

Figure 6.7: Grounding-line evolution after a sudden reduction in surface accumulation rate for the MISMIP setup for NON (in grey), HAB (in purple), HARD (in blue), SOFT (in green), HARD efficient (blue dashed line), HARD inefficient (blue dotted line), SOFT efficient (green dashed line) and SOFT inefficient (green dotted line) hydrological models.

6.3.3 Results: perturbation experiment

For each hydrological model, the initial steady state is perturbed by instantaneously reducing the net mass accumulation rate to 0.2 m a^{-1}. The ice sheet is then allowed to evolve for a period of 20,000 years with a time step of 5 years, eventually reaching a (near) steady state. The hydrological model is updated at each time step (see also appendix C). The first series of experiments consists of comparing the response of the different models (NON, HAB, HARD, SOFT), as well as the fully efficient (eff) and fully inefficient (ineff) cases for HARD and SOFT models to this perturbation. The reduction in surface accumulation generally leads to a slowdown of the ice velocity as well as a smaller ice sheet. This reduction also results in a slight grounding-line retreat (NON in figure 6.7). However, linking basal sliding to *any* of the hydrological models that are a function of effective pressure at the base of the ice sheet, leads to a significant grounding-line retreat and overall grounded mass loss (figure 6.7). Of all subglacial models, HAB is the most sensitive to the forcing, i.e., leading to the highest mass loss after forcing. Several factors may be responsible for this, as has been shown in figure 6.5c: it is not only that the effective pressure is low near or at the grounding line, but that also the effective-pressure gradient upstream of the grounding line is the highest for the HAB model. The fact that the sensitivity of grounding-line retreat increases with increasing gradient in effective pressure near the grounding line is shown in figure 6.5c. While this gradient is equally high near the grounding line for all model configurations, it drops quite quickly with distance from the grounding line for soft-bed systems, resulting in a minimal grounding-line retreat. Since per definition the NON model, representing the solution independent of effective pressure, has a zero gradient in effective pressure, it therefore leads to the least grounding-line retreat due to forcing compared to the other hydrological models, as shown above.

6.4 Application to Thwaites Glacier

6.4.1 Experimental setup

For Thwaites Glacier, necessary input data are the present-day ice-sheet surface and bed geometry from BedMachine v2 [Morlighem et al., 2019], surface mass balance and temperature from RACMO2.3p2 [van Wessem et al., 2018], and a prescribed field for the geothermal heat flux [Shapiro and Ritzwoller, 2004]. All datasets were resampled at a spatial resolution of 2 km. The simulations are performed at that

spatial resolution and with a time step of 0.05 years.

Similar to the idealized experiments, a reference state is obtained with a Weertman friction law. To obtain this state, the basal friction field is iteratively adapted to obtain a steady-state ice sheet with grounded ice thickness as close as possible to the observed thickness using a nudging method [Pollard and DeConto, 2012a; Pattyn, 2017; Coulon et al., 2024b]. For the floating ice shelves, the sub-shelf melt/accretion is adjusted to keep the ice thickness comparable to observed [Coulon et al., 2024b]. In a second step, the initial friction field corresponding to a given hydrological model is obtained with the same method as explained for the idealized experiments. Initial bedrock and surface topographies, as well as the ice velocity field can be found in the Supplementary Material S2, the friction coefficient fields after initialization in the Supplementary Material S3 and the effective pressure values for HAB, HARD and SOFT in the Supplementary Material S4. To evaluate the model drift of this initialization, the model is run forward in time according to the different hydrological models, leading to a mass change after 100 years corresponding to 1–2 mm of sea-level rise. Thanks to this small model drift, the control run does not have to be subtracted from the forcing runs, as was the case in Kazmierczak et al. [2022]. It also demonstrates the improvements that have been made in terms of model initialization [Coulon et al., 2024b].

All simulations start from this initial steady state, corresponding to the 2015 conditions. We then run the model forward until 2100, under present-day climate conditions (atmospheric and oceanic). Sub-shelf melt rates are calculated by the PICO model [Reese et al., 2018b] with an effective heat exchange velocity value of $3 \times 10^{-5}\,\mathrm{m\,s^{-1}}$, which gives a realistic melt pattern for present-day ocean temperatures and salinity. Since these dynamic melt rates replace the optimized basal melting/accretion field, the ice-sheet system is no longer in steady state anymore and the grounding line reacts to the applied oceanic forcing by a small retreat over the course of this century (Reference experiment NON in figure 6.8a). Note that the mass loss for the NON experiment results in sea-level rise on the order of 10 mm by 2100, which is an order of magnitude larger than the model drift (~ 1 mm).

This simulation under present-day forcing conditions is repeated for the different subglacial hydrological models HAB, HARD and SOFT. Akin to this, the spatial variability of the HARD and SOFT bed models is assessed by considering heterogeneous and/or mixed beds for Thwaites Glacier [Muto et al., 2019; Alley et al., 2022]. By heterogeneous we mean that the spatial field is composed of soft and hard bed portions, while for a mixed bed, we consider that a particular grid cell is composed of a mix of hard and soft bed, or $0 < \kappa < 1$. We can therefore have different cases: homogeneous uniform (the whole bed domain with either $\kappa = 0$ or $\kappa = 1$) or mixed (the whole bed domain with a constant value $0 < \kappa < 1$), as well as heterogeneous uniform (the domain composed of portions of hard bed and soft bed) and mixed ($0 \leq \kappa \leq 1$). For the heterogeneous uniform beds, Joughin et al. [2009] and Muto et al. [2019] suggest that soft beds are mainly found in subglacial depressions and hard beds generally on topographic highs, which allows us to make the separation between both based on the subglacial topography, with the soft layer occupying the deeper basins. In a first experiment, we set the transition between soft and hard bed at a bedrock elevation of 1000 m below sea level (figure 6.9c). In a second experiment a transition zone is considered (heterogeneous mixed), where κ is linearly varied between a depth of 500 and 1500 m below sea level (figure 6.9d). We tested the influence of the nature of the drainage system itself by applying only inefficient, efficient or both drainage systems for the different bed types described above.

6.4.2 Results: subglacial hydrology on homogeneous beds

As mentioned above, even under present-day atmospheric and oceanic forcing, the reference experiment NON leads to a slight retreat of the grounding line over the period 2015-2100 that continues thereafter. This is in line with large-scale model experiments [Coulon et al., 2024b] showing that Thwaites Glacier may collapse, i.e., that it will continue to retreat even if the forcing is completely stopped, under present-day climatic conditions on time scales of several centuries.

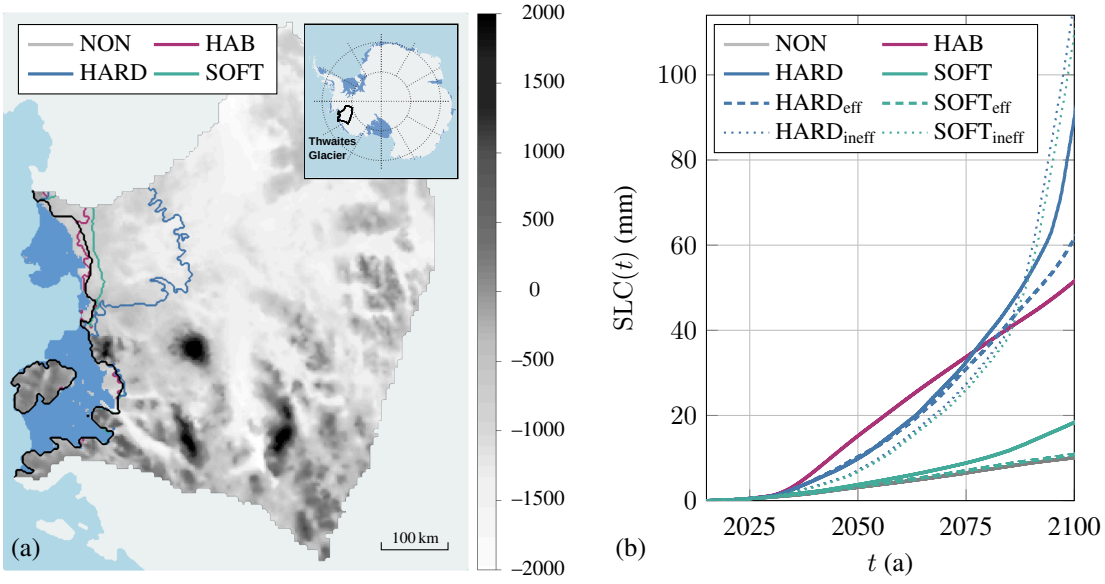

Figure 6.8: Effect of the subglacial hydrological models in the Thwaites Glacier set-up. Present-day climate conditions (atmospheric and oceanic) are applied from 2015 to 2100. **(a)** Grounding-line positions of Thwaites Glacier (bedrock elevation (m) in the background) in 2100 under constant present-day climate conditions (atmospheric and oceanic) for the NON (black), HAB (purple), HARD (blue) and SOFT (green) models. The inset in the upper right corner shows the position of Thwaites Glacier within Antarctica. **(b)** Sea-level contribution from Thwaites Glacier from 2015 to 2100 under constant present-day climate conditions (atmospheric and oceanic) for the NON (grey), HAB (purple), HARD (blue), SOFT (green), HARD efficient (blue dashed line), HARD inefficient (blue dotted line), SOFT efficient (green dashed line) and SOFT inefficient (green dotted line).

The same retreat behavior is observed for the experiment including subglacial hydrology. However, in all cases, subglacial hydrology accelerates the retreat of the grounding line by 2100 (figure 6.8a). For instance, by 2100, we observe a sea-level contribution of around 50 mm for HAB, 95 mm for HARD, 20 mm for SOFT, while only 10 mm for NON (figure 6.8b). It is important to note that for all the subglacial models a collapse of Thwaites Glacier is engaged under present-day climate forcing conditions. However, only the hard-bed model (HARD) results in a collapse in less than 100 years. Not all major mass losses coincide with a distinct grounding-line retreat, as the HAB model exhibits significant thinning of the ice for a modest grounding-line retreat compared to the other subglacial models.

The efficiency of subglacial drainage is tested for both a uniform homogeneous soft and hard bed (figure 6.9a and b). As demonstrated in the idealized experiments, it is also possible to force the drainage to be efficient (eff) or inefficient (ineff). The results corroborate the previous experiment, i.e., that for a hard bed, a large amount of ice is lost by 2100 compared to the soft bed. The only exception is that a similar amount of (high) mass loss is observed for the inefficient drainage systems both for soft and hard beds (figure 6.9a and b).

6.4.3 Results: subglacial hydrology on heterogeneous beds

Figure 6.9c and d show the grounding-line positions for a heterogeneous bed, where the subglacial basins of Thwaites are considered to be soft bed, and the topographic highs hard bed. As previously mentioned, the limit between both is set at a depth of 1000 m below present-day sea level. A peculiarity of this setting is that the present-day grounding line is situated on a hard bed, and that the soft bed region is only reached further inland. In the first experiment (figure 6.9c) the transition between both bed rheologies is sharp (uniform heterogeneous); in the second experiment (figure 6.9d) there is a transition zone (mixed heterogeneous). Despite the hard bed conditions in the present-day grounding zone, a larger mass loss by 2100 is observed for the mixed case. Similar to the previous experiment, the largest mass loss is observed for inefficient drainage, irrespective of the bed rheology.

The results on mixed heterogeneous bed experiments show that the nature of the bed near the grounding line determines the sensitivity of the glacier. With a sharp transition, the motion of the grounding line over the hard-to-soft bed system will lead to a stabilization effect delaying grounding-line retreat. Such stabilization is less pronounced for a mixed bed, where hard-bed physics also play a role in the transition zone. Similar results are presented in the Supplementary S4 with the hard and soft bed zones locations exchanged.

6.5 Discussion

We have developed a novel and unified subglacial hydrological model that incorporates efficient and inefficient drainage and that applies to both soft and hard beds. It represents different discharge types, ranging from channels and canals to cavities. While the model is a simplification compared to higher-resolution hydrological models, it seems to capture the main characteristics of subglacial flow, and incorporates the feedbacks associated with basal sliding and the ice dynamical response.

In this section, we first discuss the influence of the hydrological model and the bed type. We then describe the hydrological feedback that may explain the increased sensitivity of the ice sheet due to subglacial hydrology. Finally, we comment on the limitations of the model and suggest improvements to our model.

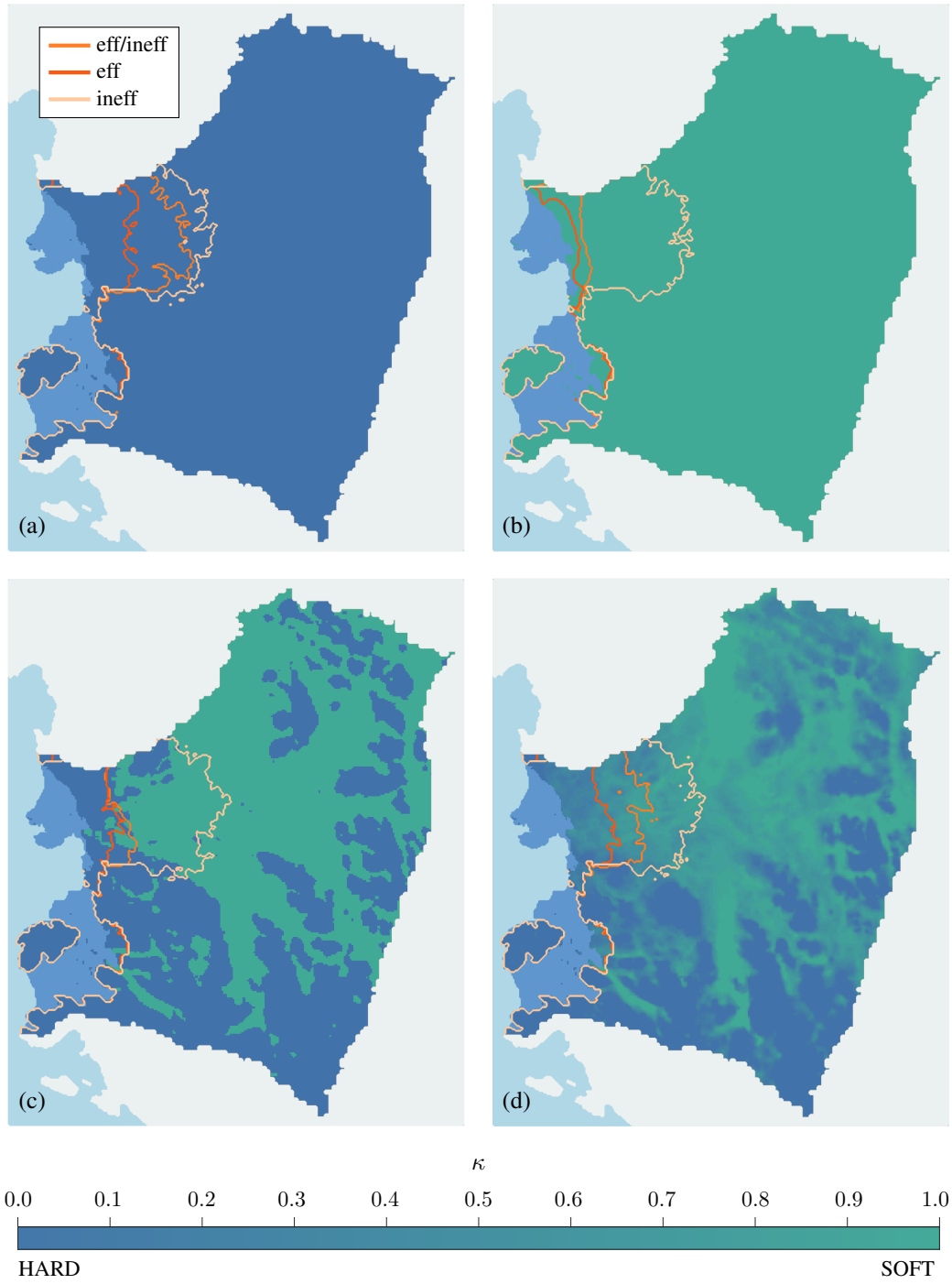

Figure 6.9: Grounding-line positions of Thwaites Glacier in 2100 under constant present-day climate conditions (atmospheric and oceanic) for the subglacial model (inefficient and efficient, entirely efficient, and entirely inefficient) on **(a)** a uniform homogeneous hard bed; **(b)** a uniform homogeneous soft bed; **(c)** a heterogeneous uniform bed, with a sharp transition and **(d)** a heterogeneous bed, with a transition zone of mixed bed.

6.5.1 Influence of subglacial conditions

Our experimental results show that subglacial hydrology and the rheology of the bed (soft, hard, and its related spatial variability) have a major impact on the dynamics of marine ice sheets and the West Antarctic Ice Sheet in particular. Taking into account subglacial hydrology systematically leads to a higher ice-sheet sensitivity for a given climate forcing. This is mainly due to the reduction of the effective pressure near the grounding line, which migrates upstream with a retreating grounding line.

Traditionally, large-scale ice-sheet models tend to calculate effective pressure at the base of the ice sheet using the HAB parametrization, based on the height above flotation. This model assumes that sea water infiltrates at the grounding line, increasing the water pressure and reducing the effective pressure in the grounding zone. This leads to significant increases in basal sliding near the grounding line. The idealized experiments clearly demonstrate that this model leads to the highest mass loss after a perturbation and probably overestimates the contribution of ice sheets to climate forcing.

However, in more complex settings, such as Thwaites Glacier, the HAB model remains sensitive, but also allows the grounding line to stabilize during its retreat on subglacial ridges. These bed peaks are known to have a strong impact on grounding-line dynamics, and their influence on ice-sheet stability is the subject of recent research [Robel et al., 2022a].

Results of our simplified hydrological model show that sliding over a hard bedrock (HARD) leads to the largest reduction of the grounded domain and the highest sea-level contribution for a given forcing, while sliding over a soft bed (SOFT) yields the smallest grounding-line retreat and sea-level contribution (figure 6.8). In terms of drainage efficiency, the concentration of water flow in efficient conduits, especially in canals, but also for channels, slows down the retreat of the grounding line, which aligns with one of the conclusions of Schoof [2010b]. This can be explained by a higher basal friction due to the higher effective pressure in hard-bed channels [Hager et al., 2022], and by the lower effective pressure variation in canals, leading to a reduced impact of subglacial hydrology on the basal friction field. It is interesting to note that in the case of hard beds, our effective-pressure results are similar to those obtained by Hager et al. [2022] with the `MALI` model [Hoffman et al., 2018], using a subglacial drainage model built on cavities and channels.

Besides the hard bed, inefficient systems also lead to the highest mass loss of Thwaites Glacier over this century. We observe that the largest mass loss occurs when the effective pressure gradient is large towards the grounding line and less so when effective pressure is low, such as in canals (figure 6.8b, see video supplements). This observation aligns with the work of Iken [1981], specifying that the highest velocities is not observed where effective pressures is lowest, but rather when cavities enlarge due to an increase in subglacial water pressure. Therefore, inefficient systems on both soft and hard beds show very similar results, which is consistent with the representation of the considered drainage systems. Such systems are quite similar as bumps in the hard system correspond to the clasts in the soft system. However, the lower effective pressure in the soft-bed system, associated with the deformation of saturated till, slows down grounding-line retreat.

In general, a soft bed near the grounding line slows down its retreat under climatic forcing. However, transitions between bed types also influence the speed of the grounding-line retreat. A binary switch from hard to soft is more likely to stabilize the grounding-line position than a smooth transition. Moreover, taking the total proportion between soft and hard beds and applying it uniformly across the entire domain does not allow to capture the variation introduced by the spatial variability of bed rheology and the associated drainage system.

6.5.2 Hydrological feedback

The increased sensitivity observed with hydrological models can be explained by a positive feedback between grounding-line migration and the reduction in basal friction at or near the grounding line. Formally, frictional stress $\boldsymbol{\tau}_\mathrm{b}$ can be split into two components: $\tilde{\boldsymbol{\tau}}_\mathrm{b}$, which is the value of the friction stress with the initial effective-pressure field, and $\Delta\tilde{\boldsymbol{\tau}}_\mathrm{b}$, which is the deviation with respect to this value:

$$\boldsymbol{\tau}_\mathrm{b} = \tilde{\boldsymbol{\tau}}_\mathrm{b} + \Delta\tilde{\boldsymbol{\tau}}_\mathrm{b}, \tag{6.11}$$

where

$$\tilde{\boldsymbol{\tau}}_\mathrm{b}(t) = CN_0 \left(\frac{\|\boldsymbol{v}_\mathrm{b}\|}{\|\boldsymbol{v}_\mathrm{b}\| + v_0} \right)^{\frac{1}{m}} \frac{\boldsymbol{v}_\mathrm{b}}{\|\boldsymbol{v}_\mathrm{b}\|}, \tag{6.12a}$$

$$\Delta\tilde{\boldsymbol{\tau}}_\mathrm{b}(t) = C\left[N(t) - N_0\right] \left(\frac{\|\boldsymbol{v}_\mathrm{b}\|}{\|\boldsymbol{v}_\mathrm{b}\| + v_0} \right)^{\frac{1}{m}} \frac{\boldsymbol{v}_\mathrm{b}}{\|\boldsymbol{v}_\mathrm{b}\|}, \tag{6.12b}$$

and where $N_0 = N(t=0)$ is the effective pressure for the initial state. Because of the initialization procedure, $\tilde{\boldsymbol{\tau}}_\mathrm{b}$ is initially the same for every hydrological model. In particular, it is also equal to the absence of subglacial hydrology (NON). Therefore, $\Delta\tilde{\boldsymbol{\tau}}_\mathrm{b}$ stems from the evolution of the subglacial system and its influence on basal friction. In other words, $\Delta\tilde{\boldsymbol{\tau}}_\mathrm{b}$ is associated with the spatial and temporal evolution of the effective pressure.

Due to the evolution of subglacial hydrology in time, an instability mechanism may appear near the grounding line, as the effective pressure is always low, and the gradient of the effective pressure is the largest (figure 6.5). The zone of low effective pressure migrates with a migrating grounding line. Such migration obviously does not take place when the subglacial hydrological field is kept constant or when subglacial hydrology is not linked to basal sliding (or not considered; NON). For a retreating grounding line, such linkage actually amplifies grounding-line retreat, as the friction stress close to the grounding line is also reduced following this retreat, leading to a positive feedback mechanism. This reduction in $\boldsymbol{\tau}_\mathrm{b}$ stems from a reduction of $\tilde{\boldsymbol{\tau}}_\mathrm{b}$, but most importantly from a large value in the magnitude of $\Delta\tilde{\boldsymbol{\tau}}_\mathrm{b}$, which is typically negative. This essentially explains the distinction between the HAB and the HARD/SOFT models. The HAB model is purely local as it depends on the geometry of the ice sheet at the position where the effective-pressure is evaluated. By contrast, the HARD/SOFT models also depend on the subglacial water flux and on the distance with respect to the grounding line. This distinction allows for a perturbation near the grounding line to 'propagate' upstream for the latter models. As this is not the case for HAB models, it potentially enables the grounding line to stabilise near a ridge, for instance. This distinction can be observed in the video supplement.

The qualitative assessment can be quantified in the case of a flowline according to the shallow-shelf approximation. Following previous work [Weertman, 1974; Schoof, 2007b, 2012], a steady-state marine ice sheet is unstable if

$$\partial_s q - a < 0, \tag{6.13}$$

in which q is the flux at the grounding line, s is a coordinate parameterizing the position along the ice sheet, and a is the net mass accumulation rate. For a large class of friction laws [Schoof, 2007c; Tsai et al., 2015; Gregov et al., 2023], the flux at the grounding line can be approximated as

$$q = q_0\, C^{-\frac{1}{m+1}} \left[-(\rho_\mathrm{w}/\rho_\mathrm{i})b\right]^r, \tag{6.14}$$

where $q_0, r > 0$. It follows that for a uniform friction coefficient, a steady-state position on a up-sloping (retrograde) bed is always unstable, i.e.,

$$\partial_s q - a = -rq(\rho_\mathrm{w}/\rho_\mathrm{i}) \left[-(\rho_\mathrm{w}/\rho_\mathrm{i})b\right]^{-1} \partial_s b - a < 0. \tag{6.15}$$

However, an ice-sheet on a downward-sloping bed can be stable. For a spatially variable friction coefficient $C = C(s)$, the instability condition becomes

$$-\frac{q\,C^{-1}\partial_s C}{m+1} - rq(\rho_\mathrm{w}/\rho_\mathrm{i})\,[-(\rho_\mathrm{w}/\rho_\mathrm{i})b]^{-1}\,\partial_s b - a < 0. \tag{6.16}$$

This inequality can be achieved more easily for a downward-sloping (prograde) bed, compared to equation (6.15). Indeed, if $\partial_s C$ is positive and large at the grounding line, then the left-hand side of (6.16) is reduced, and the instability condition is easier to fulfill. The initialization produces this condition for the HAB, HARD and SOFT models, contrary to the NON case, where $C(s)$ has to increase considerably close to the grounding line to compensate for the vanishing effective pressure in order to obtain a frictional stress similar to the one obtained by the absence of hydrology. Overall, this implies that the ice sheet is less stable, and therefore exhibits a higher sensitivity to external forcings. This instability was explored in greater details with a similar model in Lu and Kingslake [2024].

6.5.3 Model limitations

Although our simulations for hard, soft, and mixed beds allow to better assess the variability of the response of ice sheets to a climate forcing, there remain some limitations. Our subglacial hydrology models do not include variations of drainage density or of effective pressure below the resolution of the ice-sheet discretization. This is a clear limitation, as we have shown that the spatial variability plays an important role in the numerical experiments. From a physical perspective, improvements could be made on the representation of physical processes. For example, till water pressure is omitted in the soft bed model, and till deformation is only crudely parameterized. Water flow within the till and exchanges with the neighbouring area (especially in the case of a variation in ice thickness) could well modify subglacial water flow and therefore ice-sheet dynamics [Robel et al., 2023]. Recent studies have also shown that seawater intrusion may impact grounding-line dynamics through modifying the subglacial hydrology, hence increasing the instability [Robel et al., 2022b; Bradley and Hewitt, 2024]. This also suggests that the grounding line should be considered a grounding zone that allows for such intrusion, in agreement with recent observations [Rignot et al., 2024]. Furthermore, erosion, deposition and sedimentary transport processes that are not taken into account could play a role in the variability of effective pressure at the base of the ice sheet [Ng, 2000; Hewitt and Creyts, 2019; Stevens et al., 2022]. Finally, even if our results remain qualitatively valid if the parameter settings are modified (see appendix D), the latter could be subject to more scrutiny, ideally within a probabilistic framework [Bulthuis et al., 2019; Verjans et al., 2022; Coulon et al., 2024b]. This analysis could then be used to quantify the uncertainties in the projections obtained in the simulations.

6.6 Conclusions

We developed a novel and simplified model of subglacial hydrology that applies to both soft and hard beds, thereby representing both efficient and inefficient discharge types. The hydrological model is dynamically linked to an ice-sheet model (Kori-ULB) via a regularized Coulomb friction law. Despite its relative simplicity, our model allows to obtain results that agree with multiple previous studies. Our experiments are in agreement with Kazmierczak et al. [2022], showing that the type of subglacial hydrology modulates the basal sliding and that considering subglacial hydrology enhances the ice-sheet response to sliding. Our tests on the spatial and temporal variability of bed rheology also show that a soft-bed system in the grounding zone tends to stabilize a grounding line more easily compared to other bed rheologies. By investigating various drainage efficiencies, our results concur with those of Schoof [2010b] by showing that a channelization leads to ice deceleration as well as grounding-line stabilization. The switch between efficient and inefficient drainage has clearly been shown in our experiments where subglacial water input has been varied. Moreover, our results agree with Iken [1981] by the fact that the highest sliding is not occurring at the highest subglacial water pressure, but rather where basal cavities

are growing (i.e., when the basal water pressure is increasing downstream). Furthermore, we obtain the largest response in grounding-line retreat for those subglacial conditions where the gradient in effective pressure is the largest, not where its value is the lowest. Therefore, highly saturated grounding zones on soft beds seem to be less responsive than hard-bed systems, where such large gradients in the vicinity of the grounding line occur. While our results for Thwaites Glacier for a hard bed are qualitatively similar to those of Hager et al. [2022], the ability of model to reproduce such results could be studied in more detail.

Overall, our study also emphasizes the necessity for more accurate data and observations of the bed rheology of the Antarctic Ice Sheet at different spatial scales [Parizek et al., 2013; Koellner et al., 2019; Muto et al., 2019; Alley et al., 2022; Li et al., 2022; Aitken et al., 2023]. Similarly, the observation of efficient and inefficient subglacial water drainage systems and a connection with numerical results is required [Schroeder et al., 2014; Hager et al., 2022; Dow et al., 2022].

6.7 Appendix A: List of symbols

Symbol	Description	Units	Value
α	Exponent in Darcy–Weisbach relation	-	$5/4$
β	Exponent in Darcy–Weisbach relation	-	$3/2$
Γ_{d}	Boundary of the basin	m	-
Γ_{gl}	Grounding line	m	-
κ	Indicator of the heterogeneity content of the bed	-	-
ρ_{i}	Density of ice	$\mathrm{kg\,m^{-3}}$	9.17×10^3
ρ_{s}	Density of sea water	$\mathrm{kg\,m^{-3}}$	1.03×10^3
ρ_{w}	Density of fresh water	$\mathrm{kg\,m^{-3}}$	1.00×10^3
$\boldsymbol{\tau}_{\mathrm{b}}$	Basal shear stress	Pa	-
ϕ	Hydraulic potential	Pa	-
ϕ_0	Geometric potential	Pa	-
Ω	Grounded ice domain	m	-

Table 6.2: List of symbols used for the model (Greek alphabet).

Symbol	Description	Units	Value
A	Viscosity parameter in Glen's flow law	$\mathrm{Pa}^{-n}\mathrm{s}^{-1}$	-
b	Bedrock elevation	m	-
C	Friction coefficient	-	-
f	Friction coefficient for a turbulent flow	-	0.10
F_{till}	Factor for the conduits geometry in a till	-	1.10
g	Gravitational acceleration	$\mathrm{m\,s^{-2}}$	9.81
G	Geothermal heat flux	$\mathrm{W\,m^2}$	-
h	Ice thickness	m	-
h_{b}	Thickness of obstacles	m	0.10
H	Thickness of conduits	m	-
H_{hard}	Thickness of conduits over a hard bed	m	-
H_{soft}	Thickness of conduits over a soft bed	m	-
H_0	Thickness of canals	m	0.10
K	Conductivity coefficient in Darcy–Weisbach relation	$\mathrm{kg}^{s_1}\,\mathrm{m}^{s_1}\;\mathrm{s}^{s_3}$	-
L	Width of conduits	m	-
l_{c}	Distance between conduits	m	1.00×10^4
L_{w}	Latent heat of fusion of water	$\mathrm{J\,kg^{-1}}$	3.35×10^5
m	Power-law exponent	-	3.00
$\dot{m}$	Melt rate	$\mathrm{kg\,m^{-2}\,s^{-1}}$	-
$\dot{m}_{\mathrm{w}}$	Melt rate associated with the subglacial water flow	$\mathrm{kg\,m^{-2}\,s^{-1}}$	-
n	Exponent in Glen's flow law	-	3.00
$\boldsymbol{n}$	Normal vector to a boundary	m	-
N	Effective pressure	Pa	-
N_∞	Far-field effective pressure	Pa	-
$\boldsymbol{q}_{\mathrm{w}}$	Subglacial water flux	$\mathrm{m^2\,s^{-1}}$	-
q_T	Thermal conduction flux	$\mathrm{W\,m^{-2}}$	-
Q_{w}	Volumetric water flux in a conduit	$\mathrm{m^3\,s^{-1}}$	-
Q_{c}	Critical water flux in a conduit	$\mathrm{m^3\,s^{-1}}$	1.00
S	Cross-sectional area of conduits	$\mathrm{m^2}$	-
S_∞	Far-field cross-sectional area of conduits	$\mathrm{m^2}$	-

$\boldsymbol{v}$	Ice velocity	$\mathrm{m\,s^{-1}}$	-
$\boldsymbol{v}_\mathrm{b}$	Basal ice velocity	$\mathrm{m\,s^{-1}}$	-
v_0	Velocity threshold in the friction law	$\mathrm{m\,s^{-1}}$	9.51×10^{-6}
$\boldsymbol{x}$	Position	m	-

Table 6.3: List of symbols used for the model (Latin alphabet). Here, $s_1 = 1 - \beta$, $s_2 = 2\beta - 2\alpha + 1$, $s_3 = 2\beta - 3$.

6.8 Appendix B: The effective pressure near the grounding line: a boundary-layer analysis

In this appendix, we apply a boundary-layer analysis of the hydrology system close to the grounding line, and derive an approximate expression of the effective pressure in the area.

6.8.1 Problem statement

We consider a streamline of subglacial water parametrized by a parameter $s \in [0, s_\mathrm{gl}]$, where $s = s_\mathrm{gl}$ corresponds to the grounding-line position. All the parameters are fixed and the magnitude of the geometric potential gradient, $\Psi = \|\nabla\phi_0\|$, is assumed to be constant and known. The governing equations of the hydrology system are then expressed as

$$N = \phi_0 - \phi, \tag{6.17a}$$

$$\partial_t S + \partial_s Q_\mathrm{w} = \frac{\dot{M}}{\rho_\mathrm{w}}, \tag{6.17b}$$

$$Q_\mathrm{w} = -K S^\alpha |\partial_s \phi|^{\beta-2} \partial_s \phi, \tag{6.17c}$$

$$\partial_t S = \|\boldsymbol{v}_\mathrm{b}\| h_\mathrm{b} + \frac{|Q_\mathrm{w}\, \partial_s \phi|}{\rho_\mathrm{i} L_\mathrm{w}} - 2\, n^{-n} A L^2 |N|^{n-1} N, \tag{6.17d}$$

where $\dot{M}$ is the net melt rate, associated with the amount of water that reaches the conduit. As boundary conditions, we require a zero water flux at the ice divide, i.e., $Q_\mathrm{w} = 0$ at $s = 0$, and a continuity of the subglacial water pressure with the ocean water, i.e., $N = 0$ at $s = s_\mathrm{gl}$. We consider hard beds, for which $L(S) = \sqrt{S}$. For canals, $L(S) = S/H_0$, and the derivation and results are quite similar.

6.8.2 Dimensionless equations

We first make the problem and the unknowns dimensionless. We therefore write

$$\hat{s} = \frac{s}{[s]}, \quad \hat{t} = \frac{t}{[t]}, \quad \hat{\phi} = \frac{\phi}{[\phi]}, \quad \hat{N} = \frac{N}{[N]}, \quad \hat{Q}_\mathrm{w} = \frac{Q_\mathrm{w}}{[Q_\mathrm{w}]}, \quad \hat{S} = \frac{S}{[S]}. \tag{6.18}$$

The scales are chosen as follows. First, we set $[s] = s_\mathrm{gl}$ and $[\phi] = \Psi[s]$. We further choose $[t]$ to be a time scale associated with ice flow. The other scales, $[N]$, $[Q_\mathrm{w}]$, and $[S]$, are chosen such that

$$\frac{[Q_\mathrm{w}]}{[s]} = \frac{\dot{M}}{\rho_\mathrm{w}}, \quad [Q_\mathrm{w}] = K[S]^\alpha \Psi^{\beta-1}, \quad \frac{1}{\rho_\mathrm{i} L_\mathrm{w}} [Q_\mathrm{w}] \Psi = 2\, n^{-n} A [S][N]^n. \tag{6.19}$$

This leads to the following dimensionless formulation of the problem:

$$\eta \hat{N} = -\hat{s} - \hat{\phi}, \tag{6.20a}$$

$$\tau_1\, \partial_{\hat{t}} \hat{S} + \partial_{\hat{s}} \hat{Q}_\mathrm{w} = 1, \tag{6.20b}$$

$$\hat{Q}_\mathrm{w} = -\hat{S}^\alpha |\partial_{\hat{s}} \hat{\phi}|^{\beta-2} \partial_{\hat{s}} \hat{\phi}, \tag{6.20c}$$

$$\tau_2\, \partial_{\hat{t}} \hat{S} = \nu + |\hat{Q}_\mathrm{w}\, \partial_{\hat{s}} \hat{\phi}| - \hat{S} |\hat{N}|^{n-1} \hat{N}, \tag{6.20d}$$

for $0 < \hat{s} < 1$, with boundary conditions $\hat{Q}_{\mathrm{w}}(\hat{s}=0) = 0$ and $\hat{N}(\hat{s}=1) = 0$. Four dimensionless ratios appear here:

$$\eta := \frac{[N]/[s]}{\Psi}, \quad \nu := \frac{\rho_{\mathrm{i}} L_{\mathrm{w}} \|\boldsymbol{v}_{\mathrm{b}}\| h_{\mathrm{b}}}{[Q_{\mathrm{w}}]\Psi}, \quad \tau_1 := \frac{[S][s]}{[t][Q_{\mathrm{w}}]}, \quad \tau_2 := \frac{\rho_{\mathrm{i}} L_{\mathrm{w}} [S][s]}{[t][Q_{\mathrm{w}}][\phi]}. \tag{6.21}$$

The first ratio compares the magnitude of the spatial variation of N with respect to the geometric potential gradient Ψ. It thus follows that if $\eta \ll 1$, then $\partial_s \phi \approx \Psi$, while for $\eta \gg 1$, $\partial_s \phi \approx -\partial_s N$. The second parameter compares the two possible terms that lead to an opening of the cavities or of the channels: it compares the opening due to sliding over bumps of the bedrock and the melt of the conduit boundaries. The two last ratios compare the characteristic times related to changes in the water flux and in the channel thickness with respect to the characteristic time of ice flow. In particular, if $\tau_1, \tau_2 \ll 1$, which we anticipate, then the time dependency disappears from the problem and the hydrological system is in a steady state.

In what follows, we drop the hats on the dimensionless variables to simplify the notations.

6.8.3 Outer solution

For commonly used parameters, we obtain $\eta, \tau_1, \tau_2 \ll 1$ and $\nu \sim 1$. This suggests to treat η, τ_1, and τ_2 as small parameters of the problem. The leading-order solution is then given by

$$Q_{\mathrm{w}} = s, \quad S = s^{\frac{1}{\alpha}}, \quad \phi = -s, \quad N = s^{-\frac{1}{n\alpha}} (\nu + s)^{\frac{1}{n}}. \tag{6.22}$$

This effective pressure has originally been obtained by Schoof [2010b]. It is such that $N(s=1) = \nu^{1/n}$, so the Dirichlet boundary condition at the grounding line is not fulfilled. This suggests that there exists a boundary layer close to the grounding line, in which N quickly decreases to reach a zero value (figure 6.10a). We therefore refer to the leading-order solution (6.22) as the outer solution, and the inner solution, associated with the boundary layer, must be found to obtain an acceptable expression of the effective pressure.

6.8.4 Inner solution

We first eliminate Q_{w} and S from the dimensionless system of equations (6.20) to get the following equation for N only:

$$\nu + s|1 + \eta \partial_s N| = s^{\frac{1}{\alpha}} |1 + \eta \partial_s N|^{\frac{1-\beta}{\alpha}} |N|^{n-1} N, \tag{6.23}$$

for $0 < s < 1$ and with $N(s=1) = 0$. The boundary layer at the grounding line suggests the introduction of a scaling in which $\partial_s N$ becomes of order $\mathcal{O}(1)$. We therefore introduce $\mathcal{X} = \eta^{-1}(1-s)$ and rename $\mathcal{N} = N$. Then, at leading order,

$$\nu |1 - \partial_{\mathcal{X}} \mathcal{N}|^{\frac{\beta-1}{\alpha}} + |1 - \partial_{\mathcal{X}} \mathcal{N}|^{\frac{\beta+\alpha-1}{\alpha}} = |\mathcal{N}|^{n-1} \mathcal{N}, \tag{6.24}$$

for $\mathcal{X} > 0$ and with $\mathcal{N}(\mathcal{X}=0) = 0$. Because the inner solution must join the outer solution, we also have the compatibility condition $\mathcal{N} \to (\nu+1)^{\frac{1}{n}}$ as $\mathcal{X} \to +\infty$. Finding the solution of this leading-order problem is not trivial because of its non-linearity. Nonetheless, we approximate it by an expression $\tilde{\mathcal{N}}$. We require that this approximate has the correct behavior over the boundaries of the boundary layer, that is, $\tilde{\mathcal{N}} \sim \mathcal{X}$ as $\mathcal{X} \to 0$ and $\tilde{\mathcal{N}} \sim (\nu+1)^{\frac{1}{n}}$ as $\mathcal{X} \to +\infty$. We find that the following expression is a good approximation of $\mathcal{N}$ for $\nu \lesssim 1$; see figure 6.10b:

$$\tilde{\mathcal{N}} = \operatorname{erf}\left[\frac{\sqrt{\pi}}{2} \frac{\mathcal{X}}{(\nu+1)^{\frac{1}{n}}} \right] (\nu+1)^{\frac{1}{n}}, \tag{6.25}$$

where $\operatorname{erf}(x) = (2\pi)^{-1/2} \int_0^x \exp(-t^2)\,\mathrm{d}t$ is the Gauss error function.

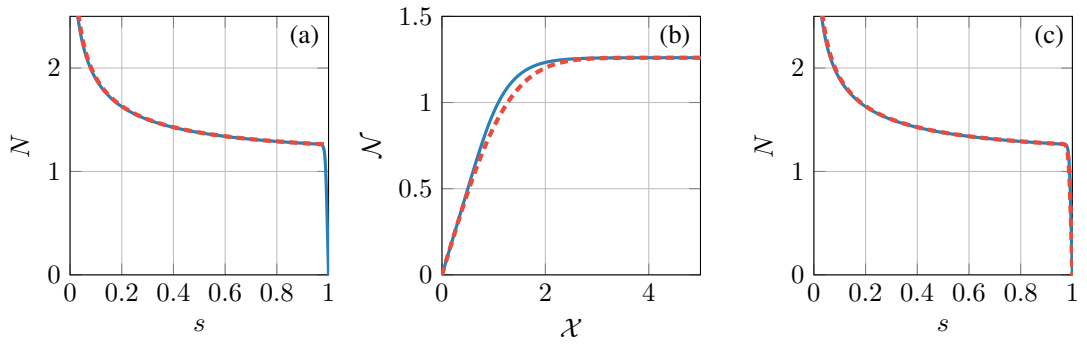

Figure 6.10: Inner, outer, and composite solutions of the dimensionless problem, for $\eta = 10^{-2}$ and $\nu = 1$. **(a)** Outer solution: numerical solution to the system of equations (6.20) (continuous line) and leading-order solution (6.22) to the outer problem (dashed line). **(b)** Inner solution: numerical solution to the equation (6.24) (continuous line) and approximate solution (6.25) (dashed line). **(c)** Composite solution: numerical solution to the system of equations (6.20) (continuous line) and composite solution (6.26) (dashed line).

6.8.5 Composite solution

The composite solution, which is valid over the whole domain, is obtained by summing the inner and outer solutions and subtracting the overlap in the matching area. This leads to the following expression:

$$N(s) = \operatorname{erf}\left[\frac{\sqrt{\pi}}{2}\frac{\eta^{-1}(1-s)}{(\nu+1)^{\frac{1}{n}}}\right](\nu+1)^{\frac{1}{n}} + s^{-\frac{1}{n\alpha}}(\nu+s)^{\frac{1}{n}} - (\nu+1)^{\frac{1}{n}}. \tag{6.26}$$

It is possible to go back to the original variables to obtain the expression of the effective pressure as a function of the original parameters. To do so, we introduce

$$N_\infty(s) = \left[\frac{\rho_\mathrm{i} L_\mathrm{w} \|\boldsymbol{v}_\mathrm{b}\| h_\mathrm{b} + (\rho_\mathrm{w}^{-1}\dot{M}s)\Psi}{2\, n^{-n}\rho_\mathrm{i} L_\mathrm{w} A (\rho_\mathrm{w}^{-1}\dot{M}s)^{\frac{1}{\alpha}} K^{-\frac{1}{\alpha}} \Psi^{\frac{1-\beta}{\alpha}}}\right]^{\frac{1}{n}}, \tag{6.27}$$

which is the outer solution written in its dimensional form. The effective pressure is then given by

$$N(s) = \operatorname{erf}\left[\frac{\sqrt{\pi}}{2}\frac{\Psi s_\mathrm{gl}}{N_\infty(s_\mathrm{gl})}\left(1 - \frac{s}{s_\mathrm{gl}}\right)\right] N_\infty(s_\mathrm{gl}) + N_\infty(s) - N_\infty(s_\mathrm{gl}). \tag{6.28}$$

Because N_∞ does not change much over the boundary layer, the previous expression can be replaced by

$$N(s) = \operatorname{erf}\left[\frac{\sqrt{\pi}}{2}\frac{\Psi s_\mathrm{gl}}{N_\infty(s)}\left(1 - \frac{s}{s_\mathrm{gl}}\right)\right] N_\infty(s) \tag{6.29a}$$

$$= \operatorname{erf}\left[\frac{\sqrt{\pi}}{2}\frac{\phi_0(s)}{N_\infty(s)}\right] N_\infty(s). \tag{6.29b}$$

This composite solution closely matches the numerical solution to the problem (figure 6.10c).

6.9 Appendix C: Effect of the coupling frequency between the hydrological and ice-sheet models

Here, we investigate the effect of the coupling frequency between the hydrological and the ice-sheet models. We show results for both MISMIP and Thwaites setups, and show that the hydrological model

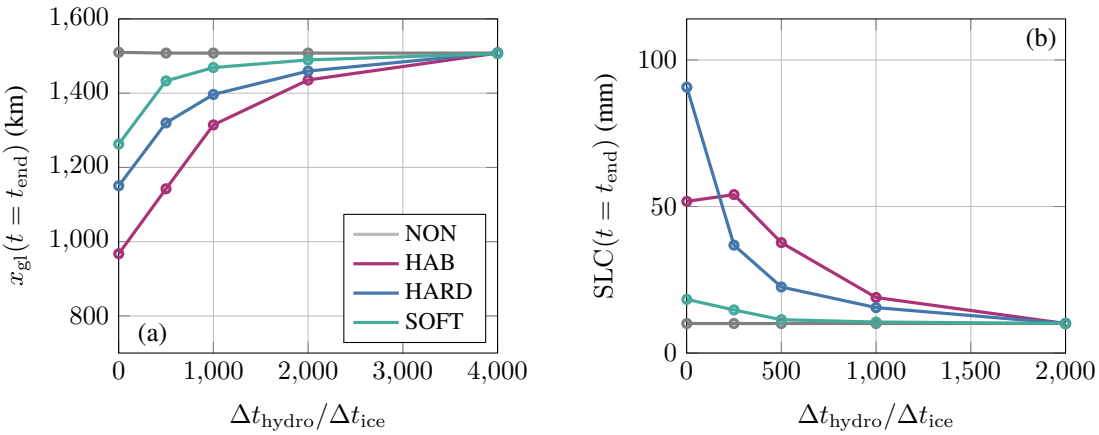

Figure 6.11: Effect of the coupling frequency between the hydrological and ice-sheet models: grounding-line position after the forcing as a function of the ratio between the time step $\Delta t_{\mathrm{hydro}}$ of the hydrological model and the time step Δt_{ice} of the ice-sheet model. Practically, we fix the ice-sheet time step and increase the time step of the hydrological model to obtain several values for $\Delta t_{\mathrm{hydro}}/\Delta t_{\mathrm{ice}}$. **(a)** MISMIP configuration: grounding-line position after the forcing. **(b)** Thwaites configuration: sea-level contribution after the forcing.

must be updated at a frequency that is at least of the same order of magnitude as the update frequency of the ice-sheet model. As a consequence, no subglacial hydrology model, no matter how complex, can improve ice-sheet simulations involving grounding-line motion if it is not updated at a sufficiently high frequency. In particular, considering a hydrological model during the initialization of an ice-sheet model but not during a forward simulation is virtually useless as the impact of the hydrological model is then almost nonexistent.

6.9.1 MISMIP

Figure 6.11a shows the grounding-line position after the same forcing as the one that was considered in section 6.3, for various update frequencies of the hydrological model. If the hydrology model is not regularly updated, then the results resemble the no-subglacial-hydrology case NON. This last case is evidently not affected by the chosen time steps. A higher sensitivity of the subglacial hydrological model also requires higher update frequency rates.

6.9.2 Thwaites

We can make the same observations in figure 6.11b as those made for the MISMIP configuration. A difference remains in the time scales considered for the two studies, and by the fact that HAB does not exhibits the largest sensitivity.

6.10 Appendix D: Influence of the unconstrained parameters of the hydrological model

We performed a sensitivity analysis of the least constrained parameters of our model, i.e., l_{c}, Q_{c}, and F_{till} (figure 6.12). It can be observed that l_{c} has only a limited effect for hard beds, while it has a more pronounced impact for soft beds. From equation (6.4), a change in l_{c} results in a change in the water flux Q_{w}, which will be important if water flow transitions from an efficient to an inefficient flow (or the reverse). However, for hard beds, the entirely efficient or inefficient cases yield similar results (figure

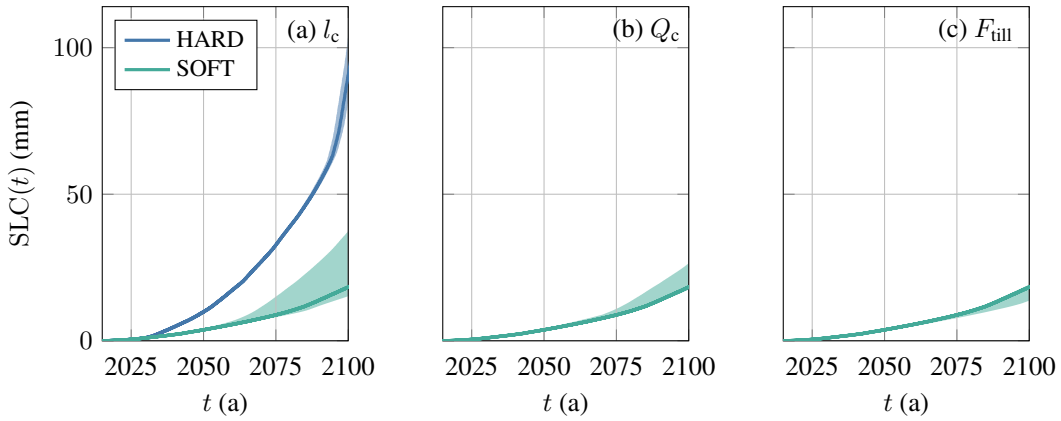

Figure 6.12: Sensitivity analysis of the results with respect to the parameters l_c, Q_c, and F_{till}. The set-up is the same as the one described in the forcing experiments over Thwaites (subsection 6.4.2; subglacial hydrology on homogeneous beds), except that different values of these parameters are chosen. The shaded areas correspond to the ranges $l_c \in [5, 15]$ km, $Q_c \in [0.5, 1.5]\,\mathrm{m}^3\,\mathrm{s}^{-1}$, and $F_{till} \in [1, 2]$, and the lines correspond to the nominal values considered in the original experiment.

6.8b). On the contrary, for soft beds, the difference between the entirely efficient or inefficient cases is more pronounced (figure 6.8b), and it follows that there is a stronger dependence with respect to l_c. For Q_c and F_{till}, the impact is limited. Finally, it can be noted the spread in the results increases over a time.

7

Singularity at pinning points

Singular behavior of marine ice sheets at pinning points:
numerical simulations and implications for grounding-line modeling
In prep.

Marine ice sheets play a crucial role in the climate system, as they are large ice masses interacting with the ocean. These ice sheets consist of grounded and floating regions, separated by the grounding line, which is key to understanding their dynamics. The balance between ice gain (from snow accumulation) and loss (through basal melt and iceberg calving) drives the evolution of ice sheets. This report focuses on the effects of pinning points –which can be defined as locations at which the floating region becomes locally grounded due to localized bedrock features– on ice-sheet dynamics. We show that pinning points can introduce a singular behavior in the governing equations for ice flow, making the linearized system ill-defined. This singularity arises due to a different momentum balance over the grounded and floating regions. Importantly, this singularity is independent of the discretization and appears even over smooth beds and with friction laws that vanish at the grounding line. Based on numerical experiments, we also show that these pinning points are such that a regularized formulation, in which the transition between the grounded and floating regions is done smoothly, leads to numerical simulations that are qualitatively different from the original, unregularized formulation of the problem. Finally, we suggest ways to handle these singularities and to improve the modeling of marine ice sheets and of their grounding lines.

7.1 Introduction

Marine ice sheets are essential components of the climate system. They consist of large masses of ice in contact with the ocean. These ice sheets are made up of two regions: a grounded region, where the ice is in contact with the bedrock, and a floating region, where the ice floats on seawater. These two regions are separated by the grounding line, which, as will be described later, is an important quantity in studying the dynamics of marine ice sheets.

The evolution of marine ice sheets over time depends on the imbalance between the gain of ice, that comes from snow accumulation at the upper surface, and the loss of ice, which is mainly due to basal melt below the ice sheet and calving due to icebergs detaching from the ice front. Under evolving atmospheric or oceanic conditions, ice sheets may therefore gain or loose mass. As a consequence, their equilibrium is modified, which leads to a modification of their geometry. Ice takes the form of a shear-thinning fluid that flows under its own weight, so that this change in geometry results in a change in the velocity pattern, which itself leads to a change in the discharge at the ice front. Hence, more ice could be released in the

ocean, which would lead to a modification of the sea level.

To understand their behavior, marine ice sheets have been studied using both analytical and numerical methods. In seminal papers, Schoof [2007b,c, 2012] showed, based on a boundary-layer analysis, that unbuttressed marine ice sheets whose grounding lines lie on upward-sloping bedrock are unstable. This has important implications; in particular, it suggests that the West Antarctic Ice Sheet is particularly sensitive to climate change: because of the topography of its bed, a perturbation in the position of the grounding line could lead to further retreat, accelerating the rate of retreat and eventually leading to a collapse [Pattyn, 2018; Coulon et al., 2024b]. The influence of bed topography has also been highlighted in a recent study by Robel et al. [2022a]. Based on numerical experiments, they showed that ice sheets exhibit ambiguous behavior at (sharp) bed peaks, either persisting at or retreating from these peaks.

In this report, we investigate the effect of pinning points on ice-sheet dynamics, in particular the effect on their grounding lines. Pinning points are closely related to bed peaks, ice rises, and ice rumples [Matsuoka et al., 2015]. Ice rises and rumples are features that are such that the floating parts of ice sheets, called ice shelves, are locally grounded in bed peaks. Depending on whether the ice flow is diverted around, or over this area, the feature is called a rise, or a ridge. Because they provide buttressing to the ice flow through friction with the bedrock, they can offer additional stability to the ice sheet. These positions are therefore known as pinning points, because they lead to grounding lines that are 'pinned' at these locations. The impact of pinning points on grounding-line dynamics has previously been studied through numerical simulations [Favier et al., 2012; Favier and Pattyn, 2015; De Rydt and Gudmundsson, 2016]. However, a theoretical understanding of their effects remains unexplored.

Here, we show that a singular behavior can appear at pinning points. This behavior is such that the linearized problem formed by the coupled mass-balance and momentum-balance equations becomes ill-defined, as components of the gradient of the momentum-balance equation become infinite. Importantly, this singularity can occur with smooth bed profiles as it is an inherent feature of the contact nature of the model, where there is a change in the stress balance in the basal and driving stresses across the grounding line. Accordingly, such singularity is expected to arise independently of the discretization that is considered in numerical simulations. This raises interesting questions, both about of the model itself and numerical simulations. In particular, this suggests that there is at the moment a bias in the treatment of the grounding line in the numerical simulations of marine ice sheets. Indeed, these typically decouple the mass-balance equation from the momentum-balance equation, therefore avoiding the singularity, but also departing from the initial problem formulation. A possibility to solve this issue would be to develop a new model formulation that allows for the presence of a 'grounding zone', for example through a regularized formulation that considers a smooth transition between the grounded and floating regions. Such an intermediate region is further corroborated by recent theoretical and observational studies associated with sub-shelf melt in a zone near the grounding line [Robel et al., 2022b; Bradley and Hewitt, 2024; Rignot et al., 2024].

This report is structured as follows. First, in section 7.2, we present the mathematical model for ice flow in marine ice-sheet systems. Then, in section 7.3, we study the linearized system that is obtained from the mass-balance and momentum-balance equations. We highlight the potential for a singularity to appear at pinning points, and subsequently introduce a regularized approach that allows this singularity to be removed thanks to a smoothing of the grounding-line definition. In section 7.4, we conduct a series of numerical experiments to investigate the effect of pinning points on grounding lines. We consider both stationary and transient results, and compare both the original and the regularized approach. Finally, we discuss our results in section 7.5 and conclude on their relevance in section 7.6.

7.2 Model

7.2.1 Notations

We use the following system of notations. If Ω is a subset of $\mathbb{R}^d$ ($d = 1, 2$), then its measure in $\mathbb{R}^d$ is noted $|\Omega|$. We use standard letters for scalars (e.g., a), bold lowercase letters for vectors (e.g., $\boldsymbol{a}$), and bold upppercase letters for second-order tensors (e.g., $\boldsymbol{A}$). If $f = f(\boldsymbol{x})$ is a scalar field, then ∇f denotes its gradient such that $\nabla f := \sum_k (\partial f / \partial x_k)\, \boldsymbol{i}_k$ in which x_k if the k-th component of $\boldsymbol{x}$ and $\boldsymbol{i}_k$ is the k-th unit vector. The Hessian of f is further denoted $\mathbf{hess} f := \sum_{k,l} (\partial^2 f / \partial x_k \partial x_l)\, \boldsymbol{i}_k \otimes \boldsymbol{i}_l$ in which $\otimes$ is the dyadic product. If $\boldsymbol{f} = \boldsymbol{f}(\boldsymbol{x})$ is a vector field, then its divergence and gradient are respectively denoted by $\mathrm{div} \boldsymbol{f} := \sum_k \partial f_k / \partial x_k$ and $\boldsymbol{\nabla f} := \sum_{k,l} (\partial f_k / \partial x_l) \boldsymbol{i}_k \otimes \boldsymbol{i}_l$ with f_k the k-th component of $\boldsymbol{f}$. If $\boldsymbol{F} = \boldsymbol{F}(\boldsymbol{x})$ is a second-order tensor field, then its divergence is written as $\mathbf{div}\, \boldsymbol{F} := \sum_l (\partial F_{k,l} / \partial x_l)\, \boldsymbol{i}_k$ with $F_{k,l}$ the (k, l) components of $\boldsymbol{F}$. Finally, if $\boldsymbol{F}$ and $\boldsymbol{G}$ are second-order tensor fields, then we write their tensor contraction (or Frobenius inner product) as $\boldsymbol{F} : \boldsymbol{G} = \sum_{k,l} f_{k,l} g_{k,l}$.

7.2.2 Strong formulation

We consider the ice flow of an isothermal marine ice sheet. We use a reduced-order model known as the shallow-shelf approximation [Morland, 1987; MacAyeal, 1989; Schoof and Hewitt, 2013]. It can be viewed as a depth-integrated model in which it is assumed that vertical shear can be neglected, so that ice essentially flows in a sliding motion. Such an approximation is frequently used to model fast-flowing ice streams [e.g. Schoof, 2007b,c; Bueler and Brown, 2009; Winkelmann et al., 2011; Pattyn, 2017]. It is formally exact for ice shelves (the floating parts of ice sheets), and a good approximation for the grounded parts of ice sheets close to the grounding line. Importantly, the vertical normal stress is cryostatic under this assumption.

The domain of interest, covered by ice, is denoted Ω. It is a connected and bounded subset of $\mathbb{R}^d$, with $d = 1$ if we consider a two-dimensional ice sheet and $d = 2$ for a three-dimensional ice sheet. It does not evolve with time. A point in Ω is denoted by $\boldsymbol{x}$. The problem then consists of determining two fields: the ice thickness $h : \Omega \times]0, T[\to \mathbb{R}_{\geq 0}$, and the horizontal ice velocity $\boldsymbol{u} : \Omega \times]0, T[\to \mathbb{R}^d$, where $T > 0$ is the time over which the problem is considered (Fig. 7.1).

Domain

The domain Ω is partitioned into three subsets: the grounded domain, Ω_g, where ice is grounded, the floating domain, Ω_f, where ice is floating, and the grounding line, Γ_gl, where ice switches from a grounded to a floating position. Under the shallow-shelf approximation, Archimedes' principle allows the following characterization of these sets:

$$\Omega_\mathrm{g} := \{\boldsymbol{x} \in \Omega : \mathcal{G}(\boldsymbol{x}, t) > 0\}\,, \tag{7.1a}$$

$$\Omega_\mathrm{f} := \{\boldsymbol{x} \in \Omega : \mathcal{G}(\boldsymbol{x}, t) < 0\}\,, \tag{7.1b}$$

$$\Gamma_\mathrm{gl} := \{\boldsymbol{x} \in \Omega : \mathcal{G}(\boldsymbol{x}, t) = 0\}\,, \tag{7.1c}$$

where $\mathcal{G}$ is the flotation function

$$\mathcal{G}(\boldsymbol{x}, t) := h(\boldsymbol{x}, t) + \frac{\rho_\mathrm{w}}{\rho} b(\boldsymbol{x}), \tag{7.2}$$

with ρ the ice density, ρ_w the water density, and b the bedrock elevation. In contrast with Ω, both Ω_g, Ω_f, and Γ_gl are functions of time, so we may write $\Omega_\mathrm{g} = \Omega_\mathrm{g}(t)$, $\Omega_\mathrm{f} = \Omega_\mathrm{f}(t)$, and $\Gamma_\mathrm{gl} = \Gamma_\mathrm{gl}(t)$. Moreover, they are not necessarily connected regions. The boundary $\Gamma := \partial\Omega$ of the domain is itself partitioned into several parts: the ice divide Γ_d, where ice starts to flow, a free-slip boundary Γ_fs, which can be associated with a symmetry plane, and a calving front Γ_cf, where ice detaches into icebergs.

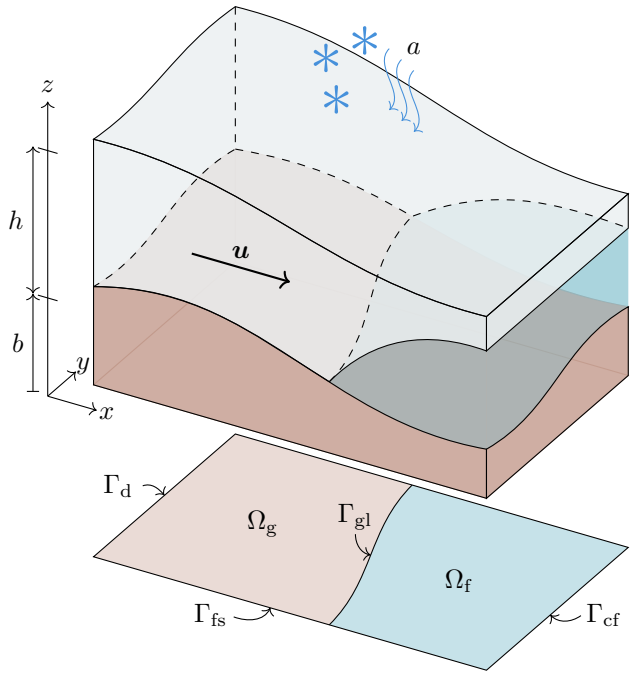

Figure 7.1: Schematic of a marine ice sheet, which is characterized by a thickness h and a horizontal velocity $\boldsymbol{u}$. Those fields are defined over a domain Ω which is partitioned into the grounded region Ω_{g}, the floating region Ω_{f}, and the grounding line Γ_{gl}. The boundary Γ of the domain Ω is split into three parts: the ice divide Γ_{d}, the free-slip boundary Γ_{fs}, and the calving front Γ_{cf}. In this figure, b denotes the bedrock elevation and a the net mass accumulation rate.

In order to simplify the analysis of the problem, we have implicitly made a series of simplifying assumptions that we now detail. Firstly, we have assumed that the bedrock elevation does not evolve and takes the form of a smooth prescribed field $b = b(\boldsymbol{x})$. This stationarity assumption amounts to neglecting the glacial isostatic adjustment mechanism associated with the reaction of the Earth's surface to changes in ice geometry [Clark and Lingle, 1977; Mitrovica et al., 2001; Coulon et al., 2021]. Second, the ice front Γ_{cf} is considered fixed, although in reality it moves according to ice-front advection and calving events [Benn et al., 2007; Joughin et al., 2012]. We note that the physics of these ice-loss mechanisms are not yet fully understood. It is this assumption that allowed us to say that Ω does not evolve with time. Third, we consider that the grounding line is such that $|\Gamma_{\mathrm{gl}}| = 0$, which guarantees that it is an object whose dimension is (at most) that of a line, hence its name [we refer to Pegler, 2018b, for the description of a set-up in which this condition does not hold]. All these assumptions are justified by the fact that we here wish to focus on the motion of the grounding line alone.

Balance equations

The equations that govern the flow of ice are mass-balance and momentum-balance equations. These are given by the following system of equations over the grounded and floating domains, respectively:

$$\partial_t h + \mathrm{div}(h\,\boldsymbol{u}) = a, \quad \text{in } \Omega_{\mathrm{g}}\times]0,T[, \tag{7.3a}$$

$$\mathbf{div}\,[2\,h\,\eta(\boldsymbol{u})\,\boldsymbol{\Sigma}(\boldsymbol{u})] + \boldsymbol{\tau}_{\mathrm{b}} = \boldsymbol{\tau}_{\mathrm{g}}, \quad \text{in } \Omega_{\mathrm{g}}\times]0,T[, \tag{7.3b}$$

and

$$\partial_t h + \mathrm{div}(h\,\boldsymbol{u}) = a, \quad \text{in } \Omega_{\mathrm{f}}\times]0,T[, \tag{7.4a}$$

$$\mathbf{div}\,[2\,h\,\eta(\boldsymbol{u})\,\boldsymbol{\Sigma}(\boldsymbol{u})] = \boldsymbol{\tau}_{\mathrm{f}}, \quad \text{in } \Omega_{\mathrm{f}}\times]0,T[. \tag{7.4b}$$

The first equations in these systems, equations (7.3a) and (7.4a), take the form of transport (hyperbolic) equations for the ice thickness, with a the net mass accumulation rate, equal to the snowfall input at the upper surface of the ice sheet, minus the melt rate at its base. The other equations in these systems, (7.3b) and (7.4b), are elliptic equations for the ice velocity. They establish a balance between the divergence of the viscous stresses, the driving stresses due to gravity, and, for the grounded domain, friction stresses. The absence of inertial terms comes from the spatial and temporal scales associated with ice flow. Here, $\boldsymbol{\Sigma}(\boldsymbol{u})$ is the membrane-deformation tensor,

$$\boldsymbol{\Sigma}(\boldsymbol{u}) := \boldsymbol{D}(\boldsymbol{u}) + [\mathrm{tr}\boldsymbol{D}(\boldsymbol{u})]\boldsymbol{I}, \tag{7.5}$$

with $\boldsymbol{D}(\boldsymbol{u}) := [\boldsymbol{\nabla u} + (\boldsymbol{\nabla u})^{\mathrm{T}}]/2$ the horizontal strain-rate tensor and $\boldsymbol{I}$ the identity tensor. The membrane-deformation tensor plays an analogous role to the strain-rate tensor in the Navier–Stokes equations, but for the shallow-shelf approximation in which the complexity of the model is reduced. The effective viscosity, $\eta(\boldsymbol{u})$, is given by

$$\eta(\boldsymbol{u}) := \tfrac{1}{2}A^{-\frac{1}{n}}\left(\|\boldsymbol{D}(\boldsymbol{u})\|_*^2 + \delta_\eta^2\right)^{\frac{1-n}{2n}}, \quad \|\boldsymbol{D}(\boldsymbol{u})\|_* := \sqrt{\tfrac{1}{2}\left[\mathrm{tr}((\boldsymbol{D}(\boldsymbol{u}))^2) + (\mathrm{tr}\,\boldsymbol{D}(\boldsymbol{u}))^2\right]}, \tag{7.6}$$

in which $A > 0$ and $n > 1$ are viscosity parameters associated a the power-law rheology, known in the glaciology literature as Glen's flow law [Glen, 1955]. The regularization parameter $\delta_\eta \ll 1$ is introduced to guarantee that the viscosity stays finite if the ice undergoes a rigid-body motion.

There are several possible parametrizations for the basal friction stress $\boldsymbol{\tau}_{\mathrm{b}}$. Here, we consider two of such friction laws. The first one is the most common one in glaciology and is known as Weertman's friction law [Weertman, 1957]. It assumes a power-law relation between the friction stress and the ice velocity:

$$\boldsymbol{\tau}_{\mathrm{b}} = -C\|\boldsymbol{u}\|^{p-1}\boldsymbol{u}, \tag{7.7}$$

with $C > 0$ and $0 < p < 1$. The second one is known as the regularized Coulomb friction law [Schoof, 2005; Joughin et al., 2019] and is expressed as

$$\boldsymbol{\tau}_{\mathrm{b}} = -\mu N\left(\frac{\|\boldsymbol{u}\|}{\|\boldsymbol{u}\| + (\mu N/C)^{1/p}}\right)^p \frac{\boldsymbol{u}}{\|\boldsymbol{u}\|}, \tag{7.8}$$

where $\mu > 0$ is an additional friction coefficient and N represents the effective pressure, defined subsequently. This law is structured such that it transitions smoothly between two regimes: the Weertman friction law at low velocity magnitudes or large effective pressures, and a Coulomb-type behavior at high velocity magnitudes or low effective pressures. The latter scenario is anticipated near the grounding line, whereas the former is expected farther inland within the ice sheet. Formally, these two regimes are described as follows:

$$\boldsymbol{\tau}_{\mathrm{b}} \sim -C\|\boldsymbol{u}\|^{p-1}\boldsymbol{u}, \quad \text{for } \|\boldsymbol{u}\| \ll (\mu N/C)^{1/p}, \tag{7.9a}$$

$$\boldsymbol{\tau}_{\mathrm{b}} \sim -\mu N\frac{\boldsymbol{u}}{\|\boldsymbol{u}\|}, \quad \text{for } \|\boldsymbol{u}\| \gg (\mu N/C)^{1/p}. \tag{7.9b}$$

Form a physical point of view, such a behavior is desirable as it can be used to model the effect of subglacial cavitation over hard beds or of bed deformation at the ice-bed interface over soft beds [Schoof, 2005; Zoet and Iverson, 2020]. Accordingly, the regularized Coulomb law has been proposed as a unified friction law by the glaciological community [Minchew and Joughin, 2020]. The effective pressure N introduced in (7.8) is defined as an effective difference between the pressure applied by the ice sheet on the underlying bed and the subglacial water pressure. The most simple model for N assumes a perfect connection of the subglacial water with the ocean [e.g., Tsai et al., 2015], so that, over the grounded region,

$$N = \rho g h - \rho_{\mathrm{w}} g \max(0, -b). \tag{7.10}$$

Interestingly, close to the grounding line $b \leq 0$, so $N = \rho g \mathcal{G}$. To avoid any confusion with the regularization that is introduced later on in this report, we now refer to this law as the 'Schoof' friction law.

Finally, $\boldsymbol{\tau}_\mathrm{g}$ and $\boldsymbol{\tau}_\mathrm{f}$ denote the driving stresses, that are due to gravity, over the grounded and floating regions, respectively. In general, the driving stress may be written as $\rho g h \nabla s$ with g the acceleration of gravity and in which s denotes the upper-surface elevation, so that gravity leads to a flattening of ice sheets. The distinction between $\boldsymbol{\tau}_\mathrm{g}$ and $\boldsymbol{\tau}_\mathrm{f}$ stems from the different form that this surface elevation takes over the grounded and the floating regions: for the former, the surface elevation is the sum of the bedrock elevation and of the ice thickness: $s = b + h$. By contrast, for the latter, it is directly proportional to the ice thickness, as a consequence of the flotation state of ice shelves: $s = (1 - \rho/\rho_\mathrm{w})h$. It follows that

$$\boldsymbol{\tau}_\mathrm{g} = \rho g h \nabla (b + h), \tag{7.11a}$$

$$\boldsymbol{\tau}_\mathrm{f} = \rho \left(1 - \frac{\rho}{\rho_\mathrm{w}}\right) g h \nabla h. \tag{7.11b}$$

Initial, transmission, and boundary conditions

To close the system of equations, it is necessary to add a collection of initial, transmission, and boundary conditions. Firstly, we prescribe the initial ice-sheet geometry:

$$h = h_0, \quad \text{on } \Omega \times \{t = 0\}. \tag{7.12}$$

We also enforce transmission conditions, namely, we require that both the ice thickness and the normal component of the stress tensor are continuous across the grounding line:

$$[\![h]\!] = 0, \quad \text{at } \Gamma_\mathrm{gl} \times]0, T[, \tag{7.13a}$$

$$[\![2\, h\, \eta(\boldsymbol{u})\, \boldsymbol{\Sigma}(\boldsymbol{u}) \cdot \boldsymbol{n}]\!] = \boldsymbol{0}, \quad \text{at } \Gamma_\mathrm{gl} \times]0, T[, \tag{7.13b}$$

where $[\![\cdot]\!]$ is the jump operator and $\boldsymbol{n}$ is the normal vector to the grounding line. The former is formally defined, for a field $f = f(\boldsymbol{x})$, as

$$[\![f(\boldsymbol{x})]\!] := \lim_{\substack{\boldsymbol{y} \to \boldsymbol{x} \\ \boldsymbol{y} \in \Omega_\mathrm{f}}} f(\boldsymbol{y}) - \lim_{\substack{\boldsymbol{y} \to \boldsymbol{x} \\ \boldsymbol{y} \in \Omega_\mathrm{g}}} f(\boldsymbol{y}), \quad \forall\, \boldsymbol{x} \in \Gamma_\mathrm{gl}, \tag{7.14}$$

provided these limits exist.

Finally, the following boundary conditions are imposed:

$$\boldsymbol{u} = \boldsymbol{0}, \quad \text{on } \Gamma_\mathrm{d} \times]0, T[, \tag{7.15a}$$

$$\boldsymbol{u} \cdot \boldsymbol{n} = 0, \quad \text{on } \Gamma_\mathrm{fs} \times]0, T[, \tag{7.15b}$$

$$(\boldsymbol{I} - \boldsymbol{n} \otimes \boldsymbol{n})\, [2\, h\, \eta\, \boldsymbol{\Sigma}] \cdot \boldsymbol{n} = \boldsymbol{0}, \quad \text{on } \Gamma_\mathrm{fs} \times]0, T[, \tag{7.15c}$$

$$[2\, h\, \eta\, \boldsymbol{\Sigma}] \cdot \boldsymbol{n} = \boldsymbol{\tau}_\mathrm{cf}, \quad \text{on } \Gamma_\mathrm{cf} \times]0, T[, \tag{7.15d}$$

with $\boldsymbol{n}$ the outward normal to the boundary of the domain. Equation (7.15a) states that ice is motionless at the ice divide. Equation (7.15b) prohibits the penetration of ice through the free-slip boundary, while equation (7.15c) enforces a zero shear value at that boundary. Finally, equation (7.15d) is a consequence of the continuity of the horizontal component of the stress tensor at the ice-ocean interface: the horizontal component of the (depth-integrated) stress tensor in the ice must be compensated by the (depth-integrated) water pressure in the ocean, which is such that

$$\boldsymbol{\tau}_\mathrm{cf} = \frac{1}{2} \rho \left(1 - \frac{\rho}{\rho_\mathrm{w}}\right) g h^2\, \boldsymbol{n}. \tag{7.16}$$

7.2.3 Weak formulation

Here, we consider the weak formulation associated with the system of equations formed by equations (7.3), (7.4), (7.12), (7.13), and (7.15). To do so, we introduce the following functional spaces:

$$\mathcal{S}_h := \{h : \Omega \to \mathbb{R} \text{ with } h \text{ sufficiently smooth}\}, \tag{7.17a}$$

$$\mathcal{S}_{\boldsymbol{u}} := \{\boldsymbol{u} : \Omega \to \mathbb{R}^d \text{ with } \boldsymbol{u} \text{ sufficiently smooth, } \boldsymbol{u}|_{\Gamma_\mathrm{d}} = \boldsymbol{0},\ \boldsymbol{u}\cdot\boldsymbol{n}|_{\Gamma_\mathrm{fs}} = 0\}, \tag{7.17b}$$

and we further set $\mathcal{S}_\phi := \mathcal{S}_h$ and $\mathcal{S}_{\boldsymbol{\phi}} := \mathcal{S}_{\boldsymbol{u}}$. By 'sufficiently smooth', we here mean that the integrals appearing in the resulting weak formulation, obtained hereafter, exist. Multiplying the mass and momentum balance equations (7.3)–(7.4) by test functions $\phi \in \mathcal{S}_\phi$ and $\boldsymbol{\phi} \in \mathcal{S}_{\boldsymbol{\phi}}$ and integrating them over Ω leads to the following equations:

$$\int_\Omega \partial_t h\,\phi\,\mathrm{d}\Omega + \int_\Omega \mathrm{div}(h\,\boldsymbol{u})\,\phi\,\mathrm{d}\Omega = \int_\Omega a\,\phi\,\mathrm{d}\Omega, \tag{7.18a}$$

$$\int_\Omega \mathbf{div}[2\,h\,\eta\,\boldsymbol{\Sigma}]\cdot\boldsymbol{\phi}\,\mathrm{d}\Omega + \int_{\Omega_\mathrm{g}} \boldsymbol{\tau}_\mathrm{b}\cdot\boldsymbol{\phi}\,\mathrm{d}\Omega = \int_{\Omega_\mathrm{g}} \boldsymbol{\tau}_\mathrm{g}\cdot\boldsymbol{\phi}\,\mathrm{d}\Omega + \int_{\Omega_\mathrm{f}} \boldsymbol{\tau}_\mathrm{f}\cdot\boldsymbol{\phi}\,\mathrm{d}\Omega. \tag{7.18b}$$

For the purposes of this report, we already discretize this system in time. We write $\partial_t h = (h - \tilde{h})/\Delta t$ with $\tilde{h}$ the (known) thickness obtained at time t, h the (unknown) thickness at time $t + \Delta t$, and Δt the time step. We also understand $\boldsymbol{u}$ as the (unknown) horizontal velocity at time $t + \Delta t$. Then, we integrate the equations by parts, and apply the boundary conditions (7.15) together with the definition of the set $\mathcal{S}_{\boldsymbol{\phi}}$. This yields the following formulation:

Formulation (Weak formulation)**.** *Find* $(h, \boldsymbol{u}) \in \mathcal{S}_h \times \mathcal{S}_{\boldsymbol{u}}$ *s.t.*

$$\int_\Omega (h - \tilde{h})/\Delta t\,\phi\,\mathrm{d}\Omega + \int_{\Gamma_\mathrm{cf}} h\,\boldsymbol{u}\cdot\boldsymbol{n}\,\phi\,\mathrm{d}\Gamma - \int_\Omega h\,\boldsymbol{u}\cdot\nabla\phi\,\mathrm{d}\Omega - \int_\Omega a\,\phi\,\mathrm{d}\Omega = 0, \tag{7.19a}$$

$$\int_\Omega 2\,h\,\eta\,\boldsymbol{\Sigma} : \boldsymbol{\nabla}\boldsymbol{\phi}\,\mathrm{d}\Omega + \int_{\Omega_\mathrm{g}} (\boldsymbol{\tau}_\mathrm{g} - \boldsymbol{\tau}_\mathrm{b})\cdot\boldsymbol{\phi}\,\mathrm{d}\Omega + \int_{\Omega_\mathrm{f}} \boldsymbol{\tau}_\mathrm{f}\cdot\boldsymbol{\phi}\,\mathrm{d}\Omega + \int_{\Gamma_\mathrm{cf}} \boldsymbol{\tau}_\mathrm{cf}\cdot\boldsymbol{\phi}\,\mathrm{d}\Omega = 0, \tag{7.19b}$$

for all $(\phi, \boldsymbol{\phi}) \in \mathcal{S}_\phi \times \mathcal{S}_{\boldsymbol{\phi}}$.

We may write this concisely as

$$F_h(h, \boldsymbol{u}; \phi) = 0, \quad \forall\,\phi \in \mathcal{S}_\phi, \tag{7.20a}$$

$$F_{\boldsymbol{u}}(h, \boldsymbol{u}; \boldsymbol{\phi}) = 0, \quad \forall\,\boldsymbol{\phi} \in \mathcal{S}_{\boldsymbol{\phi}}. \tag{7.20b}$$

Note that by formally taking the limit $\Delta t \to +\infty$, i.e., by removing the first term in (7.19a), we recover a steady-state formulation. We also note that the study of the momentum-balance equation alone has already been done in the literature, in particular in its variational formulation; we refer the interested reader to Schoof [2006, 2010a] and Jouvet [2015].

7.3 Grounding-line motion and singularity

7.3.1 The linearized problem

In practice, to solve the system of equations (7.20), one may rely on a Newton procedure. After discretizating in space the equations, one linearizes them around a current estimate $(h, \boldsymbol{u})$. This gives a system of algebraic linear equations that can be solved, leading to an updated estimate. By repeating this process, a solution to the problem may be found. The study of this linearized problem is of great interest as it allows us to determine whether or not a solution can be found using this iterative method and, if so, how quickly it will converge to that solution. It can also be used to determine the stability of

equilibrium positions. Here we consider the linearization of (7.20) without prior discretization. The motivation behind this choice is to show properties of the linearization that cannot be attributed to a specific discretization and are therefore expected to hold independently of the discretization adopted.

The linearization of the system of equations (7.20) reads as follows:

Formulation (Linearized problem)**.** *Find* $(\delta h, \delta \boldsymbol{u})$ *with* $(h + \delta h, \boldsymbol{u} + \delta \boldsymbol{u}) \in \mathcal{S}_h \times \mathcal{S}_{\boldsymbol{u}}$ *s.t.*

$$\langle D_h F_h(h, \boldsymbol{u}; \phi), \delta h \rangle + \langle D_{\boldsymbol{u}} F_h(h, \boldsymbol{u}; \phi), \delta \boldsymbol{u} \rangle = -F_h(h, \boldsymbol{u}; \phi), \quad \forall\, \phi \in \mathcal{S}_\phi, \tag{7.21a}$$

$$\langle D_h F_{\boldsymbol{u}}(h, \boldsymbol{u}; \boldsymbol{\phi}), \delta h \rangle + \langle D_{\boldsymbol{u}} F_{\boldsymbol{u}}(h, \boldsymbol{u}; \boldsymbol{\phi}), \delta \boldsymbol{u} \rangle = -F_{\boldsymbol{u}}(h, \boldsymbol{u}; \boldsymbol{\phi}), \quad \forall\, \boldsymbol{\phi} \in \mathcal{S}_{\boldsymbol{\phi}}. \tag{7.21b}$$

Here, $D_h F_h$ and $D_{\boldsymbol{u}} F_h$ are the Gâteaux derivatives of F_h with respect to h and $\boldsymbol{u}$, respectively. Similarly, $D_h F_{\boldsymbol{u}}$ and $D_{\boldsymbol{u}} F_{\boldsymbol{u}}$ are the Gâteaux derivatives of $F_{\boldsymbol{u}}$ with respect to h and $\boldsymbol{u}$, respectively. The symbol $\langle \cdot, \cdot \rangle$ denotes the duality pairing so that, for example, $\langle D_h F_h(h, \boldsymbol{u}; \phi), \delta h \rangle$ denotes the Gâteaux differential of F_h with respect to h, evaluated at $(h, \boldsymbol{u}; \phi)$, and in the direction δh. The analytical expressions of the terms appearing in (7.21) can be found in the appendix A.

A difficulty appears in the computation of $D_h F_{\boldsymbol{u}}$. Indeed, the residual $F_{\boldsymbol{u}}$ takes the form of a sum of integrals, some of which being defined over the sets Ω_{g} and Ω_{f}. Such terms are those associated with the driving stresses $\boldsymbol{\tau}_{\mathrm{g}}$ and $\boldsymbol{\tau}_{\mathrm{f}}$, and with the friction stresses $\boldsymbol{\tau}_{\mathrm{b}}$. Because Ω_{g} and Ω_{f} depend on h, computing the Gâteaux derivatives of these terms leads to two types of contribution: one that is associated with a change in the grounded or floating domain, and one that is associated with a change in the integrated quantity (i.e., a change in the stresses). To formalize this, we write

$$\langle D_h F_{\boldsymbol{u}}(h, \boldsymbol{u}; \boldsymbol{\phi}), \delta h \rangle = \langle D_h|_{\Gamma_{\mathrm{gl}}} F_{\boldsymbol{u}}(h, \boldsymbol{u}; \boldsymbol{\phi}), \delta h \rangle + \langle D_h|_{\delta\Gamma_{\mathrm{gl}}} F_{\boldsymbol{u}}(h, \boldsymbol{u}; \boldsymbol{\phi}), \delta h \rangle, \tag{7.22}$$

in which $D_h|_{\Gamma_{\mathrm{gl}}} F_{\boldsymbol{u}}$ is associated with a change of the integrated quantity, the grounded and floating regions being held fixed. By contrast, $D_h|_{\delta\Gamma_{\mathrm{gl}}} F_{\boldsymbol{u}}$ is associated with a change in the grounded and floating regions; this time, it is the integrated quantities that are being held fixed. The latter can therefore be interpreted as a shape derivative [see, e.g., Allaire et al., 2021].

These different derivatives may be obtained by explicitly writing the dependency of $F_{\boldsymbol{u}}$ with respect to h through a presence in the integrands, and through the moving grounded and floating regions. To do so, we assume $\boldsymbol{u}$ and $\boldsymbol{\phi}$ fixed and write

$$F_{\boldsymbol{u}}(h, \boldsymbol{u}; \boldsymbol{\phi}) = G(h, \Omega_{\mathrm{g}}(h), \Omega_{\mathrm{f}}(h)), \tag{7.23}$$

where G has the structure described above. It follows that the different terms in the right-hand side of (7.22) can be computed as

$$\langle D_h|_{\Gamma_{\mathrm{gl}}} F_{\boldsymbol{u}}(h, \boldsymbol{u}; \boldsymbol{\phi}), \delta h \rangle := \lim_{\theta \to 0} \frac{G(h + \theta\, \delta h, \Omega_{\mathrm{g}}(h), \Omega_{\mathrm{f}}(h)) - G(h, \Omega_{\mathrm{g}}(h), \Omega_{\mathrm{f}}(h))}{\theta}, \tag{7.24a}$$

$$\langle D_h|_{\delta\Gamma_{\mathrm{gl}}} F_{\boldsymbol{u}}(h, \boldsymbol{u}; \boldsymbol{\phi}), \delta h \rangle := \lim_{\theta \to 0} \frac{G(h, \Omega_{\mathrm{g}}(h + \theta\, \delta h), \Omega_{\mathrm{f}}(h + \theta\, \delta h)) - G(h, \Omega_{\mathrm{g}}(h), \Omega_{\mathrm{f}}(h))}{\theta}. \tag{7.24b}$$

The first term can be easily computed. For the second term, we have the following result. Its proof, together with that of the other propositions of this report, can be found in the appendix B.

Proposition (Expression of the shape derivative)**.** *If* $\|\nabla \mathcal{G}\| \neq 0$ *at* Γ_{gl}*, then*

$$\langle D_h|_{\delta\Gamma_{\mathrm{gl}}} F_{\boldsymbol{u}}(h, \boldsymbol{u}; \boldsymbol{\phi}), \delta h \rangle = \int_{\Gamma_{\mathrm{gl}}} (\boldsymbol{\tau}_{\mathrm{g}} - \boldsymbol{\tau}_{\mathrm{f}} - \boldsymbol{\tau}_{\mathrm{b}}) \cdot \boldsymbol{\phi}\, \|\nabla \mathcal{G}\|^{-1} \delta h \, \mathrm{d}\Gamma. \tag{7.25}$$

Several comments can be made regarding this result. We first note that the expression for the shape derivative involves the inverse of $\|\nabla\mathcal{G}\|$. This factor can be interpreted as a grounding-line sensitivity: it corresponds to the number of meters the grounding line advances per meter of grounding-line thickness increase. Given its importance and since the above result requires $\|\nabla\mathcal{G}\| \neq 0$ to hold, we investigate it further in the next subsection. We further note that, importantly, the shape derivative arises because the governing equations differ over evolving domains (the grounded and floating regions). If this were not the case, such a contribution would naturally not appear.

7.3.2 Singularity

The previous discussion reveals the importance of the magnitude of the gradient of the flotation function $\mathcal{G}$. To clarify our vocabulary, we introduce the following definition.

Definition (Pinning point)**.** *A pinning point $\boldsymbol{x}_{\mathrm{gl}} \in \Gamma_{\mathrm{gl}}$ is a point that is such that $\|\nabla\mathcal{G}\| = 0$ at $\boldsymbol{x}_{\mathrm{gl}}$.*

Such a definition is purely mathematical. Nevertheless, an equivalent geometrical characterization can be obtained, linking this definition to what is meant by a pinning point in a glaciological context. The following result formalizes this.

Proposition (Geometrical characterization of a pinning point)**.** *A pinning point $\boldsymbol{x}_{\mathrm{gl}} \in \Gamma_{\mathrm{gl}}$ is a point that is such that the ice-sheet lower surface is locally tangent to the bedrock.*

It follows that, at a pinning point, the shape-derivative expression (7.25) does not hold, as $\|\nabla\mathcal{G}\|^{-1}$ is formally infinite at such a position. Physically, the grounding line is displaced by a quantity that is not proportional to the perturbation δh; in other words, the grounding-line sensitivity is infinite. This singularity can be attributed to several physical situations. An example is the situation of an ice shelf that becomes locally in contact with a bump in the underlying bedrock. At the moment when the ice shelf is in contact with the underlying bedrock bump, it is tangential to it, so we are indeed in the context of a pinning point. If the ice shelf gets thicker, there will be the creation of one or several grounding lines in that area, associated with the local anchoring of the shelf in the bedrock.

Pinning points can be classified based on the following result.

Proposition (Local behavior around a pinning point)**.** *Around a pinning point $\boldsymbol{x}_{\mathrm{gl}}$, the flotation function admits the following expansion:*

$$\mathcal{G}(\boldsymbol{x}) = \frac{1}{2}(\boldsymbol{x} - \boldsymbol{x}_{\mathrm{gl}}) \cdot \mathbf{hess}\,\mathcal{G}(\boldsymbol{x}_{\mathrm{gl}}) \cdot (\boldsymbol{x} - \boldsymbol{x}_{\mathrm{gl}}) + \mathcal{O}(\|\boldsymbol{x} - \boldsymbol{x}_{\mathrm{gl}}\|^3). \tag{7.26}$$

It follows that a pinning point can be characterized according to the Hessian of $\mathcal{G}$ at $\boldsymbol{x}_{\mathrm{gl}}$. For a two-dimensional ice sheet ($d = 1$), the Hessian is a scalar, so the local behavior of the flotation function depends on the sign of this scalar. In particular, if it is non-zero, then the flotation has a local parabolic profile. For a three-dimensional ice sheet ($d = 2$), pinning points can be classified according to the eigenvalues λ_1, λ_2 of the Hessian. For example, the surface $z = \mathcal{G}(\boldsymbol{x})$ then locally corresponds to an elliptic paraboloid if λ_1 and λ_2 are non-zero and of the same sign and to a hyperbolic paraboloid if λ_1 and λ_2 are of opposite sign.

7.3.3 A regularized approach

The singularity mentioned above appears as a feature that is associated with both the fact that the grounding line moves whenever there is a change in the ice thickness, and the fact that there are different equations that govern the ice-sheet dynamics over the grounded and floating regions. It follows that a way to avoid having to deal with this singularity consists in adopting a regularized approach in which there is no abrupt change in the governing equations when switching between the grounded and floating regions. Specifically, one can develop a formulation in which the transition between the grounded and floating

regions occurs progressively.

To obtain this formulation, we start from the original expression of the momentum-balance equation (7.19b):

$$\int_\Omega 2\,h\,\eta\,\boldsymbol{\Sigma} : \boldsymbol{\nabla}\boldsymbol{\phi}\,\mathrm{d}\Omega + \int_{\Omega_\mathrm{g}} (\boldsymbol{\tau}_\mathrm{g} - \boldsymbol{\tau}_\mathrm{b}) \cdot \boldsymbol{\phi}\,\mathrm{d}\Omega + \int_{\Omega_\mathrm{f}} \boldsymbol{\tau}_\mathrm{f} \cdot \boldsymbol{\phi}\,\mathrm{d}\Omega + \int_{\Gamma_\mathrm{cf}} \boldsymbol{\tau}_\mathrm{cf} \cdot \boldsymbol{\phi}\,\mathrm{d}\Omega = 0. \tag{7.27}$$

This can be equivalently written as follows:

$$\int_\Omega 2\,h\,\eta\,\boldsymbol{\Sigma} : \boldsymbol{\nabla}\boldsymbol{\phi}\,\mathrm{d}\Omega + \int_{\Omega} 1_\mathrm{g}(\boldsymbol{\tau}_\mathrm{g} - \boldsymbol{\tau}_\mathrm{b}) \cdot \boldsymbol{\phi}\,\mathrm{d}\Omega + \int_{\Omega} 1_\mathrm{f}\boldsymbol{\tau}_\mathrm{f} \cdot \boldsymbol{\phi}\,\mathrm{d}\Omega + \int_{\Gamma_\mathrm{cf}} \boldsymbol{\tau}_\mathrm{cf} \cdot \boldsymbol{\phi}\,\mathrm{d}\Omega = 0, \tag{7.28}$$

in which we have introduced the indicator function $1_\mathrm{g} = 1_\mathrm{g}(\boldsymbol{x})$ (resp. $1_\mathrm{f} = 1_\mathrm{f}(\boldsymbol{x})$) which is equal to one if $\boldsymbol{x} \in \Omega_\mathrm{g}$ (resp. $\boldsymbol{x} \in \Omega_\mathrm{f}$) and to zero otherwise. A regularized formulation is then obtained by replacing the indicator functions with smooth versions of these functions that approximate them. Here, we consider the following expressions for the smoothed indicator functions (we denote them with hats):

$$\hat{1}_\mathrm{g}(\boldsymbol{x}) := \frac{1}{1 + \exp(-\mathcal{G}(\boldsymbol{x})/\mathcal{G}_0)}, \tag{7.29a}$$

$$\hat{1}_\mathrm{f}(\boldsymbol{x}) := \frac{\exp(-\mathcal{G}(\boldsymbol{x})/\mathcal{G}_0)}{1 + \exp(-\mathcal{G}(\boldsymbol{x})/\mathcal{G}_0)}, \tag{7.29b}$$

in which the length $\mathcal{G}_0 > 0$ plays the role of a regularization parameter. These smoothened functions are presented in figure 7.2. We note that these functions have the following properties:

$$0 < \hat{1}_\mathrm{g}(\boldsymbol{x}) < 1, \tag{7.30a}$$

$$0 < \hat{1}_\mathrm{f}(\boldsymbol{x}) < 1, \tag{7.30b}$$

$$\hat{1}_\mathrm{g}(\boldsymbol{x}) + \hat{1}_\mathrm{f}(\boldsymbol{x}) = 1, \tag{7.30c}$$

$$\hat{1}_\mathrm{g}(\boldsymbol{x}) \to 1_\mathrm{g}(\boldsymbol{x}), \quad \text{as } \mathcal{G}_0 \to 0, \tag{7.30d}$$

$$\hat{1}_\mathrm{f}(\boldsymbol{x}) \to 1_\mathrm{f}(\boldsymbol{x}), \quad \text{as } \mathcal{G}_0 \to 0, \tag{7.30e}$$

for almost all $\boldsymbol{x} \in \Omega$. Any pair of smooth functions that obey these equations is likely to be a valid candidate for the construction of a regularized formulation. By replacing the indicator functions with their smoothened counterparts, equation (7.28) becomes

$$\int_\Omega 2\,h\,\eta\,\boldsymbol{\Sigma} : \boldsymbol{\nabla}\boldsymbol{\phi}\,\mathrm{d}\Omega + \int_{\Omega} \hat{1}_\mathrm{g}(\boldsymbol{\tau}_\mathrm{g} - \hat{\boldsymbol{\tau}}_\mathrm{b}) \cdot \boldsymbol{\phi}\,\mathrm{d}\Omega + \int_{\Omega} \hat{1}_\mathrm{f}\boldsymbol{\tau}_\mathrm{f} \cdot \boldsymbol{\phi}\,\mathrm{d}\Omega + \int_{\Gamma_\mathrm{cf}} \boldsymbol{\tau}_\mathrm{cf} \cdot \boldsymbol{\phi}\,\mathrm{d}\Omega = 0. \tag{7.31}$$

Therefore, the friction stress $\boldsymbol{\tau}_\mathrm{b}$ and the driving stresses $\boldsymbol{\tau}_\mathrm{g}$ and $\boldsymbol{\tau}_\mathrm{f}$ are now considered over the full domain of the marine ice sheet. From a mathematical point of view, the effect of these stresses becomes non-local in the sense that their influence is considered to be non-zero outside the regions on which they were originally supposed to apply. Nonetheless, their contribution is weighted by a factor that decreases exponentially fast with respect to the distance from the original region on which these stresses were originally defined.

Note that we have also replaced the basal friction stress $\boldsymbol{\tau}_\mathrm{b}$ by a smoothened counterpart $\hat{\boldsymbol{\tau}}_\mathrm{b}$ in (7.31). The reason to do so is that that the friction stress is originally defined over the grounded region, and extending its definition over the floating region might lead to a non-smooth expression. It turns out that for the Weertman friction law, this issue does not appear. However, the Schoof friction law involves the effective pressure which by definition vanishes over the floating region. The effective pressure is then continuous but not continuously differentiable across the grounding line. It follows that the friction stress

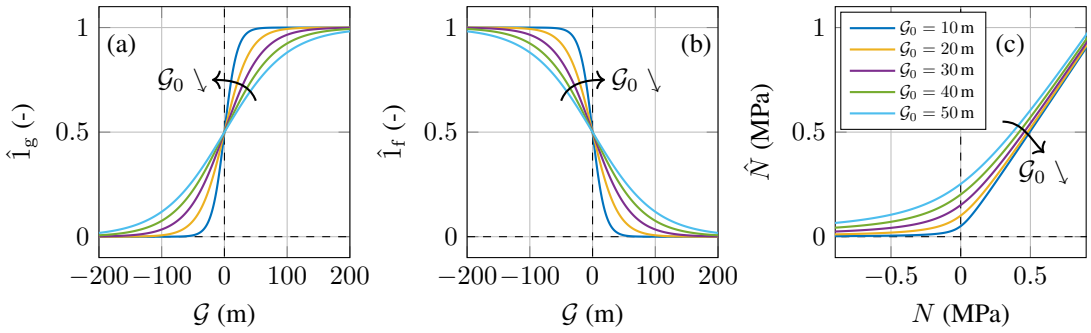

Figure 7.2: Smoothened functions used to define the regularized formulation of the problem. **(a)** Smoothened version of the indicator function 1_g for the grounded region Ω_g. **(b)** Smoothened version of the indicator function 1_f for the floating Ω_f. **(c)** Smoothened version of the effective pressure N.

itself is not smooth across the grounding line. A possibility to avoid this consists in regularizing the effective pressure by replacing it with a smooth version $\hat{N}$ that also depends, for consistency, on $\mathcal{G}_0$:

$$\hat{\boldsymbol{\tau}}_b = -\mu \hat{N} \left(\frac{\|\boldsymbol{u}\|}{\|\boldsymbol{u}\| + (\mu \hat{N}/C)^{1/p}} \right)^p \frac{\boldsymbol{u}}{\|\boldsymbol{u}\|}, \quad \hat{N} := \frac{N + \sqrt{N^2 + (\rho g \mathcal{G}_0)^2}}{2}; \tag{7.32}$$

see figure 7.2c.

Overall, the following formulation is obtained, which is the regularized version of the system of equations (7.19).

Formulation (Regularized weak formulation)**.** *Find* $(h, \boldsymbol{u}) \in \mathcal{S}_h \times \mathcal{S}_{\boldsymbol{u}}$ *s.t.*

$$\int_\Omega (h - \tilde{h})/\Delta t \, \phi \, \mathrm{d}\Omega + \int_{\Gamma_{cf}} h \, \boldsymbol{u} \cdot \boldsymbol{n} \, \phi \, \mathrm{d}\Gamma - \int_\Omega h \, \boldsymbol{u} \cdot \nabla \phi \, \mathrm{d}\Omega - \int_\Omega a \, \phi \, \mathrm{d}\Omega = 0, \tag{7.33a}$$

$$\int_\Omega 2 \, h \, \eta \, \boldsymbol{\Sigma} : \boldsymbol{\nabla} \boldsymbol{\phi} \, \mathrm{d}\Omega + \int_\Omega \hat{1}_g (\boldsymbol{\tau}_g - \hat{\boldsymbol{\tau}}_b) \cdot \boldsymbol{\phi} \, \mathrm{d}\Omega + \int_\Omega \hat{1}_f \boldsymbol{\tau}_f \cdot \boldsymbol{\phi} \, \mathrm{d}\Omega + \int_{\Gamma_{cf}} \boldsymbol{\tau}_{cf} \cdot \boldsymbol{\phi} \, \mathrm{d}\Omega = 0, \tag{7.33b}$$

for all $(\phi, \boldsymbol{\phi}) \in \mathcal{S}_\phi \times \mathcal{S}_{\boldsymbol{\phi}}$.

Such a regularized approach has been considered in the finite-element ice-sheet code `Ua` [Gudmundsson et al., 2012]. This code has been verified in inter-comparison studies [Pattyn et al., 2013; Cornford et al., 2020; Levermann et al., 2020] and used to obtain projections in Antarctica [e.g., Reed et al., 2023]. The use of a regularized friction term has also been considered in Pattyn et al. [2006].

7.4 Numerical experiments

In this section, we conduct a series of numerical experiments in order to investigate the following elements:

(i) the presence of discontinuities in the stress distribution across the grounding line;

(ii) the influence that pinning points have on ice-sheet dynamics;

(iii) the effect of the friction law on the two previous points;

(iv) the differences in the results obtained with the original and regularized formulations.

The experiments are designed to be as simple as possible so that the results are easy to interpret. In what follows, we first describe the numerical set-up that consists in the description of the physical and numerical parameters and of the bed elevation profiles. Then, we show various numerical results. We first compute the stress distribution profiles at steady state (with the Weertman/Schoof friction laws). We also compute bifurcation plots corresponding to the set of steady-state solutions associated with various values of the parameter a (with the Weertman/Schoof friction laws, with the original/regularized formulations, and with/without pinning points). Finally, we compute the transient evolution of marine ice sheets, starting from a steady state that is perturbed due to a variation in the parameter a (with the Weertman/Schoof friction laws, with the original/regularized formulations, and with/without pinning points).

7.4.1 Set-up

We consider two-dimensional ice sheets, defined over a domain $\Omega =]0, x_{\mathrm{cf}}[$, in which x_{cf}, the position of the calving front, is set to $x_{\mathrm{cf}} = 1800\,\mathrm{km}$. The position $x = 0\,\mathrm{km}$ corresponds to the ice divide. The physical parameters used in the numerical experiments and their values are shown in table 7.1.

Description	Symbol	Value	Units
Ice density	ρ	910	$\mathrm{kg\,m^{-3}}$
Water density	ρ_{w}	1028	$\mathrm{kg\,m^{-3}}$
Gravity acceleration	g	9.81	$\mathrm{m\,s^{-2}}$
Friction coefficient	C	7.624×10^6	$\mathrm{Pa\,m^{-1/3}\,s^{1/3}}$
Friction coefficient	μ	0.4	-
Ice viscosity coefficient	A	4.9×10^{-25}	$\mathrm{Pa^{-3}\,s^{-1}}$
Ice viscosity exponent	n	3	-
Net mass accumulation rate	a	0.3	$\mathrm{m\,year^{-1}}$
Viscosity regularization parameter	δ_η	10^{-12}	$\mathrm{s^{-1}}$

Table 7.1: (Default) physical parameters used in the numerical experiments.

Two bedrock profiles are considered. The first one serves as a reference bedrock and is such that we do not expect any pinning point to appear. It takes the form of a polynomial expression in the position:

$$b_{\mathrm{bg}}(x) = b_0 + b_2 \left(\frac{x}{L_0}\right)^2 + b_4 \left(\frac{x}{L_0}\right)^4 + b_6 \left(\frac{x}{L_0}\right)^6. \tag{7.34}$$

Such an expression is frequently used in numerical experiments that involve marine ice sheets [e.g., Pattyn et al., 2012]. We also consider a bedrock profile with a smooth bed peak that should lead to the creation of a pinning point:

$$b_{\mathrm{pp}}(x) = b_{\mathrm{bg}}(x) + A_{\mathrm{pp}} \exp\left[-\frac{1}{2}\left(\frac{x - x_{\mathrm{pp}}}{L_{\mathrm{pp}}}\right)^2\right]. \tag{7.35}$$

The values of the parameters appearing in these expressions are specified in table 7.2.

The numerical simulations are obtained based on a finite-element discretization of the weak formulations (7.19) and (7.33). The mesh is uniform and consists of 10^4 elements, i.e., the resolution is set to $\Delta x = 180\,\mathrm{m}$. The original formulation involves elements that contain both grounded and floating regions. To obtain an exact integration in the finite-element assembly, we apply a quadrature rule on each grounded and floating sub-regions over these elements [see Seroussi et al., 2014, SEP2]. Finally, for the transient simulations, we stabilize the hyperbolic part of the equations by adding an artificial diffusive term in the mass-balance equation [Kelly et al., 1980; dos Santos et al., 2021].

Description	Symbol	Value	Units
Bed amplitude	b_0	$+0729.00$	m
Bed amplitude	b_2	-2184.80	m
Bed amplitude	b_4	$+1031.72$	m
Bed amplitude	b_6	-0151.72	m
Characteristic length	L_0	7.5×10^5	m
Bed amplitude	A_{pp}	370	m
Characteristic length	L_{pp}	10^5	m
Bump location	x_{pp}	1.3×10^6	m

Table 7.2: Parameters for the definition of the two bed profiles considered in the numerical experiments.

7.4.2 Stress distribution

We start with the solutions associated with the default physical parameters (Tab. 7.1) and with the first bedrock profile. The numerical solutions are obtained by considering the steady-state version of the original formulation. Specifically, a Newton scheme is applied to the discretized version of the non-linear system of equations (7.19), until convergence is reached in which the residuals of both the mass-balance and momentum-balance equations are sufficiently small. The obtained profiles are shown in figure 7.3 for both the Weertman and Schoof friction laws.

These results highlight the different stress regimes over the grounded and floating regions. For the Weertman friction law, the momentum balance over the grounded region essentially corresponds to a balance between the friction and driving stresses, the divergence of the viscous stresses being negligible. Such behavior is expected; see, e.g., Sergienko and Wingham [2022]. At the grounding line, the basal friction switches from a relatively high value of $\sim 200\,\mathrm{kPa}$ to a zero value over the floating region. To guarantee that the momentum-balance equation is conserved, the magnitude of the driving stress is then also greatly reduced. We note that the divergence of the viscous stresses jumps is also discontinuous at the grounding line, but the jump is much smaller than the one of the other components of the momentum balance.

These results can be compared with those obtained with the Schoof friction law. For that law, the stress distribution is seemingly similar far from the grounding line. This is expected as in that case, the velocities are relatively low, so that the Schoof friction law essentially reduces to the Weertman friction law (see equation (7.9a)). However, the behavior close to the grounding line is different. Firstly, the grounding-line position is located slightly upstream ($\sim 60\,\mathrm{km}$) compared to the Weertman case. The upper surface of the ice sheet is also more flat near the grounding line, which is a feature of the Coulomb-like behavior in that region [Tsai et al., 2015]. In terms of the momentum-balance equation, there is a boundary layer close to the grounding line in which each type of stress (viscous, driving, and friction) contributes to the equilibrium [Gregov et al., 2023]. There is again a discontinuity in the stress distribution, in that both the divergence of the viscous stresses and the driving stress are discontinuous across the grounding line. Nonetheless, this magnitude of the jump is much smaller compared to the one that was observed for the Weertman friction law ($\sim 40\,\mathrm{kPa}$).

7.4.3 Steady states

The second type of results consists in bifurcation plots (also called bifurcation diagrams). Here, we view a as a free parameter and obtain the set of steady-state solutions associated with varying values of this parameter. In order to obtain two-dimensional plots, we use the grounded-domain extent, $|\Omega_{\mathrm{g}}|$, to represent the state of the system. Hence, bifurcation pots characterize the relation between $|\Omega_{\mathrm{g}}|$ and a. The rationale behind the use of $|\Omega_{\mathrm{g}}|$ is that it has a simple interpretation for simple configurations in

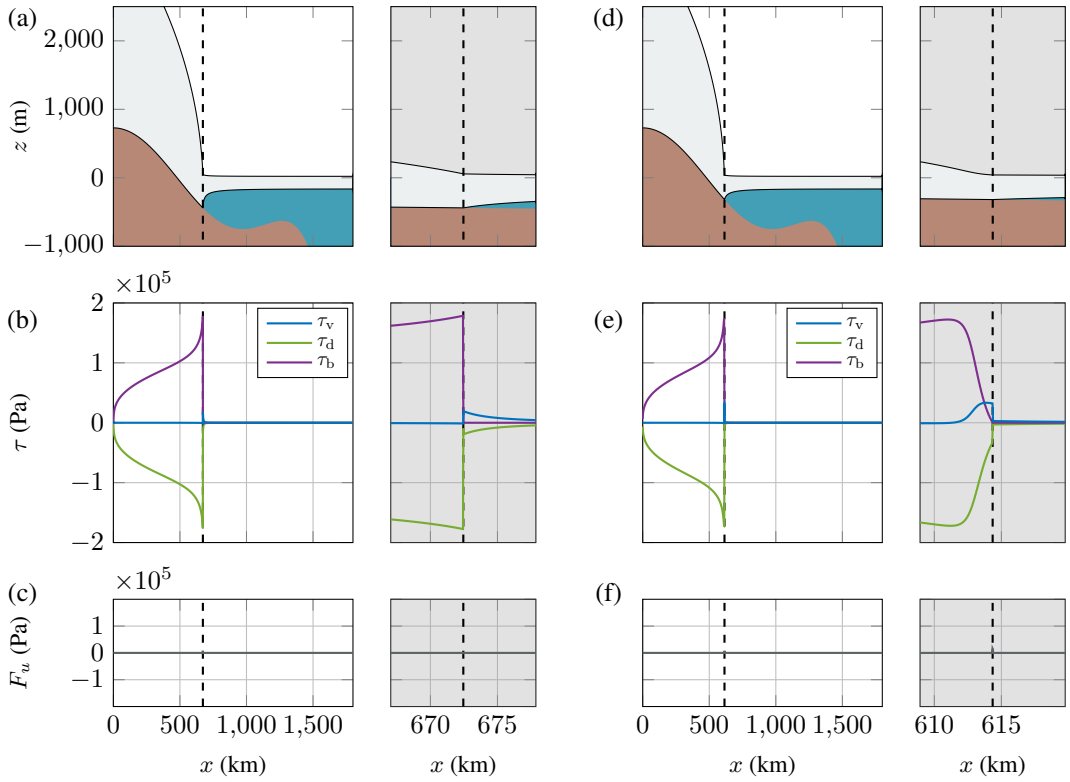

Figure 7.3: Steady-state solutions corresponding to the original formulation with the Weertman (left) and Schoof (right) friction laws. **(a)**, **(b)**, and **(c)**: geometry, stress distribution, and residual of the momentum-balance for the solution obtained with the Weertman friction law. **(d)**, **(e)**, and **(f)**: geometry, stress distribution, and residual of the momentum-balance for the solution obtained with the Schoof friction law. The smaller darker panels correspond to a zoom near the grounding line, which is drawn as a black dashed vertical line. These panels have been obtained with a higher resolution ($\Delta x = 18\,\mathrm{m}$). For the panels associated with the stress distributions, τ_v, τ_d, and τ_b respectively correspond to the divergence of the viscous stresses, to the driving stresses, and to the basal friction stresses.

which the ice is in a grounded state and then becomes floating (see, e.g., Fig. 7.3). Indeed, in that case, $|\Omega_\mathrm{g}|$ is equal to the grounding-line position x_gl, which is the unique element of the grounding-line set: $\Gamma_\mathrm{gl} = \{x_\mathrm{gl}\}$. Bifurcation diagrams involving x_gl are standard in glaciology [e.g., Schoof, 2007b; Pattyn et al., 2012; Mulder et al., 2018]. In particular, bifurcation plots have previously been obtained for the Weertman and Schoof friction laws for such simple configurations based on boundary-layer analyses [Schoof, 2007b,c; Tsai et al., 2015; Gregov et al., 2023]. The advantage of using $|\Omega_\mathrm{g}|$ is that this variable makes sense for more complex configurations –which we will encounter here– in which Γ_gl does not contain a single element.

To obtain bifurcation plots, we rely on numerical continuation methods [Allgower and Georg, 1990; Govaerts, 2000]. We consider the two formulations (original/regularized), the two bed types, and the two friction laws (Weertman/Schoof). For the regularized formulation, we rely on a pseudo-arclength continuation method which is the standard continuation method [Keller, 1977, 1987; Mulder et al., 2018]. However, we do not apply this method for the original formulation, as it requires the governing equations to be sufficiently regular (typically, at least continuously differentiable), which is not the case here. Hence, we use an alternative continuation method which is based on a scalar constraint function that is modified at each step of the continuation method. These two methods are described in the appendix C.

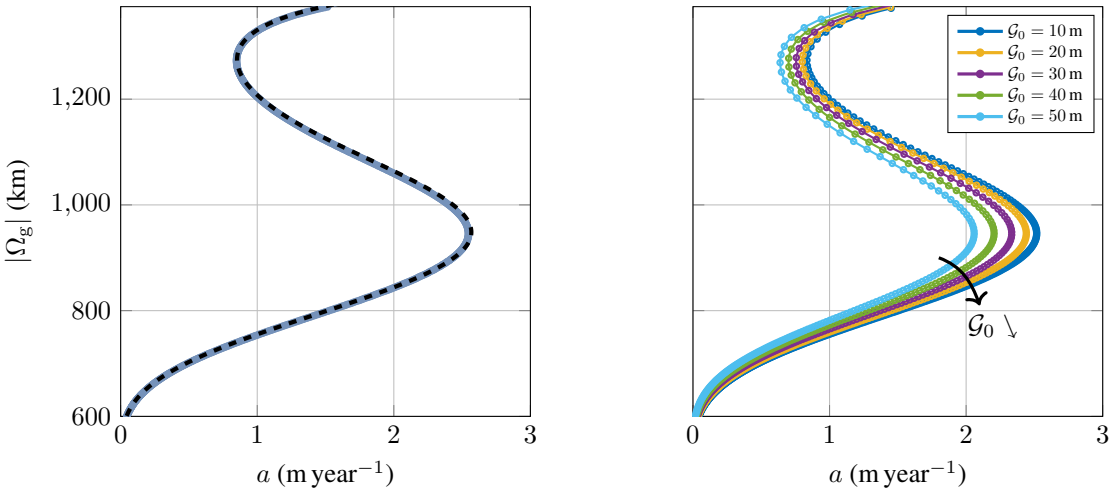

(a) Original formulation.

(b) Regularized formulation.

Figure 7.4: Bifurcation curves of the grounded-region extent $|\Omega_g|$ expressed as a function of the net mass accumulation rate a for the first bed type and for the Weertman friction law. **(a)** Numerical results obtained with the original problem formulation (blue line) and steady-state solution obtained with a boundary-layer analysis (dashed black line) [Schoof, 2007b,c]. **(b)** Numerical results obtained with several values of the parameter $\mathcal{G}_0$ of the regularized formulation.

The obtained bifurcation plots for the first bed type are shown in figure 7.4 (Weertman friction law) and in figure 7.5 (Schoof friction law). The plots associated with the second bed type are shown in figure 7.6 (Weertman friction law) and in figure 7.7 (Schoof friction law). Several comments can be made. On the one hand, for the first bed type, all the bifurcations plots are continuous, and qualitatively similar between the results obtained with the original and the regularized formulations. When the value of $\mathcal{G}_0$ is reduced, the bifurcation diagram of the regularized formulation gets closer to the bifurcation diagram of the original formulation. However, this is not the case for the second bed type, for which the bifurcation curve stops at two locations when considering the original formulation. Here, such stops mean that the numerical continuation method did not find any solution beyond the red crosses. These stops are not present in the results associated with the regularized formulation, for which the bifurcation plots still consists in continuous curves, whatever the value of $\mathcal{G}_0$ considered. On the other hand, we remark that the results are qualitatively similar for the Weertman and Schoof friction laws, suggesting that similar conclusions can be made irrespective of the specific type of friction law that is adopted.

The differences observed when considering the two formulations with the second bed type suggest to look closer at the associated results. We have shown in figure 7.8 the ice-sheet profiles associated with the red crosses of figure 7.6a. It then clearly appears that these points are pinning points as the ice shelves are tangent to the bedrock for these configurations. In terms of the classification described in subsection 7.3.2, we recognize the parabolic behavior of the flotation function near the pinning points. We have also shown in figure 7.9 the intermediate states corresponding to the vertical part of the bifurcation plots observed in figure 7.6b. We observe a progressive retreat of the grounding line, for which the ice sheet takes a series of (nonphysical) intermediate geometries, with a small gap separating the shelf from the bedrock near the grounding line.

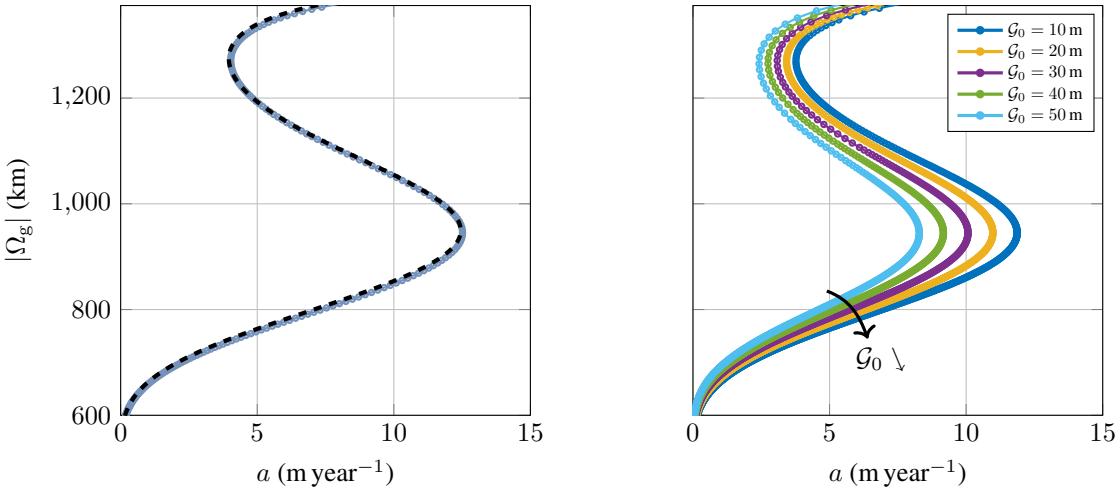

(a) Original formulation.

(b) Regularized formulation.

Figure 7.5: Bifurcation curves of the grounded-region extent $|\Omega_g|$ expressed as a function of the net mass accumulation rate a for the first bed type and for the Schoof friction law. **(a)** Numerical results obtained with the original problem formulation (blue line) and steady-state solution obtained with a boundary-layer analysis (dashed black line) [Tsai et al., 2015]. **(b)** Numerical results obtained with several values of the parameter $\mathcal{G}_0$ of the regularized formulation.

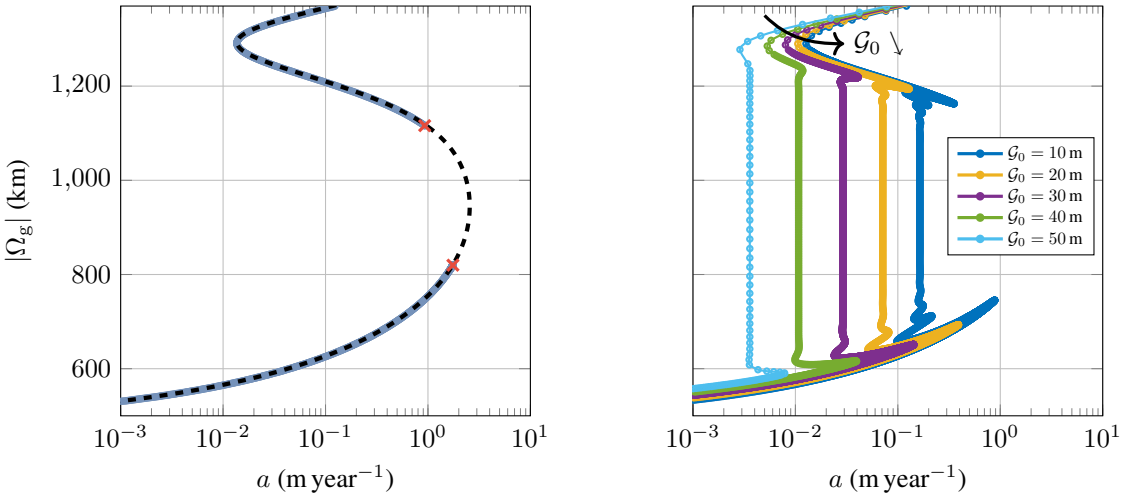

(a) Original formulation.

(b) Regularized formulation.

Figure 7.6: Bifurcation curves of the grounded-region extent $|\Omega_g|$ expressed as a function of the net mass accumulation rate a for the second bed type and for the Weertman friction law. **(a)** Numerical results obtained with the original problem formulation (blue line) and steady-state solution obtained with a boundary-layer analysis (dashed black line) [Schoof, 2007b,c]. **(b)** Numerical results obtained with several values of the parameter $\mathcal{G}_0$ of the regularized formulation.

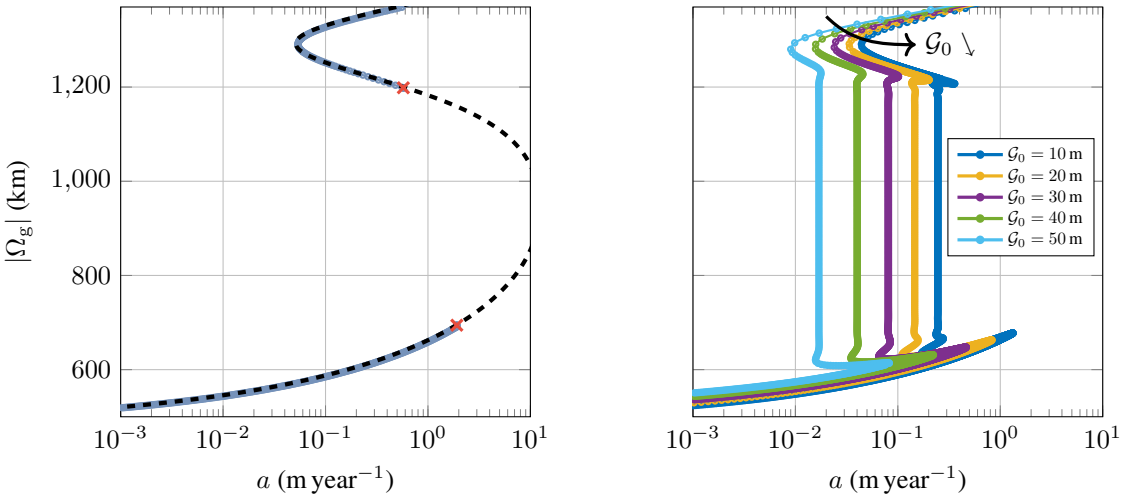

(a) Original formulation.

(b) Regularized formulation.

Figure 7.7: Bifurcation curves of the grounded-region extent $|\Omega_g|$ expressed as a function of the net mass accumulation rate a for the second bed type and for the Schoof friction law. **(a)** Numerical results obtained with the original problem formulation (blue line) and steady-state solution obtained with a boundary-layer analysis (dashed black line) [Tsai et al., 2015]. **(b)** Numerical results obtained with several values of the parameter $\mathcal{G}_0$ of the regularized formulation.

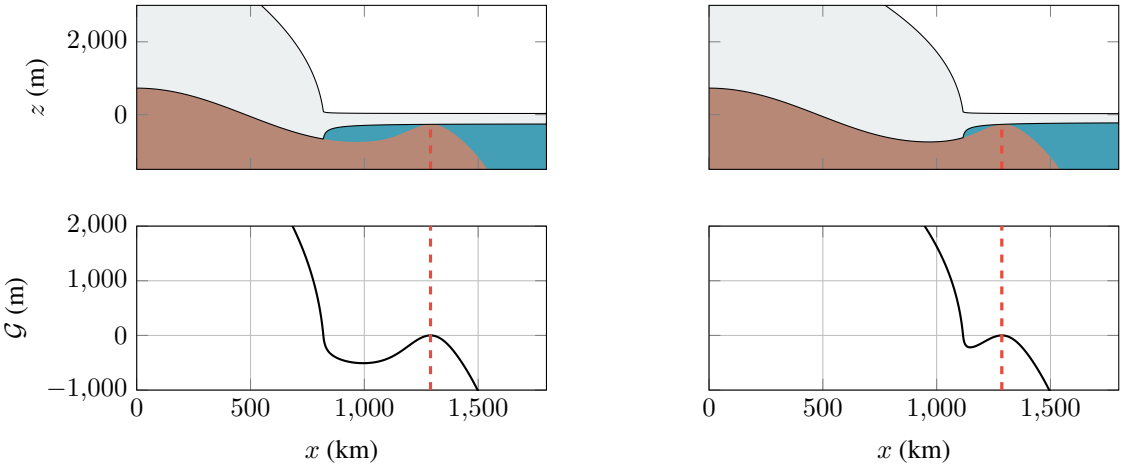

Figure 7.8: Ice-sheet profiles and expression of the flotation function $\mathcal{G}$ as a function of the x coordinate for the two pinning-point configurations identified in figure 7.6. The red dashed line corresponds to the position x_{gl} of the pinning point itself, i.e., to the point that is such that $\mathcal{G}(x_{gl}) = \partial_x \mathcal{G}(x_{gl}) = 0$.

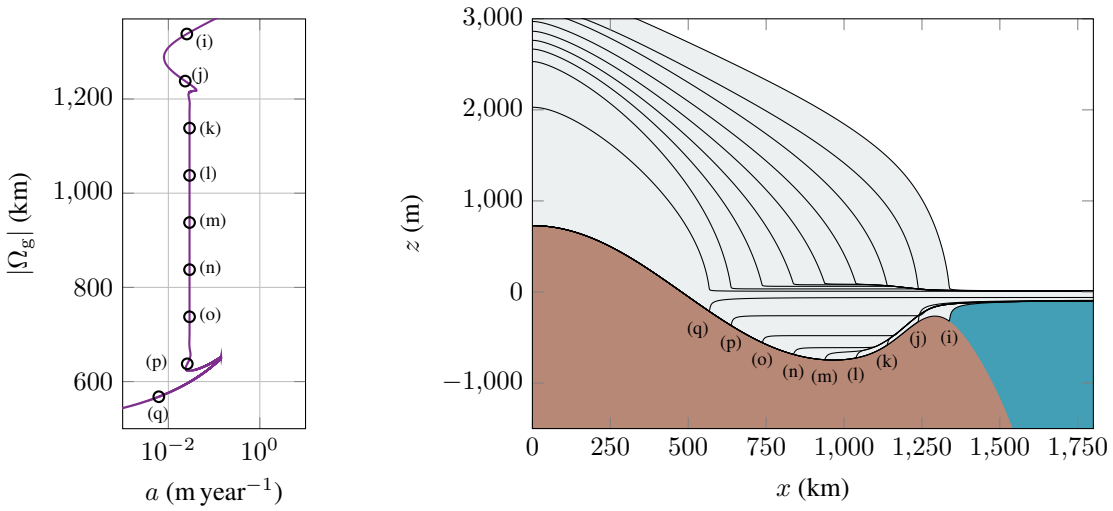

(a) Bifurcation curve.

(b) Ice-sheet geometry.

Figure 7.9: Results associated with the bifurcation curve of the regularized formulation with $\mathcal{G}_0 = 30\,\mathrm{m}$ (Fig 7.6b). Bifurcation curves of the grounded-region extent $|\Omega_g|$ expressed as a function of the net mass accumulation rate a, in the case of a bed that leads to pinning points. **(a)** Bifurcation curve of the grounded-region extent $|\Omega_g|$ expressed as a function of the net mass accumulation rate a (mauve line) and points of interest (black circles). **(b)** Ice-sheet profiles corresponding to the points of interest.

7.4.4 Transient states

Finally, we consider the transient evolution of marine ice-sheet systems modeled with both formulations (original/regularized) and both bed types. Given that the previous results have been found to be similar for both friction laws, we here only consider the Weertman friction law.

Concretely, we start from equilibrium positions associated with a value of the net mass accumulation rate of $a = 1.8\,\mathrm{m\,year^{-1}}$. For such value, all configurations (with both formulations and both bed types) are such that the grounding line is located at $x_{\mathrm{gl}} \approx 1400\,\mathrm{km}$. Then, we modify the value of a in such a way that the new associated steady state is located around $x_{\mathrm{gl}} \approx 500\,\mathrm{km}$, upstream of the bed bump that is located around $x = 1000\,\mathrm{km}$. To do so, we divide a by a factor of 10^3. By doing so, the grounding line will progressively retreat in order to reach this new steady state. In particular, there will be a point where it will be located in the region in which the bedrock has a positive slope, and we expect a fast retreat in that area.

For the regularized formulation, we rely on an implicit time-integration scheme that considers the system formed by the mass-balance and momentum-balance equations in a monolithic way (i.e., we consider the system (7.33)). At each time step, a Newton method is applied in order to find a numerical solution. An adaptive time-step scheme is used in which the time step is increased or reduced as a function of the number iterations done by the Newton method at the previous time step. For the original formulation, the monolithic formulation is not adapted as we have found that the simulations stop (i.e., the time step reaches a zero value) because a pinning point is met. Therefore, we instead rely on an iterative approach in which the mass-balance and momentum-balance equations are solved one after the other. Again, these equations are solved with a Newton method, and an adaptive time-step scheme is used.

Numerical results are shown in figures 7.10 and 7.11, where the evolution of $|\Omega_g|$ is shown as a function of time t. The conclusions are sensibly similar to the ones that have been obtained for the study of steady states. For the first type of bed, the transient evolution is similar for both formulations, and

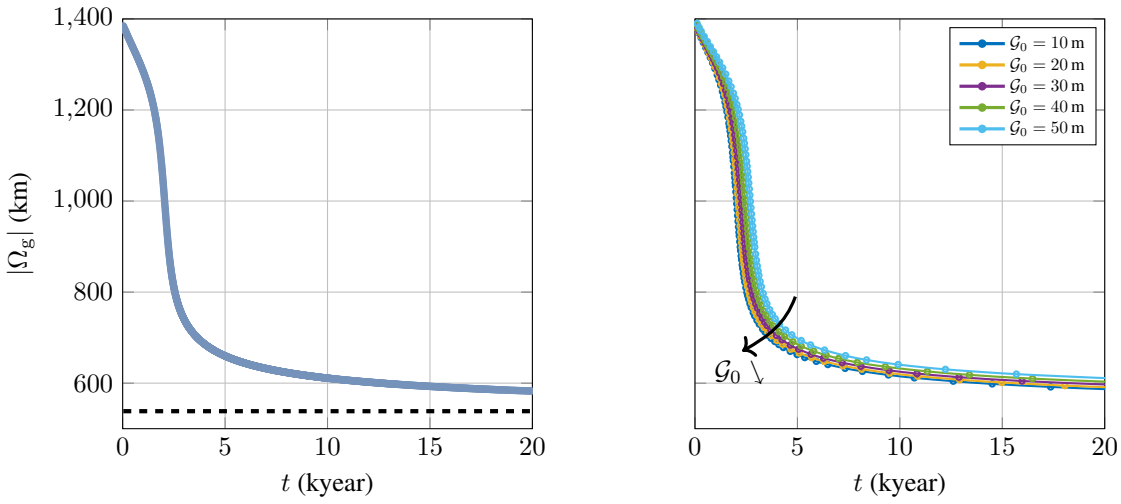

(a) Original formulation.

(b) Regularized formulation.

Figure 7.10: Evolution over time of the grounded-region extent $|\Omega_g|$ after a perturbation in the net mass accumulation rate, in the case of a bed that does not lead to pinning points. **(a)** Numerical results obtained with the original problem formulation (blue line) and steady-state solution obtained with a boundary-layer analysis (dashed black line) [Schoof, 2007b,c]. **(b)** Numerical results obtained with several values of the parameter $\mathcal{G}_0$ of the regularized formulation.

the solution associated with the regularized formulation gets closer to that associated with the original one as $\mathcal{G}_0 \to 0$. By contrast, for the second type of bed, the differences are much more pronounced between both formulations; in particular, there is a higher sensitivity with respect to the regularization parameter $\mathcal{G}_0$, and there are qualitative differences in the way the grounding line retreats. For the original formulation, we observe oscillations associated with an ice shelf that locally comes in contact with the bedrock and then detaches, causing the marine ice sheet to move back and forth (Fig. 7.12a and 7.13a). For the regularized formulation, this back-and-forth movement is absent, and the grounding line retreats in an almost monotonic fashion (Fig. 7.12b and 7.13b).

7.5 Discussion

In this section, we discuss and interpret our results. First, we analyze the effect of pinning points on the dynamics of marine ice sheets. Then, we discuss the origin of the singularity, mentioned in section 7.3, as it leads to numerical issues with pinning points. Finally, we propose a number of possible approaches to the treatment of this singularity. To this end, we suggest using appropriate specific numerical methods or modifying the treatment of the grounding line in the formulation of the problem.

7.5.1 Impact of pinning points

Pinning points give the following results regardless of the friction law (Weertman/Schoof):

- Bifurcation plots obtained with the original formulation stop at the location of pinning points.
- There are qualitative differences between the results obtained with the original and regularized formulations for both steady-state and transient simulations.

The first point can be explained by the fact that the Jacobian matrix contains an element that becomes very large near a pinning point, namely the (discretized version of the) shape derivative (7.25). This

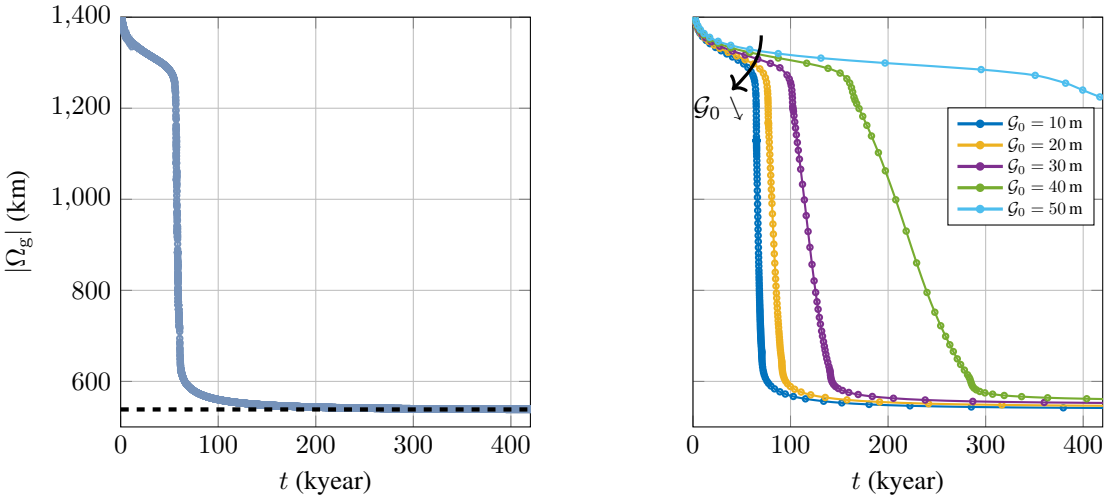

(a) Original formulation.

(b) Regularized formulation.

Figure 7.11: Evolution over time of the grounded-region extent $|\Omega_g|$ after a perturbation in the net mass accumulation rate, in the case of a bed that leads to pinning points. **(a)** Numerical results obtained with the original problem formulation (blue line) and steady-state solution obtained with a boundary-layer analysis (dashed black line) [Schoof, 2007b,c]. **(b)** Numerical results obtained with several values of the parameter $\mathcal{G}_0$ of the regularized formulation.

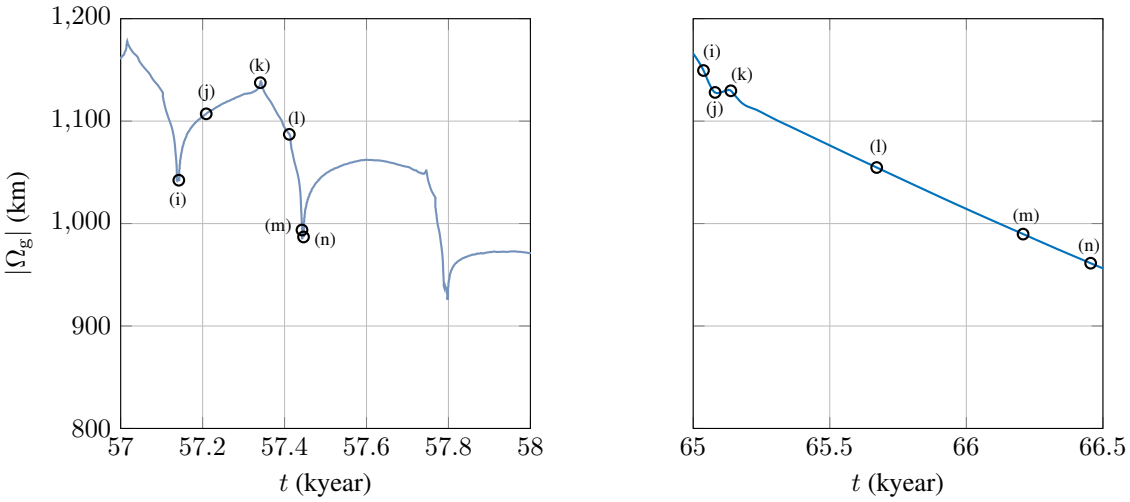

(a) Original formulation.

(b) Regularized formulation.

Figure 7.12: Zoom on the evolution over time of the grounded-region extent $|\Omega_g|$ after a perturbation in the net mass accumulation rate, in the case of a bed leads to pinning points (Fig. 7.11). **(a)** Numerical results obtained with the original problem formulation (blue line) and points of interest (black circles). **(b)** Numerical results obtained with $\mathcal{G}_0 = 10$ m in the regularized formulation (blue line) and points of interest (black circles).

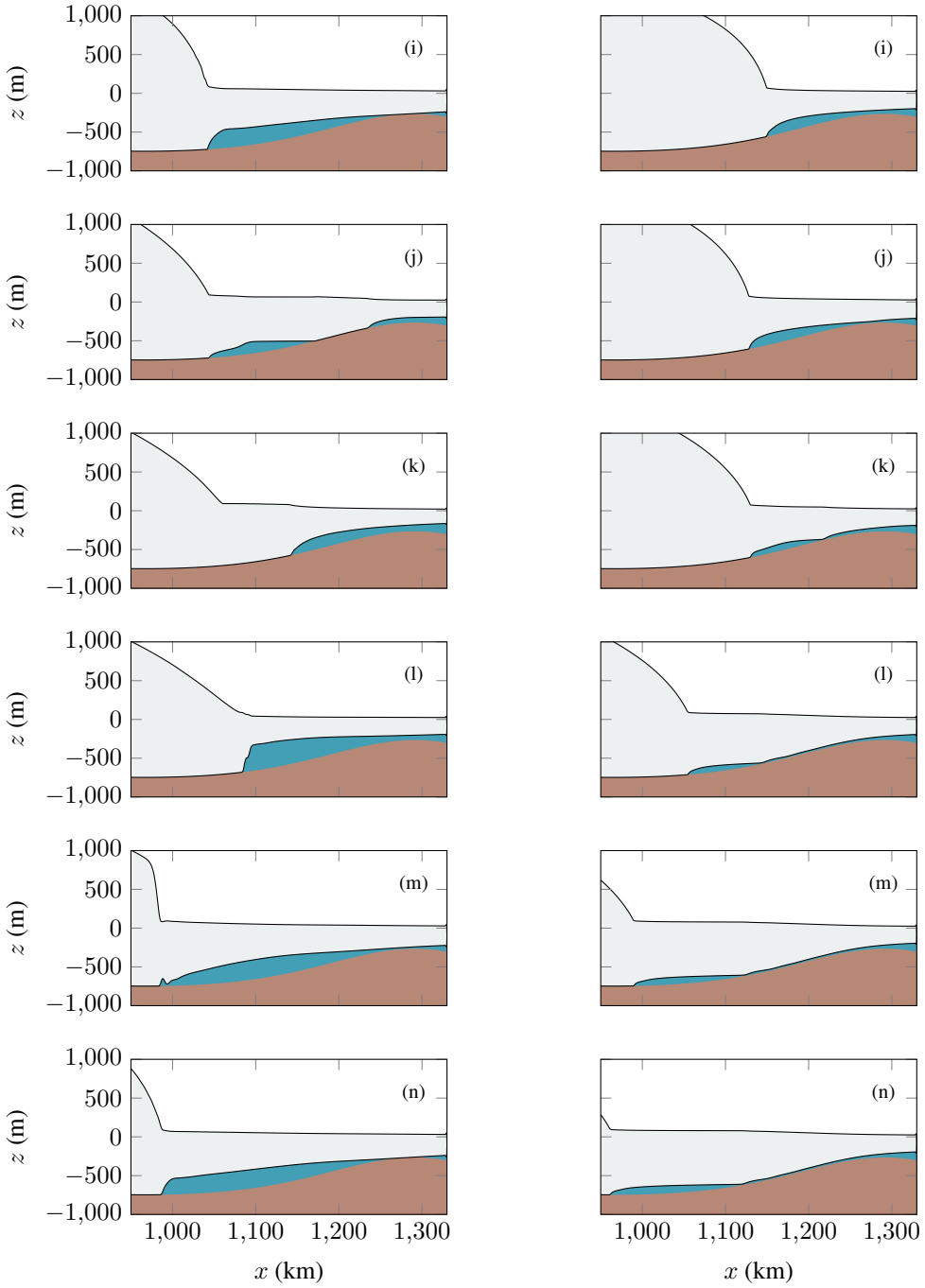

(a) Original formulation.

(b) Regularized formulation.

Figure 7.13: Ice-sheet profiles corresponding to the points of interest identified in figure 7.12.

term involves the evaluation of the inverse of $\|\nabla\mathcal{G}\|$, which tends toward infinity as a pinning point is approached. Consequently, the Newton method is unable to find a solution (Fig. 7.6 and 7.7). Note that this does not imply that there is no steady-state solution beyond the pinning points. That being said, the presence of the singularity within the weak formulation (prior to discretization) suggests that such behavior will occur regardless of the discretization used.

The second point implies that the regularization parameter $\mathcal{G}_0$ acts as a singular perturbation to the governing equations if pinning points are encountered in the numerical simulations. Indeed, in such cases, the solution to the regularized problem does not converge to the solution of the original problem as $\mathcal{G}_0 \to 0$. These differences between the results of the two formulations can be explained by the non-local character of the friction and driving stresses in the regularized formulation (7.33). This non-locality for example allows the friction stress to act on a part of the ice that is floating, provided it is sufficiently close to the bedrock (Fig. 7.9). In particular, this leads to a smoother evolution of the system, as changes are progressively introduced, in contrast to the original formulation.

7.5.2 Origin of the singularity

The singularity observed with pinning points when considering the original formulation is caused by three elements:

(i) a grounding line that separates the grounded and the floating regions and that depends on h;

(ii) a zero gradient value of the flotation function, leading to an infinite grounding-line sensitivity;

(iii) a discontinuity in some of the terms of the governing equations across the grounding line.

The first of these elements is an essential feature of marine ice sheets, which consist of grounded and floating regions that evolve over time. Similarly, the second element is a condition associated with the geometry of ice sheets. However, the third element is associated with the dynamics of ice sheets, and we now discuss it.

There are two reasons for the terms in the governing equations to be discontinuous: there can be a discontinuity in the friction stress and/or a discontinuity in the driving stress. The discontinuity in the friction stress is easy to understand, as it simply follows from the fact that friction is only applied to the grounded region. Hence, it will lead to a discontinuous contribution in the momentum-balance equation if its value at the grounding line is non-zero (such as for the Weertman friction law). The discontinuity in the driving stress is more subtle. In general, the driving stress is given by $\rho g h \nabla s$, with s the upper-surface elevation. There is a discontinuity in the driving stress because the upper-surface gradient takes a different form over the grounded and floating regions (see equations (7.11a) and (7.11b)). The discontinuity in the upper-surface gradient was highlighted by Wilchinsky and Chugunov [2000] and later reviewed by Schoof [2011]. It turns out that it is a consequence of the reduced-order model used here: the shallow-shelf approximation. With this model, the vertical normal stress is cryostatic, so one may use Archimedes' principle to separate the grounded and floating regions. However, this assumption is not valid at the grounding line, where there is actually a boundary layer that allows the upper-surface elevation to connect smoothly between the grounded and floating regions [Schoof, 2011]. This boundary layer takes the form of a shelf that bends as a viscous beam, in which horizontal gradients of the shear stress in the ice are significant (note that such gradients are absent in the shallow-shelf approximation). Geometrically, this boundary layer leads to small oscillations in the upper-surface elevation profiles in a very small region near the grounding line; such features have been confirmed based on high-resolution numerical simulations [see the inset of Fig. 2 in Durand et al., 2009].

An important comment here is that the singularity presented above has nothing to do with potential bed irregularities; in particular, it has been observed for smooth bed profiles. Rather, the singularity can

be explained as a consequence of a discontinuous friction or driving stress, the latter arising from the simplifying assumptions made to obtain the reduced-order model considered here.

7.5.3 Perspectives

There are several ways to handle the identified singularity at pinning points. Given that the origin of this singularity is linked to a reduced-order flow model, a natural option would be to consider a higher-order flow model in which there is no assumption on the vertical component of the momentum-balance equation (which is here assumed to be cryostatic). However, such an assumption is oftentimes the basis of high-order flow models, such as the Blatter–Pattyn model [Blatter, 1995; Pattyn, 2003]. It follows that one might need to consider a model of ice flow that does not rely on any additional assumptions. In the context of glaciology, such a model is known as the full-Stokes model [e.g., Greve and Blatter, 2009]. However, the simulations and analysis of marine ice sheets with such a model are notably difficult for two reasons: on the one hand, they are extremely computationally expensive, as one here needs to resolve the viscous beam boundary layer [Durand et al., 2009]. On the other hand, there is a more fundamental issue, in that marine ice sheets, when modeled with the full-Stokes model, form obstacle problems in which variational inequalities have to be solved [Stubblefield et al., 2021; de Diego et al., 2022, 2023]. Such problems are known to be non-smooth, so it is unclear whether the singularity would actually disappear. We note that this gives another interpretation to the singularity observed in this report: it can be viewed as a remaining artifact of the obstacle-problem structure of the flow in marine ice sheets.

We now describe two alternative approaches that do not rely on a higher-order flow model. The first consists of relying on methods that may be better suited to dealing with moving interfaces. Such methods include more elaborate types of discretizations or solving strategies. Among these, we mention the use of front-tracking methods [e.g., level-set methods; Osher and Fedkiw, 2001, 2003], moving grids [e.g., arbitrary Lagrangian–Eulerian methods; Donea et al., 2004; Moës et al., 2023], or enriched functional spaces capable of handling discontinuities [e.g., extended finite-element methods; Moës et al., 1999; Khoei, 2014] as potential leads. Such methods have typically been used to handle problems in computational mechanics that involve discontinuities, e.g., fracture and contact mechanics. To the best of our knowledge, such methods have not yet been widely used in the glaciological context to handle grounding-line motion, with the exception of a few recent studies [Hossain et al., 2020; Thacher et al., 2024].

The second approach involves questioning the grounding-line concept. Grounding lines can be seen as a mathematical abstraction of a real, complex physical system (the interface between the grounded and floating regions). However, the discrete nature of grounding lines appears to introduce additional complexity to the problem. A proposed solution is to replace the concept of a ‘grounding line’ with a ‘grounding zone’, where the transition between grounded and floating regions occurs over a finite area. This model is physically motivated by the difficulty of pinpointing the position of grounding lines, given small-scale spatial variations (e.g., localized seawater intrusions) and temporal changes (e.g., tidal effects). In particular, recent theoretical and observational studies have highlighted widespread seawater intrusions in West Antarctica, creating a zone with increased sub-shelf melt near the grounding line [Robel et al., 2022b; Bradley and Hewitt, 2024; Rignot et al., 2024]. An example of such a model is the regularized approach presented in subsection 7.3.3. However, determining the value of the regularization parameter $\mathcal{G}_0$ remains a challenge. One possibility is to characterize the grounding zone –for instance, by determining its typical spatial extent– and then assign a corresponding value to $\mathcal{G}_0$. Given the current limited understanding of the various thermal, hydrological, and sedimentary processes in this region, this issue remains unresolved and is an active area of research [e.g., Kowal and Worster, 2020; Hogan et al., 2023; Parizek, 2024].

7.6 Conclusion

In this report, we have studied the effects of pinning points on marine ice-sheet dynamics. Starting from the mass-balance and momentum-balance equations, we have highlighted that a (strong) coupling between these two equations could lead to a singularity in which one of the components of the linearized problem becomes unbounded. This term is associated with the motion of the grounded and floating regions in response to changes in ice thickness when an ice shelf comes into contact with a bump in the underlying bedrock or detaches from it, leading to a pinning point. Based on numerical simulations of simple cases, we have compared several configurations. Specifically, we have demonstrated that pinning points lead to (i) stops in the bifurcation plots and (ii) qualitative differences when comparing the results to those obtained using a regularized approach, in which the transition between the grounded and floating regions is progressive. These results were obtained with a smooth bedrock profile and two qualitatively different friction laws (Weertman and regularized Coulomb), suggesting that these features are inherent to the governing equations themselves. Finally, we have suggested several approaches to address the identified singularities, based on the use of specific numerical methods or modifications to the concept of grounding line.

The numerical simulations presented here are relatively simple. Therefore, it remains necessary to study in detail the impact of pinning points and their treatment in other contexts. A first possible extension concerns the initialization of marine ice sheets. In practice, ice-sheet geometries and parameters are initialized in such a way that the resulting thickness and velocity fields are compatible with observations. Such a problem takes the form of an inverse problem in which the misfit between observations and computed quantities is minimized under the constraint that the governing equations of the problem are satisfied. This is typically done by considering observed surface velocities with the constraint that the momentum-balance equation is satisfied [e.g., Arthern and Gudmundsson, 2010; Morlighem et al., 2010; Petra et al., 2012]. However, it has been found that adding the mass-balance equation as an additional constraint leads to an initial state that results in numerical simulations that are more physically sound [Perego et al., 2014]. This suggests that the singularity identified here could also be present in such inversion procedures, given that they also involve the coupling between the mass-balance and momentum-balance equations. Additional studies are necessary to investigate this.

Another extension concerns the impact of pinning points and their treatment in more realistic setups. In reality, marine ice sheets are subject to additional complex physical processes, such as damage propagation or oceanic sub-shelf melt. Such studies are particularly necessary for examining Thwaites Glacier (West Antarctica), where observations have shown that the grounding line is currently rapidly retreating [e.g., Mouginot et al., 2014; Rignot et al., 2014], potentially contributing significantly to future sea-level rise; this glacier could contribute up to ~ 0.65 m of sea-level elevation [Morlighem, 2020]. Indeed, it appears that pinning points are among the various factors influencing future grounding-line retreat rates [Docquier et al., 2014; Benn et al., 2022; Wild et al., 2022].

7.7 Appendix A: Analytical expressions of the terms appearing in the linearized problem

Here we write the analytical expressions of the different terms that appear in the linearized problem (7.21).

7.7.1 Residuals

$$F_h(h,\boldsymbol{u};\phi) := \int_\Omega (h-\tilde{h})/\Delta t\,\phi\,\mathrm{d}\Omega + \int_{\Gamma_{\mathrm{cf}}} h\,\boldsymbol{u}\cdot\boldsymbol{n}\,\phi\,\mathrm{d}\Gamma - \int_\Omega h\,\boldsymbol{u}\cdot\nabla\phi\,\mathrm{d}\Omega - \int_\Omega a\,\phi\,\mathrm{d}\Omega, \tag{7.36a}$$

$$\begin{aligned} F_{\boldsymbol{u}}(h,\boldsymbol{u};\boldsymbol{\phi}) := &\int_\Omega 2\,h\,\eta\,\boldsymbol{\Sigma}:\boldsymbol{\nabla}\boldsymbol{\phi}\,\mathrm{d}\Omega + \int_{\Omega_{\mathrm{g}}} \boldsymbol{\tau}_{\mathrm{g}}\cdot\boldsymbol{\phi}\,\mathrm{d}\Omega - \int_{\Omega_{\mathrm{g}}} \boldsymbol{\tau}_{\mathrm{b}}\cdot\boldsymbol{\phi}\,\mathrm{d}\Omega + \int_{\Omega_{\mathrm{f}}} \boldsymbol{\tau}_{\mathrm{f}}\cdot\boldsymbol{\phi}\,\mathrm{d}\Omega \\ &+ \int_{\Gamma_{\mathrm{cf}}} \boldsymbol{\tau}_{\mathrm{cf}}\cdot\boldsymbol{\phi}\,\mathrm{d}\Omega. \end{aligned} \tag{7.36b}$$

7.7.2 Gâteaux differentials

$$\langle D_h F_h(h,\boldsymbol{u};\phi),\delta h\rangle = \int_\Omega \delta h/\Delta t\,\phi\,\mathrm{d}\Omega + \int_{\Gamma_{\mathrm{cf}}} \delta h\,\boldsymbol{u}\cdot\boldsymbol{n}\,\phi\,\mathrm{d}\Gamma - \int_\Omega \delta h\,\boldsymbol{u}\cdot\nabla\phi\,\mathrm{d}\Omega, \tag{7.37a}$$

$$\langle D_{\boldsymbol{u}} F_h(h,\boldsymbol{u};\phi),\delta\boldsymbol{u}\rangle = \int_{\Gamma_{\mathrm{cf}}} h\,\delta\boldsymbol{u}\cdot\boldsymbol{n}\,\phi\,\mathrm{d}\Gamma - \int_\Omega h\,\delta\boldsymbol{u}\cdot\nabla\phi\,\mathrm{d}\Omega, \tag{7.37b}$$

$$\begin{aligned} \langle D_h F_{\boldsymbol{u}}(h,\boldsymbol{u};\boldsymbol{\phi}),\delta h\rangle = &\int_\Omega 2\,\delta h\,\eta\,\boldsymbol{\Sigma}:\boldsymbol{\nabla}\boldsymbol{\phi}\,\mathrm{d}\Omega + \int_{\Omega_{\mathrm{g}}} \langle D_h\boldsymbol{\tau}_{\mathrm{g}},\delta h\rangle\cdot\boldsymbol{\phi}\,\mathrm{d}\Omega \\ &- \int_{\Omega_{\mathrm{g}}} \langle D_h\boldsymbol{\tau}_{\mathrm{b}},\delta h\rangle\cdot\boldsymbol{\phi}\,\mathrm{d}\Omega + \int_{\Omega_{\mathrm{f}}} \langle D_h\boldsymbol{\tau}_{\mathrm{f}},\delta h\rangle\cdot\boldsymbol{\phi}\,\mathrm{d}\Omega \\ &+ \int_{\Gamma_{\mathrm{cf}}} \langle D_h\boldsymbol{\tau}_{\mathrm{cf}},\delta h\rangle\cdot\boldsymbol{\phi}\,\mathrm{d}\Gamma + \int_{\Gamma_{\mathrm{g1}}} (\boldsymbol{\tau}_{\mathrm{g}}-\boldsymbol{\tau}_{\mathrm{f}}-\boldsymbol{\tau}_{\mathrm{b}})\cdot\boldsymbol{\phi}\,\|\nabla\mathcal{G}\|^{-1}\,\delta h\,\mathrm{d}\Gamma, \end{aligned} \tag{7.37c}$$

$$\begin{aligned} \langle D_{\boldsymbol{u}} F_{\boldsymbol{u}}(h,\boldsymbol{u};\boldsymbol{\phi}),\delta\boldsymbol{u}\rangle = &\int_\Omega h\,\langle D_{\boldsymbol{u}}\eta,\delta\boldsymbol{u}\rangle\,\boldsymbol{\Sigma}:\boldsymbol{\nabla}\boldsymbol{\phi}\,\mathrm{d}\Omega + \int_\Omega h\,\eta\,\langle D_{\boldsymbol{u}}\boldsymbol{\Sigma},\delta\boldsymbol{u}\rangle:\boldsymbol{\nabla}\boldsymbol{\phi}\,\mathrm{d}\Omega \\ &- \int_{\Omega_{\mathrm{g}}} \langle D_{\boldsymbol{u}}\boldsymbol{\tau}_{\mathrm{b}},\delta\boldsymbol{u}\rangle\cdot\boldsymbol{\phi}\,\mathrm{d}\Omega. \end{aligned} \tag{7.37d}$$

Here,

$$\langle D_h\boldsymbol{\tau}_{\mathrm{g}},\delta h\rangle = \rho g\delta h\nabla(b+h) + \rho g h\nabla\delta h, \tag{7.38a}$$

$$\langle D_h\boldsymbol{\tau}_{\mathrm{f}},\delta h\rangle = \rho g\left(1-\tfrac{\rho}{\rho_{\mathrm{w}}}\right)\nabla(h\,\delta h), \tag{7.38b}$$

$$\langle D_h\boldsymbol{\tau}_{\mathrm{cf}},\delta h\rangle = \rho\left(1-\tfrac{\rho}{\rho_{\mathrm{w}}}\right) g\,h\,\delta h\,\boldsymbol{n}, \tag{7.38c}$$

$$\langle D_{\boldsymbol{u}}\boldsymbol{\Sigma},\delta\boldsymbol{u}\rangle = \boldsymbol{\Sigma}(\delta\boldsymbol{u}), \tag{7.38d}$$

$$\langle D_{\boldsymbol{u}}\eta,\delta\boldsymbol{u}\rangle = \tfrac{1}{2}A^{-\frac{1}{n}}\left(\|\boldsymbol{D}(\boldsymbol{u})\|_*^2+\delta_\eta^2\right)^{\frac{1-3n}{2n}}\left[\mathrm{tr}(\boldsymbol{D}(\boldsymbol{u})\boldsymbol{D}(\delta\boldsymbol{u})) - \mathrm{tr}(\boldsymbol{D}(\boldsymbol{u}))\,\mathrm{tr}(\boldsymbol{D}(\delta\boldsymbol{u}))\right]. \tag{7.38e}$$

For the derivatives of the basal friction stress, we distinguish the two friction laws. For the Weertman law, we have

$$\langle D_{\boldsymbol{u}}\boldsymbol{\tau}_{\mathrm{b}},\delta h\rangle = 0, \tag{7.39a}$$

$$\langle D_{\boldsymbol{u}}\boldsymbol{\tau}_{\mathrm{b}},\delta\boldsymbol{u}\rangle = -C\,\|\boldsymbol{u}\|^{p-3}\left[(p-1)(\boldsymbol{u}\cdot\delta\boldsymbol{u})\boldsymbol{u} + \|\boldsymbol{u}\|^2\delta\boldsymbol{u}\right]. \tag{7.39b}$$

For the Schoof friction law, we have

$$\langle D_{\boldsymbol{u}}\boldsymbol{\tau}_{\mathrm{b}}, \delta h\rangle = -\rho g\mu \left(\frac{\|\boldsymbol{u}\|}{\|\boldsymbol{u}\| + (\mu N/C)^{1/p}}\right)^{p+1} \frac{\boldsymbol{u}}{\|\boldsymbol{u}\|}\delta h, \tag{7.40a}$$

$$\langle D_{\boldsymbol{u}}\boldsymbol{\tau}_{\mathrm{b}}, \delta \boldsymbol{u}\rangle = -\frac{\mu N}{\|\boldsymbol{u}\|^4}\left(\frac{\|\boldsymbol{u}\|}{\|\boldsymbol{u}\| + (\mu N/C)^{1/p}}\right)^{p} \left[p\,(\mu N/C)^{1/p}\,(\boldsymbol{u}\cdot\delta\boldsymbol{u})\boldsymbol{u} + \|\boldsymbol{u}\|^3\delta\boldsymbol{u} - (\boldsymbol{u}\cdot\delta\boldsymbol{u})\|\boldsymbol{u}\|\boldsymbol{u}\right]. \tag{7.40b}$$

7.8 Appendix B: Proofs of the propositions

Proposition (Expression of the shape derivative)**.** *If* $\|\nabla\mathcal{G}\| \neq 0$ *at* Γ_{gl}*, then*

$$\langle\, D_h|_{\delta\Gamma_{\mathrm{gl}}} F_{\boldsymbol{u}}(h, \boldsymbol{u}; \boldsymbol{\phi}), \delta h\rangle = \int_{\Gamma_{\mathrm{gl}}(h)} (\boldsymbol{\tau}_{\mathrm{g}} - \boldsymbol{\tau}_{\mathrm{f}} - \boldsymbol{\tau}_{\mathrm{b}})\cdot\boldsymbol{\phi}\,\|\nabla\mathcal{G}\|^{-1}\delta h\,\mathrm{d}\Gamma. \tag{7.41}$$

Proof. It suffices to prove that, for any function f that does not depend on h, we have

$$\langle D_h F(h), \delta h\rangle = \int_{\Gamma_{\mathrm{gl}}(h)} f\,\|\nabla\mathcal{G}\|^{-1}\delta h\,\mathrm{d}\Gamma, \quad F(h) := \int_{\Omega_{\mathrm{g}}(h)} f\,\mathrm{d}\Omega. \tag{7.42}$$

To show this result, we interpret it as a rewriting of Reynolds' theorem. Given a domain ω that evolves over time t, Reynolds' theorem states that

$$\partial_t \int_\omega f\,\mathrm{d}\Omega = \int_{\partial\omega} f\,\boldsymbol{w}\cdot\boldsymbol{n}\,\mathrm{d}\Gamma. \tag{7.43}$$

Here, f is a function that does not depend on t, $\partial\omega$ is the boundary to ω, $\boldsymbol{w}$ is its velocity, and $\boldsymbol{n}$ is its outward normal. We note if we consider this result at $t = 0$, then that the fact that $\boldsymbol{w}$ is the velocity of the boundary $\partial\omega$ can be formally written by the condition

$$\partial\omega(t) = (\mathbf{id} + t\,\boldsymbol{w} + o(t))\,\partial\omega(0), \quad \text{for } t \to 0, \tag{7.44}$$

in which **id** denotes the identity mapping.

First, we write the Gâteaux differential appearing in (7.42) as the derivative of a function that depends on a time-like parameter θ. To do so, we introduce the function $\tilde{F}(\theta) := F(h + \theta\delta h)$. Then, we have

$$\tilde{F}'(0) := \lim_{\theta\to 0}\frac{\tilde{F}(\theta) - \tilde{F}(0)}{\theta} = \lim_{\theta\to 0}\frac{F(h+\theta\delta h) - F(h)}{\theta} = \langle D_h F(h), \delta h\rangle. \tag{7.45}$$

The function $\tilde{F}$ can be written as

$$\tilde{F}(\theta) = \int_\omega f\,\mathrm{d}\Omega, \tag{7.46}$$

in which ω is a set that evolves with θ according to $\omega(\theta) = \Omega_{\mathrm{g}}(h+\theta\delta h)$. Hence, one can apply Reynolds' theorem (7.43) to get

$$\partial_\theta \int_\omega f\,\mathrm{d}\Omega = \int_{\partial\omega} f\,\boldsymbol{w}\cdot\boldsymbol{n}\,\mathrm{d}\Gamma, \tag{7.47}$$

where $\partial\omega(\theta) = \Gamma_{\mathrm{gl}}(h + \theta\delta h)$, and where $\boldsymbol{w}$ is the pseudo-velocity of this boundary. Evaluating this expression at $\theta = 0$ yields

$$\langle D_h F(h), \delta h\rangle = \int_{\Gamma_{\mathrm{gl}}(h)} f\,\boldsymbol{w}\cdot\boldsymbol{n}\,\mathrm{d}\Gamma. \tag{7.48}$$

This is exactly (7.42) provided we show that $\boldsymbol{w}$ is such that $\boldsymbol{w}\cdot\boldsymbol{n} = \|\nabla\mathcal{G}\|^{-1}\delta h$. To do so, we prove that Γ_{gl} evolves according to

$$\Gamma_{\mathrm{gl}}(\theta) = (\mathbf{id} + \theta\,\boldsymbol{n}\|\nabla\mathcal{G}\|^{-1}\,\delta h + o(\theta))\,\Gamma_{\mathrm{gl}}(0), \quad \text{for } \theta \to 0. \tag{7.49}$$

Let us show that every element of the right-hand side of (7.49) is also an element of the left-hand side of (7.49). Consider a point $\boldsymbol{x}_{\mathrm{gl}}^0 \in \Gamma_{\mathrm{gl}}(0)$; we then have to show that $\boldsymbol{x}_{\mathrm{gl}}^\theta := \boldsymbol{x}_{\mathrm{gl}}^0 + \theta\, \boldsymbol{n}\, \|\nabla \mathcal{G}\|^{-1}\, \delta h(\boldsymbol{x}_{\mathrm{gl}}^0)$ belongs to $\Gamma_{\mathrm{gl}}(\theta)$ as $\theta \to 0$. In other words, $\boldsymbol{x}_{\mathrm{gl}}^\theta$ should verify the equation

$$(h + \theta\, \delta h) + \frac{\rho_{\mathrm{w}}}{\rho} b = o(\theta), \quad \text{for } \theta \to 0. \tag{7.50}$$

Evaluating the left-hand side at $\boldsymbol{x}_{\mathrm{gl}}^\theta$ successively yields

$$\begin{aligned}
\big(h(\boldsymbol{x}_{\mathrm{gl}}^\theta) + \theta\, \delta h(\boldsymbol{x}_{\mathrm{gl}}^\theta)\big) + \frac{\rho_{\mathrm{w}}}{\rho} b(\boldsymbol{x}_{\mathrm{gl}}^\theta) &= \mathcal{G}(\boldsymbol{x}_{\mathrm{gl}}^\theta) + \theta\, \delta h(\boldsymbol{x}_{\mathrm{gl}}^\theta) && \text{(7.51a)}\\
&= \nabla \mathcal{G}(\boldsymbol{x}_{\mathrm{gl}}^0) \cdot (\boldsymbol{x}_{\mathrm{gl}}^\theta - \boldsymbol{x}_{\mathrm{gl}}^0) + \mathcal{O}(\theta^2) + \theta\, \delta h(\boldsymbol{x}_{\mathrm{gl}}^\theta) && \text{(7.51b)}\\
&= -\theta\, \delta h(\boldsymbol{x}_{\mathrm{gl}}^0) + \theta \delta h(\boldsymbol{x}_{\mathrm{gl}}^\theta) + \mathcal{O}(\theta^2) && \text{(7.51c)}\\
&= \mathcal{O}(\theta^2), && \text{(7.51d)}
\end{aligned}$$

where we have used the fact that $\boldsymbol{n} = -\nabla \mathcal{G}/\|\nabla \mathcal{G}\|$. It follows that $\boldsymbol{x}_{\mathrm{gl}}^\theta \in \Gamma_{\mathrm{gl}}(\theta)$ for sufficiently small θ. Analogously, it can be shown that every element of the left-hand side of (7.49) is also an element of the left-hand side of (7.49), which concludes. □

Proposition (Geometrical characterization of a pinning point)**.** *A pinning point $\boldsymbol{x}_{\mathrm{gl}} \in \Gamma_{\mathrm{gl}}$ is a point that is such that the ice-sheet lower surface is locally tangent to the bedrock.*

Proof. If the neighborhood of the pinning point is grounded, then the lower-surface elevation l in that neighborhood is given by b, so the claim follows. If the neighborhood of the pinning point is floating, then $l = -(\rho/\rho_{\mathrm{w}})h$, from which $\nabla l = -(\rho/\rho_{\mathrm{w}})\nabla h$. On the other hand, the condition $\|\nabla \mathcal{G}\| = 0$ can be written as $\nabla[h + (\rho_{\mathrm{w}}/\rho)b] = 0$ or, equivalently, as $\nabla b = -(\rho/\rho_{\mathrm{w}})\nabla h$, from which the claim follows. □

Proposition (Local behavior around a pinning point)**.** *Around a pinning point $\boldsymbol{x}_{\mathrm{gl}}$, the flotation function admits the following expansion:*

$$\mathcal{G}(\boldsymbol{x}) = \frac{1}{2}(\boldsymbol{x} - \boldsymbol{x}_{\mathrm{gl}}) \cdot \mathbf{hess}\, \mathcal{G}(\boldsymbol{x}_{\mathrm{gl}}) \cdot (\boldsymbol{x} - \boldsymbol{x}_{\mathrm{gl}}) + \mathcal{O}(\|\boldsymbol{x} - \boldsymbol{x}_{\mathrm{gl}}\|^3). \tag{7.52}$$

Proof. The result follows from the application of Taylor's expansion around $\boldsymbol{x}_{\mathrm{gl}}$, the definition of a pinning point, and the assumed smooth nature of the bedrock elevation. □

7.9 Appendix C: Continuation methods

In this section, we describe the continuation methods used in subsection 7.4.3. The first method is classical [e.g., Keller, 1977, 1987]. The second method can be seen a modification of the first method that removes the requirement to compute the tangent to the solution curve at each step. It is inspired by Mittelmann [1987]. We consider a general setup in which a system is governed by M (algebraic) equations, noted

$$\boldsymbol{F}(\boldsymbol{X}, \alpha) = \mathbf{0}, \tag{7.53}$$

in which $\boldsymbol{X} \in \mathbb{R}^M$ represents the state of the system and $\alpha \in \mathbb{R}$ represents a parameter of the problem. The goal of numerical continuation is to obtain, starting from a solution $(\boldsymbol{X}_0, \alpha_0)$ of (7.53), a successive number of points $(\boldsymbol{X}_1, \alpha_1), (\boldsymbol{X}_2, \alpha_2), \ldots$ that are also solutions of (7.53). By doing so, we eventually obtain an approximation to the solution curve that pass through $(\boldsymbol{X}_0, \alpha_0)$, hence the name 'continuation'. Ideally, numerical continuation methods should be sufficiently robust to pass through bifurcation points, which are associated with a change in the qualitative features of the system.

7.9.1 Pseudo-arclength continuation

In the pseudo-arclength continuation, the idea is to parametrize the solution curve by an arclength coordinate s, so that we write $\boldsymbol{X} = \boldsymbol{X}(s)$ and $\alpha = \alpha(s)$. Hence, along the solution curve, we have $\boldsymbol{F}(\boldsymbol{X}(s), \alpha(s)) = \boldsymbol{0}$. Differentiating this relation with respect to s yields

$$D_{\boldsymbol{X}}\boldsymbol{F} \cdot \boldsymbol{X}' + D_\alpha \boldsymbol{F}\, \alpha' = \boldsymbol{0}. \tag{7.54}$$

This equation defines the tangent $(\boldsymbol{X}', \alpha')$ to the solution curve, up to a proportionality constant. To fully characterize the tangent, one can assume that this tangent is normalized, so that

$$\|\boldsymbol{X}'\|^2 + |\alpha'|^2 = 1. \tag{7.55}$$

The pseudo-arclength continuation can be introduced based on a predictor-corrector approach. Assume that the point $(\boldsymbol{X}_0, \alpha_0)$ is known, together with the tangent $(\boldsymbol{X}_0', \alpha_0')$ at that location. The predictor step consists of moving along this tangent by a quantity Δs:

$$(\boldsymbol{X}_0^\dagger, \alpha_0^\dagger) = (\boldsymbol{X}_0, \alpha_0) + \Delta s\, (\boldsymbol{X}_0', \alpha_0'). \tag{7.56}$$

In the corrector step, a solution to the equations (7.53) is sought. However, it is required that the solution belongs to the hyperplane that is perpendicular to the tangent $(\boldsymbol{X}_0', \alpha_0')$ and passes through the point $(\boldsymbol{X}_0^\dagger, \alpha_0^\dagger)$ (see Fig. 7.14). Formally, this condition can be written as

$$N(\boldsymbol{X}, \alpha) := \boldsymbol{X}_0' \cdot (\boldsymbol{X} - \boldsymbol{X}_0) + \alpha_0'(\alpha - \alpha_0) - \Delta s = 0, \tag{7.57}$$

which can be seen as a linearization of (7.55). The equations (7.53) and (7.57) form a system of $(M+1)$ equations for the $(M+1)$ unknowns $(\boldsymbol{X}, \alpha)$. A Newton procedure can then be applied to find a solution. Once this is done, the procedure starts again, with $(\boldsymbol{X}_1, \alpha_1)$ as the starting point instead of $(\boldsymbol{X}_0, \alpha_0)$.

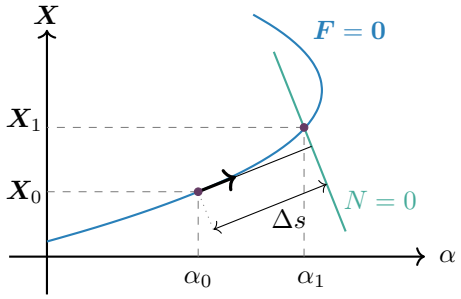

Figure 7.14: Illustration of the pseudo-arclength continuation method. Starting from a known solution $(\boldsymbol{X}_0, \alpha_0)$, the next solution $(\boldsymbol{X}_1, \alpha_1)$ is sought as a solution to the governing equations ($\boldsymbol{F} = \boldsymbol{0}$, blue curve) that lies on the hyperplane perpendicular to the tangent of the curve and that is located at a distance Δs from the known solution ($N = 0$, green line).

To determine the new tangent to the curve, one can rely on finite-difference approximations, e.g., based on $(\boldsymbol{X}_1', \alpha_1') = (\boldsymbol{X}_1 - \boldsymbol{X}_0, \alpha_1 - \alpha_0)/\Delta s$. Another possibility is to solve equation (7.54) together with (7.57), which form $(M+1)$ equations for the $(M+1)$ unknowns $(\boldsymbol{X}_1', \alpha_1')$. Additionally, we note that the step Δs can be adapted during the continuation procedure as a function of the number of iterations in the Newton procedure at the previous step, similar to what is done in adaptive time stepping.

7.9.2 Objective-based continuation

The pseudo-arclength continuation method requires that the solution curve is sufficiently smooth to be efficient. In particular, it is necessary that the tangent is well-defined. Here, we propose a method that

does not rely on the tangent. The method relies instead on the assumption that there is some quantity $C = C(\boldsymbol{X}, \alpha)$ that increases or decreases when moving along the solution curve. This quantity should be a function that is easy to compute. Initially, we have $C_0 = C(\boldsymbol{X}_0, \alpha_0)$. The next solution should then satisfy $C(\boldsymbol{X}_1, \alpha_1) = C_0 + \Delta C$, where ΔC is a prescribed increment. Concretely, this continuation method is similar to the pseudo-arclength continuation method, except that the additional constraint $N = 0$ is now given by

$$N(\boldsymbol{X}, \alpha) = C(\boldsymbol{X}, \alpha) - C(\boldsymbol{X}_0, \alpha_0) - \Delta C = 0. \tag{7.58}$$

Here, the step ΔC can be increased or decreased in an adaptive manner.

For the marine ice-sheet problem considered in this report, the state $\boldsymbol{X}$ of the system is the set of nodal values of the finite-element discretization, and α is the net mass accumulation rate a. We have found that a practical and efficient quantity for C is the volume of seawater in a region near the grounding line obtained at the previous solution. Indeed, this quantity is expected to increase if the grounding line retreats. Starting from a geometry that corresponds to a large value for the grounding-line position, the continuation method will then allow sampling of the full range of grounding-line positions corresponding to various ice-sheet geometries. Formally, we introduce the set $\Gamma_{\mathrm{gl},r}$ as the region of points that is within a radius r of the grounding line:

$$\Gamma_{\mathrm{gl},r} := \{\boldsymbol{x} \in \Omega : \mathrm{dist}(\boldsymbol{x}, \Gamma_{\mathrm{gl}}) < r\}. \tag{7.59}$$

We then define the volume of seawater in that region as

$$V_{\mathrm{w}} := \int_{\Gamma_{\mathrm{gl},r}} h_{\mathrm{w}} \, \mathrm{d}\Omega, \quad h_{\mathrm{w}} := -\frac{\rho}{\rho_{\mathrm{w}}} h - b, \tag{7.60}$$

where h_{w} is the height of the seawater column. Note that $h_{\mathrm{w}} = 0$ over the grounding region. It is this volume that corresponds to the quantity C in the previous discussion. Importantly, it is a linear function of $\boldsymbol{X}$ as it is proportional to the thickness, so its computation is easy.

Part III

Conclusions and directions for future work

8

Conclusions and perspectives

Finally, we conclude this thesis by presenting conclusions and perspectives. First, we summarize the different parts of this manuscript, highlighting the key points that have been discussed (section 8.1). We then move on to suggestions for future work (section 8.2). In this second section, we first propose perspectives related to the original contributions of this thesis. Secondly, we propose more global perspectives related to the field of marine ice-sheet modeling and simulations.

8.1 Summary and conclusions

The first part of this thesis was dedicated to a general overview of the modeling of marine ice sheets. In chapter 2, we first presented the equations governing the dynamics of ice sheets. Starting from the conservation principles of continuum mechanics, the local conservation equations for mass, momentum, and energy were established. These were then specialized to the case of ice sheets, by taking advantage of the shallow nature of their geometry and the specific rheology of ice. By adding initial and boundary conditions, this led to the system of equations governing the movement of ice. This system was discussed, particularly in relation to the difficulties associated with its resolution, and the limitations of its validity. Finally, interactions with other components of the Earth System (ice-atmosphere, ice-ocean, and ice-bedrock) were briefly mentioned.

In chapter 3, we discussed the main approximations used to simplify the equations governing the motion of ice sheets. Starting from the full-Stokes model, we showed how the Blatter–Pattyn, shallow-shelf, and shallow-ice models can be derived, and we discussed the properties of these models. Finally, we identified some of the main codes used within the glaciology community and have discussed the efforts undertaken by the community to compare both the ice-flow models and the codes in which they are implemented.

In chapter 4, we presented the current state of the literature on subglacial conditions. More specifically, we first introduced the main models for basal friction, both on a hard bed and on a soft bed. Then, we reviewed the subglacial hydrological models. We were able to highlight that there is a large number of them, related to the type of bed (hard/soft), their efficiency (efficient/inefficient), and their spatial nature (distributed/localized). Finally, we discussed the problem of introducing several hydrological components into a single model and presented several recently developed approaches to achieve this goal.

The second part of this thesis was dedicated to original contributions. In chapter 5, we investigated flux conditions, which are expressions that relate the flux at the grounding line to the ice thickness at that location. Flux conditions had already been derived for several friction laws, particularly for the Weertman law [Schoof, 2007b,c] and for the Coulomb law [Tsai et al., 2015]. Here, we extended these results to derive friction laws for the Budd law. Our results thus generalize the flux conditions associated

with the Weertman and Coulomb laws, as these are special cases of the Budd law. One key result of our analysis concerns the importance of the friction value at the grounding line. If this value is non-zero, the problem simplifies because it can be shown that the divergence of membrane stress can be neglected over the whole grounded part of the ice sheets. The mechanical balance in this region is thus reduced to an equilibrium between the gravitational driving stress and basal friction. However, in the case where friction vanishes at the grounding line, the mechanical equilibrium becomes more complex, with each type of stress (membrane-stress divergence, gravitational driving stress, and basal friction) contributing to the stress balance within a boundary layer near the grounding line.

The second original contribution (chapter 6) addresses the influence of subglacial conditions on the evolution of marine ice sheets over centennial timescales. We developed a simplified subglacial hydrology model that allows for rapid simulation of subglacial hydrology, the latter being coupled to the evolution of marine ice sheets. This model is capable of simulating both distributed and localized systems on hard and soft beds. It was implemented in the large-scale ice-sheet code `Kori-ULB`, which enabled testing on a realistic case, namely Thwaites Glacier. The results showed that accounting for subglacial hydrology in ice-sheet models could significantly increase their contribution to sea-level rise. This can be explained by an instability mechanism between the ice motion and the hydrology system. Furthermore, this increase depends on the type of bed near the grounding line.

The third contribution (chapter 7) addresses the effect of pinning points on marine ice-sheet systems. We highlighted the fact that pinning points create singularities in the system of equations governing the motion of marine ice-sheets, namely the mass and momentum-balance equation. These singularities occur even for smooth beds; in fact, they are associated with a discontinuity in the basal friction and gravitational driving stresses across the grounding line as the ice sheet transitions from a grounded to a floating state. It is possible to avoid such singularities by regularizing the grounding line, so that the transition from the grounded to the floating region is no longer abrupt but gradual. However, such an approach significantly modifies the original equations, since they behave in a qualitatively different way, independently of the value of the regularization parameter. Mathematically, the presence of this regularization parameter appears as a singular perturbation of the original equations. This suggests that either special numerical methods must be used to simulate marine ice sheets near pinning points, or the grounding-line model must be modified, for example in favor of a grounding-zone model.

Overall, these contributions highlight the importance of subglacial conditions on the dynamics of marine ice sheets. Each time, it has been shown that the basal conditions in the vicinity of the grounding line –including basal friction, subglacial hydrology, bed elevation, and bed type– have a significant impact on its motion. Furthermore, these studies have revealed the presence of boundary layers associated with the distribution of stresses in the ice and with the spatial variation of effective pressure. This suggests that, in order to obtain robust simulations of ice sheets, particular attention must be paid to this region. This can be done through the development and incorporation of specific models for marine ice sheets and/or a sufficiently high spatial resolution. The flux conditions of chapter 5, the effective-pressure parametrization of chapter 6, and the grounding-zone model suggested in chapter 7 are possible approaches for achieving this objective.

8.2 Suggestions and perspectives for future work

8.2.1 Perspectives related to the original contributions

Contribution 1: extension of flux conditions

The research undertaken in the first contribution of this thesis can be pursued in several directions. The first possibility concerns the hydrological model. In this study, we considered very simple hydrological models that lead to explicit algebraic expressions for the effective pressure. The simplicity of such models

is a weakness of the study. The way in which the boundary layer at the grounding line is modified when the ice sheet is coupled with a more elaborate hydrological model could be studied. We note that it is possible to anticipate the effect of such a coupling. Indeed, it seems that a hydrological model connected to the ocean necessarily leads to a boundary layer for the effective pressure near the grounding line, in which the effective pressure behaves similarly to the N_A model [Lu and Kingslake, 2024; Kazmierczak et al., 2024]. Moreover, such a boundary layer typically extends over several kilometers. This suggests that the 'mechanical' boundary layer is entirely embedded in the 'hydrological' boundary layer. Therefore, the results obtained with the N_A model should hold even when a more complex hydrological model is applied, as the effective pressure near the grounding line boundary layer will closely match that predicted by the N_A model.

Another area of research concerns the use of flux conditions in large-scale ice-sheet codes. Indeed, flux conditions are used to improve the accuracy of these models by integrating grounding-line dynamics through the use of flux conditions as corrections for the fluxes at the grounding lines [Docquier et al., 2011; Pattyn et al., 2012; Pollard and DeConto, 2012b, 2020]. Although certain criticisms have been expressed at the use of flux conditions [e.g., Reese et al., 2018b; Sergienko and Wingham, 2022], the fact remains that flux conditions make it possible to improve the accuracy of low-resolution models. The study of flux conditions is therefore an important area of research, since they can greatly speed up large-scale numerical simulations. In fact, the problem considered here corresponds more generally to a homogenization problem: we are trying to determine average fields (velocity, pressure, etc) from a relatively low resolution model. Ideally, the latter is obtained by averaging the equations of the high-resolution model. As these equations are non-linear, new terms appear in the mean model obtained: the mean of the high-resolution model does not correspond to a low-resolution model for the mean fields. This is an analytical approach, but numerical methods also exist to take account of small-scale physics in low-resolution models [e.g., multiscale methods; Efendiev and Hou, 2009; Abdulle et al., 2012]. Such approaches are currently underdeveloped in the field of glaciology, as they are relatively technical. However, there is great potential in view of the results of these methods in other fields [e.g., mechanics of composite materials, polymer dynamics, or flows in porous media; Hou and Wu, 1997; Chung et al., 2015; Vassaux et al., 2019], and the benefits they would have on the performance of ice-sheet codes.

Contribution 2: efficient and simplified hydrological model

The subglacial hydrology model presented in the second contribution of this thesis can be improved in several ways. We propose three here, each of which is associated with a weakness or limitation of the model.

Firstly, the distribution of conduits and the space between conduits is currently parametrized through the distance between conduits l_c which is taken to be uniform and independent of the type of drainage system. This is one of the weaknesses of the model; for example, this distance is the same for linked-cavities and canals, which form distributed systems, and channels, which form localized systems. One way of remedying this would be to revise the parametrization of effective pressure by considering, for distributed systems (linked-cavities and canals), a parametrization based on the distributed flow $\boldsymbol{q}_w$ rather than on the volume flow Q_w. By comparing the effective-pressure expression thus obtained with the original effective-pressure expression for channels, it should then be possible to obtain a unified parametrization which is such that the length l_c is associated only with the channels. An estimate of l_c for that case can then be obtained from observations of the distance between eskers. Note that this is again conceptually a homogenization problem, so the previous comments also apply here.

The model can also be improved by incorporating new physical processes. At present, the inefficient model for soft beds is simply a modification of the linked-cavities model on hard beds. In order to better represent the physics of soft beds, one possibility would be to consider the compression of the till and the

water flow between the water present in the till and the hydrological system present between the till and the ice. Another element that could be improved concerns the modeling of hydrology near the grounding line. Our results show that the shape of the effective pressure near the grounding line is an essential element in ice-sheet dynamics. Thus, the dynamics of the hydrology in this zone could be the subject of more detailed studies, given that there are processes not yet included in large-scale hydrological models; this is for example the case sea-water intrusion, which is known to play an important role [Robel et al., 2022b; Bradley and Hewitt, 2024; Rignot et al., 2024].

Finally, the model could be improved by using observational data and comparing it with other hydrological models. The use of data makes it possible to calibrate the model parameters; moreover, this can be done within a probabilistic framework so that uncertainties can be quantified [e.g., following Coulon et al., 2024a,b]. In this context, it would be particularly interesting to carry out calibrated simulations at the Antarctic scale. In this way, we could update the results of Kazmierczak et al. [2022], assessing the effect of subglacial hydrology on Antarctic ice-sheet dynamics in the coming centuries, but this time with a more elaborate hydrological model that will have been calibrated.

Contribution 3: singularity at pinning points

The third contribution is a work-in-progress report. It can be improved in several ways. First, the source of the singularity could be further clarified. It would indeed be interesting to determine whether it is, as suggested in the report, a consequence of the shallow-shelf approximation. In other words, it would be interesting to know whether or not the singular behavior at pinning points is an intrinsic physical feature of marine ice sheets. One way to investigate this would be to rerun the simulations using a full-Stokes model and examine whether the identified features (e.g., stops in bifurcation curves and oscillations in transient simulations) disappear or persist. A simpler approach would be to conduct numerical tests with different types of regularization, for example, by regularizing only the friction stress but not the driving stress (and vice-versa). Second, the technical details could be further specified; in particular, the functional spaces of the velocity and thickness fields could be made more precise. Finally, more broadly, the report could be refined to better highlight the practical significance of the results. Essentially, this means emphasizing the impact of the singularity, namely the dependence on how the grounding line is accounted for numerically (with a regularized approach or not) and, in cases where a regularization approach is used, the strong dependence on the regularization parameter.

Generally speaking, this contribution questions the relevance of the concept of a grounding line. This leads to a number of interesting research possibilities. Essentially, there are two possibilities: either the grounding line model is appropriate, or it is not. In the first case, it is necessary to develop numerical methods capable of rigorously taking into account the singularity associated with the grounded region/floating region transition in the case of pinning points. One way of approaching this problem is to consider the marine ice-sheet problem as an obstacle problem, where the 'obstacle' is the bedrock. Obstacle problems are classical in the field of computational contact mechanics, so many methods for efficiently solving such problems have already been developed. However, such an approach has only recently been developed in the field of glaciology; de Diego et al. [2022, 2023] have for example shown that such a framework could be applied to the full–Stokes model applied to marine ice sheets. However, preliminary work suggests that applying such a framework to the SSA model is not an easy task, given the non-standard form of the equations in that model [Bosten, 2019; Gregov et al., 2022].

If the grounding-line concept is called into question, it is then necessary to develop a new model for marine ice sheets. A regularized approach such as that used in the Úa model is possible [Gudmundsson, 2013], but it raises the question of the value of the regularization parameter. Another approach would be to develop a grounding-zone model, taking into account the gradual nature of a transition between the grounded zone and the floating zone as well as the various physical processes taking place. In particular, it seems that the evolution of both subglacial hydrology and sediment are important controls that should

therefore be included in such a model [Kowal and Worster, 2020; Bradley and Hewitt, 2024; Rignot et al., 2024].

Finally, the difficulties encountered when studying a marine ice-sheet subject to pinning points suggest another more fundamental research direction. These difficulties are associated with the non-smooth nature of the equations governing the motion of ice sheets under the SSA model. Non-smooth models are in fact more common than they appear in physical systems; for example, the contact problems mentioned above are examples of this. A major difficulty in the study of such systems is that the usual methods –for example, sensitivity analysis and continuation methods– are based on the assumption that the systems are at least continuously differentiable. Since this is not the case for non-smooth systems, new tools have to be developed to both study and solve such systems. Possibilities include generalizations of the notion of gradient to mappings that are less regular [Shevitz and Paden, 1994; Stechlinski et al., 2018], the use of adjoint smooth quantities [Miersemann and Mittelmann, 1989, 1991], and regularization approaches [Chen et al., 2000].

8.2.2 Other perspectives

Improvement of the modeling of basal friction

The understanding of basal friction has undergone a number of developments over the last few years, culminating in a so-called 'unified friction law' which currently seems to have a consensus in terms of its ability to take into account viscous and plastic behavior, and which is suitable for both hard and soft beds. However, this does not mean that our understanding of basal friction and how to account for it in models is complete. So far, the most extensive studies to provide a theoretical basis for friction laws are typically based on the study of sliding on water-filled cavities [Fowler, 1986a, 1987; Schoof, 2005; Gagliardini et al., 2007]. This can lead to some strange behavior; for example, the effective pressure in channels is typically quite high, so that using a friction law with $\tau_\mathrm{b} \propto N$ would lead to a high basal friction value, whereas it is physically expected to be low at this location. This apparent paradox is resolved by remembering that both τ_b and N are average values, which therefore do not apply here at the channel apex, but over a representative spatial area. However, this highlights that the application of friction laws depends on the resolution of the models and the configuration chosen. With the development of increasingly high-resolution ice-sheet models and the inclusion of new types of hydrological systems that interact with ice motion, it appears that further studies on basal friction are needed. One possible research direction would be to characterize the basal friction that should be attributed to a channel, as illustrated in the example above.

An alternative way of assessing the validity of friction laws would be to rely on the observations we have of the dynamics of glaciers and ice sheets. By comparing these with the results of numerical simulations associated with several friction laws [in a similar way to, e.g., Brondex et al., 2019], it should be possible to see whether one friction law produces better results than the others. However, there are several difficulties in carrying out such a study. On the one hand, observational data remains relatively limited, and is confined to recent years. Over such a small time span, it seems complicated to be able to distinguish the trajectories associated with several different friction laws in the numerical simulations. On the other hand, there is currently uncertainty both in the observations and in the parametrization of physical processes other than basal friction in the ice-sheet models. This uncertainty leads to predictions that take the form of confidence intervals rather than point predictions. It is therefore not clear that the different friction laws can be distinguished if this uncertainty is such that the confidence intervals between the different friction laws overlap. However, this remains a direction of research to keep in mind, particularly with the accumulating observational data on glaciers and ice sheets.

Application of Lagrangian/Eulerian methods to ice-sheet dynamics

Ice-sheet models are typically described in terms of an Eulerian formalism (see section 2.2). The advantage of this is that the quantities of interest (velocity, pressure, etc) can be described numerically on a fixed, potentially regular mesh. This simplifies both the implementation of ice-flow codes, and their parallelization so that they can be used on high-performance computing infrastructures. However, the inclusion of new physics in ice-sheet models has challenged this approach. Indeed, damage is a material property, so a Lagrangian approach seems more appropriate to model it. This is also the case for localized drainage systems such as channels, which could be described using a Lagrangian formalism allowing greater freedom with regard to their position. Possible research directions include the use of methods based on a Lagrangian approach on a moving finite-element mesh, in order to retain convergence properties and a code structure similar to Eulerian codes. This is the case of the updated-Lagrangian method and of the particle finite-element method [Oñate and Carbonell, 2014; Jiménez et al., 2017; Cremonesi et al., 2020]. Another direction would be to combine Lagrangian and Eulerian approaches to obtain a method based on a mixed formalism [Foucard et al., 2015; Trouette et al., 2020].

Efficient calibration and uncertainty quantification

An area that has not been explored at all in this thesis concerns model calibration; in other words, the identification of the initial state and the value of initial parameters in simulations. This is a major area of research in the field of glaciology. This is indeed a particularly challenging problem: we need to solve an inverse problem, i.e., identify the model parameters (typically, the friction coefficients) that are such that the model response matches the observations (typically, the value of the surface velocity). The difficulty here stems from the complexity of the model, which makes such inverse simulations computationally very costly, and from the fact that the unknown is a spatial field and not a scalar. Since both models and observations are subject to error, the inversion should ideally be performed within a probabilistic framework (typically, using a Bayesian approach), so as to obtain a parameter distribution that is compatible with the observations. The model can then be simulated in a forward direction, taking into account the uncertainties obtained for the parameters; these can then be propagated to quantify the uncertainties on the model outputs.

There are several directions of research to make the calibration of ice-sheet models more efficient. One approach is to use a combination of models of varying complexity [Jakeman et al., 2024]. Another approach is to create a surrogate model in place of the ice-sheet model, based for example on machine-learning methods. Combined with the use of GPUs, these can result in a fast computational code, reducing the cost of numerical simulations (direct and inverse) by several orders of magnitude [Jouvet et al., 2021; Jouvet, 2022; Jouvet and Cordonnier, 2023; He et al., 2023; Howard et al., 2023].

Bibliography

Abdulle, A., Weinan, E., Engquist, B., and Vanden-Eijnden, E. (2012). The heterogeneous multiscale method. *Acta Numerica*, 21, 1–87, https://doi.org/10.1017/s0962492912000025.

Agosta, C., Amory, C., Kittel, C., Orsi, A., Favier, V., Gallée, H., van den Broeke, M. R., Lenaerts, J. T. M., van Wessem, J. M., van de Berg, W. J., and Fettweis, X. (2019). Estimation of the Antarctic surface mass balance using the regional climate model MAR (1979–2015) and identification of dominant processes. *The Cryosphere*, 13(1), 281–296, https://doi.org/10.5194/tc-13-281-2019.

Aitken, A. R. A., Delaney, I., Pirot, G., and Werder, M. A. (2024). Modelling subglacial fluvial sediment transport with a graph-based model, Graphical Subglacial Sediment Transport (GraphSSeT). *The Cryosphere*, 18(9), 4111–4136, https://doi.org/10.5194/tc-18-4111-2024.

Aitken, A. R. A., Li, L., Kulessa, B., Schroeder, D., Jordan, T. A., Whittaker, J. M., Anandakrishnan, S., Dawson, E. J., Wiens, D. A., Eisen, O., and Siegert, M. J. (2023). Antarctic Sedimentary Basins and Their Influence on Ice-Sheet Dynamics. *Reviews of Geophysics*, 61(3), https://doi.org/10.1029/2021rg000767.

Allaire, G., Dapogny, C., and Jouve, F. (2021). Chapter 1 - Shape and topology optimization. In A. Bonito and R. H. Nochetto (Eds.), *Geometric Partial Differential Equations - Part II*, volume 22 of *Handbook of Numerical Analysis*, (pp. 1–132). Elsevier, https://doi.org/https://doi.org/10.1016/bs.hna.2020.10.004.

Alley, R., Blankenship, D., Rooney, S., and Bentley, C. (1989). Water-pressure Coupling of Sliding and Bed Deformation: III. Application to Ice Stream B, Antarctica. *Journal of Glaciology*, 35(119), 130–139, https://doi.org/10.3189/002214389793701572.

Alley, R. B., Holschuh, N., Parizek, B., Zoet, L. K., Riverman, K., Muto, A., Christianson, K., Clyne, E., Anandakrishnan, S., and Stevens, N. T. (2022). GHOSTly flute music: drumlins, moats and the bed of Thwaites Glacier. *Annals of Glaciology*, 63(87–89), 153–157, https://doi.org/10.1017/aog.2023.43.

Allgower, E. L. and Georg, K. (1990). *Numerical Continuation Methods*. Springer Berlin Heidelberg, https://doi.org/10.1007/978-3-642-61257-2.

Arnold, N. and Sharp, M. (2002). Flow variability in the Scandinavian ice sheet: modelling the coupling between ice sheet flow and hydrology. *Quaternary Science Reviews*, 21(4–6), 485–502, https://doi.org/10.1016/s0277-3791(01)00059-2.

Arthern, R. J. and Gudmundsson, G. H. (2010). Initialization of ice-sheet forecasts viewed as an inverse Robin problem. *Journal of Glaciology*, 56(197), 527–533, https://doi.org/10.3189/002214310792447699.

Arthern, R. J., Hindmarsh, R. C. A., and Williams, C. R. (2015). Flow speed within the Antarctic ice sheet and its controls inferred from satellite observations. *Journal of Geophysical Research: Earth Surface*, 120(7), 1171–1188, https://doi.org/10.1002/2014jf003239.

Asay-Davis, X. S., Cornford, S. L., Durand, G., Galton-Fenzi, B. K., Gladstone, R. M., Gudmundsson, G. H., Hattermann, T., Holland, D. M., Holland, D., Holland, P. R., Martin, D. F., Mathiot, P., Pattyn, F., and Seroussi, H. (2016). Experimental design for three interrelated marine ice sheet and ocean model intercomparison projects: MISMIP v. 3 (MISMIP +), ISOMIP v. 2 (ISOMIP +) and MISOMIP v. 1 (MISOMIP1). *Geoscientific Model Development*, 9(7), 2471–2497, https://doi.org/10.5194/gmd-9-2471-2016.

Ashmore, D. W. and Bingham, R. G. (2014). Antarctic subglacial hydrology: current knowledge and future challenges. *Antarctic Science*, 26(6), 758–773, https://doi.org/10.1017/s0954102014000546.

Baral, D. R., Hutter, K., and Greve, R. (2001). Asymptotic Theories of Large-Scale Motion, Temperature, and Moisture Distribution in Land-Based Polythermal Ice Sheets: A Critical Review and New Developments. *Applied Mechanics Reviews*, 54(3), 215–256, https://doi.org/10.1115/1.3097296.

Bassis, J. N., Berg, B., Crawford, A. J., and Benn, D. I. (2021). Transition to marine ice cliff instability controlled by ice thickness gradients and velocity. *Science*, 372(6548), 1342–1344, https://doi.org/10.1126/science.abf6271.

Bassis, J. N., Crawford, A., Kachuck, S. B., Benn, D. I., Walker, C., Millstein, J., Duddu, R., Aström, J., Fricker, H. A., and Luckman, A. (2024). Stability of Ice Shelves and Ice Cliffs in a Changing Climate. *Annual Review of Earth and Planetary Sciences*, 52(1), 221–247, https://doi.org/10.1146/annurev-earth-040522-122817.

Beaud, F., Aati, S., Delaney, I., Adhikari, S., and Avouac, J.-P. (2022). Surge dynamics of Shisper Glacier revealed by time-series correlation of optical satellite images and their utility to substantiate a generalized sliding law. *The Cryosphere*, 16(8), 3123–3148, https://doi.org/10.5194/tc-16-3123-2022.

Bell, R. E., Banwell, A. F., Trusel, L. D., and Kingslake, J. (2018). Antarctic surface hydrology and impacts on ice-sheet mass balance. *Nature Climate Change*, 8(12), 1044–1052, https://doi.org/10.1038/s41558-018-0326-3.

Bell, R. E. and Seroussi, H. (2020). History, mass loss, structure, and dynamic behavior of the Antarctic Ice Sheet. *Science*, 367(6484), 1321–1325, https://doi.org/10.1126/science.aaz5489.

Benn, D. I., Luckman, A., Aström, J. A., Crawford, A. J., Cornford, S. L., Bevan, S. L., Zwinger, T., Gladstone, R., Alley, K., Pettit, E., and Bassis, J. (2022). Rapid fragmentation of Thwaites Eastern Ice Shelf. *The Cryosphere*, 16(6), 2545–2564, https://doi.org/10.5194/tc-16-2545-2022.

Benn, D. I., Warren, C. R., and Mottram, R. H. (2007). Calving processes and the dynamics of calving glaciers. *Earth-Science Reviews*, 82(3-4), 143–179, https://doi.org/10.1016/j.earscirev.2007.02.002.

Bernales, J., Rogozhina, I., Greve, R., and Thomas, M. (2017). Comparison of hybrid schemes for the combination of shallow approximations in numerical simulations of the Antarctic Ice Sheet. *The Cryosphere*, 11(1), 247–265, https://doi.org/10.5194/tc-11-247-2017.

Beyer, S., Kleiner, T., Aizinger, V., Rückamp, M., and Humbert, A. (2018). A confined-unconfined aquifer model for subglacial hydrology and its application to the Northeast Greenland Ice Stream. *The Cryosphere*, 12(12), 3931–3947, https://doi.org/10.5194/tc-12-3931-2018.

Bindschadler, R. (1983). The Importance of Pressurized Subglacial Water in Separation and Sliding at the Glacier Bed. *Journal of Glaciology*, 29(101), 3–19, https://doi.org/10.3189/s0022143000005104.

Blatter, H. (1995). Velocity and stress fields in grounded glaciers: a simple algorithm for including deviatoric stress gradients. *Journal of Glaciology*, 41(138), 333–344, https://doi.org/10.3189/s002214300001621x.

Book, C., Hoffman, M. J., Kachuck, S. B., Hillebrand, T. R., Price, S. F., Perego, M., and Bassis, J. N. (2022). Stabilizing effect of bedrock uplift on retreat of Thwaites Glacier, Antarctica, at centennial timescales. *Earth and Planetary Science Letters*, 597, 117798, https://doi.org/10.1016/j.epsl.2022.117798.

Bosten, A. (2019). *Towards a contact formulation for efficient numerical simulation of marine ice-sheet instabilities*. Master's thesis, Université de Liège.

Boulton, G. S. and Hindmarsh, R. C. A. (1987). Sediment deformation beneath glaciers: Rheology and geological consequences. *Journal of Geophysical Research: Solid Earth*, 92(B9), 9059–9082, https://doi.org/10.1029/jb092ib09p09059.

Bradley, A. T. and Hewitt, I. J. (2024). Tipping point in ice-sheet grounding-zone melting due to ocean water intrusion. *Nature Geoscience*, 17(7), 631–637, https://doi.org/10.1038/s41561-024-01465-7.

Brinkerhoff, D., Truffer, M., and Aschwanden, A. (2017). Sediment transport drives tidewater glacier periodicity. *Nature Communications*, 8(1), https://doi.org/10.1038/s41467-017-00095-5.

Brondex, J., Gagliardini, O., Gillet-Chaulet, F., and Durand, G. (2017). Sensitivity of grounding line dynamics to the choice of the friction law. *Journal of Glaciology*, 63(241), 854–866, https://doi.org/10.1017/jog.2017.51.

Brondex, J., Gillet-Chaulet, F., and Gagliardini, O. (2019). Sensitivity of centennial mass loss projections of the Amundsen basin to the friction law. *The Cryosphere*, 13(1), 177–195, https://doi.org/10.5194/tc-13-177-2019.

Bronselaer, B., Winton, M., Griffies, S. M., Hurlin, W. J., Rodgers, K. B., Sergienko, O. V., Stouffer, R. J., and Russell, J. L. (2018). Change in future climate due to Antarctic meltwater. *Nature*, 564(7734), 53–58, https://doi.org/10.1038/s41586-018-0712-z.

Brown, J., Smith, B., and Ahmadia, A. (2013). Achieving Textbook Multigrid Efficiency for Hydrostatic Ice Sheet Flow. *SIAM Journal on Scientific Computing*, 35(2), B359–b375, https://doi.org/10.1137/110834512.

Budd, W. and Jacka, T. (1989). A review of ice rheology for ice sheet modelling. *Cold Regions Science and Technology*, 16(2), 107–144, https://doi.org/10.1016/0165-232x(89)90014-1.

Budd, W. F. and Jenssen, D. (1987). *Numerical Modelling of the Large-Scale Basal Water Flux under the West Antarctic Ice Sheet*, In *Dynamics of the West Antarctic Ice Sheet*, (pp. 293–320). Springer Netherlands, https://doi.org/10.1007/978-94-009-3745-1_16.

Budd, W. F., Keage, P. L., and Blundy, N. A. (1979). Empirical Studies of Ice Sliding. *Journal of Glaciology*, 23(89), 157–170, https://doi.org/10.3189/s0022143000029804.

Budd, W. F. and Warner, R. C. (1996). A computer scheme for rapid calculations of balance-flux distributions. *Annals of Glaciology*, 23, 21–27, https://doi.org/10.3189/s0260305500013215.

Bueler, E. (2022). Performance analysis of high-resolution ice-sheet simulations. *Journal of Glaciology*, 69(276), 930–935, https://doi.org/10.1017/jog.2022.113.

Bueler, E. and Brown, J. (2009). Shallow shelf approximation as a "sliding law" in a thermomechanically coupled ice sheet model. *Journal of Geophysical Research*, 114(F3), https://doi.org/10.1029/2008jf001179.

Bueler, E. and van Pelt, W. (2015). Mass-conserving subglacial hydrology in the Parallel Ice Sheet Model version 0.6. *Geoscientific Model Development*, 8(6), 1613–1635, https://doi.org/10.5194/gmd-8-1613-2015.

Bulthuis, K., Arnst, M., Sun, S., and Pattyn, F. (2019). Uncertainty quantification of the multi-centennial response of the Antarctic ice sheet to climate change. *The Cryosphere*, 13(4), 1349–1380, https://doi.org/10.5194/tc-13-1349-2019.

Burgard, C., Jourdain, N. C., Mathiot, P., Smith, R. S., Schäfer, R., Caillet, J., Finn, T. S., and Johnson, J. E. (2023). Emulating Present and Future Simulations of Melt Rates at the Base of Antarctic Ice Shelves With Neural Networks. *Journal of Advances in Modeling Earth Systems*, 15(12), https://doi.org/10.1029/2023ms003829.

Burgard, C., Jourdain, N. C., Reese, R., Jenkins, A., and Mathiot, P. (2022). An assessment of basal melt parameterisations for Antarctic ice shelves. *The Cryosphere*, 16(12), 4931–4975, https://doi.org/10.5194/tc-16-4931-2022.

Chen, X., Nashed, Z., and Qi, L. (2000). Smoothing Methods and Semismooth Methods for Nondifferentiable Operator Equations. *SIAM Journal on Numerical Analysis*, 38(4), 1200–1216, https://doi.org/10.1137/s0036142999356719.

Christian, J. E., Robel, A. A., and Catania, G. (2022). A probabilistic framework for quantifying the role of anthropogenic climate change in marine-terminating glacier retreats. *The Cryosphere*, 16(7), 2725–2743, https://doi.org/10.5194/tc-16-2725-2022.

Christian, J. E., Robel, A. A., Proistosescu, C., Roe, G., Koutnik, M., and Christianson, K. (2020). The contrasting response of outlet glaciers to interior and ocean forcing. *The Cryosphere*, 14(7), 2515–2535, https://doi.org/10.5194/tc-14-2515-2020.

Chung, E. T., Efendiev, Y., and Lee, C. S. (2015). Mixed Generalized Multiscale Finite Element Methods and Applications. *Multiscale Modeling & Simulation*, 13(1), 338–366, https://doi.org/10.1137/140970574.

Clark, J. A. and Lingle, C. S. (1977). Future sea-level changes due to West Antarctic ice sheet fluctuations. *Nature*, 269(5625), 206–209, https://doi.org/10.1038/269206a0.

Clarke, G. K. C. (1996). Lumped-element analysis of subglacial hydraulic circuits. *Journal of Geophysical Research: Solid Earth*, 101(B8), 17547–17559, https://doi.org/10.1029/96jb01508.

Clarke, G. K. C. (2005). Subglacial Processes. *Annual Review of Earth and Planetary Sciences*, 33(1), 247–276, https://doi.org/10.1146/annurev.earth.33.092203.122621.

Cornford, S. L., Martin, D. F., Graves, D. T., Ranken, D. F., Le Brocq, A. M., Gladstone, R. M., Payne, A. J., Ng, E. G., and Lipscomb, W. H. (2013). Adaptive mesh, finite volume modeling of marine ice sheets. *Journal of Computational Physics*, 232(1), 529–549, https://doi.org/10.1016/j.jcp.2012.08.037.

Cornford, S. L., Seroussi, H., Asay-Davis, X. S., Gudmundsson, G. H., Arthern, R., Borstad, C., Christmann, J., Dias dos Santos, T., Feldmann, J., Goldberg, D., Hoffman, M. J., Humbert, A., Kleiner, T., Leguy, G., Lipscomb, W. H., Merino, N., Durand, G., Morlighem, M., Pollard, D., Rückamp, M., Williams, C. R., and Yu, H. (2020). Results of the third Marine Ice Sheet Model Intercomparison Project (MISMIP+). *The Cryosphere*, 14(7), 2283–2301, https://doi.org/10.5194/tc-14-2283-2020.

Coulon, V., Bulthuis, K., Whitehouse, P. L., Sun, S., Haubner, K., Zipf, L., and Pattyn, F. (2021). Contrasting Response of West and East Antarctic Ice Sheets to Glacial Isostatic Adjustment. *Journal of Geophysical Research: Earth Surface*, 126(7), https://doi.org/10.1029/2020jf006003.

Coulon, V., De Rydt, J., Gregov, T., Qin, Q., and Pattyn, F. (2024a). Future Freshwater Fluxes From the Antarctic Ice Sheet. *Geophysical Research Letters*, 51(23), https://doi.org/10.1029/2024gl111250.

Coulon, V., Klose, A. K., Kittel, C., Edwards, T., Turner, F., Winkelmann, R., and Pattyn, F. (2024b). Disentangling the drivers of future Antarctic ice loss with a historically calibrated ice-sheet model. *The Cryosphere*, 18(2), 653–681, https://doi.org/10.5194/tc-18-653-2024.

Cremonesi, M., Franci, A., Idelsohn, S., and Oñate, E. (2020). A State of the Art Review of the Particle Finite Element Method (PFEM). *Archives of Computational Methods in Engineering*, 27(5), 1709–1735, https://doi.org/10.1007/s11831-020-09468-4.

Creyts, T. T. and Schoof, C. G. (2009). Drainage through subglacial water sheets. *Journal of Geophysical Research: Earth Surface*, 114(F4), https://doi.org/10.1029/2008jf001215.

Cuffey, K. and Paterson, W. S. B. (2010). *The Physics of Glaciers. 4th ed.* Elsevier, New York.

Dakos, V., Boulton, C. A., Buxton, J. E., Abrams, J. F., Arellano-Nava, B., Armstrong McKay, D. I., Bathiany, S., Blaschke, L., Boers, N., Dylewsky, D., López-Martínez, C., Parry, I., Ritchie, P., van der Bolt, B., van der Laan, L., Weinans, E., and Kéfi, S. (2024). Tipping point detection and early warnings in climate, ecological, and human systems. *Earth System Dynamics*, 15(4), 1117–1135, https://doi.org/10.5194/esd-15-1117-2024.

Damsgaard, A., Goren, L., and Suckale, J. (2020). Water pressure fluctuations control variability in sediment flux and slip dynamics beneath glaciers and ice streams. *Communications Earth & Environment*, 1(1), https://doi.org/10.1038/s43247-020-00074-7.

Damsgaard, A., Suckale, J., Piotrowski, J. A., Houssais, M., Siegfried, M. R., and Fricker, H. A. (2017). Sediment behavior controls equilibrium width of subglacial channels. *Journal of Glaciology*, 63(242), 1034–1048, https://doi.org/10.1017/jog.2017.71.

Dawson, E. J., Schroeder, D. M., Chu, W., Mantelli, E., and Seroussi, H. (2022). Ice mass loss sensitivity to the Antarctic ice sheet basal thermal state. *Nature Communications*, 13(1), https://doi.org/10.1038/s41467-022-32632-2.

de Diego, G. G., Farrell, P. E., and Hewitt, I. J. (2022). Numerical approximation of viscous contact problems applied to glacial sliding. *Journal of Fluid Mechanics*, 938, https://doi.org/10.1017/jfm.2022.178.

de Diego, G. G., Farrell, P. E., and Hewitt, I. J. (2023). On the Finite Element Approximation of a Semicoercive Stokes Variational Inequality Arising in Glaciology. *SIAM Journal on Numerical Analysis*, 61(1), 1–25, https://doi.org/10.1137/21m1437640.

De Rydt, J. and Gudmundsson, G. H. (2016). Coupled ice shelf-ocean modeling and complex grounding line retreat from a seabed ridge. *Journal of Geophysical Research: Earth Surface*, 121(5), 865–880, https://doi.org/10.1002/2015jf003791.

DeConto, R. M., Pollard, D., Alley, R. B., Velicogna, I., Gasson, E., Gomez, N., Sadai, S., Condron, A., Gilford, D. M., Ashe, E. L., Kopp, R. E., Li, D., and Dutton, A. (2021). The Paris Climate Agreement and future sea-level rise from Antarctica. *Nature*, 593(7857), 83–89, https://doi.org/10.1038/s41586-021-03427-0.

Delaney, I., Anderson, L., and Herman, F. (2023). Modeling the spatially distributed nature of subglacial sediment transport and erosion. *Earth Surface Dynamics*, 11(4), 663–680, https://doi.org/10.5194/esurf-11-663-2023.

Delaney, I., Werder, M. A., and Farinotti, D. (2019). A Numerical Model for Fluvial Transport of Subglacial Sediment. *Journal of Geophysical Research: Earth Surface*, 124(8), 2197–2223, https://doi.org/10.1029/2019jf005004.

Dias dos Santos, T., Morlighem, M., and Brinkerhoff, D. (2022). A new vertically integrated MOno-Layer Higher-Order (MOLHO) ice flow model. *The Cryosphere*, 16(1), 179–195, https://doi.org/10.5194/tc-16-179-2022.

Dijkstra, H. A. (2013). *Nonlinear Climate Dynamics*. Cambridge University Press, https://doi.org/10.1017/cbo9781139034135.

Docquier, D., Perichon, L., and Pattyn, F. (2011). Representing Grounding Line Dynamics in Numerical Ice Sheet Models: Recent Advances and Outlook. *Surveys in Geophysics*, 32(4–5), 417–435, https://doi.org/10.1007/s10712-011-9133-3.

Docquier, D., Pollard, D., and Pattyn, F. (2014). Thwaites Glacier grounding-line retreat: influence of width and buttressing parameterizations. *Journal of Glaciology*, 60(220), 305–313, https://doi.org/10.3189/2014jog13j117.

Donea, J., Huerta, A., Ponthot, J.-P., and Rodríguez-Ferran, A. (2004). *Arbitrary Lagrangian–Eulerian Methods*, In *Encyclopedia of Computational Mechanics*, chapter 14. John Wiley & Sons, Ltd, https://doi.org/https://doi.org/10.1002/0470091355.ecm009.

dos Santos, T. D., Morlighem, M., and Seroussi, H. (2021). Assessment of numerical schemes for transient, finite-element ice flow models using ISSM v4.18. *Geoscientific Model Development*, 14(5), 2545–2573, https://doi.org/10.5194/gmd-14-2545-2021.

Dow, C. F. (2022a). Hidden rivers under Antarctica impact ice flow and stability. *Nature Geoscience*, 15(11), 869–870, https://doi.org/10.1038/s41561-022-01060-8.

Dow, C. F. (2022b). The role of subglacial hydrology in Antarctic ice sheet dynamics and stability: a modelling perspective. *Annals of Glaciology*, 63(87–89), 49–54, https://doi.org/10.1017/aog.2023.9.

Dow, C. F., Ross, N., Jeofry, H., Siu, K., and Siegert, M. J. (2022). Antarctic basal environment shaped by high-pressure flow through a subglacial river system. *Nature Geoscience*, 15(11), 892–898, https://doi.org/10.1038/s41561-022-01059-1.

Downs, J. and Johnson, J. V. (2022). A rapidly retreating, marine-terminating glacier's modeled response to perturbations in basal traction. *Journal of Glaciology*, (pp. 1–10)., https://doi.org/10.1017/jog.2022.5.

Drews, R., Pattyn, F., Hewitt, I. J., Ng, F. S. L., Berger, S., Matsuoka, K., Helm, V., Bergeot, N., Favier, L., and Neckel, N. (2017). Actively evolving subglacial conduits and eskers initiate ice shelf channels at an Antarctic grounding line. *Nature Communications*, 8(1), https://doi.org/10.1038/ncomms15228.

Duddu, R. and Waisman, H. (2012). A nonlocal continuum damage mechanics approach to simulation of creep fracture in ice sheets. *Computational Mechanics*, 51(6), 961–974, https://doi.org/10.1007/s00466-012-0778-7.

Dukowicz, J. K., Price, S. F., and Lipscomb, W. H. (2010). Consistent approximations and boundary conditions for ice-sheet dynamics from a principle of least action. *Journal of Glaciology*, 56(197), 480–496, https://doi.org/10.3189/002214310792447851.

Dukowicz, J. K., Price, S. F., and Lipscomb, W. H. (2011). Incorporating arbitrary basal topography in the variational formulation of ice-sheet models. *Journal of Glaciology*, 57(203), 461–467, https://doi.org/10.3189/002214311796905550.

Durand, G., Gagliardini, O., Zwinger, T., Meur, E. L., and Hindmarsh, R. C. (2009). Full Stokes modeling of marine ice sheets: influence of the grid size. *Annals of Glaciology*, 50(52), 109–114, https://doi.org/10.3189/172756409789624283.

Edwards, T. L., Brandon, M. A., Durand, G., Edwards, N. R., Golledge, N. R., Holden, P. B., Nias, I. J., Payne, A. J., Ritz, C., and Wernecke, A. (2019). Revisiting Antarctic ice loss due to marine ice-cliff instability. *Nature*, 566(7742), 58–64, https://doi.org/10.1038/s41586-019-0901-4.

Edwards, T. L., Fettweis, X., Gagliardini, O., Gillet-Chaulet, F., Goelzer, H., Gregory, J. M., Hoffman, M., Huybrechts, P., Payne, A. J., Perego, M., Price, S., Quiquet, A., and Ritz, C. (2014). Probabilistic parameterisation of the surface mass balance-elevation feedback in regional climate model simulations of the Greenland ice sheet. *The Cryosphere*, 8(1), 181–194, https://doi.org/10.5194/tc-8-181-2014.

Efendiev, Y. and Hou, T. Y. (2009). *Multiscale finite element methods*. Surveys and Tutorials in the Applied Mathematical Sciences. Springer.

Eyring, V., Bony, S., Meehl, G. A., Senior, C. A., Stevens, B., Stouffer, R. J., and Taylor, K. E. (2016). Overview of the Coupled Model Intercomparison Project Phase 6 (CMIP6) experimental design and organization. *Geoscientific Model Development*, 9(5), 1937–1958, https://doi.org/10.5194/gmd-9-1937-2016.

Farinotti, D., Huss, M., Fürst, J. J., Landmann, J., Machguth, H., Maussion, F., and Pandit, A. (2019). A consensus estimate for the ice thickness distribution of all glaciers on Earth. *Nature Geoscience*, 12(3), 168–173, https://doi.org/10.1038/s41561-019-0300-3.

Farrell, W. E. and Clark, J. A. (1976). On Postglacial Sea Level. *Geophysical Journal International*, 46(3), 647–667, https://doi.org/10.1111/j.1365-246X.1976.tb01252.x.

Favier, L., Durand, G., Cornford, S. L., Gudmundsson, G. H., Gagliardini, O., Gillet-Chaulet, F., Zwinger, T., Payne, A. J., and Le Brocq, A. M. (2014). Retreat of Pine Island Glacier controlled by marine ice-sheet instability. *Nature Climate Change*, 4(2), 117–121, https://doi.org/10.1038/nclimate2094.

Favier, L., Gagliardini, O., Durand, G., and Zwinger, T. (2012). A three-dimensional full Stokes model of the grounding line dynamics: effect of a pinning point beneath the ice shelf. *The Cryosphere*, 6(1), 101–112, https://doi.org/10.5194/tc-6-101-2012.

Favier, L., Jourdain, N. C., Jenkins, A., Merino, N., Durand, G., Gagliardini, O., Gillet-Chaulet, F., and Mathiot, P. (2019). Assessment of sub-shelf melting parameterisations using the ocean-ice-sheet coupled model NEMO(v3.6)-Elmer/Ice(v8.3). *Geoscientific Model Development*, 12(6), 2255–2283, https://doi.org/10.5194/gmd-12-2255-2019.

Favier, L. and Pattyn, F. (2015). Antarctic ice rise formation, evolution, and stability. *Geophysical Research Letters*, 42(11), 4456–4463, https://doi.org/10.1002/2015gl064195.

Felden, A. M., Martin, D. F., and Ng, E. G. (2023). SUHMO: an adaptive mesh refinement SUbglacial Hydrology MOdel v1.0. *Geoscientific Model Development*, 16(1), 407–425, https://doi.org/10.5194/gmd-16-407-2023.

Flowers, G. E. (2015). Modelling water flow under glaciers and ice sheets. *Proceedings of the Royal Society A: Mathematical, Physical and Engineering Sciences*, 471(2176), 20140907, https://doi.org/10.1098/rspa.2014.0907.

Flowers, G. E. and Clarke, G. K. C. (2002). A multicomponent coupled model of glacier hydrology 1. Theory and synthetic examples. *Journal of Geophysical Research: Solid Earth*, 107(B11), https://doi.org/10.1029/2001jb001122.

Foucard, L., Aryal, A., Duddu, R., and Vernerey, F. (2015). A coupled Eulerian–Lagrangian extended finite element formulation for simulating large deformations in hyperelastic media with moving free boundaries. *Computer Methods in Applied Mechanics and Engineering*, 283, 280–302, https://doi.org/10.1016/j.cma.2014.09.016.

Fountain, A. G. and Walder, J. S. (1998). Water flow through temperate glaciers. *Reviews of Geophysics*, 36(3), 299–328, https://doi.org/10.1029/97rg03579.

Fowler, A. C. (1986a). A sliding law for glaciers of constant viscosity in the presence of subglacial cavitation. *Proceedings of the Royal Society of London. A. Mathematical and Physical Sciences*, 407(1832), 147–170, https://doi.org/10.1098/rspa.1986.0090.

Fowler, A. C. (1986b). Sub-Temperate Basal Sliding. *Journal of Glaciology*, 32(110), 3–5, https://doi.org/10.3189/s0022143000006808.

Fowler, A. C. (1987). Sliding with Cavity Formation. *Journal of Glaciology*, 33(115), 255–267, https://doi.org/10.3189/s0022143000008820.

Fowler, A. C. (2002). Rheology of subglacial till. *Journal of Glaciology*, 48(163), 631–632, https://doi.org/10.3189/s0022143000209787.

Fowler, A. C. (2003). On the rheology of till. *Annals of Glaciology*, 37, 55–59, https://doi.org/10.3189/172756403781815951.

Fowler, A. C. (2009). Instability modelling of drumlin formation incorporating lee-side cavity growth. *Proceedings of the Royal Society A: Mathematical, Physical and Engineering Sciences*, 465(2109), 2681–2702, https://doi.org/10.1098/rspa.2008.0490.

Fowler, A. C. (2010a). The formation of subglacial streams and mega-scale glacial lineations. *Proceedings of the Royal Society A: Mathematical, Physical and Engineering Sciences*, 466(2123), 3181–3201, https://doi.org/10.1098/rspa.2010.0009.

Fowler, A. C. (2010b). The instability theory of drumlin formation applied to Newtonian viscous ice of finite depth. *Proceedings of the Royal Society A: Mathematical, Physical and Engineering Sciences*, 466(2121), 2673–2694, https://doi.org/10.1098/rspa.2010.0017.

Fowler, A. C. (2010c). Weertman, Lliboutry and the development of sliding theory. *Journal of Glaciology*, 56(200), 965–972, https://doi.org/10.3189/002214311796406112.

Fowler, A. C. (2011). *Mathematical Geoscience*. Springer London, https://doi.org/10.1007/978-0-85729-721-1.

Fowler, A. C. (2018). The philosopher in the kitchen: the role of mathematical modelling in explaining drumlin formation. *Gff*, 140(2), 93–105, https://doi.org/10.1080/11035897.2018.1444671.

Fowler, A. C. and Larson, D. A. (1978). On the flow of polythermal glaciers - I. Model and preliminary analysis. *Proceedings of the Royal Society of London. A. Mathematical and Physical Sciences*, 363(1713), 217–242, https://doi.org/10.1098/rspa.1978.0165.

Fowler, A. C. and Ng, F. (2021). *Glaciers and Ice Sheets in the Climate System: The Karthaus Summer School Lecture Notes*. Springer International Publishing, https://doi.org/10.1007/978-3-030-42584-5.

Fowler, A. C. and Walder, J. (1993). Creep closure of channels in deforming subglacial till. *Proceedings of the Royal Society of London. Series A: Mathematical and Physical Sciences*, 441(1911), 17–31, https://doi.org/10.1098/rspa.1993.0046.

Gagliardini, O., Cohen, D., Råback, P., and Zwinger, T. (2007). Finite-element modeling of subglacial cavities and related friction law. *Journal of Geophysical Research*, 112(F2), https://doi.org/10.1029/2006jf000576.

Gagliardini, O. and Werder, M. A. (2018). Influence of increasing surface melt over decadal timescales on land-terminating Greenland-type outlet glaciers. *Journal of Glaciology*, 64(247), 700–710, https://doi.org/10.1017/jog.2018.59.

Gagliardini, O., Zwinger, T., Gillet-Chaulet, F., Durand, G., Favier, L., de Fleurian, B., Greve, R., Malinen, M., Martín, C., Råback, P., Ruokolainen, J., Sacchettini, M., Schäfer, M., Seddik, H., and Thies, J. (2013). Capabilities and performance of Elmer/Ice, a new-generation ice sheet model. *Geoscientific Model Development*, 6(4), 1299–1318, https://doi.org/10.5194/gmd-6-1299-2013.

Garbe, J., Albrecht, T., Levermann, A., Donges, J. F., and Winkelmann, R. (2020). The hysteresis of the Antarctic Ice Sheet. *Nature*, 585(7826), 538–544, https://doi.org/10.1038/s41586-020-2727-5.

Gilbert, A., Gimbert, F., Thøgersen, K., Schuler, T. V., and Kääb, A. (2022). A Consistent Framework for Coupling Basal Friction With Subglacial Hydrology on Hard-Bedded Glaciers. *Geophysical Research Letters*, 49(13), https://doi.org/10.1029/2021gl097507.

Gillet-Chaulet, F., Gagliardini, O., Meyssonnier, J., Montagnat, M., and Castelnau, O. (2005). A user-friendly anisotropic flow law for ice-sheet modeling. *Journal of Glaciology*, 51(172), 3–14, https://doi.org/10.3189/172756505781829584.

Gillet-Chaulet, F., Gagliardini, O., Meyssonnier, J., Zwinger, T., and Ruokolainen, J. (2006). Flow-induced anisotropy in polar ice and related ice-sheet flow modelling. *Journal of Non-Newtonian Fluid Mechanics*, 134(1–3), 33–43, https://doi.org/10.1016/j.jnnfm.2005.11.005.

Gillett, N. P., Kirchmeier-Young, M., Ribes, A., Shiogama, H., Hegerl, G. C., Knutti, R., Gastineau, G., John, J. G., Li, L., Nazarenko, L., Rosenbloom, N., Seland, Ø., Wu, T., Yukimoto, S., and Ziehn, T. (2021). Constraining human contributions to observed warming since the pre-industrial period. *Nature Climate Change*, 11(3), 207–212, https://doi.org/10.1038/s41558-020-00965-9.

Glen, J. W. (1955). The creep of polycrystalline ice. *Proceedings of the Royal Society of London. Series A. Mathematical and Physical Sciences*, 228(1175), 519–538, https://doi.org/10.1098/rspa.1955.0066.

Goeller, S., Thoma, M., Grosfeld, K., and Miller, H. (2013). A balanced water layer concept for subglacial hydrology in large-scale ice sheet models. *The Cryosphere*, 7(4), 1095–1106, https://doi.org/10.5194/tc-7-1095-2013.

Goldberg, D. N. (2011). A variationally derived, depth-integrated approximation to a higher-order glaciological flow model. *Journal of Glaciology*, 57(201), 157–170, https://doi.org/10.3189/002214311795306763.

Goldsby, D. L. and Kohlstedt, D. L. (2001). Superplastic deformation of ice: Experimental observations. *Journal of Geophysical Research: Solid Earth*, 106(B6), 11017–11030, https://doi.org/10.1029/2000jb900336.

Gomez, N., Mitrovica, J. X., Huybers, P., and Clark, P. U. (2010). Sea level as a stabilizing factor for marine-ice-sheet grounding lines. *Nature Geoscience*, 3(12), 850–853, https://doi.org/10.1038/ngeo1012.

Govaerts, W. J. F. (2000). *Numerical methods for bifurcations of dynamical equilibria*. Philadelphia, Pa.: Society for Industrial and Applied Mathematics.

Gowan, E. J., Hinck, S., Niu, L., Clason, C., and Lohmann, G. (2023). The impact of spatially varying ice sheet basal conditions on sliding at glacial time scales. *Journal of Glaciology*, 69(276), 1056–1070, https://doi.org/10.1017/jog.2022.125.

Gregov, T., Pattyn, F., and Arnst, M. (2022). A primal-dual formulation for numerical simulations of marine ice sheets with various friction laws. *ECCOMAS Congress 2022*, Oslo, Norway.

Gregov, T., Pattyn, F., and Arnst, M. (2023). Grounding-line flux conditions for marine ice-sheet systems under effective-pressure-dependent and hybrid friction laws. *Journal of Fluid Mechanics*, 975, https://doi.org/10.1017/jfm.2023.760.

Greve, R. and Blatter, H. (2009). *Dynamics of Ice Sheets and Glaciers*. Springer Berlin Heidelberg, https://doi.org/10.1007/978-3-642-03415-2.

Gudmundsson, G. H. (2013). Ice-shelf buttressing and the stability of marine ice sheets. *The Cryosphere*, 7(2), 647–655, https://doi.org/10.5194/tc-7-647-2013.

Gudmundsson, G. H., Krug, J., Durand, G., Favier, L., and Gagliardini, O. (2012). The stability of grounding lines on retrograde slopes. *The Cryosphere*, 6(6), 1497–1505, https://doi.org/10.5194/tc-6-1497-2012.

Gudmundsson, G. H., Paolo, F. S., Adusumilli, S., and Fricker, H. A. (2019). Instantaneous Antarctic ice sheet mass loss driven by thinning ice shelves. *Geophysical Research Letters*, 46(23), 13903–13909, https://doi.org/10.1029/2019gl085027.

Hageman, T., Mejía, J., Duddu, R., and Martínez-Pañeda, E. (2024). Ice viscosity governs hydraulic fracture that causes rapid drainage of supraglacial lakes. *The Cryosphere*, 18(9), 3991–4009, https://doi.org/10.5194/tc-18-3991-2024.

Hager, A. O., Hoffman, M. J., Price, S. F., and Schroeder, D. M. (2022). Persistent, extensive channelized drainage modeled beneath Thwaites Glacier, West Antarctica. *The Cryosphere*, 16(9), 3575–3599, https://doi.org/10.5194/tc-16-3575-2022.

Hansen, D. D., Warburton, K. L. P., Zoet, L. K., Meyer, C. R., Rempel, A. W., and Stubblefield, A. G. (2024). Presence of Frozen Fringe Impacts Soft-Bedded Slip Relationship. *Geophysical Research Letters*, 51(12), https://doi.org/10.1029/2023gl107681.

Harper, J. T., Humphrey, N. F., Pfeffer, W. T., and Lazar, B. (2007). Two modes of accelerated glacier sliding related to water. *Geophysical Research Letters*, 34(12), https://doi.org/10.1029/2007gl030233.

Haseloff, M. and Sergienko, O. V. (2018). The effect of buttressing on grounding line dynamics. *Journal of Glaciology*, 64(245), 417–431, https://doi.org/10.1017/jog.2018.30.

Haseloff, M. and Sergienko, O. V. (2022). Effects of calving and submarine melting on steady states and stability of buttressed marine ice sheets. *Journal of Glaciology*, 68(272), 1149–1166, https://doi.org/10.1017/jog.2022.29.

He, Q., Perego, M., Howard, A. A., Karniadakis, G. E., and Stinis, P. (2023). A hybrid deep neural operator/finite element method for ice-sheet modeling. *Journal of Computational Physics*, 492, 112428, https://doi.org/10.1016/j.jcp.2023.112428.

Heinlein, A., Perego, M., and Rajamanickam, S. (2022). FROSch Preconditioners for Land Ice Simulations of Greenland and Antarctica. *SIAM Journal on Scientific Computing*, 44(2), B339–b367, https://doi.org/10.1137/21m1395260.

Helanow, C., Iverson, N. R., Woodard, J. B., and Zoet, L. K. (2021). A slip law for hard-bedded glaciers derived from observed bed topography. *Science Advances*, 7(20), https://doi.org/10.1126/sciadv.abe7798.

Henann, D. L. and Kamrin, K. (2013). A predictive, size-dependent continuum model for dense granular flows. *Proceedings of the National Academy of Sciences*, 110(17), 6730–6735, https://doi.org/10.1073/pnas.1219153110.

Herterich, K. (1987). *On the Flow within the Transition Zone between Ice Sheet and Ice Shelf*, In *Dynamics of the West Antarctic Ice Sheet*, (pp. 185–202). Springer Netherlands, https://doi.org/10.1007/978-94-009-3745-1_11.

Hewitt, I. J. (2009). *Mathematical modelling of geophysical melt drainage*. PhD thesis, University of Oxford.

Hewitt, I. J. (2011). Modelling distributed and channelized subglacial drainage: the spacing of channels. *Journal of Glaciology*, 57(202), 302–314, https://doi.org/10.3189/002214311796405951.

Hewitt, I. J. (2013). Seasonal changes in ice sheet motion due to melt water lubrication. *Earth and Planetary Science Letters*, 371-372, 16–25, https://doi.org/10.1016/j.epsl.2013.04.022.

Hewitt, I. J. (2020). Subglacial Plumes. *Annual Review of Fluid Mechanics*, 52(1), 145–169, https://doi.org/10.1146/annurev-fluid-010719-060252.

Hewitt, I. J. (2023). Glacier Sliding. *Lecture notes of the Karthaus Summer School*.

Hewitt, I. J. and Creyts, T. T. (2019). A Model for the Formation of Eskers. *Geophysical Research Letters*, 46(12), 6673–6680, https://doi.org/10.1029/2019gl082304.

Hewitt, I. J. and Schoof, C. (2017). Models for polythermal ice sheets and glaciers. *The Cryosphere*, 11(1), 541–551, https://doi.org/10.5194/tc-11-541-2017.

Hewitt, I. J., Schoof, C., and Werder, M. A. (2012). Flotation and free surface flow in a model for subglacial drainage. Part 2. Channel flow. *Journal of Fluid Mechanics*, 702, 157–187, https://doi.org/10.1017/jfm.2012.166.

Hill, E. A., Gudmundsson, G. H., and Chandler, D. M. (2024). Ocean warming as a trigger for irreversible retreat of the Antarctic ice sheet. *Nature Climate Change*, 14(11), 1165–1171, https://doi.org/10.1038/s41558-024-02134-8.

Hill, T., Flowers, G. E., Hoffman, M. J., Bingham, D., and Werder, M. A. (2023). Improved representation of laminar and turbulent sheet flow in subglacial drainage models. *Journal of Glaciology*, (pp. 1–14)., https://doi.org/10.1017/jog.2023.103.

Hindmarsh, R. (1997). Deforming beds: Viscous and plastic scales of deformation. *Quaternary Science Reviews*, 16(9), 1039–1056, https://doi.org/10.1016/s0277-3791(97)00035-8.

Hindmarsh, R. C. (2012). An observationally validated theory of viscous flow dynamics at the ice-shelf calving front. *Journal of Glaciology*, 58(208), 375–387, https://doi.org/10.3189/2012jog11j206.

Hindmarsh, R. C. A. (2004). A numerical comparison of approximations to the Stokes equations used in ice sheet and glacier modeling. *Journal of Geophysical Research: Earth Surface*, 109(F1), https://doi.org/10.1029/2003jf000065.

Hoffman, M. and Price, S. (2014). Feedbacks between coupled subglacial hydrology and glacier dynamics. *Journal of Geophysical Research: Earth Surface*, 119(3), 414–436, https://doi.org/10.1002/2013jf002943.

Hoffman, M. J., Perego, M., Price, S. F., Lipscomb, W. H., Zhang, T., Jacobsen, D., Tezaur, I., Salinger, A. G., Tuminaro, R., and Bertagna, L. (2018). MPAS-Albany Land Ice (MALI): a variable-resolution ice sheet model for Earth system modeling using Voronoi grids. *Geoscientific Model Development*, 11(9), 3747–3780, https://doi.org/10.5194/gmd-11-3747-2018.

Hogan, K. A., Warburton, K. L. P., Graham, A. G. C., Neufeld, J. A., Hewitt, D. R., Dowdeswell, J. A., and Larter, R. D. (2023). Towards modelling of corrugation ridges at ice-sheet grounding lines. *The Cryosphere*, 17(7), 2645–2664, https://doi.org/10.5194/tc-17-2645-2023.

Hossain, M. A., Pimentel, S., and Stockie, J. M. (2020). Modelling dynamic ice-sheet boundaries and grounding line migration using the level set method. *Journal of Glaciology*, 66(259), 766–776, https://doi.org/10.1017/jog.2020.45.

Hou, T. Y. and Wu, X.-H. (1997). A Multiscale Finite Element Method for Elliptic Problems in Composite Materials and Porous Media. *Journal of Computational Physics*, 134(1), 169–189, https://doi.org/10.1006/jcph.1997.5682.

Howard, A. A., Perego, M., Karniadakis, G. E., and Stinis, P. (2023). Multifidelity deep operator networks for data-driven and physics-informed problems. *Journal of Computational Physics*, 493, 112462, https://doi.org/10.1016/j.jcp.2023.112462.

Hubbard, B. P., Sharp, M. J., Willis, I. C., Nielsen, M. K., and Smart, C. C. (1995). Borehole water-level variations and the structure of the subglacial hydrological system of Haut Glacier d'Arolla, Valais, Switzerland. *Journal of Glaciology*, 41(139), 572–583, https://doi.org/10.3189/s0022143000034894.

Huber, M. and Knutti, R. (2011). Anthropogenic and natural warming inferred from changes in Earth's energy balance. *Nature Geoscience*, 5(1), 31–36, https://doi.org/10.1038/ngeo1327.

Hutter, K. (1982). A mathematical model of polythermal glaciers and ice sheets. *Geophysical & Astrophysical Fluid Dynamics*, 21(3–4), 201–224, https://doi.org/10.1080/03091928208209013.

Hutter, K. (1983). *The Application of the Shallow-Ice Approximation*, In *Theoretical Glaciology*, (pp. 256–332). Springer Netherlands, https://doi.org/10.1007/978-94-015-1167-4_5.

Huybrechts, P. and de Wolde, J. (1999). The Dynamic Response of the Greenland and Antarctic Ice Sheets to Multiple-Century Climatic Warming. *Journal of Climate*, 12(8), 2169–2188, https://doi.org/10.1175/1520-0442(1999)012<2169:tdrotg>2.0.co;2.

Iken, A. (1981). The Effect of the Subglacial Water Pressure on the Sliding Velocity of a Glacier in an Idealized Numerical Model. *Journal of Glaciology*, 27(97), 407–421, https://doi.org/10.3189/s0022143000011448.

Iken, A. and Bindschadler, R. A. (1986). Combined measurements of Subglacial Water Pressure and Surface Velocity of Findelengletscher, Switzerland: Conclusions about Drainage System and Sliding Mechanism. *Journal of Glaciology*, 32(110), 101–119, https://doi.org/10.3189/s0022143000006936.

Iken, A., Echelmeyer, K., Harrison, W., and Funk, M. (1993). Mechanisms of fast flow in Jakobshavns Isbræ, West Greenland: Part I. Measurements of temperature and water level in deep boreholes. *Journal of Glaciology*, 39(131), 15–25, https://doi.org/10.3189/s0022143000015689.

IPCC (2021). Climate Change 2021: The Physical Science Basis. Contribution of Working Group I to the Sixth Assessment Report of the Intergovernmental Panel on Climate Change, edited by Masson-Delmotte, V., Zhai, P., Pörtner, H.-O., Roberts, D., Skea, J., Shukla, P. R., and others. https://doi.org/10.1017/9781009157896.

Isaac, T., Petra, N., Stadler, G., and Ghattas, O. (2015a). Scalable and efficient algorithms for the propagation of uncertainty from data through inference to prediction for large-scale problems, with application to flow of the Antarctic ice sheet. *Journal of Computational Physics*, 296, 348–368, https://doi.org/10.1016/j.jcp.2015.04.047.

Isaac, T., Stadler, G., and Ghattas, O. (2015b). Solution of Nonlinear Stokes Equations Discretized By High-Order Finite Elements on Nonconforming and Anisotropic Meshes, with Application to Ice Sheet Dynamics. *SIAM Journal on Scientific Computing*, 37(6), B804–b833, https://doi.org/10.1137/140974407.

Iverson, N. R., Baker, R. W., Hooke, R. L., Hanson, B., and Jansson, P. (1999). Coupling between a glacier and a soft bed: I. A relation between effective pressure and local shear stress determined from till elasticity. *Journal of Glaciology*, 45(149), 31–40, https://doi.org/10.3189/s0022143000003014.

Iverson, N. R., Hooyer, T. S., and Baker, R. W. (1998). Ring-shear studies of till deformation: Coulomb-plastic behavior and distributed strain in glacier beds. *Journal of Glaciology*, 44(148), 634–642, https://doi.org/10.3189/s0022143000002136.

Iverson, N. R. and Iverson, R. M. (2001). Distributed shear of subglacial till due to Coulomb slip. *Journal of Glaciology*, 47(158), 481–488, https://doi.org/10.3189/172756501781832115.

Iverson, N. R. and Zoet, L. K. (2015). Experiments on the dynamics and sedimentary products of glacier slip. *Geomorphology*, 244, 121–134, https://doi.org/10.1016/j.geomorph.2015.03.027.

Jakeman, J. D., Perego, M., Seidl, D. T., Hartland, T. A., Hillebrand, T. R., Hoffman, M. J., and Price, S. F. (2024). An evaluation of multi-fidelity methods for quantifying uncertainty in projections of ice-sheet mass-change. *EGUsphere preprint*, https://doi.org/10.5194/egusphere-2024-2209.

Jenkins, A., Nicholls, K. W., and Corr, H. F. J. (2010). Observation and Parameterization of Ablation at the Base of Ronne Ice Shelf, Antarctica. *Journal of Physical Oceanography*, 40(10), 2298–2312, https://doi.org/10.1175/2010jpo4317.1.

Jenkins, A., Shoosmith, D., Dutrieux, P., Jacobs, S., Kim, T. W., Lee, S. H., Ha, H. K., and Stammerjohn, S. (2018). West Antarctic Ice Sheet retreat in the Amundsen Sea driven by decadal oceanic variability. *Nature Geoscience*, 11(10), 733–738, https://doi.org/10.1038/s41561-018-0207-4.

Jezek, K. C., Alley, R. B., and Thomas, R. H. (1985). Rheology of Glacier Ice. *Science*, 227(4692), 1335–1337, https://doi.org/10.1126/science.227.4692.1335.

Jiménez, S., Duddu, R., and Bassis, J. (2017). An updated-Lagrangian damage mechanics formulation for modeling the creeping flow and fracture of ice sheets. *Computer Methods in Applied Mechanics and Engineering*, 313, 406–432, https://doi.org/10.1016/j.cma.2016.09.034.

Johnson, J. and Fastook, J. L. (2002). Northern Hemisphere glaciation and its sensitivity to basal melt water. *Quaternary International*, 95–96, 65–74, https://doi.org/10.1016/s1040-6182(02)00028-9.

Jop, P., Forterre, Y., and Pouliquen, O. (2006). A constitutive law for dense granular flows. *Nature*, 441(7094), 727–730, https://doi.org/10.1038/nature04801.

Joughin, I., Alley, R. B., and Holland, D. M. (2012). Ice-Sheet Response to Oceanic Forcing. *Science*, 338(6111), 1172–1176, https://doi.org/10.1126/science.1226481.

Joughin, I., Smith, B. E., and Medley, B. (2014). Marine Ice Sheet Collapse Potentially Under Way for the Thwaites Glacier Basin, West Antarctica. *Science*, 344(6185), 735–738, https://doi.org/10.1126/science.1249055.

Joughin, I., Smith, B. E., and Schoof, C. G. (2019). Regularized Coulomb Friction Laws for Ice Sheet Sliding: Application to Pine Island Glacier, Antarctica. *Geophysical Research Letters*, 46(9), 4764–4771, https://doi.org/10.1029/2019gl082526.

Joughin, I., Tulaczyk, S., Bamber, J. L., Blankenship, D., Holt, J. W., Scambos, T., and Vaughan, D. G. (2009). Basal conditions for Pine Island and Thwaites Glaciers, West Antarctica, determined using satellite and airborne data. *Journal of Glaciology*, 55(190), 245–257, https://doi.org/10.3189/002214309788608705.

Jourdain, N. C., Asay-Davis, X., Hattermann, T., Straneo, F., Seroussi, H., Little, C. M., and Nowicki, S. (2020). A protocol for calculating basal melt rates in the ISMIP6 Antarctic ice sheet projections. *The Cryosphere*, 14(9), 3111–3134, https://doi.org/10.5194/tc-14-3111-2020.

Jouvet, G. (2014). A multilayer ice-flow model generalising the shallow shelf approximation. *Journal of Fluid Mechanics*, 764, 26–51, https://doi.org/10.1017/jfm.2014.689.

Jouvet, G. (2015). Multilayer shallow shelf approximation: Minimisation formulation, finite element solvers and applications. *Journal of Computational Physics*, 287, 60–76, https://doi.org/10.1016/j.jcp.2015.02.006.

Jouvet, G. (2016). Mechanical error estimators for shallow ice flow models. *Journal of Fluid Mechanics*, 807, 40–61, https://doi.org/10.1017/jfm.2016.593.

Jouvet, G. (2022). Inversion of a Stokes glacier flow model emulated by deep learning. *Journal of Glaciology*, 69(273), 13–26, https://doi.org/10.1017/jog.2022.41.

Jouvet, G. and Cordonnier, G. (2023). Ice-flow model emulator based on physics-informed deep learning. *Journal of Glaciology*, (pp. 1–15)., https://doi.org/10.1017/jog.2023.73.

Jouvet, G., Cordonnier, G., Kim, B., Lüthi, M., Vieli, A., and Aschwanden, A. (2021). Deep learning speeds up ice flow modelling by several orders of magnitude. *Journal of Glaciology*, 68(270), 651–664, https://doi.org/10.1017/jog.2021.120.

Jouvet, G. and Gräser, C. (2013). An adaptive Newton multigrid method for a model of marine ice sheets. *Journal of Computational Physics*, 252, 419–437, https://doi.org/10.1016/j.jcp.2013.06.032.

Kamb, B. (1970). Sliding motion of glaciers: Theory and observation. *Reviews of Geophysics*, 8(4), 673–728, https://doi.org/10.1029/rg008i004p00673.

Kamb, B. (1987). Glacier surge mechanism based on linked cavity configuration of the basal water conduit system. *Journal of Geophysical Research: Solid Earth*, 92(B9), 9083–9100, https://doi.org/10.1029/jb092ib09p09083.

Kamb, B. (1991). Rheological nonlinearity and flow instability in the deforming bed mechanism of ice stream motion. *Journal of Geophysical Research: Solid Earth*, 96(B10), 16585–16595, https://doi.org/10.1029/91jb00946.

Kamb, B., Raymond, C. F., Harrison, W. D., Engelhardt, H., Echelmeyer, K. A., Humphrey, N., Brugman, M. M., and Pfeffer, T. (1985). Glacier Surge Mechanism: 1982-1983 Surge of Variegated Glacier, Alaska. *Science*, 227(4686), 469–479, https://doi.org/10.1126/science.227.4686.469.

Kazmierczak, E., Gregov, T., Coulon, V., and Pattyn, F. (2024). A fast and simplified subglacial hydrological model for the Antarctic Ice Sheet and outlet glaciers. *The Cryosphere*, 18(12), 5887–5911, https://doi.org/10.5194/tc-18-5887-2024.

Kazmierczak, E., Sun, S., Coulon, V., and Pattyn, F. (2022). Subglacial hydrology modulates basal sliding response of the Antarctic ice sheet to climate forcing. *The Cryosphere*, 16(10), 4537–4552, https://doi.org/10.5194/tc-16-4537-2022.

Keller, H. B. (1977). Numerical solution of bifurcation and nonlinear eigenvalue problems. In *Applications of Bifurcation Theory (Proc. Advanced Sem., Univ. Wisconsin, Madison, Wis., 1976)*, Publ. Math. Res. Center, No. 38, (pp. 359–384). Academic Press.

Keller, H. B. (1987). *Lectures on Numerical Methods in Bifurcation Problems*. Bombay: Tata Institute of Fundamental Research.

Kelly, D. W., Nakazawa, S., Zienkiewicz, O. C., and Heinrich, J. C. (1980). A note on upwinding and anisotropic balancing dissipation in finite element approximations to convective diffusion problems. *International Journal for Numerical Methods in Engineering*, 15(11), 1705–1711, https://doi.org/10.1002/nme.1620151111.

Khoei, A. R. (2014). *Extended Finite Element Method: Theory and Applications*. Wiley, https://doi.org/10.1002/9781118869673.

Kittel, C., Amory, C., Agosta, C., Jourdain, N. C., Hofer, S., Delhasse, A., Doutreloup, S., Huot, P.-V., Lang, C., Fichefet, T., and Fettweis, X. (2021). Diverging future surface mass balance between the Antarctic ice shelves and grounded ice sheet. *The Cryosphere*, 15(3), 1215–1236, https://doi.org/10.5194/tc-15-1215-2021.

Klose, A. K., Coulon, V., Pattyn, F., and Winkelmann, R. (2024). The long-term sea-level commitment from Antarctica. *The Cryosphere*, 18(9), 4463–4492, https://doi.org/10.5194/tc-18-4463-2024.

Koellner, S., Parizek, B. R., Alley, R. B., Muto, A., and Holschuh, N. (2019). The impact of spatially-variable basal properties on outlet glacier flow. *Earth and Planetary Science Letters*, 515, 200–208, https://doi.org/10.1016/j.epsl.2019.03.026.

Kowal, K. N. and Worster, M. G. (2020). The formation of grounding zone wedges: theory and experiments. *Journal of Fluid Mechanics*, 898, https://doi.org/10.1017/jfm.2020.393.

Kyrke-Smith, T. M. and Fowler, A. C. (2014). Subglacial swamps. *Proceedings of the Royal Society A: Mathematical, Physical and Engineering Sciences*, 470(2171), 20140340, https://doi.org/10.1098/rspa.2014.0340.

Kyrke-Smith, T. M., Gudmundsson, G. H., and Farrell, P. E. (2018). Relevance of Detail in Basal Topography for Basal Slipperiness Inversions: A Case Study on Pine Island Glacier, Antarctica. *Frontiers in Earth Science*, 6, https://doi.org/10.3389/feart.2018.00033.

Kyrke-Smith, T. M., Katz, R. F., and Fowler, A. C. (2014). Subglacial hydrology and the formation of ice streams. *Proceedings of the Royal Society A: Mathematical, Physical and Engineering Sciences*, 470(2161), 20130494, https://doi.org/10.1098/rspa.2013.0494.

Kyrke-Smith, T. M., Katz, R. F., and Fowler, A. C. (2015). Subglacial hydrology as a control on emergence, scale, and spacing of ice streams. *Journal of Geophysical Research: Earth Surface*, 120(8), 1501–1514, https://doi.org/10.1002/2015jf003505.

Lai, C.-Y., Kingslake, J., Wearing, M. G., Chen, P.-H. C., Gentine, P., Li, H., Spergel, J. J., and van Wessem, J. M. (2020). Vulnerability of Antarctica's ice shelves to meltwater-driven fracture. *Nature*, 584(7822), 574–578, https://doi.org/10.1038/s41586-020-2627-8.

Lappegard, G., Kohler, J., Jackson, M., and Hagen, J. O. (2006). Characteristics of subglacial drainage systems deduced from load-cell measurements. *Journal of Glaciology*, 52(176), 137–148, https://doi.org/10.3189/172756506781828908.

Larour, E., Seroussi, H., Morlighem, M., and Rignot, E. (2012). Continental scale, high order, high spatial resolution, ice sheet modeling using the Ice Sheet System Model (ISSM). *Journal of Geophysical Research: Earth Surface*, 117(F1), https://doi.org/10.1029/2011jf002140.

Lazeroms, W. M. J., Jenkins, A., Rienstra, S. W., and van de Wal, R. S. W. (2019). An Analytical Derivation of Ice-Shelf Basal Melt Based on the Dynamics of Meltwater Plumes. *Journal of Physical Oceanography*, 49(4), 917–939, https://doi.org/10.1175/jpo-d-18-0131.1.

Le Brocq, A., Payne, A., Siegert, M., and Alley, R. (2009). A subglacial water-flow model for West Antarctica. *Journal of Glaciology*, 55(193), 879–888, https://doi.org/10.3189/002214309790152564.

Le Brocq, A. M., Payne, A. J., and Siegert, M. J. (2006). West Antarctic balance calculations: Impact of flux-routing algorithm, smoothing algorithm and topography. *Computers & Geosciences*, 32(10), 1780–1795, https://doi.org/10.1016/j.cageo.2006.05.003.

Le Meur, E. and Huybrechts, P. (1996). A comparison of different ways of dealing with isostasy: examples from modelling the Antarctic ice sheet during the last glacial cycle. *Annals of Glaciology*, 23, 309–317, https://doi.org/10.3189/s0260305500013586.

Lenton, T. M. (2011). Early warning of climate tipping points. *Nature Climate Change*, 1(4), 201–209, https://doi.org/10.1038/nclimate1143.

Lenton, T. M. (2013). Environmental Tipping Points. *Annual Review of Environment and Resources*, 38(1), 1–29, https://doi.org/10.1146/annurev-environ-102511-084654.

Levermann, A. and Winkelmann, R. (2016). A simple equation for the melt elevation feedback of ice sheets. *The Cryosphere*, 10(4), 1799–1807, https://doi.org/10.5194/tc-10-1799-2016.

Levermann, A., Winkelmann, R., Albrecht, T., Goelzer, H., Golledge, N. R., Greve, R., Huybrechts, P., Jordan, J., Leguy, G., Martin, D., Morlighem, M., Pattyn, F., Pollard, D., Quiquet, A., Rodehacke, C., Seroussi, H., Sutter, J., Zhang, T., Van Breedam, J., Calov, R., DeConto, R., Dumas, C., Garbe, J., Gudmundsson, G. H., Hoffman, M. J., Humbert, A., Kleiner, T., Lipscomb, W. H., Meinshausen, M., Ng, E., Nowicki, S. M. J., Perego, M., Price, S. F., Saito, F., Schlegel, N.-J., Sun, S., and van de Wal, R. S. W. (2020). Projecting Antarctica's contribution to future sea level rise from basal ice shelf melt using linear response functions of 16 ice sheet models (LARMIP-2). *Earth System Dynamics*, 11(1), 35–76, https://doi.org/10.5194/esd-11-35-2020.

Lhermitte, S., Sun, S., Shuman, C., Wouters, B., Pattyn, F., Wuite, J., Berthier, E., and Nagler, T. (2020). Damage accelerates ice shelf instability and mass loss in Amundsen Sea Embayment. *Proceedings of the National Academy of Sciences*, 117(40), 24735–24741, https://doi.org/10.1073/pnas.1912890117.

Li, L., Aitken, A. R. A., Lindsay, M. D., and Kulessa, B. (2022). Sedimentary basins reduce stability of Antarctic ice streams through groundwater feedbacks. *Nature Geoscience*, 15(8), 645–650, https://doi.org/10.1038/s41561-022-00992-5.

Lipscomb, W. H., Price, S. F., Hoffman, M. J., Leguy, G. R., Bennett, A. R., Bradley, S. L., Evans, K. J., Fyke, J. G., Kennedy, J. H., Perego, M., Ranken, D. M., Sacks, W. J., Salinger, A. G., Vargo, L. J., and Worley, P. H. (2019). Description and evaluation of the Community Ice Sheet Model (CISM) v2.1. *Geoscientific Model Development*, 12(1), 387–424, https://doi.org/10.5194/gmd-12-387-2019.

Livingstone, S. J., Clark, C. D., Woodward, J., and Kingslake, J. (2013). Potential subglacial lake locations and meltwater drainage pathways beneath the Antarctic and Greenland ice sheets. *The Cryosphere*, 7(6), 1721–1740, https://doi.org/10.5194/tc-7-1721-2013.

Lliboutry, L. (1968). General Theory of Subglacial Cavitation and Sliding of Temperate Glaciers. *Journal of Glaciology*, 7(49), 21–58, https://doi.org/10.3189/s0022143000020396.

Lliboutry, L. (1979). A critical review of analytical approximate solutions for steady state velocities and temperatures in cold ice-sheets. *Zeitschrift für Gletscherkunde und Glazialgeologie*, 35(2), 135–148.

Löfgren, A., Ahlkrona, J., and Helanow, C. (2022). Increasing stable time-step sizes of the free-surface problem arising in ice-sheet simulations. *Journal of Computational Physics: X*, 16, 100114, https://doi.org/10.1016/j.jcpx.2022.100114.

Lu, G. and Kingslake, J. (2024). Two-way coupling between ice flow and channelized subglacial drainage enhances modeled marine-ice-sheet retreat. *The Cryosphere*, 18(11), 5301–5321, https://doi.org/10.5194/tc-18-5301-2024.

Ma, Y., Gagliardini, O., Ritz, C., Gillet-Chaulet, F., Durand, G., and Montagnat, M. (2010). Enhancement factors for grounded ice and ice shelves inferred from an anisotropic ice-flow model. *Journal of Glaciology*, 56(199), 805–812, https://doi.org/10.3189/002214310794457209.

MacAyeal, D. R. (1989). Large-scale ice flow over a viscous basal sediment: Theory and application to ice stream B, Antarctica. *Journal of Geophysical Research: Solid Earth*, 94(B4), 4071–4087, https://doi.org/10.1029/jb094ib04p04071.

Maier, N., Humphrey, N., Harper, J., and Meierbachtol, T. (2019). Sliding dominates slow-flowing margin regions, Greenland Ice Sheet. *Science Advances*, 5(7), https://doi.org/10.1126/sciadv.aaw5406.

Mantelli, E., Haseloff, M., and Schoof, C. (2019). Ice sheet flow with thermally activated sliding. Part 1: the role of advection. *Proceedings of the Royal Society A: Mathematical, Physical and Engineering Sciences*, 475(2230), 20190410, https://doi.org/10.1098/rspa.2019.0410.

Mantelli, E. and Schoof, C. (2019). Ice sheet flow with thermally activated sliding. Part 2: the stability of subtemperate regions. *Proceedings of the Royal Society A: Mathematical, Physical and Engineering Sciences*, 475(2231), 20190411, https://doi.org/10.1098/rspa.2019.0411.

Martin, M. A., Winkelmann, R., Haseloff, M., Albrecht, T., Bueler, E., Khroulev, C., and Levermann, A. (2011). The Potsdam Parallel Ice Sheet Model (PISM-PIK) –Part 2: Dynamic equilibrium simulation of the Antarctic ice sheet. *The Cryosphere*, 5(3), 727–740, https://doi.org/10.5194/tc-5-727-2011.

Matsuoka, K., Hindmarsh, R. C., Moholdt, G., Bentley, M. J., Pritchard, H. D., Brown, J., Conway, H., Drews, R., Durand, G., Goldberg, D., Hattermann, T., Kingslake, J., Lenaerts, J. T., Martín, C., Mulvaney, R., Nicholls, K. W., Pattyn, F., Ross, N., Scambos, T., and Whitehouse, P. L. (2015). Antarctic ice rises and rumples: Their properties and significance for ice-sheet dynamics and evolution. *Earth-Science Reviews*, 150, 724–745, https://doi.org/10.1016/j.earscirev.2015.09.004.

McArthur, K., McCormack, F. S., and Dow, C. F. (2023). Basal conditions of Denman Glacier from glacier hydrology and ice dynamics modeling. *The Cryosphere*, 17(11), 4705–4727, https://doi.org/10.5194/tc-17-4705-2023.

Meyer-Peter, E. and Mueller, R. (1948). Formulas for bedload transport. In *Proceedings of the 2nd meeting of the International Association for Hydraulic Structures Research* (pp. 39–64). Delft.

Miersemann, E. and Mittelmann, H. D. (1989). Continuation for parametrized nonlinear variational inequalities. *Journal of Computational and Applied Mathematics*, 26(1–2), 23–34, https://doi.org/10.1016/0377-0427(89)90145-3.

Miersemann, E. and Mittelmann, H. D. (1991). Stability and continuation of solutions to obstacle problems. *Journal of Computational and Applied Mathematics*, 35(1–3), 5–31, https://doi.org/10.1016/0377-0427(91)90195-p.

Millstein, J. D., Minchew, B. M., and Pegler, S. S. (2022). Ice viscosity is more sensitive to stress than commonly assumed. *Communications Earth & Environment*, 3(1), https://doi.org/10.1038/s43247-022-00385-x.

Minchew, B. and Joughin, I. (2020). Toward a universal glacier slip law. *Science*, 368(6486), 29–30, https://doi.org/10.1126/science.abb3566.

Mitrovica, J. X., Tamisiea, M. E., Davis, J. L., and Milne, G. A. (2001). Recent mass balance of polar ice sheets inferred from patterns of global sea-level change. *Nature*, 409(6823), 1026–1029, https://doi.org/10.1038/35059054.

Mittelmann, H. D. (1987). On Continuation for Variational Inequalities. *SIAM Journal on Numerical Analysis*, 24(6), 1374–1381, https://doi.org/10.1137/0724088.

Mobasher, M. E., Duddu, R., Bassis, J. N., and Waisman, H. (2016). Modeling hydraulic fracture of glaciers using continuum damage mechanics. *Journal of Glaciology*, 62(234), 794–804, https://doi.org/10.1017/jog.2016.68.

Moës, N., Dolbow, J., and Belytschko, T. (1999). A finite element method for crack growth without remeshing. *International Journal for Numerical Methods in Engineering*, 46(1), 131–150, https://doi.org/10.1002/(sici)1097-0207(19990910)46:1<131::aid-nme726>3.0.co;2-j.

Moës, N., Remacle, J.-F., Lambrechts, J., Lé, B., and Chevaugeon, N. (2023). The eXtreme Mesh deformation approach (X-MESH) for the Stefan phase change model. *Journal of Computational Physics*, 477, 111878, https://doi.org/10.1016/j.jcp.2022.111878.

Morecroft, M. D., Duffield, S., Harley, M., Pearce-Higgins, J. W., Stevens, N., Watts, O., and Whitaker, J. (2019). Measuring the success of climate change adaptation and mitigation in terrestrial ecosystems. *Science*, 366(6471), https://doi.org/10.1126/science.aaw9256.

Morland, L. W. (1987). Unconfined Ice-Shelf Flow. In *Dynamics of the West Antarctic Ice Sheet*, (pp. 99–116). Springer Netherlands, https://doi.org/10.1007/978-94-009-3745-1_6.

Morland, L. W. and Johnson, I. R. (1980). Steady Motion of Ice Sheets. *Journal of Glaciology*, 25(92), 229–246, https://doi.org/10.3189/s0022143000010467.

Morlighem, M. (2011). *Ice sheet properties inferred by combining numerical modeling and remote sensing data*. PhD thesis, Ecole Centrale Paris.

Morlighem, M. (2020). MEaSUREs BedMachine Antarctica, Version 2. https://doi.org/10.5067/e1ql9hfq7a8m.

Morlighem, M., Goldberg, D., Barnes, J. M., Bassis, J. N., Benn, D. I., Crawford, A. J., Gudmundsson, G. H., and Seroussi, H. (2024). The West Antarctic Ice Sheet may not be vulnerable to marine ice cliff instability during the 21st century. *Science Advances*, 10(34), https://doi.org/10.1126/sciadv.ado7794.

Morlighem, M., Rignot, E., Binder, T., Blankenship, D., Drews, R., Eagles, G., Eisen, O., Ferraccioli, F., Forsberg, R., Fretwell, P., Goel, V., Greenbaum, J. S., Gudmundsson, H., Guo, J., Helm, V., Hofstede, C., Howat, I., Humbert, A., Jokat, W., Karlsson, N. B., Lee, W. S., Matsuoka, K., Millan, R., Mouginot, J., Paden, J., Pattyn, F., Roberts, J., Rosier, S., Ruppel, A., Seroussi, H., Smith, E. C., Steinhage, D., Sun, B., van den Broeke, M. R., van Ommen, T. D., van Wessem, M., and Young, D. A. (2019). Deep glacial troughs and stabilizing ridges unveiled beneath the margins of the Antarctic ice sheet. *Nature Geoscience*, 13(2), 132–137, https://doi.org/10.1038/s41561-019-0510-8.

Morlighem, M., Rignot, E., Seroussi, H., Larour, E., Ben Dhia, H., and Aubry, D. (2010). Spatial patterns of basal drag inferred using control methods from a full-Stokes and simpler models for Pine Island Glacier, West Antarctica. *Geophysical Research Letters*, 37(14), https://doi.org/10.1029/2010gl043853.

Morlighem, M., Williams, C. N., Rignot, E., An, L., Arndt, J. E., Bamber, J. L., Catania, G., Chauché, N., Dowdeswell, J. A., Dorschel, B., Fenty, I., Hogan, K., Howat, I., Hubbard, A., Jakobsson, M., Jordan, T. M., Kjeldsen, K. K., Millan, R., Mayer, L., Mouginot, J., Noël, B. P. Y., O'Cofaigh, C., Palmer, S., Rysgaard, S., Seroussi, H., Siegert, M. J., Slabon, P., Straneo, F., van den Broeke, M. R., Weinrebe, W., Wood, M., and Zinglersen, K. B. (2017). BedMachine v3: Complete Bed Topography and Ocean Bathymetry Mapping of Greenland From Multibeam Echo Sounding Combined With Mass Conservation. *Geophysical Research Letters*, 44(21), https://doi.org/10.1002/2017gl074954.

Mouginot, J., Rignot, E., and Scheuchl, B. (2014). Sustained increase in ice discharge from the Amundsen Sea Embayment, West Antarctica, from 1973 to 2013. *Geophysical Research Letters*, 41(5), 1576–1584, https://doi.org/10.1002/2013gl059069.

Mulder, T. E., Baars, S., Wubs, F. W., and Dijkstra, H. A. (2018). Stochastic marine ice sheet variability. *Journal of Fluid Mechanics*, 843, 748–777, https://doi.org/10.1017/jfm.2018.148.

Muto, A., Alley, R. B., Parizek, B. R., and Anandakrishnan, S. (2019). Bed-type variability and till (dis)continuity beneath Thwaites Glacier, West Antarctica. *Annals of Glaciology*, 60(80), 82–90, https://doi.org/10.1017/aog.2019.32.

Ng, F. S. L. (1998). *Mathematical modelling of subglacial drainage and erosion*. PhD thesis, University of Oxford.

Ng, F. S. L. (2000). Canals under sediment-based ice sheets. *Annals of Glaciology*, 30, 146–152, https://doi.org/10.3189/172756400781820633.

Nicholls, R. J. and Cazenave, A. (2010). Sea-Level Rise and Its Impact on Coastal Zones. *Science*, 328(5985), 1517–1520, https://doi.org/10.1126/science.1185782.

Nicholls, R. J., Lincke, D., Hinkel, J., Brown, S., Vafeidis, A. T., Meyssignac, B., Hanson, S. E., Merkens, J.-L., and Fang, J. (2021). A global analysis of subsidence, relative sea-level change and coastal flood exposure. *Nature Climate Change*, 11(4), 338–342, https://doi.org/10.1038/s41558-021-00993-z.

Nye, J. F. (1953). The flow law of ice from measurements in glacier tunnels, laboratory experiments and the Jungfraufirn borehole experiment. *Proceedings of the Royal Society of London. Series A. Mathematical and Physical Sciences*, 219(1139), 477–489, https://doi.org/10.1098/rspa.1953.0161.

Nye, J. F. (1957). The distribution of stress and velocity in glaciers and ice-sheets. *Proceedings of the Royal Society of London. Series A. Mathematical and Physical Sciences*, 239(1216), 113–133, https://doi.org/10.1098/rspa.1957.0026.

Nye, J. F. (1969). A calculation on the sliding of ice over a wavy surface using a Newtonian viscous approximation. *Proceedings of the Royal Society of London. A. Mathematical and Physical Sciences*, 311(1506), 445–467, https://doi.org/10.1098/rspa.1969.0127.

Nye, J. F. (1970). Glacier sliding without cavitation in a linear viscous approximation. *Proceedings of the Royal Society of London. A. Mathematical and Physical Sciences*, 315(1522), 381–403, https://doi.org/10.1098/rspa.1970.0050.

Nye, J. F. (1976). Water Flow in Glaciers: Jökulhlaups, Tunnels and Veins. *Journal of Glaciology*, 17(76), 181–207, https://doi.org/10.3189/s002214300001354x.

Oñate, E. and Carbonell, J. M. (2014). Updated lagrangian mixed finite element formulation for quasi and fully incompressible fluids. *Computational Mechanics*, 54(6), 1583–1596, https://doi.org/10.1007/s00466-014-1078-1.

Oerlemans, J. (1981). Some basic experiments with a vertically-integrated ice sheet model. *Tellus*, 33(1), 1–11, https://doi.org/10.1111/j.2153-3490.1981.tb01726.x.

Osher, S. and Fedkiw, R. (2003). *Level Set Methods and Dynamic Implicit Surfaces*. Springer New York, https://doi.org/10.1007/b98879.

Osher, S. and Fedkiw, R. P. (2001). Level Set Methods: An Overview and Some Recent Results. *Journal of Computational Physics*, 169(2), 463–502, https://doi.org/10.1006/jcph.2000.6636.

Parizek, B. R. (2024). Grounding Zones: The "Inland" Dynamic Interface Between Seawater, Outlet Glaciers, Subglacial Meltwater Routing, and Ice-Shelf Processes. *Geophysical Research Letters*, 51(15), https://doi.org/10.1029/2024gl110427.

Parizek, B. R., Christianson, K., Anandakrishnan, S., Alley, R. B., Walker, R. T., Edwards, R. A., Wolfe, D. S., Bertini, G. T., Rinehart, S. K., Bindschadler, R. A., and Nowicki, S. M. J. (2013). Dynamic (in)stability of Thwaites Glacier, West Antarctica. *Journal of Geophysical Research: Earth Surface*, 118(2), 638–655, https://doi.org/10.1002/jgrf.20044.

Parker, G. (1978). Self-formed straight rivers with equilibrium banks and mobile bed. Part 1. The sand-silt river. *Journal of Fluid Mechanics*, 89(1), 109–125, https://doi.org/10.1017/s0022112078002499.

Paterson, W. S. B. (1994). *The physics of glaciers*. Oxford, OX, England Tarrytown, N.Y., U.S.A: Pergamon.

Pattyn, F. (1996). Numerical modelling of a fast-flowing outlet glacier: experiments with different basal conditions. *Annals of Glaciology*, 23, 237–246, https://doi.org/10.3189/s0260305500013495.

Pattyn, F. (2003). A new three-dimensional higher-order thermomechanical ice sheet model: Basic sensitivity, ice stream development, and ice flow across subglacial lakes. *Journal of Geophysical Research*, 108(B8), https://doi.org/10.1029/2002jb002329.

Pattyn, F. (2010). Antarctic subglacial conditions inferred from a hybrid ice sheet/ice stream model. *Earth and Planetary Science Letters*, 295(3–4), 451–461, https://doi.org/10.1016/j.epsl.2010.04.025.

Pattyn, F. (2017). Sea-level response to melting of Antarctic ice shelves on multi-centennial timescales with the fast Elementary Thermomechanical Ice Sheet model (f.ETISh v1.0). *The Cryosphere*, 11(4), 1851–1878, https://doi.org/10.5194/tc-11-1851-2017.

Pattyn, F. (2018). The paradigm shift in Antarctic ice sheet modelling. *Nature Communications*, 9(1), https://doi.org/10.1038/s41467-018-05003-z.

Pattyn, F. (2023). Numerical modelling of ice sheets and ice shelves. *Lecture notes of the Karthaus Summer School*.

Pattyn, F., De Brabander, S., and Huyghe, A. (2005). Basal and thermal control mechanisms of the Ragnhild glaciers, East Antarctica. *Annals of Glaciology*, 40, 225–231, https://doi.org/10.3189/172756405781813672.

Pattyn, F., Huyghe, A., De Brabander, S., and De Smedt, B. (2006). Role of transition zones in marine ice sheet dynamics. *Journal of Geophysical Research: Earth Surface*, 111(F2), https://doi.org/10.1029/2005jf000394.

Pattyn, F. and Morlighem, M. (2020). The uncertain future of the Antarctic Ice Sheet. *Science*, 367(6484), 1331–1335, https://doi.org/10.1126/science.aaz5487.

Pattyn, F., Perichon, L., Aschwanden, A., Breuer, B., de Smedt, B., Gagliardini, O., Gudmundsson, G. H., Hindmarsh, R. C. A., Hubbard, A., Johnson, J. V., Kleiner, T., Konovalov, Y., Martin, C., Payne, A. J., Pollard, D., Price, S., Rückamp, M., Saito, F., Souček, O., Sugiyama, S., and Zwinger, T. (2008). Benchmark experiments for higher-order and full-Stokes ice sheet models (ISMIP-HOM). *The Cryosphere*, 2(2), 95–108, https://doi.org/10.5194/tc-2-95-2008.

Pattyn, F., Perichon, L., Durand, G., Favier, L., Gagliardini, O., Hindmarsh, R. C., Zwinger, T., Albrecht, T., Cornford, S., Docquier, D., Fürst, J. J., Goldberg, D., Gudmundsson, G. H., Humbert, A., Hütten, M., Huybrechts, P., Jouvet, G., Kleiner, T., Larour, E., Martin, D., Morlighem, M., Payne, A. J., Pollard, D., Rückamp, M., Rybak, O., Seroussi, H., Thoma, M., and Wilkens, N. (2013). Grounding-line migration in plan-view marine ice-sheet models: results of the ice2sea MISMIP3d intercomparison. *Journal of Glaciology*, 59(215), 410–422, https://doi.org/10.3189/2013jog12j129.

Pattyn, F., Schoof, C., Perichon, L., Hindmarsh, R. C. A., Bueler, E., de Fleurian, B., Durand, G., Gagliardini, O., Gladstone, R., Goldberg, D., Gudmundsson, G. H., Huybrechts, P., Lee, V., Nick, F. M., Payne, A. J., Pollard, D., Rybak, O., Saito, F., and Vieli, A. (2012). Results of the Marine Ice Sheet Model Intercomparison Project, MISMIP. *The Cryosphere*, 6(3), 573–588, https://doi.org/10.5194/tc-6-573-2012.

Pegler, S. S. (2016). The dynamics of confined extensional flows. *Journal of Fluid Mechanics*, 804, 24–57, https://doi.org/10.1017/jfm.2016.516.

Pegler, S. S. (2018a). Marine ice sheet dynamics: the impacts of ice-shelf buttressing. *Journal of Fluid Mechanics*, 857, 605–647, https://doi.org/10.1017/jfm.2018.741.

Pegler, S. S. (2018b). Suppression of marine ice sheet instability. *Journal of Fluid Mechanics*, 857, 648–680, https://doi.org/10.1017/jfm.2018.742.

Pelle, T., Greenbaum, J. S., Dow, C. F., Jenkins, A., and Morlighem, M. (2023). Subglacial discharge accelerates future retreat of Denman and Scott Glaciers, East Antarctica. *Science Advances*, 9(43), https://doi.org/10.1126/sciadv.adi9014.

Perego, M., Gunzburger, M., and Burkardt, J. (2012). Parallel finite-element implementation for higher-order ice-sheet models. *Journal of Glaciology*, 58(207), 76–88, https://doi.org/10.3189/2012jog11j063.

Perego, M., Price, S., and Stadler, G. (2014). Optimal initial conditions for coupling ice sheet models to Earth system models. *Journal of Geophysical Research: Earth Surface*, 119(9), 1894–1917, https://doi.org/10.1002/2014jf003181.

Petra, N., Martin, J., Stadler, G., and Ghattas, O. (2014). A Computational Framework for Infinite-Dimensional Bayesian Inverse Problems, Part II: Stochastic Newton MCMC with Application to Ice Sheet Flow Inverse Problems. *SIAM Journal on Scientific Computing*, 36(4), A1525–a1555, https://doi.org/10.1137/130934805.

Petra, N., Zhu, H., Stadler, G., Hughes, T. J., and Ghattas, O. (2012). An inexact Gauss–Newton method for inversion of basal sliding and rheology parameters in a nonlinear Stokes ice sheet model. *Journal of Glaciology*, 58(211), 889–903, https://doi.org/10.3189/2012jog11j182.

Pollard, D. and DeConto, R. M. (2012a). A simple inverse method for the distribution of basal sliding coefficients under ice sheets, applied to Antarctica. *The Cryosphere*, 6(5), 953–971, https://doi.org/10.5194/tc-6-953-2012.

Pollard, D. and DeConto, R. M. (2012b). Description of a hybrid ice sheet-shelf model, and application to Antarctica. *Geoscientific Model Development*, 5(5), 1273–1295, https://doi.org/10.5194/gmd-5-1273-2012.

Pollard, D. and DeConto, R. M. (2020). Improvements in one-dimensional grounding-line parameterizations in an ice-sheet model with lateral variations (PSUICE3D v2.1). *Geoscientific Model Development*, 13(12), 6481–6500, https://doi.org/10.5194/gmd-13-6481-2020.

Purich, A. and England, M. H. (2023). Projected Impacts of Antarctic Meltwater Anomalies over the Twenty-First Century. *Journal of Climate*, 36(8), 2703–2719, https://doi.org/10.1175/jcli-d-22-0457.1.

Reed, B., Green, J. A. M., Jenkins, A., and Gudmundsson, G. H. (2023). Recent irreversible retreat phase of Pine Island Glacier. *Nature Climate Change*, 14(1), 75–81, https://doi.org/10.1038/s41558-023-01887-y.

Reese, R., Albrecht, T., Mengel, M., Asay-Davis, X., and Winkelmann, R. (2018a). Antarctic sub-shelf melt rates via PICO. *The Cryosphere*, 12(6), 1969–1985, https://doi.org/10.5194/tc-12-1969-2018.

Reese, R., Garbe, J., Hill, E. A., Urruty, B., Naughten, K. A., Gagliardini, O., Durand, G., Gillet-Chaulet, F., Gudmundsson, G. H., Chandler, D., Langebroek, P. M., and Winkelmann, R. (2023). The stability of present-day Antarctic grounding lines – Part 2: Onset of irreversible retreat of Amundsen Sea glaciers under current climate on centennial timescales cannot be excluded. *The Cryosphere*, 17(9), 3761–3783, https://doi.org/10.5194/tc-17-3761-2023.

Reese, R., Winkelmann, R., and Gudmundsson, G. H. (2018b). Grounding-line flux formula applied as a flux condition in numerical simulations fails for buttressed Antarctic ice streams. *The Cryosphere*, 12(10), 3229–3242, https://doi.org/10.5194/tc-12-3229-2018.

Rignot, E., Ciraci, E., Scheuchl, B., Tolpekin, V., Wollersheim, M., and Dow, C. (2024). Widespread seawater intrusions beneath the grounded ice of Thwaites Glacier, West Antarctica. *Proceedings of the National Academy of Sciences*, 121(22), https://doi.org/10.1073/pnas.2404766121.

Rignot, E. and Mouginot, J. (2012). Ice flow in Greenland for the International Polar Year 2008–2009. *Geophysical Research Letters*, 39(11), https://doi.org/10.1029/2012gl051634.

Rignot, E., Mouginot, J., Morlighem, M., Seroussi, H., and Scheuchl, B. (2014). Widespread, rapid grounding line retreat of Pine Island, Thwaites, Smith, and Kohler glaciers, West Antarctica, from 1992 to 2011. *Geophysical Research Letters*, 41(10), 3502–3509, https://doi.org/10.1002/2014gl060140.

Ritz, C., Edwards, T. L., Durand, G., Payne, A. J., Peyaud, V., and Hindmarsh, R. C. A. (2015). Potential sea-level rise from Antarctic ice-sheet instability constrained by observations. *Nature*, 528(7580), 115–118, https://doi.org/10.1038/nature16147.

Robel, A. A., DeGiuli, E., Schoof, C., and Tziperman, E. (2013). Dynamics of ice stream temporal variability: Modes, scales, and hysteresis. *Journal of Geophysical Research: Earth Surface*, 118(2), 925–936, https://doi.org/10.1002/jgrf.20072.

Robel, A. A., Pegler, S. S., Catania, G., Felikson, D., and Simkins, L. M. (2022a). Ambiguous stability of glaciers at bed peaks. *Journal of Glaciology*, 68(272), 1177–1184, https://doi.org/10.1017/jog.2022.31.

Robel, A. A., Roe, G. H., and Haseloff, M. (2018). Response of Marine-Terminating Glaciers to Forcing: Time Scales, Sensitivities, Instabilities, and Stochastic Dynamics. *Journal of Geophysical Research: Earth Surface*, 123(9), 2205–2227, https://doi.org/10.1029/2018jf004709.

Robel, A. A., Schoof, C., and Tziperman, E. (2016). Persistence and variability of ice-stream grounding lines on retrograde bed slopes. *The Cryosphere*, 10(4), 1883–1896, https://doi.org/10.5194/tc-10-1883-2016.

Robel, A. A., Seroussi, H., and Roe, G. H. (2019). Marine ice sheet instability amplifies and skews uncertainty in projections of future sea-level rise. *Proceedings of the National Academy of Sciences*, 116(30), 14887–14892, https://doi.org/10.1073/pnas.1904822116.

Robel, A. A., Sim, S. J., Meyer, C., Siegfried, M. R., and Gustafson, C. D. (2023). Contemporary ice sheet thinning drives subglacial groundwater exfiltration with potential feedbacks on glacier flow. *Science Advances*, 9(33), https://doi.org/10.1126/sciadv.adh3693.

Robel, A. A., Wilson, E., and Seroussi, H. (2022b). Layered seawater intrusion and melt under grounded ice. *The Cryosphere*, 16(2), 451–469, https://doi.org/10.5194/tc-16-451-2022.

Robin, G. d. Q., Swithinbank, C., Smith, B., et al. (1970). Radio echo exploration of the Antarctic ice sheet. *International Association of Scientific Hydrology Publication*, 86, 97–115.

Robinson, A., Alvarez-Solas, J., Montoya, M., Goelzer, H., Greve, R., and Ritz, C. (2020). Description and validation of the ice-sheet model Yelmo (version 1.0). *Geoscientific Model Development*, 13(6), 2805–2823, https://doi.org/10.5194/gmd-13-2805-2020.

Rosier, S. H. R., Reese, R., Donges, J. F., De Rydt, J., Gudmundsson, G. H., and Winkelmann, R. (2021). The tipping points and early warning indicators for Pine Island Glacier, West Antarctica. *The Cryosphere*, 15(3), 1501–1516, https://doi.org/10.5194/tc-15-1501-2021.

Röthlisberger, H. (1972). Water Pressure in Intra- and Subglacial Channels. *Journal of Glaciology*, 11(62), 177–203, https://doi.org/10.3189/s0022143000022188.

Ryser, C., Lüthi, M. P., Andrews, L. C., Hoffman, M. J., Catania, G. A., Hawley, R. L., Neumann, T. A., and Kristensen, S. S. (2014). Sustained high basal motion of the Greenland ice sheet revealed by borehole deformation. *Journal of Glaciology*, 60(222), 647–660, https://doi.org/10.3189/2014jog13j196.

Saramito, P. (2016). *Complex fluids: Modeling and Algorithms*. Springer International Publishing, https://doi.org/10.1007/978-3-319-44362-1.

Schoof, C. (2003). The effect of basal topography on ice sheet dynamics. *Continuum Mechanics and Thermodynamics*, 15(3), 295–307, https://doi.org/10.1007/s00161-003-0119-3.

Schoof, C. (2005). The effect of cavitation on glacier sliding. *Proceedings of the Royal Society A: Mathematical, Physical and Engineering Sciences*, 461(2055), 609–627, https://doi.org/10.1098/rspa.2004.1350.

Schoof, C. (2006). A variational approach to ice stream flow. *Journal of Fluid Mechanics*, 556, 227, https://doi.org/10.1017/s0022112006009591.

Schoof, C. (2007a). Cavitation on Deformable Glacier Beds. *SIAM Journal on Applied Mathematics*, 67(6), 1633–1653, https://doi.org/10.1137/050646470.

Schoof, C. (2007b). Ice sheet grounding line dynamics: Steady states, stability, and hysteresis. *Journal of Geophysical Research*, 112(F3), https://doi.org/10.1029/2006jf000664.

Schoof, C. (2007c). Marine ice-sheet dynamics. Part 1. The case of rapid sliding. *Journal of Fluid Mechanics*, 573, 27–55, https://doi.org/10.1017/s0022112006003570.

Schoof, C. (2007d). Pressure-dependent viscosity and interfacial instability in coupled ice-sediment flow. *Journal of Fluid Mechanics*, 570, 227–252, https://doi.org/10.1017/s0022112006002874.

Schoof, C. (2010a). Coulomb friction and other sliding laws in a higher order glacier flow model. *Mathematical Models and Methods in Applied Sciences*, 20(01), 157–189, https://doi.org/10.1142/s0218202510004180.

Schoof, C. (2010b). Ice-sheet acceleration driven by melt supply variability. *Nature*, 468(7325), 803–806, https://doi.org/10.1038/nature09618.

Schoof, C. (2011). Marine ice sheet dynamics. Part 2. A Stokes flow contact problem. *Journal of Fluid Mechanics*, 679, 122–155, https://doi.org/10.1017/jfm.2011.129.

Schoof, C. (2012). Marine ice sheet stability. *Journal of Fluid Mechanics*, 698, 62–72, https://doi.org/10.1017/jfm.2012.43.

Schoof, C., Davis, A. D., and Popa, T. V. (2017). Boundary layer models for calving marine outlet glaciers. *The Cryosphere*, 11(5), 2283–2303, https://doi.org/10.5194/tc-11-2283-2017.

Schoof, C. and Hewitt, I. J. (2013). Ice-Sheet Dynamics. *Annual Review of Fluid Mechanics*, 45(1), 217–239, https://doi.org/10.1146/annurev-fluid-011212-140632.

Schoof, C. and Hewitt, I. J. (2016). A model for polythermal ice incorporating gravity-driven moisture transport. *Journal of Fluid Mechanics*, 797, 504–535, https://doi.org/10.1017/jfm.2016.251.

Schoof, C., Hewitt, I. J., and Werder, M. A. (2012). Flotation and free surface flow in a model for subglacial drainage. Part 1. Distributed drainage. *Journal of Fluid Mechanics*, 702, 126–156, https://doi.org/10.1017/jfm.2012.165.

Schoof, C. and Hindmarsh, R. C. A. (2010). Thin-Film Flows with Wall Slip: An Asymptotic Analysis of Higher Order Glacier Flow Models. *The Quarterly Journal of Mechanics and Applied Mathematics*, 63(1), 73–114, https://doi.org/10.1093/qjmam/hbp025.

Schroeder, D. M., Blankenship, D. D., Young, D. A., Witus, A. E., and Anderson, J. B. (2014). Airborne radar sounding evidence for deformable sediments and outcropping bedrock beneath Thwaites Glacier, West Antarctica. *Geophysical Research Letters*, 41(20), 7200–7208, https://doi.org/10.1002/2014gl061645.

Sergienko, O. and Wingham, D. J. (2024). Diverse behaviors of marine ice sheets in response to temporal variability of the atmospheric and basal conditions. *Journal of Glaciology*, (pp. 1–12)., https://doi.org/10.1017/jog.2024.43.

Sergienko, O. V. (2012). The effects of transverse bed topography variations in ice-flow models. *Journal of Geophysical Research: Earth Surface*, 117(F3), https://doi.org/10.1029/2011jf002203.

Sergienko, O. V. (2022a). Marine outlet glacier dynamics, steady states and steady-state stability. *Journal of Glaciology*, (pp. 1–15)., https://doi.org/10.1017/jog.2022.13.

Sergienko, O. V. (2022b). No general stability conditions for marine ice-sheet grounding lines in the presence of feedbacks. *Nature Communications*, 13(1), https://doi.org/10.1038/s41467-022-29892-3.

Sergienko, O. V. and Haseloff, M. (2023). 'Stable' and 'unstable' are not useful descriptions of marine ice sheets in the Earth's climate system. *Journal of Glaciology*, (pp. 1–17)., https://doi.org/10.1017/jog.2023.40.

Sergienko, O. V. and Wingham, D. J. (2019). Grounding line stability in a regime of low driving and basal stresses. *Journal of Glaciology*, 65(253), 833–849, https://doi.org/10.1017/jog.2019.53.

Sergienko, O. V. and Wingham, D. J. (2022). Bed topography and marine ice-sheet stability. *Journal of Glaciology*, 68(267), 124–138, https://doi.org/10.1017/jog.2021.79.

Seroussi, H., Morlighem, M., Larour, E., Rignot, E., and Khazendar, A. (2014). Hydrostatic grounding line parameterization in ice sheet models. *The Cryosphere*, 8(6), 2075–2087, https://doi.org/10.5194/tc-8-2075-2014.

Seroussi, H., Nowicki, S., Payne, A. J., Goelzer, H., Lipscomb, W. H., Abe-Ouchi, A., Agosta, C., Albrecht, T., Asay-Davis, X., Barthel, A., Calov, R., Cullather, R., Dumas, C., Galton-Fenzi, B. K., Gladstone, R., Golledge, N. R., Gregory, J. M., Greve, R., Hattermann, T., Hoffman, M. J., Humbert, A., Huybrechts, P., Jourdain, N. C., Kleiner, T., Larour, E., Leguy, G. R., Lowry, D. P., Little, C. M., Morlighem, M., Pattyn, F., Pelle, T., Price, S. F., Quiquet, A., Reese, R., Schlegel, N.-J., Shepherd, A., Simon, E., Smith, R. S., Straneo, F., Sun, S., Trusel, L. D., Van Breedam, J., van de Wal, R. S. W., Winkelmann, R., Zhao, C., Zhang, T., and Zwinger, T. (2020). ISMIP6 Antarctica: a multi-model ensemble of the Antarctic ice sheet evolution over the 21st century. *The Cryosphere*, 14(9), 3033–3070, https://doi.org/10.5194/tc-14-3033-2020.

Seroussi, H., Nowicki, S., Simon, E., Abe-Ouchi, A., Albrecht, T., Brondex, J., Cornford, S., Dumas, C., Gillet-Chaulet, F., Goelzer, H., Golledge, N. R., Gregory, J. M., Greve, R., Hoffman, M. J., Humbert, A., Huybrechts, P., Kleiner, T., Larour, E., Leguy, G., Lipscomb, W. H., Lowry, D., Mengel, M., Morlighem, M., Pattyn, F., Payne, A. J., Pollard, D., Price, S. F., Quiquet, A., Reerink, T. J., Reese, R., Rodehacke, C. B., Schlegel, N.-J., Shepherd, A., Sun, S., Sutter, J., Van Breedam, J., van de Wal, R. S. W., Winkelmann, R., and Zhang, T. (2019). initMIP-Antarctica: an ice sheet model initialization experiment of ISMIP6. *The Cryosphere*, 13(5), 1441–1471, https://doi.org/10.5194/tc-13-1441-2019.

Shapiro, N. M. and Ritzwoller, M. H. (2004). Inferring surface heat flux distributions guided by a global seismic model: particular application to Antarctica. *Earth and Planetary Science Letters*, 223(1), 213–224, https://doi.org/https://doi.org/10.1016/j.epsl.2004.04.011.

Shevitz, D. and Paden, B. (1994). Lyapunov stability theory of nonsmooth systems. *IEEE Transactions on Automatic Control*, 39(9), 1910–1914, https://doi.org/10.1109/9.317122.

Shreve, R. L. (1972). Movement of Water in Glaciers. *Journal of Glaciology*, 11(62), 205–214, https://doi.org/10.3189/s002214300002219x.

Shreve, R. L. (1984). Glacier Sliding at Subfreezing Temperatures. *Journal of Glaciology*, 30(106), 341–347, https://doi.org/10.3189/s0022143000006195.

Smith, B. E., Fricker, H. A., Joughin, I. R., and Tulaczyk, S. (2009). An inventory of active subglacial lakes in Antarctica detected by ICESat (2003–2008). *Journal of Glaciology*, 55(192), 573–595, https://doi.org/10.3189/002214309789470879.

Sommers, A., Rajaram, H., and Morlighem, M. (2018). SHAKTI: Subglacial Hydrology and Kinetic, Transient Interactions v1.0. *Geoscientific Model Development*, 11(7), 2955–2974, https://doi.org/10.5194/gmd-11-2955-2018.

Stechlinski, P., Khan, K. A., and Barton, P. I. (2018). Generalized Sensitivity Analysis of Nonlinear Programs. *SIAM Journal on Optimization*, 28(1), 272–301, https://doi.org/10.1137/17m1120385.

Stevens, D., Ely, J. C., Livingstone, S. J., Clark, C. D., Butcher, F. E. G., and Hewitt, I. (2022). Effects of basal topography and ice-sheet surface slope in a subglacial glaciofluvial deposition model. *Journal of Glaciology*, 69(274), 397–409, https://doi.org/10.1017/jog.2022.71.

Storrar, R. D., Stokes, C. R., and Evans, D. J. (2014). Morphometry and pattern of a large sample (>20, 000) of Canadian eskers and implications for subglacial drainage beneath ice sheets. *Quaternary Science Reviews*, 105, 1–25, https://doi.org/10.1016/j.quascirev.2014.09.013.

Stubblefield, A. G., Spiegelman, M., and Creyts, T. T. (2021). Variational formulation of marine ice-sheet and subglacial-lake grounding-line dynamics. *Journal of Fluid Mechanics*, 919, https://doi.org/10.1017/jfm.2021.394.

Sun, S., Cornford, S. L., Moore, J. C., Gladstone, R., and Zhao, L. (2017). Ice shelf fracture parameterization in an ice sheet model. *The Cryosphere*, 11(6), 2543–2554, https://doi.org/10.5194/tc-11-2543-2017.

Sun, S., Pattyn, F., Simon, E. G., Albrecht, T., Cornford, S., Calov, R., Dumas, C., Gillet-Chaulet, F., Goelzer, H., Golledge, N. R., Greve, R., Hoffman, M. J., Humbert, A., Kazmierczak, E., Kleiner, T., Leguy, G. R., Lipscomb, W. H., Martin, D., Morlighem, M., Nowicki, S., Pollard, D., Price, S., Quiquet, A., Seroussi, H., Schlemm, T., Sutter, J., van de Wal, R. S. W., Winkelmann, R., and Zhang, T. (2020). Antarctic ice sheet response to sudden and sustained ice-shelf collapse (ABUMIP). *Journal of Glaciology*, 66(260), 891–904, https://doi.org/10.1017/jog.2020.67.

Tezaur, I. K., Perego, M., Salinger, A. G., Tuminaro, R. S., and Price, S. F. (2015). Albany/FELIX: a parallel, scalable and robust, finite element, first-order Stokes approximation ice sheet solver built for advanced analysis. *Geoscientific Model Development*, 8(4), 1197–1220, https://doi.org/10.5194/gmd-8-1197-2015.

Thacher, W., Johansen, H., and Martin, D. (2024). A high order cut-cell method for solving the shallow-shelf equations. *Journal of Computational Science*, 80, 102319, https://doi.org/10.1016/j.jocs.2024.102319.

Trouette, B., Atallah, G. H., and Vincent, S. (2020). A Mixed Eulerian–Lagrangian scheme for scalar transport. *Acta Mechanica*, 231(9), 3525–3549, https://doi.org/10.1007/s00707-020-02727-2.

Tsai, V. C., Stewart, A. L., and Thompson, A. F. (2015). Marine ice-sheet profiles and stability under Coulomb basal conditions. *Journal of Glaciology*, 61(226), 205–215, https://doi.org/10.3189/2015jog14j221.

Tulaczyk, S., Kamb, W. B., and Engelhardt, H. F. (2000a). Basal mechanics of Ice Stream B, west Antarctica: 1. Till mechanics. *Journal of Geophysical Research: Solid Earth*, 105(B1), 463–481, https://doi.org/10.1029/1999jb900329.

Tulaczyk, S., Kamb, W. B., and Engelhardt, H. F. (2000b). Basal mechanics of Ice Stream B, west Antarctica: 2. Undrained plastic bed model. *Journal of Geophysical Research: Solid Earth*, 105(B1), 483–494, https://doi.org/10.1029/1999jb900328.

Tuminaro, R., Perego, M., Tezaur, I., Salinger, A., and Price, S. (2016). A Matrix Dependent/Algebraic Multigrid Approach for Extruded Meshes with Applications to Ice Sheet Modeling. *SIAM Journal on Scientific Computing*, 38(5), C504–c532, https://doi.org/10.1137/15m1040839.

van der Wel, N., Christoffersen, P., and Bougamont, M. (2013). The influence of subglacial hydrology on the flow of Kamb Ice Stream, West Antarctica. *Journal of Geophysical Research: Earth Surface*, 118(1), 97–110, https://doi.org/10.1029/2012jf002570.

van Wessem, J. M., van de Berg, W. J., Noël, B. P. Y., van Meijgaard, E., Amory, C., Birnbaum, G., Jakobs, C. L., Krüger, K., Lenaerts, J. T. M., Lhermitte, S., Ligtenberg, S. R. M., Medley, B., Reijmer, C. H., van Tricht, K., Trusel, L. D., van Ulft, L. H., Wouters, B., Wuite, J., and van den Broeke, M. R. (2018). Modelling the climate and surface mass balance of polar ice sheets using RACMO2 – Part 2: Antarctica (1979–2016). *The Cryosphere*, 12(4), 1479–1498, https://doi.org/10.5194/tc-12-1479-2018.

Vassaux, M., Richardson, R. A., and Coveney, P. V. (2019). The heterogeneous multiscale method applied to inelastic polymer mechanics. *Philosophical Transactions of the Royal Society A: Mathematical, Physical and Engineering Sciences*, 377(2142), 20180150, https://doi.org/10.1098/rsta.2018.0150.

Vaughan, D. G. (1995). Tidal flexure at ice shelf margins. *Journal of Geophysical Research: Solid Earth*, 100(B4), 6213–6224, https://doi.org/10.1029/94jb02467.

Verjans, V. and Robel, A. (2024). Accelerating Subglacial Hydrology for Ice Sheet Models With Deep Learning Methods. *Geophysical Research Letters*, 51(2), https://doi.org/10.1029/2023gl105281.

Verjans, V., Robel, A. A., Seroussi, H., Ultee, L., and Thompson, A. F. (2022). The Stochastic Ice-Sheet and Sea-Level System Model v1.0 (StISSM v1.0). *Geoscientific Model Development*, 15(22), 8269–8293, https://doi.org/10.5194/gmd-15-8269-2022.

Walder, J. S. (1982). Stability of Sheet Flow of Water Beneath Temperate Glaciers and Implications for Glacier Surging. *Journal of Glaciology*, 28(99), 273–293, https://doi.org/10.3189/s0022143000011631.

Walder, J. S. (1986). Hydraulics of Subglacial Cavities. *Journal of Glaciology*, 32(112), 439–445, https://doi.org/10.3189/s0022143000012156.

Walder, J. S. and Fowler, A. (1994). Channelized subglacial drainage over a deformable bed. *Journal of Glaciology*, 40(134), 3–15, https://doi.org/10.3189/s0022143000003750.

Warburton, K., Meyer, C., and Sommers, A. (2024). Numerical and physical instability of subglacial water flow. *EarthArXiv preprint*, https://doi.org/10.31223/x54t32.

Warburton, K. L. P., Hewitt, D. R., and Neufeld, J. A. (2023). Shear dilation of subglacial till results in time-dependent sliding laws. *Proceedings of the Royal Society A: Mathematical, Physical and Engineering Sciences*, 479(2269), https://doi.org/10.1098/rspa.2022.0536.

Watkins, J., Carlson, M., Shan, K., Tezaur, I., Perego, M., Bertagna, L., Kao, C., Hoffman, M. J., and Price, S. F. (2023). Performance portable ice-sheet modeling with MALI. *The International Journal of High Performance Computing Applications*, 37(5), 600–625, https://doi.org/10.1177/10943420231183688.

Wauthy, S., Tison, J.-L., Inoue, M., El Amri, S., Sun, S., Fripiat, F., Claeys, P., and Pattyn, F. (2024). Spatial and temporal variability of environmental proxies from the top 120m of two ice cores in Dronning Maud Land (East Antarctica). *Earth System Science Data*, 16(1), 35–58, https://doi.org/10.5194/essd-16-35-2024.

Weertman, J. (1957). On the Sliding of Glaciers. *Journal of Glaciology*, 3(21), 33–38, https://doi.org/10.3189/s0022143000024709.

Weertman, J. (1972). General theory of water flow at the base of a glacier or ice sheet. *Reviews of Geophysics*, 10(1), 287–333, https://doi.org/10.1029/rg010i001p00287.

Weertman, J. (1974). Stability of the Junction of an Ice Sheet and an Ice Shelf. *Journal of Glaciology*, 13(67), 3–11, https://doi.org/10.3189/s0022143000023327.

Weertman, J. (1983). Creep Deformation of Ice. *Annual Review of Earth and Planetary Sciences*, 11(1), 215–240, https://doi.org/10.1146/annurev.ea.11.050183.001243.

Weertman, J. and Birchfield, G. E. (1982). Subglacial Water flow Under Ice Streams and West Antarctic Ice-Sheet Stability. *Annals of Glaciology*, 3, 316–320, https://doi.org/10.3189/s0260305500002998.

Weis, M., Greve, R., and Hutter, K. (1999). Theory of shallow ice shelves. *Continuum Mechanics and Thermodynamics*, 11(1), 15–50, https://doi.org/10.1007/s001610050102.

Werder, M. A., Hewitt, I. J., Schoof, C. G., and Flowers, G. E. (2013). Modeling channelized and distributed subglacial drainage in two dimensions. *Journal of Geophysical Research: Earth Surface*, 118(4), 2140–2158, https://doi.org/10.1002/jgrf.20146.

Whitehouse, P. L. (2018). Glacial isostatic adjustment modelling: historical perspectives, recent advances, and future directions. *Earth Surface Dynamics*, 6(2), 401–429, https://doi.org/10.5194/esurf-6-401-2018.

Wilchinsky, A. V. and Chugunov, V. A. (2000). Ice-stream-ice-shelf transition: theoretical analysis of two-dimensional flow. *Annals of Glaciology*, 30, 153–162, https://doi.org/10.3189/172756400781820868.

Wild, C. T., Alley, K. E., Muto, A., Truffer, M., Scambos, T. A., and Pettit, E. C. (2022). Weakening of the pinning point buttressing Thwaites Glacier, West Antarctica. *The Cryosphere*, 16(2), 397–417, https://doi.org/10.5194/tc-16-397-2022.

Willis, I. C., Pope, E. L., Leysinger Vieli, G. J.-M., Arnold, N. S., and Long, S. (2016). Drainage networks, lakes and water fluxes beneath the Antarctic ice sheet. *Annals of Glaciology*, 57(72), 96–108, https://doi.org/10.1017/aog.2016.15.

Winkelmann, R., Martin, M. A., Haseloff, M., Albrecht, T., Bueler, E., Khroulev, C., and Levermann, A. (2011). The Potsdam Parallel Ice Sheet Model (PISM-PIK) –Part 1: Model description. *The Cryosphere*, 5(3), 715–726, https://doi.org/10.5194/tc-5-715-2011.

Winkelmann, R., Steinert, N. J., McKay, D. I. A., Brovkin, V., Kääb, A., and Notz, D. (2023). Tipping points in the cryosphere. In T. M. Lenton, D. I. Armstron McKay, S. Lorani, J. F. Abrams, S. J. Lade, J. F. Donges, and others (Eds.), *The Global Tipping Points: Report 2023*, (pp. 56–77). Exeter: University of Exeter.

Zhong, S., Kang, K., A, G., and Qin, C. (2022). CitcomSVE: A Three-Dimensional Finite Element Software Package for Modeling Planetary Mantle's Viscoelastic Deformation in Response to Surface and Tidal Loads. *Geochemistry, Geophysics, Geosystems*, 23(10), https://doi.org/10.1029/2022gc010359.

Zimmerman, R. W., Al-Yaarubi, A., Pain, C. C., and Grattoni, C. A. (2004). Non-linear regimes of fluid flow in rock fractures. *International Journal of Rock Mechanics and Mining Sciences*, 41, 163–169, https://doi.org/10.1016/j.ijrmms.2004.03.036.

Zoet, L. K. and Iverson, N. R. (2015). Experimental determination of a double-valued drag relationship for glacier sliding. *Journal of Glaciology*, 61(225), 1–7, https://doi.org/10.3189/2015jog14j174.

Zoet, L. K. and Iverson, N. R. (2020). A slip law for glaciers on deformable beds. *Science*, 368(6486), 76–78, https://doi.org/10.1126/science.aaz1183.